Anisotropy and deformation in the Earth's mantle: seismological observations, geodynamical models, and laboratory experiments

by

Maureen Devaney Long

B.S. Geology
Rensselaer Polytechnic Institute, 2000

Submitted to the Department of Earth, Atmospheric, and Planetary Sciences
in partial fulfillment of the requirements for the degree of

Doctor of Philosophy

at the

MASSACHUSETTS INSTITUTE OF TECHNOLOGY

June 2006

Author……

Department of Earth, Atmospheric, and Planetary Sciences
May 5, 2006

Certified by……

Robert D. van der Hilst
Cecil and Ida Green Professor of Earth and Planetary Sciences
Thesis Supervisor

Accepted by……...

Maria T. Zuber
E. A. Griswold Professor of Geophysics
Head, Department of Earth, Atmospheric, and Planetary Sciences

Anisotropy and deformation in the Earth's mantle: seismological observations, geodynamical models, and laboratory experiments

by

Maureen Devaney Long

Submitted to the Department of Earth, Atmospheric, and Planetary Sciences
on May 5, 2006 in partial fulfillment of the requirements for the degree of
Doctor of Philosophy in Geophysics

Abstract

In this thesis I report the results of several studies of elastic anisotropy and deformation in the Earth's mantle, using shear wave splitting measurements, numerical models of geodynamical processes, and laboratory experiments on mantle minerals. I evaluate the performance of several methods for measuring shear wave splitting at broadband stations, and discuss how different measurements can inform our interpretation of mantle anisotropy. I describe a set of shear wave splitting measurements from both teleseismic and local earthquakes at 65 stations of the F-net array in Japan. I find considerable evidence from the measured splitting patterns for complex and heterogeneous anisotropy beneath Japan associated with the subduction of the Pacific and Philippine Sea plates beneath Eurasia. The comparison of teleseismic and local splitting at stations in southwestern Japan provides strong evidence for trench-parallel anisotropy in the mantle wedge above the subducting slab. I consider several scenarios that would produce the observed anisotropy and conclude that the most likely model for deformation beneath the Ryukyu arc is corner flow in the mantle wedge, with a region extending ~ 150 kilometers from the trench dominated by B-type olivine fabric. To characterize further the detailed pattern of flow and anisotropy, I evaluate a series of two-dimensional finite element models that describe the subduction of the Philippine Sea plate beneath southwestern Japan, and compare the resulting flow field, strain, and anisotropy in the mantle wedge to F-net shear wave splitting observations. To complement this forward modeling approach, I develop and implement a method for the 2.5-D inversion of shear wave splitting intensity measurements for anisotropic structure in the upper mantle. I present preliminary anisotropic models for southwestern Japan and discuss strategies for explicitly integrating the tomographic inversion of splitting intensity data with numerical models that describe geodynamic processes in the wedge. Finally, I describe a series of laboratory experiments characterizing deformation and the resulting lattice preferred orientation in magnesiowüstite, a lower mantle mineral, and discuss the implications for the interpretation of seismic anisotropy at the base of the mantle.

Thesis supervisor: Robert D. van der Hilst
Title: Cecil and Ida Green Professor of Earth and Planetary Sciences

Acknowledgements

Writing a doctoral dissertation is not easy. However, I have had the enormous fortune of spending the past five and a half years surrounded by supportive advisors, talented scientists, gifted fellow students, a loving family, and fantastic friends. It is both a pleasure and an honor to offer thanks to the many people who have helped me along the way.

First and foremost, I owe a huge debt of gratitude to my thesis supervisor, Rob van der Hilst. Rob has been a terrific advisor from the very first day I arrived at MIT with a vague notion that I wanted to study seismic anisotropy. He has offered me both the freedom to follow my research interests wherever they led and the guidance I needed to mold my work into a thesis that I am quite proud of. Rob's support and encouragement have helped me at every step of the way and I'm happy and grateful to have had the opportunity to work with him for nearly six years. I've also had the pleasure of working very closely with Martijn de Hoop of Purdue University. Martijn's keen scientific insight has helped to shape the later stages of my thesis research and this work owes a great deal to his ideas. I thank Martijn for all of his help and encouragement, his hospitality during visits to Colorado and Indiana, and his unending patience with my occasionally silly questions about the tough math stuff.

I'd like to thank the rest of my thesis committee, Brad Hager, Shun Karato, Tim Grove, and Stéphane Rondenay. I've had the pleasure of working closely with Brad on the modeling aspects of my thesis work and he has made me into at least an amateur geodynamicist: thanks, Brad, for all your help. I have especially enjoyed having Shun Karato from Yale on my committee; Shun hired me as an undergraduate intern in his lab at the University of Minnesota when I was nineteen years old and a sophomore in college. The two summers I spent in his lab taught me how scientific research was done and piqued my interest in seismic anisotropy, and it has been terrific to continue collaborating with Shun during my Ph.D. research. Tim's door is always open to talk science, and he generously offered help and lab resources when I was working on my

deformation experiments. Stéphane has been a wonderful source of ideas, resources, suggestions, and encouragement over the past three years, and a great committee chair!

Many other faculty members in the EAPS department have helped to shape my ideas; I would especially like to thank Brian Evans, Dale Morgan, Wiki Royden, Dan Shim, and Maria Zuber. I did my undergraduate work in the terrific Earth and Environmental Sciences department at Rensselaer Polytechnic Institute, and I am enormously grateful for the excellent preparation I received there. I'd like to acknowledge the influence of several RPI professors: thanks to Frank Spear, Bruce Watson, Steve Roecker, and especially Rob McCaffrey, my undergraduate research advisor. I've been fortunate to interact with scientists at several different institutions during my graduate career, and I'd especially like to thank Sébastien Chevrot of the Observatoire Midi-Pyrénées in Toulouse, France, Sara Pozgay of Washington University in St. Louis, Zhenting Jiang of Yale University, and Peter Van Keken and Erik Kneller of the University of Michigan for their help and hospitality.

The fifth floor of the Green Building has been an amazing place to come to work every day and do science (and have some fun). It's impossible to thank every denizen of the 5th floor who has helped me out during my tenure here, but I'd like to single out a few people. Frederik Simons and Keli Kárason were terrific officemates and scientific "big brothers" during my first couple of years at MIT. The series of great officemates has continued: thanks to Ping Wang, Chang Li, Sandeep Rekhi, Javier Santillán, and Emily Roland for putting up with me. Caroline Beghein was not only a wonderful officemate but is a very dear friend: thanks for everything! I've been lucky to enjoy both close friendship and great scientific collaboration with Einat Lev. Thanks also to Chin-wu Chen, James Dennedy-Frank, Sarah Stewart Johnson, Rosalee Lamm, Lisa Lassner, Erwan Mazarico, Emily Van Ark, Huajian Yao, and many, many others (you know who you are!) who have made my time on the 5th floor so special.

I received a very good piece of advice from Steve Roecker, one of my professors at RPI and an EAPS alum, when I was deciding where to go to grad school. Steve told me to keep in mind that I would learn as much, if not more, from my fellow students as from my professors. With all due respect to my professors, of course, I've found this to be very true, and the fantastic graduate student body in EAPS is one of my favorite things about

this department. So: thanks to each and every one of my fellow students (and postdocs!) who have made EAPS such a great place to learn to be a scientist. Naming everyone individually would run these acknowledgments to an impractical length, but I would like to especially thank Maggie Benoit, Jeremy Boyce, Kristen Cook, Ben Crosby, Brian deMartin, Becky Flowers, Kevin Frye, Eric Hetland, Kate (Ruhl) Huntington, Doug Jerolmack, Joel Johnson, Brendan Meade, Will Ouimet, Taylor Schildgen, Blair Schoene, Steve Singletary, Kyle Straub, Chris Studnicki-Gizbert, Youshun Sun, Jessica Warren, Cam Wobus, and Xiaohui Xiao. Thanks to everybody for your support, your scientific insights, your willingness to endlessly discuss the Red Sox, and your friendship.

I owe a huge debt of gratitude to various support staff in the department. Thanks to Vicki McKenna and Carol Sprague in the Education Office for all their help over the years. Linda Meinke keeps the computers running and has bailed me out more than once when I couldn't get software to install or when I accidentally deleted a directory. Jacqui Taylor and Roberta Allard on the 9th floor have helped me out with all kinds of logistics and are always up for a chat. And a big thank you goes to Beth MacEachran, who runs the 5th floor with grace and style, and who mixes the best Cosmopolitans I've ever tasted. Thanks as well to my MIT friends outside EAPS, who have helped to keep me sane and smiling. Thank you to all the friends I've made in the Graduate Student Council, Dance Troupe, Kinaesthetics Lab, and the Tech Catholic Community, especially Elizabeth Basha, Christine Ng, and Ashley Predith – love you, ladies!

Finally, and most importantly, thank you to my family. I've been blessed with the best and most supportive family known to humankind, and not one word of this thesis would have been written without their never-ending love and support. Thanks to my parents, Nancy and Joe, for always encouraging me to follow my dreams and for always being there with a shoulder to cry on when needed. Mom and Dad, I love you and your support means so much. My brother Patrick and sisters Kate and Betsy are three of my best friends in the world – thanks for everything and I love you guys to bits. Thanks to my stepmother Jessica and all of the Martin clan, to my Aunt Kathy and Uncle Cliff, to my cousin Allison who has been such a great roommate this year, and to all my extended family. A person would be fortunate to have one person in their life who truly believes in them, and just in my family I've got dozens. Thanks.

Contents

List of Figures and Tables

Introduction

The phenomenon of elastic anisotropy, which manifests itself in the dependence of seismic velocities upon the direction of propagation or the polarization of the phase of interest, has been observed in many regions of the solid Earth. Seismic anisotropy has been observed or inferred in shallow crustal settings, the upper mantle and the transition zone, the D'' region above the core-mantle boundary, and the Earth's solid inner core. Because of the relationships between the occurrence and character of anisotropy and past and present deformation, the delineation and interpretation of seismic anisotropy has become an integral part of studies of tectonic and dynamic processes in the Earth's interior.

In the Earth's mantle, seismic anisotropy can arise when a volume of mantle rock, made up of individual mineral crystals that are themselves anisotropic, is systematically deformed by tectonic processes such as subduction or mantle convection. For example, when an aggregate of crystals of olivine (the dominant upper mantle mineral) undergoes deformation to high strains, individual grains in the rock volume tend to align along a preferred orientation, and seismic waves that traverse the upper mantle will sense the resulting anisotropy. Because of this crucial link between tectonic deformation and the resulting seismic anisotropy, studies of anisotropy can provide constraints on the causes, mechanisms, and consequences of deformation in the Earth's mantle. Seismic anisotropy is studied from a variety of different perspectives by different branches of geophysics: seismologists use observations of seismic waves to gain insight about the strength and

geometry of anisotropy in the Earth's interior, mineral physicists conduct laboratory experiments of deformation of mantle materials and measure the resulting anisotropy, and geodynamicists conduct numerical or physical simulations of tectonic processes and compare predictions from these experiments to observations.

Anisotropy in the Earth's mantle has been studied using a variety of seismological observables, including measurements of direction-dependent *Pn* velocities, the anomalous splitting of normal modes, the azimuthal dependence of surface wave phase velocities, and the Love-Rayleigh velocity discrepancy, which is indicative of radial anisotropy. A particularly powerful tool for studying mantle anisotropy is the observation of shear wave splitting. Upon propagation through an anisotropic medium, a shear wave is split into two orthogonally polarized components and accumulates a delay time between the fast and slow components; this phenomenon is analogous to optical birefringence. Shear wave splitting is particularly well suited to studying anisotropy because it is an unambiguous indicator of anisotropy and is unaffected by isotropic wavespeed heterogeneity. However, the interpretation of shear wave splitting measurements is often difficult, in part because splitting is a path-integrated measurement and without additional information one cannot uniquely locate the source of the anisotropy along the wave's path. Despite this limitation, splitting measurements of shear phases that traverse the mantle, particularly *SKS* waves, have become popular for studying anisotropy and deformation in the mantle.

One type of tectonic setting where measurements of shear wave splitting are particularly useful – and particularly intriguing – is that associated with subduction, where slabs of cold, dense oceanic lithosphere descend into the mantle. Subduction zones

play a crucial role in plate tectonics, the generation of melt, and the recycling of crust and volatiles, and are prime sites of the natural hazards of volcanoes and earthquakes, but the pattern of deformation in the upper mantle associated with subduction is very poorly understood. The study of anisotropy associated with subduction can contribute greatly to our understanding of how deformation is accommodated, but the interpretation of anisotropic indicators is particularly difficult and non-unique in a complicated tectonic setting such as a subduction zone. A variety of physical processes may affect the three-dimensional anisotropic structure of subduction zones; moreover, the presence of volatiles in the mantle wedge can dramatically affect the relationship between strain and the resulting anisotropy. Although seismic anisotropy has been found to be nearly ubiquitous in subduction zone settings, the interpretation of shear wave splitting measurements in these regions remains difficult and controversial, and many subduction-related processes related to the accommodation of deformation remain poorly constrained.

Another region of the Earth's interior where indicators of anisotropy can shed light on enigmatic deformational processes is the D'' region, which extends for ~ 300 km above the core-mantle boundary. Observations of anisotropy in D'', mainly from the splitting of shear waves with nearly horizontal paths through the base of the mantle, are robust but have proved extremely controversial to interpret. Two different mechanisms for D'' anisotropy have been proposed. One is the lattice preferred orientation (LPO) of anisotropic minerals due to high-strain horizontal deformation at the core-mantle boundary. A second possible mechanism is the shape preferred orientation (SPO) of isotropic inclusions within the surrounding mantle material, which could take the form of

partial melt, infiltrated core material, or elastically distinct materials carried to the base of the mantle through subduction. It has proven difficult to discriminate between the two hypotheses, and the mechanism (and therefore the correct interpretation) for anisotropy in the D'' region is not well understood.

The goal of the work described in this thesis is to explore several aspects of elastic anisotropy in the upper and lowermost mantle and to integrate constraints from different disciplines to determine relationships between seismologically inferred anisotropy and tectonic deformation. A large portion of the dissertation explores the nature of upper mantle anisotropy beneath Japan using observations of shear wave splitting and numerical models of flow in the mantle associated with the subducting plate. Japan overlies the subduction of the Pacific and Philippine Sea plates beneath Eurasia; its proximity to mantle flow associated with the subduction of plates with different ages, thermal histories, and slab morphologies makes it an excellent natural laboratory for the study of deformation patterns associated with different subduction regimes. Additionally, the region features dense geophysical instrumentation and large amounts of high-quality seismic data are available. We use data from F-net, a network of 87 permanent broadband stations throughout Japan maintained by the Japanese National Research Institute for Earth Science and Disaster Prevention.

Chapter 1 of this thesis reports on a study comparing different shear wave splitting measurement methods for teleseismic phases recorded at permanent stations in Japan. The estimation of splitting parameters from broadband recordings is not entirely straightforward, especially in complicated tectonic regions where the anisotropic structure is also likely to be complex, and several previous studies have noted

discrepancies among measurement methods. In this study, we evaluated three different splitting measurement methods and tested a variety of filtering and windowing schemes, and found that the methods were more likely to disagree at stations which overlie complex anisotropic structures, such as multiple layers of anisotropy.

In **Chapter 2**, we present a teleseismic shear wave splitting data set for 64 stations of F-net. We have constructed a splitting data set of ~ 2000 high-quality splitting measurements, covering a wide range of incidence angles, incoming polarization azimuths, and backazimuths. We have found that most F-net stations exhibit splitting behavior that is more complicated than a simple, homogeneous, single-layer anisotropic model would predict, and that complexity in anisotropic structure tends to correlate geographically with complexity in slab morphology as inferred from seismicity and seismic tomography. These observations suggest that the three-dimensional structure of the Pacific plate induces complex flow patterns in the upper mantle, and that this is manifested in shear wave splitting measurements.

Teleseismic shear wave splitting measurements give us an excellent picture of upper mantle anisotropy, but because splitting is a path-integrated measurement we have very poor control on the depth extent of the anisotropy. **Chapter 3** describes a set of splitting measurements from earthquakes originating in the Philippine slab beneath the Ryukyu arc. By comparing local splitting measurements with teleseismic splitting we can place some depth constraints on the location of anisotropy. We have found that the majority of measured fast directions throughout the Ryukyu arc are trench-parallel, and that local splitting agrees very well with teleseismic splitting, which suggests that the anisotropy is located in the mantle wedge above the slab. In this chapter we also examine

in detail several scenarios for upper mantle deformation that are consistent with trench-parallel anisotropy in the mantle wedge. We conclude that the most likely model for Ryukyu anisotropy is corner flow in the corner of the mantle wedge combined with B-type olivine fabric, which causes the fast direction of anisotropy to orient 90° from the prevailing flow direction.

To aid the interpretation of our F-net shear wave splitting data set in terms of mantle deformation, we combine seismological observations with numerical models of geodynamical processes. In **Chapter 4** of this thesis, we explore a series of two-dimensional finite element models of the flow induced in the mantle wedge due to the subduction of the Philippine Sea plate beneath southwestern Japan. For each model, we calculate predicted shear wave splitting from the behavior of the finite strain field, and compare these predictions to the detailed shear wave splitting dataset described in Chapters 2 and 3. We have found that in general, two-dimensional flow models explain the splitting observed in southwestern Japan fairly well. We find that the details of the predicted splitting patterns at individual stations for models with different rheological properties are substantially different. Rigorous analysis of the detailed splitting patterns observed at F-net stations will likely allow us to discriminate among different rheological models for flow in the mantle wedge, and to accurately delineate the region of the wedge dominated by B-type fabric. The work described in this chapter shows the promise of comparing splitting observations with numerical models of anisotropy development as a tool for the rigorous interpretation of splitting measurements. Additionally, this chapter provides a starting model for the formal inversion of splitting data.

Chapter 5 presents work towards the goal of integrating geodynamical models and the inversion of shear wave splitting measurements for anisotropic structure. The direct inversion of splitting measurements is not usually attempted because of the limitations imposed by sparse data sets, but the dense station coverage in Japan allows us to invert splitting intensities measured at F-net stations for anisotropic models in a 2.5-D framework. In this approach, we use the predictions of geodynamical models as a starting model for the inversion. We use the Born approximation for anisotropic elastic media under the assumption of weak anisotropy to derive expressions for finite-frequency sensitivity kernels for our chosen anisotropic parameters, and use the sensitivities calculated in this way in the normal equations for the inversion. In this chapter, we discuss the theoretical framework for the combined inversion/modeling approach, apply the technique to a subset of the splitting dataset presented earlier in the thesis, present preliminary anisotropic models for southwestern Japan, and discuss strategies for explicitly integrating the constraints obtained from the inversion with the flow modeling framework described in Chapter 4.

In **Chapter 6**, we shift the focus of the thesis from upper mantle anisotropy to anisotropy in the lowermost mantle. Observations of anisotropy in the D'' layer at the base of the mantle are plentiful and can provide important constraints on the structure and dynamics of this region. However, there is no consensus on the origin of anisotropic structure in D'', and it has proven difficult to discriminate among competing models for D'' anisotropy. One mechanism that has been proposed is the LPO of magnesiowüstite [(Mg,Fe)O], which is highly anisotropic at lower mantle pressures. Here we describe a series of laboratory experiments on the deformation and resulting LPO of (Mg,Fe)O, and

predict the anisotropy and shear wave splitting behavior that would result. We find that the predicted patterns of anisotropy are generally consistent with seismological observations of D'' anisotropy, and predict that if LPO of (Mg,Fe)O is the mechanism for D'' anisotropy, then azimuthal variations in splitting should be present. This prediction may provide a means for discriminating among various hypotheses for anisotropy at the base of the mantle, and may provide guidance for the design of seismological experiments for studying D'' anisotropy.

To summarize, the work presented in this thesis contributes to our comprehension of mantle anisotropy and deformation in several ways. The work presented in Chapter 1 has produced insight into the behavior of shear wave measurement methods in noisy and complex environments, and lays the groundwork for the construction of the data set presented in Chapters 2 and 3. The collection of measurements at F-net stations described in these chapters represents a large, high-quality, unusually comprehensive shear wave splitting data set in a particularly complicated tectonic setting. The numerical modeling study (Chapter 4) and the companion inversion study (Chapter 5) make two fundamental contributions to our understanding of upper mantle anisotropy. First, the theoretical description and implementation of a new method for splitting intensity tomography represents a large and important step forward in the investigation of shear wave splitting. Second, the explicit integration of geodynamical modeling and the inversion of seismic data provides an exciting and powerful avenue for the interpretation of shear wave splitting data sets in terms of mantle deformation and tectonic processes. This thesis has yielded a model for anisotropy beneath southwestern Japan (Chapters 3-5) associated with the subduction at the Ryukyu arc and has increased our understanding of how

tectonic deformation is accommodated in this region. Finally, the work described in Chapter 6 helps to clarify how the LPO of (Mg,Fe)O may contribute to anisotropy in the lowermost mantle, and may aid in the design of future seismological studies of D'' anisotropy.

The material presented in this dissertation has been published (Chapters 1 and 2), accepted for publication (Chapters 3 and 6), or is in preparation for submission (Chapters 4 and 5). The thesis chapter titles vary from their published form; therefore, the corresponding publications are listed below, in the same order:

Long, M. D., van der Hilst, R. D., 2005a. Estimating shear wave splitting parameters from broadband recordings in Japan: A comparison of three methods. Bull. Seism. Soc. Am. 95, 1346-1358.

Long, M. D., van der Hilst, R. D., 2005b. Upper mantle anisotropy beneath Japan from shear wave splitting. Phys. Earth Planet. Inter. 151, 206-222.

Long, M. D., van der Hilst, R. D., 2006. Shear wave splitting from local events beneath the Ryukyu Arc: Trench-parallel anisotropy in the mantle wedge. Phys. Earth Planet. Inter., in press.

Long, M. D., de Hoop, M. V., Hager, B. H., van der Hilst, R. D., 2006a. Two-dimensional modeling of subduction zone anisotropy with applications to southwestern Japan. In preparation for submission to Geophys. J. Int.

Long, M. D., de Hoop, M. V., van der Hilst, R. D., Hager, B. H., 2006b. Inversion of shear wave splitting intensities for anisotropic structure and coupling with numerical flow models. In preparation for submission to J. Geophys. Res.

Long, M. D., Xiao, X., Jiang, Z., Evans, B., Karato, S.-i., 2006. Lattice preferred orientation in deformed polycrystalline (Mg,Fe)O and implications for seismic anisotropy in D''. Phys. Earth Planet. Inter., in press.

Chapter 1

A comparison of shear wave splitting measurement methods[1]

Abstract

The goal of this study is to evaluate the performance of different splitting measurement techniques in the particularly complicated tectonic setting of subduction beneath Japan. We use data from the broadband Japanese F-net array and consider the methods due to Silver and Chan (1991), Levin et al. (1999), and Chevrot (2000). We find that the results generally agree well with each other, although discrepancies arise if the anisotropy beneath the station is more complex than the simple single-layer anisotropic model often assumed in splitting studies. A combination of multichannel and single-record methods may serve as a powerful tool for recognizing complexities and for characterizing upper mantle anisotropy beneath a station.

1. Introduction

Measurements of seismic anisotropy, a phenomenon in which the velocity of a seismic wave depends on its polarization or propagation direction, can potentially illuminate important questions about deformational processes in the Earth. Upon propagation through an anisotropic medium, a shear wave will be "split" into a fast and a

[1] Published as: Long, M. D., van der Hilst, R. D., 2005a. Estimating shear wave splitting parameters from broadband recordings: A comparison of three methods. Bull. Seism. Soc. Am. 95, 1346-1358.

slow component and will accumulate a delay time between the orthogonally polarized components (Keith and Crampin, 1977). The fast direction φ represents the polarization direction of the fast shear wave and the delay time δt represents the time difference between the fast and the slow arrivals. If the relationships between tectonic processes and strain and between strain and anisotropy are known, then shear wave splitting measurements can provide us with information about causes, mechanisms, and consequences of deformation in the Earth (Silver, 1996; Park and Levin, 2002). Studies of upper mantle anisotropy (and its relationships with deformation and tectonics) from shear wave splitting observations have become popular in the last two decades (e.g. Ando et al., 1983; Silver and Chan, 1988; Vinnik et al., 1989a; Savage and Silver, 1993). Splitting observations are an unambiguous indicator of anisotropy (Babuska and Cara, 1991) and avoid the inherent tradeoff between anisotropy and lateral wavespeed heterogeneity of direction-dependent traveltime measurements and suface wave studies (e.g. Forsyth, 1975; Simons et al., 2002). However, the measured splitting parameters for a single shear phase represent a path-integrated picture of anisotropy; without additional information it is not possible to infer where along the path the anisotropy is located.

Although shear wave splitting studies are a powerful and popular method for characterizing upper mantle anisotropy and deformation, the measurement of splitting parameters from broadband recordings of shear phases is not entirely straightforward. Typical split times due to upper mantle anisotropy average ~ 1 second and range up to ~ 2.0-2.5 seconds (Savage, 1999); this is much smaller than the characteristic periods of phases used to probe upper mantle anisotropy (core-refracted *SKS*-type and teleseismic direct *S* phases). Therefore, the split shear waves usually do not achieve a clear separation

on the horizontal components. Additionally, most shear wave splitting measurement methods rely on the simplifying assumption that the measured phase has passed through a single anisotropic layer with a horizontal axis of symmetry. If this condition is violated, then the measured splitting parameters are merely "apparent" measurements and their variation with respect to parameters such as backazimuth and angle of incidence must be examined.

Several different methods have been developed to measure shear wave splitting parameters from broadband records. Silver and Chan (1988, 1991) developed a method that measures splitting parameters from a single horizontal-component recording that grid-searches for the best-fitting (φ, δt) that produces the most nearly singular covariance matrix between the splitting-corrected horizontal components. A similar method, based on maximizing the cross-correlation between corrected components, has been used by Fukao (1984), Bowman and Ando (1987), and Levin et al. (1999). Recently, Chevrot (2000) developed a method that estimates the splitting parameters (φ, δt) from the relative amplitudes of the radial and transverse seismogram components as a function of incoming polarization angle. In addition to the different measurement methods used, shear wave splitting studies often differ in key aspects of data processing, such as filtering schemes, windowing of the seismic phase of interest, and treatment of the instrument response.

This study is motivated by observations of several authors (e.g. Levin et al., 1999, 2004; Menke and Levin, 2003) that different measurement methods can give substantially different results; these differences have been attributed in part to complex anisotropic structure beneath the stations (in this paper, we use the term "complex anisotropy" to

describe any anisotropic structure that is more complicated than a single, laterally homogenous, horizontal anisotropic layer). Most comparisons among measurement methods have relied on synthetic data or have been fairly qualitative. Here, we evaluate the performance of different methods when applied to broadband seismic data from two stations of the F-net network in Japan, a particularly complicated tectonic region. Studies of shear wave splitting are becoming increasingly common, but the performance of splitting measurement techniques are usually not evaluated in detail before their application to complex regions. Our aim here is to evaluate differences among splitting measurement methods in this particularly complex region before these splitting techniques are applied across the rest of the array.

Studies of shear wave splitting due to upper mantle anisotropy most commonly use core-refracted shear phases such as *SKS*, *PKS*, *SKKS*, etc. Core-refracted phases have two important advantages for shear wave splitting. First, there is no contamination from near-source anisotropy; splitting must be due to anisotropic signal between the core-mantle boundary and the receiver. Second, the initial polarization of the incoming wave is constrained by the *P*-to-*SV* conversion at the core-mantle boundary. The nearly vertical incidence of *SKS*-type phases severely limits the depth resolution of splitting measurements, however, and the backazimuthal coverage at individual stations for *SKS*-type phases is often poor. These disadvantages can be ameliorated by the addition of direct *S* phases from teleseismic events; however, contamination from source-side anisotropy must then be assessed and accounted for.

In this study we examine shear wave splitting at two stations from *F*-net, a network of broadband stations in Japan. This is part of a larger effort to characterize

anisotropy and mantle deformation beneath Japan using shear wave splitting measurements (Long and van der Hilst, 2005b). The primary objective of this paper is to evaluate and compare different shear wave splitting measurement methods applied to real seismic data in a complicated region. Both stations have been in operation since 1995 and provide clean, high-quality data; additionally, the data coverage with respect to backazimuth and/or incoming polarization azimuth and incidence angle is excellent. We wish to answer several questions. For "ideal" stations, with good data coverage and signal-to-noise ratio, do different splitting methods yield the same best-fitting splitting parameters? Do different methods give us consistent insight into the nature of anisotropy beneath the station? Can we achieve reliable shear wave splitting measurements in a complex region and be sure that our characterization of anisotropy is not dependent on the measurement method used? What are the advantages and disadvantages of each method? Can different measurement methods yield ambiguous or even contradicting results? If so, what are the implications for the inferred anisotropic models? Do the methods respond differently to changes in pre-processing procedure, such as the use of different filtering schemes?

In designing this study, we have chosen a subset of available splitting methods to evaluate. Many methods have been developed to constrain anisotropic models beneath seismic stations, such as those of Wolfe and Silver (1998), Rumpker and Silver (1998), Restivo and Helffrich (1999), and Menke and Levin (2003). We have selected three measurement methods that make relatively few assumptions about the anisotropic structure beneath the station, and we test if a consistent picture of anisotropy emerges

with each of the measurement methods and if the use of different methods can lead to different and useful insights.

2. Splitting measurement methods

2.1 The Silver and Chan (1991) method (hereinafter SC1991)

This method operates upon the principle that the best-fitting splitting parameters φ and δt correspond to a certain inverse splitting operator that best linearizes the *S* wave particle motion when the effect of the anisotropy is removed. In order to find the best splitting parameters, a grid search over possible (φ, δt) values is performed. Vidale (1986) demonstrated that the inverse splitting operator can be found from the time-domain covariance matrix of the horizontal particle motion. If the (orthogonal) horizontal components make angles of φ and $\varphi + \pi/2$ with the wave's polarization vector $\boldsymbol{p}$, and the time lag is given by δt, the covariance matrix C_{ij} between the (orthogonal) horizontal components u is given by

$$\boldsymbol{C} = C_{ij}(\varphi, \delta t) = \int_{-\infty}^{\infty} u_i(t) u_j(t-\delta t) \mathrm{d}t, \; \mathrm{i,j,} = 1,2.$$

A quantitative measure of the linearity of the particle motion is given by the eigenvalues of $\boldsymbol{C}$. For the isotropic case, the *S* wave particle motion is linear and $\boldsymbol{C}$ will have one nonzero eigenvalue; in the presence of anisotropy, $\boldsymbol{C}$ will have two. Therefore, the inverse splitting operator that best corrects for the presence of anisotropy will result in a corrected horizontal covariance matrix that is most nearly singular. The most nearly singular corrected covariance matrix is found by maximizing λ_1 (the larger eigenvalue), or from an equivalent eigenvalue-based measurement of linearity. Errors are estimated using a Fischer test formulation. We use a value of one degree of freedom per second;

this is based on the rule of thumb given by Silver and Chan (1991) that assumes a stationary noise process and estimates the degrees of freedom directly from broadband data.

2.2 The cross-correlation method (e.g. Levin et al., 1999; hereinafter LMP1999)

The cross-correlation method used by Fukao (1984), Bowman and Ando (1987), Levin et al. (1999), and others is very similar in concept to SC1991. This method also uses a grid search to find the pair of splitting parameters (φ, δt) that corresponds to the most nearly singular covariance matrix. However, the measure of linearity used in the correlation method is not the maximization of λ_1 but the minimization of the determinant of the covariance matrix. This is mathematically equivalent to maximizing the cross-correlation between the horizontal components (Silver and Chan, 1991). This maximization of the cross-correlation can be visualized as searching for the inverse splitting operator that maximizes the similarity in the pulse shapes of the corrected seismogram components (Levin et al., 1999). In other words, this method tries to accommodate the prediction that the *S* wave, after traveling through an anisotropic medium, should be composed of two orthogonally polarized pulses with identical shape, but time-delayed with respect to one other. Measurements of splitting parameters using the LMP1999 technique presented in this paper were made using an implementation of the cross-correlation algorithm as presented in Levin et al. (1999). Uncertainties in the splitting parameters are computed using the metric described by these authors and are based on the deviations from perfect cross-correlation (presumed to be caused by stochastic noise in the seismograms) for the best-fitting splitting parameters.

2.3 The Chevrot (2000) method (hereinafter C2000)

The above methods can be referred to as "single-record" methods. The "multichannel" method developed by Chevrot (2000) takes a very different approach to estimating splitting parameters. It is based upon the predicted variation of the amplitudes of the transverse components with incoming polarization angle (equivalent to the backazimuth for *SKS*-type phases). For the case where δt is small compared to the dominant period of the waveform, the radial and transverse components for a vertically incident shear pulse with waveform *w(t)* and polarization $\boldsymbol{p}$ are given by (Silver and Chan, 1988; Chevrot, 2000):

$$R(t) \approx w(t)$$

$$T(t) \approx -1/2\ (\delta t \sin 2\beta)\ w'(t),$$

where *w'(t)* is the time derivative of the radial waveform *w(t)*, and β is the angle between the fast axis φ and the incoming polarization direction $\boldsymbol{p}$. In the C2000 method, the amplitude of the transverse component relative to the derivative of the radial component is referred to as the splitting intensity, the azimuthal dependence of the splitting intensity is referred to as the splitting function, and the splitting vector is the ensemble of estimates of the splitting function obtained at different incoming polarization angles represented in the data set for a certain station. When a plot of the splitting vector is produced, the best splitting parameters are estimated by fitting a $\sin(2\theta)$ curve to the splitting vector. The amplitude of the sinusoid gives the best-fitting delay time, and the fast axis can be inferred from the phase of the sinusoid at the origin. An illustration of the variations in transverse component amplitude with incoming polarization is given in Figure 1, in

which radial and transverse components for shear arrivals at *F*-net station TKA with similar incoming polarization angles have been stacked in 20° bins.

3. Data

In this study we utilize data from two broadband stations in the *F*-net network. Station SGN is located near Tokyo, in central Honshu, and station TKA is located in southern Kyushu (Figure 2). Both stations have been in operation since 1995; the measurements presented in this paper come from data collected between 1995 and 2002. We selected clean recordings of teleseismic *S* phases (in the 40°-80° epicentral distance range), *SKS* (85°-120°), and *SKKS* (beyond 105°), as well as slab events located directly beneath the stations. An event map is shown in Figure 3. We restricted our use of direct *S* phases to deep (>200 km) events to reduce contamination from source-side anisotropy for teleseismic *S* and to ensure that we sample as much of the upper mantle as possible for local *S*. We have extensively tested our *F*-net splitting measurements to show that source-side contamination from direct teleseismic *S* phases is not a major factor in this dataset. In these tests, we looked for systematic variation in measured splitting parameters due to variations in source depth or region. With the exception of a few intermediate-depth events from the Tonga subduction zone, which were subsequently removed from the dataset, we found no evidence for systematic source side contamination. These tests are described in detail in Long and van der Hilst (2005b). With the use of direct *S* phases in addition to core-refracted phases we ensure that our dataset covers a wide range of backazimuths, initial polarization azimuths, and incidence angles. Good data coverage in terms of initial polarization azimuths is necessary for the implementation of multichannel

method; additionally, good coverage in terms of all three parameters is necessary to gain sensitivity to structures more complex than a single horizontal anisotropic layer.

All of the broadband data were bandpass filtered using a 4-pole Butterworth filter with corner frequencies at 0.02 Hz and 0.125 Hz. In order to implement the multichannel method, the two horizontal components were rotated by the measured incoming polarization angle to separate the radial and transverse components. For all phases the initial polarization angle (direction of maximum polarization) was measured directly from the seismogram. This was done by computing the direction of maximum polarization using a covariance measure; see Vidale (1986). Although the shear wave particle motions are elliptical due to the effect of splitting, the direction of maximum polarization can be retrieved because the splitting times are much smaller than the dominant period of the incoming phase. For *SKS* and *SKKS* phases, which generally had smaller signal-to-noise ratios than the direct *S* phases, the measured incoming polarization angle was compared to the backazimuth. The vast majority agreed to within 10°, and those records that did not (due to low signal-to-noise ratio or phase misidentification) were discarded. The rotated horizontal traces were then standardized by a deconvolution of the radial waveform from the radial and transverse components. For all records the shape of the transverse waveform was compared to the time derivative of the radial waveform, and traces for which the transverse waveform did not match the predicted shape were discarded. In this way, all records were visually checked for satisfactory signal to noise ratio and waveform clarity. Seismograms for an *SKS* arrival recorded at station TKA in various stages of processing are shown in Figure 4.

4. Splitting measurements for *F*-net stations

4.1 Station TKA

At station TKA we identified 36 very high-quality recordings of shear phases from which we measured shear wave splitting (28 teleseismic *S*, 5 local *S*, 2 *SKS*, 1 *SKKS*). Measured splitting parameters from each of the three methods are shown in Figure 5; for each method, the measurements are plotted as a function of incoming polarization azimuth. The C2000 splitting vector exhibits a striking sin(2θ) dependence, although there is some scatter in the best fit to the data that is larger in amplitude than the size of the 2σ formal error bars. However, a fit of a sin(2θ) curve to the splitting vector allows us to retrieve best-fit splitting parameters of $\varphi = 49.9° \pm 1.4°$, $\delta t = 0.60$ sec $\pm$ 0.03 sec. The good fit of a sin(2θ) curve to the splitting vector TKA demonstrates that the C2000 method works well with the two modifications we have introduced: (i) the use of direct *S* phases in addition to *SKS*-type phases and (ii) the use of splitting intensity measurements from individual records in the construction of the splitting vector rather than stacking several measurements in each backazimuthal window. Indeed, several studies (e.g. Schulte-Pelkum and Blackman, 2003) have demonstrated that stacking or averaging splitting measurements in backazimuthal windows results in a loss of sensitivity to complex anisotropic structure.

The results from the LMP1999 and SC1991 measurements are also plotted as a function of incoming polarization azimuth in Figure 5. It should be noted that there are fewer usable measurements for these two methods than for multichannel method. This is due to the different treatment of null splitting measurements by the two classes of method. Measurements of little or no splitting are easily incorporated using the C2000

method, because these are simply represented by splitting intensities close to zero. Null splitting is represented on the plots of single-record measurements with crosses; however, splitting parameters cannot be extracted from records with null or near-null splitting using the single-record measurement methods. The average split times obtained with single-record methods tend to be larger than the δt obtained with the multichannel method; moreover, both single-record methods have a tendency to obtain unreasonably large split times for some records with small amplitudes on the transverse components (this phenomenon has been observed by several other authors, including Silver and Chan, 1991 and Levin et al., 1999). In general, however, the three methods yield comparable average splitting measurements for station TKA, and the splitting patterns obtained with all three methods are generally consistent with a single-layer model of anisotropy beneath station TKA.

4.2 Station SGN

Splitting results for station SGN are shown in Figure 6. At this station we obtained measurements for 21 teleseismic *S* recordings, 3 local S, 9 SKS, and 5 *SKKS*. The splitting vector obtained with the multichannel method deviates more from a simple $\sin(2\theta)$ variation than the vector at station TKA. We can still fit a $\sin(2\theta)$ curve to the splitting vector and obtain splitting parameters (φ = -48.0° ± 1.1°, δt = 0.57 sec ± 0.03 sec), but the scatter in the data suggests a deviation from simple anisotropy beneath this station. The LMP1999 results at this station (Figure 6) also exhibit intriguing complexity; the plot of measured fast directions as a function of incoming polarization angle reveals a clear 90° periodicity, which is characteristic of two anisotropic layers (Silver and Savage,

1994; Özalaybey and Savage, 1994). It is difficult to discern a clear periodicity in the LMP1999 δt measurements, however, and these measurements also deviate significantly from the predictions of a simple anisotropic model. SC1991, curiously, yields fewer stable measurements at SGN than the LMP1999 method, and it does not yield a 90° periodicity. The average δt obtained with SC1991 is significantly higher than the averages obtained with the other two methods, and the formal errors for individual SC1991 measurements are larger than the formal errors for LMP1999 measurements.

Can we attribute the differences in splitting pattern between stations TKA and SGN to differences in data quality or differences in source-side contamination from direct *S* phases? We do not observe any difference in signal-to-noise ratios between the two stations; TKA and SGN are both very high-quality stations and only records with very clear, low-noise shear arrivals are retained in this study. As discussed in detail in Long and van der Hilst (2005b), there is good evidence that source-side contamination from direct *S* phases is not a large factor in this splitting dataset. Additionally, we note that the source distribution for the two stations is nearly identical; therefore, the character of source-side contamination, if present, should not be different for the two stations. A difference in the anisotropic geometry beneath the two stations is therefore the most likely explanation for the observed difference in splitting pattern. Because a 90º periodicity is observed at station SGN, two distinct anisotropic layers are likely present beneath this station.

5. Comparison of results from three measurement methods

We now compare more directly the splitting results from the three different splitting methods at stations TKA, where splitting is generally consistent with a simple anisotropic model, and SGN, where the splitting patterns deviate significantly from predictions of simple anisotropy, and where a two-layer model may be needed to explain the data. The three methods agree very well at station TKA. It is difficult to compare directly individual measurements from the multichannel approach with those of the single-record methods, but a direct comparison of the SC1991 and LMP1999 measurements for station TKA is shown in Figure 7. We find that for *every* recording for which both methods yield a usable measurement the measurements agree within their formal 2σ errors. (For the purpose of this comparison, we adopt the very inclusive definition that a "usable" measurement has a 2σ error in fast direction of less than ± 45° and a 2σ error in δt that is less than the magnitude of δt itself; that is, the range of δt values allowed by the data does not include zero.) We can find some events for which the SC1991 measurement yields a more tightly constrained estimate with smaller formal errors than the LMP1999 method, but examples of the opposite can also be found.

At station SGN we also find that the average splitting parameters obtained with each method agree fairly well, with the exception of the large average δt obtained with the SC1991 method. However, if we compare the two single-record methods directly (Figure 8) we see that there are several events for which the two methods yield measurements that disagree. Additionally, SC1991 yields far fewer usable measurements than the LMP1999 method. We propose that complexity in anisotropic structure (for instance, the presence of two distinct anisotropic layers) produces both the discrepancies

between the two methods and in the smaller number of usable SC1991 measurements. The presence of multiple anisotropic layers, and therefore multiple splitting that is measured as an "apparent" single-splitting measurement (Silver and Savage, 1994), probably subtly distorts waveforms such that the SC1991 method is more likely to be unstable, and such that the two methods are more likely to disagree.

We also test how the three methods respond to different filtering schemes. Several studies have found that splitting measurements can be frequency dependent (e.g. Clitheroe and van der Hilst, 1998; Matcham et al., 2000). All data presented so far in this paper were bandpass filtered between periods of 8 and 50 seconds. To asses the effects of different filtering schemes on the splitting measurements, we experimented with a variety of high-, low-, and bandpass filters. Generally, we find that the measured fast direction does not depend on the filtering scheme used, and that the first-order effect on measured δt values is to decrease the split time when primarily high-frequency signals were used. To illustrate this, we show filtering tests on TKA data for each method using high- and low-pass Butterworth filters with a corner frequency of 0.2 Hz (5 second period). The results of these filter tests are shown in Figure 9. In general, fewer usable measurements were made using the high- and low-pass filtering schemes than with the bandpass filter. For the multichannel method the best splitting parameters obtained with the low-pass filtering scheme (φ = 53.5° ± 2.4°, δt = 0.54 sec ± 0.06 sec) were consistent with the results with the original filter (φ = 49.9° ± 1.4°, δt = 0.60 sec ± 0.03 sec), while the effect of the high-pass filter was to decrease the amplitude of the sinusoid and increase the errors on the individual measurements (φ = 59.7° ± 7.8°, δt = 0.24 sec ± 0.07 sec). For the single-record methods, the most noticeable effect of the high- and low-pass filtering

scheme was to dramatically decrease the number of usable measurements, making rigorous comparisons difficult. It is not obvious for the data used here that discrepancies between high-, low-, and bandpass filtered single-record measurements are systematic. It seems that of the three methods considered here, the multichannel method is the least dependent on the filter scheme used.

6. Discussion

With our analysis of the performance of three splitting measurement methods at *F*-net stations SGN and TKA we have shown that each of the methods have distinct advantages and disadvantages. The multichannel method of Chevrot (2000) provides a natural way of investigating the backazimuthal variations of splitting parameters that is associated with complex anisotropic structure, as well as a natural way of incorporating null splitting measurements into an averaging scheme. Additionally, the multichannel method is more robust against changes in frequency content than the single-record methods. However, the multichannel method has the disadvantage of requiring adequate data coverage in backazimuth (or incoming polarization azimuth for direct *S*), which is often impossible to achieve with *SKS*-type phases alone and can be difficult to achieve even with the use of direct *S* phases. Also, the multichannel method requires an accurate measurement of initial polarization, which is straightforward for *SKS*-type phases but less accurate for direct *S*. The SC1991 method has the advantage of being applicable to a single record, and it does not need an accurate initial polarization measurement. Additionally, we have shown that SC1991 sometimes out-performs the LMP1999 method on individual records. However, both single-record methods are sensitive to the filtering

scheme used, and both have drawbacks regarding the definition of null splitting measurements and their incorporation into averaging schemes. The SC1991 method appears to yield fewer usable measurements and larger error bars for stations that overlie complex anisotropic structures (for example, multiple layers). Of course, this can be viewed as an advantage, rather than a disadvantage; the larger error bars and smaller number of measurements perhaps accurately reflects the uncertainty associated with interpreting complex anisotropy beneath the station. However, if the "apparent" measured splitting parameters can be properly interpreted in terms of complex anisotropy, then the measurement methods which yield greater numbers of usable measurements may be viewed as more robust. For example, the LMP1999 method yielded more usable measurements than the SC1991 method at station SGN; additionally, it can sometimes outperform it on individual records even for "simple" stations (e.g. TKA). Aside from this, it shares many of the same advantages and disadvantages of the SC1991 method.

Because each of the three methods has distinct advantages and disadvantages, and because the most time-consuming and labor-intensive part of making shear wave splitting measurements is not in the measurements per se but rather in the data preprocessing and selection, it may be advisable to use a combination of all three measurement methods. This is especially true if the data suggest that the station is located above complex anisotropic structure, where a combination of the multichannel and single-record methods can be especially powerful. The LMP1999 method seems to outperform the SC1991 method at stations overlying complex anisotropic structures, in the sense that it yields a greater number of usable measurements with generally smaller error bars, but SC1991 can occasionally yield better-constrained estimates than the LMP1999 method for

individual records. Therefore, the application of both the SC1991 and LMP1999 methods increases the number of usable measurements at a given station.

In situations where the anisotropic structure beneath the station is complex, the average splitting parameters obtained either by taking a weighted average of individual single-record measurements or by fitting a $\sin(2\theta)$ curve to the multichannel splitting vector may have little physical meaning. However, a qualitative comparison of the multichannel and single-record methods can be very useful, as each method can yield different insights upon visual inspection. In addition, the differences in splitting behavior between station TKA and station SGN suggest that a quantitative comparison of the single-measurement methods (SC1991 and LMP1999) can increase confidence in individual splitting measurements for stations in regions that may overlie complex geological structures. Discrepancies between measured splitting parameters outside the 2σ confidence intervals indicate that 1) complex anisotropy is likely, and that good coverage in incoming polarization angle is needed to fully characterize the anisotropy, and that 2) the individual records exhibiting discrepancies should not be included in the interpretation of the splitting parameters. This allows the analyst to discard questionable measurements and thus instills more confidence in the results.

In the case of the stations discussed in this paper, the combination of measurement methods and good data coverage allow us to characterize the anisotropic structure beneath TKA and SGN with a high degree of confidence. Station TKA, which is located at the northernmost part of the Ryukyu arc (Figure 2), exhibits a splitting pattern that is consistent with a single anisotropic layer, and we find a fast direction that trends NE-SW. This direction, parallel to the strike of the Ryukyu trench and perpendicular to

the direction of convergence at the Ryukyu arc, is consistent with the fast directions at other Ryukyu arc stations (Long and van der Hilst, 2005b). Station SGN is located in a more tectonically complicated region and overlies a region of complicated slab morphology (see Long and van der Hilst, 2005b, and references therein). The more complicated splitting pattern exhibited at station SGN, and the existence of discrepancies among the splitting measurement methods at this station, are consistent with a two-layer anisotropic model.

7. Summary

We have evaluated the performance of three different methods of estimating shear wave splitting parameters from broadband recordings for the two Japanese stations considered. We generally find that the three methods agree well with each other, although the presence of complex anisotropy (inferred from backazimuthal variations in apparent splitting parameters) beneath the seismic station can introduce discrepancies among the methods. The Silver and Chan (1991) method seems particularly affected by the presence of complex anisotropy beneath the station. We find that the multichannel method of Chevrot (2000) is more robust when the data are subjected different filters than the single-record methods of Silver and Chan (1991) and Levin et al. (1999). We conclude that a combination of multichannel and single-record methods can serve as a powerful tool for characterizing anisotropy beneath a seismic station, especially in the presence of anisotropic structure that is more complex than a simple single, horizontal anisotropic layer model. Specifically, a comparison among the three methods can help identify stations which overlie anisotropic structure that is more complex than a simple,

horizontal anisotropic layer, and the analysis of discrepancies between single-record SC1991 and LMP1999 measurement methods can help identify individual measurements that are unreliable.

8. Acknowledgements

The authors thank Sebastien Chevrot for assistance with data processing and for providing his splitting codes, and thank Bill Menke for making his cross-correlation code freely available. We thank the Japanese National Research Institute for Earth Science and Disaster Prevention for maintaining the *F*-net array and making the data freely available and easily accessible. This paper was greatly improved by insightful comments from Matt Fouch and an anonymous reviewer. This research was supported by NSF grant EAR-0337697 and by an NSF Graduate Research Fellowship awarded to M.D.L.

Figure Captions

Figure 1. Illustration of the multichannel method using data from F-net station TKA. In the left panel, radial component traces for a variety of incoming polarization angles are shown. Traces are stacked in 20° polarization angle bins, and radial trace amplitudes have been normalized to 1. In the right panel, the corresponding stacked transverse traces are shown. To the left of the traces is the incoming polarization angle range; to the right of the traces is the number of records in the stack. The dependence of the transverse component on incoming polarization angle is clearly shown.

Figure 2. A station map for F-net. Stations in the network are marked with small circles; the two stations examined in this study, SGN and TKA, are marked with large triangles.

Figure 3. Local and teleseismic events used in this study.

Figure 4. Record of an SKS phase at station TKA in various stages of processing. At top left, a raw, unfiltered three-component seismogram is shown. At top right, the traces have been bandpass filtered with corner frequencies at 0.02 Hz and 0.125 Hz, and the expected travel times from the iasp91 earth model for *SKS* and *SKKS* are shown. At bottom left, the filtered horizontal traces have been rotated by the backazimuth to show the radial component (bottom trace) and transverse component (middle trace). The radial component has been deconvolved from both horizontal traces to standardize them. In the top trace, the transverse component is overlain with the time derivative of the radial

component. As expected, the transverse component has the shape of the radial component derivative.

Figure 5. Results of splitting analysis for F-net station TKA for three measurement methods. Circles represent direct S phases, and triangles represent core-refracted phases. Null measurements are shown with crosses for the SC1991 and LMP1999 methods. All measurements are plotted as a function of incoming polarization angle, which is measured directly from the seismogram for S phases, and is equal to the backazimuth for SKS/SKKS. Polarization angles were measured between 0° and 180°, but measured angles for events with backazimuths between 270° and 90° were adjusted by adding 180° to the polarization angle. Therefore, arrivals with similar measured polarizations coming from events with widely different backazimuths will plot 180° apart on these diagrams. All error bars are 2σ.

Figure 6. Similar to Figure 5, but showing results from station SGN.

Figure 7. A direct comparison of the splitting measurements at station TKA using the so-called single-record methods. SC1991 measurements are plotted as circles, while LMP1999 measurements are plotted as triangles. Only those events which yielded a well-constrained measurement using both methods are shown on this plot. All error bars are 2σ.

Figure 8. Similar to Figure 7, but displaying splitting measurements for station SGN.

Figure 9a. Results of filter tests for station TKA for the C2000 method. Each plot shows the results yielded by three different filtering schemes – bandpass filtered between 0.02 and 0.125 Hz, highpass filtered at 0.20 Hz, and lowpass filtered at 0.20 Hz.

Figure 9b. Results of filter tests with the SC1991 method for each of the filtering schemes discussed above. The horizontal lines on each plot indicate the average splitting parameters obtained with the C2000 method for each frequency band.

Figure 9c. Results of filter tests with the LMP1999 method for each of the filtering schemes discussed above. The horizontal lines on each plot indicate the average splitting parameters obtained with the C2000 method for each frequency band.

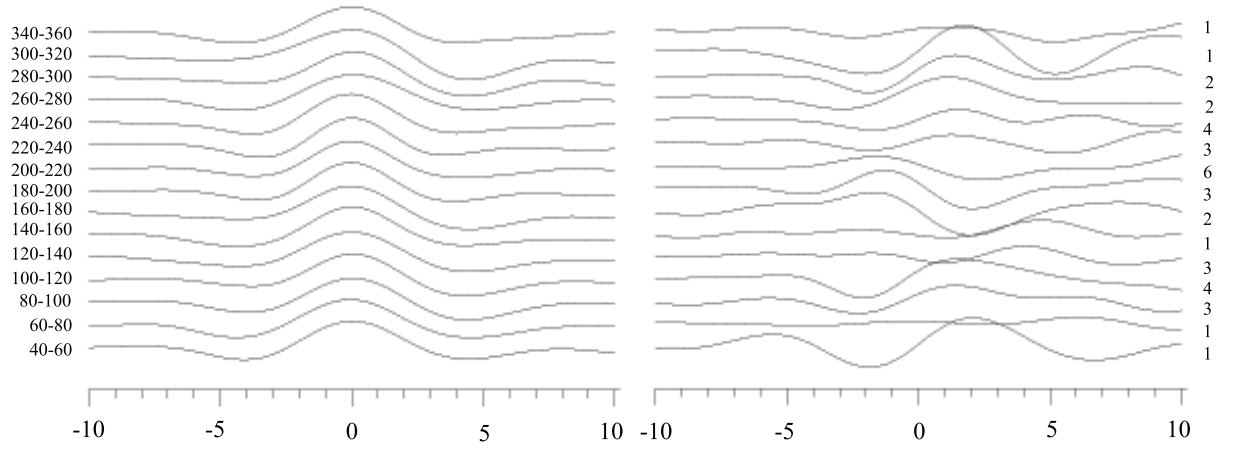
340-360
300-320
280-300
260-280
240-260
220-240
200-220
180-200
160-180
140-160
120-140
100-120
80-100
60-80
40-60
-10
-5
0
5
10
-10
-5
0
5
10
1
1
2
2
4
3
6
3
2
1
3
4
3
1
1

Figure 1

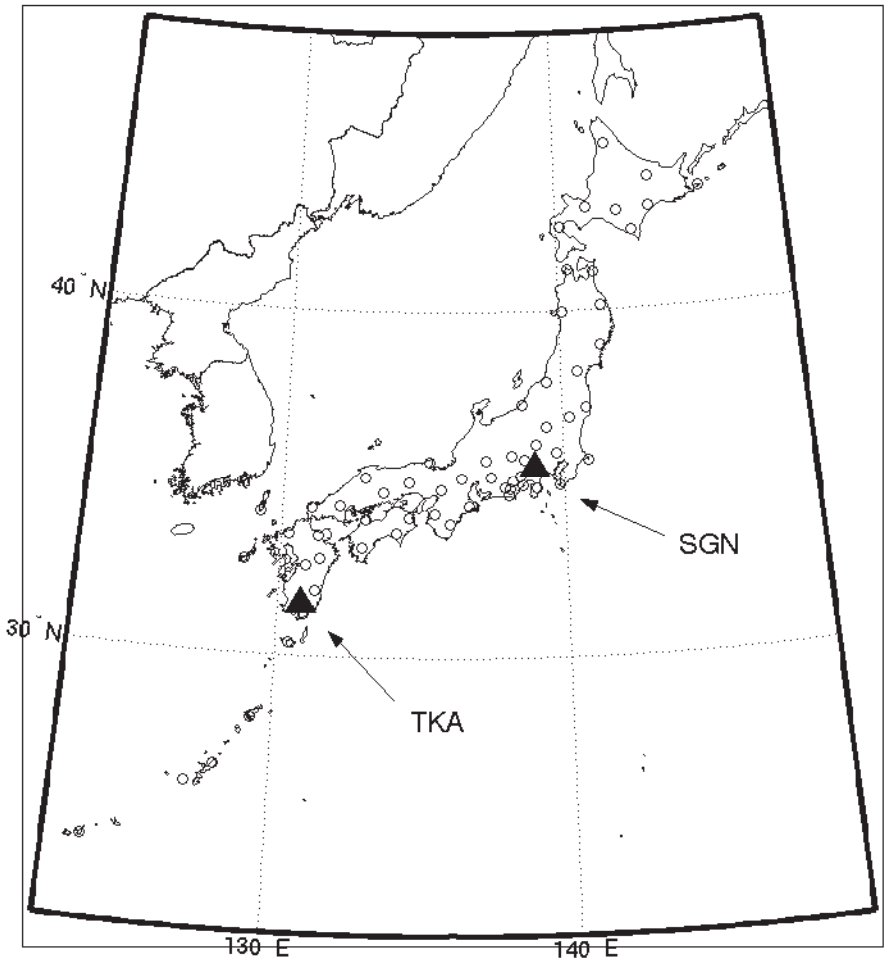

Figure 2

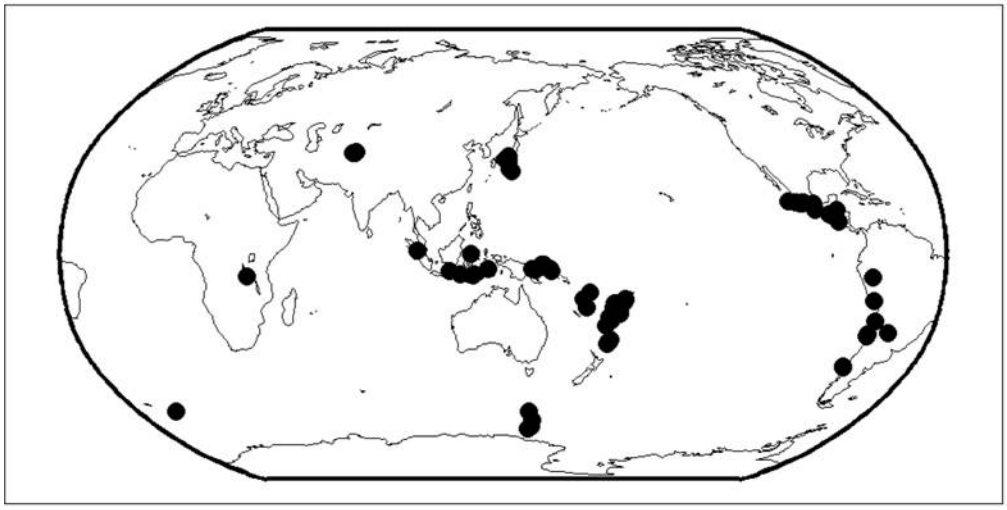

Figure 3

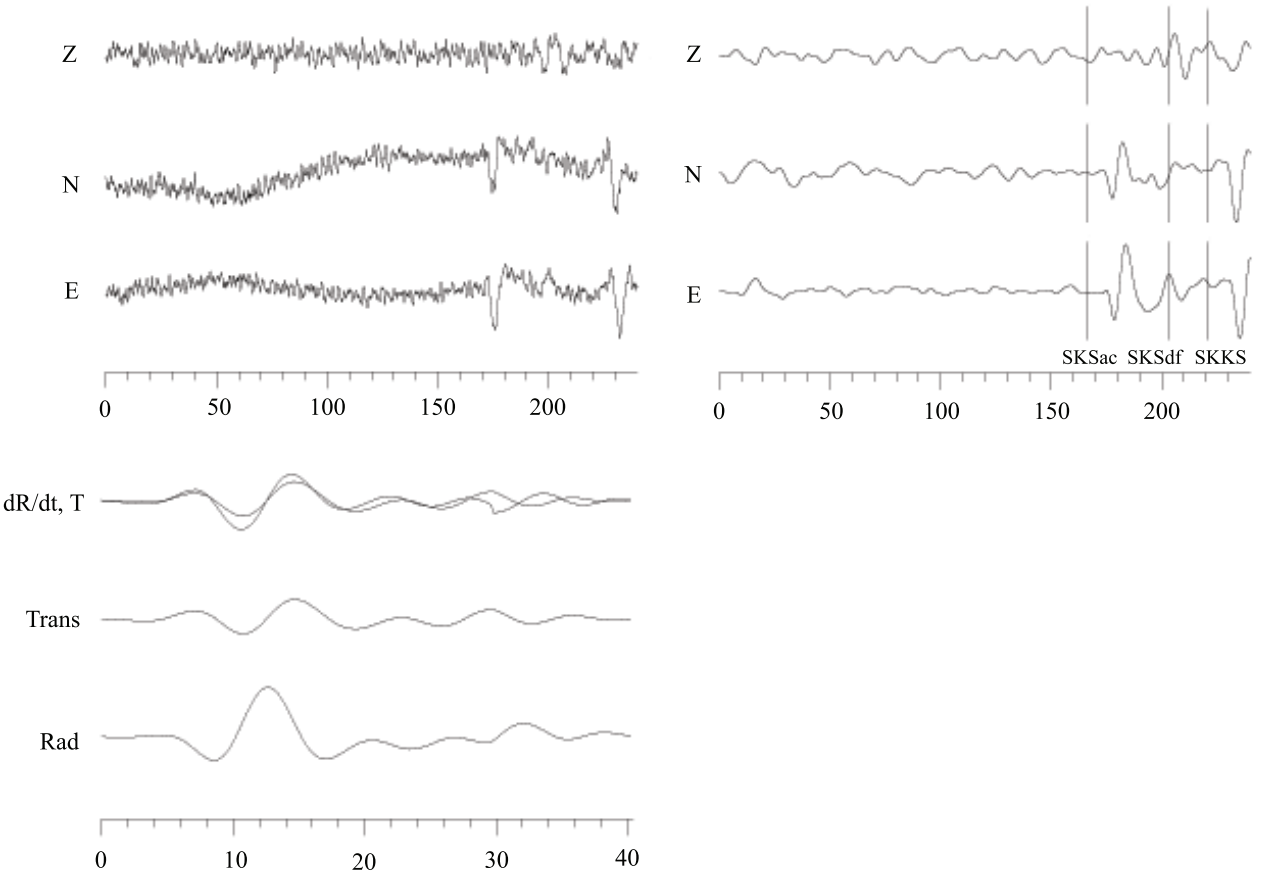
Z
N
E
0
50
100
150
200
Z
N
E
SKSac
SKSdf
SKKS
0
50
100
150
200
dR/dt, T
Trans
Rad
0
10
20
30
40

Figure 4

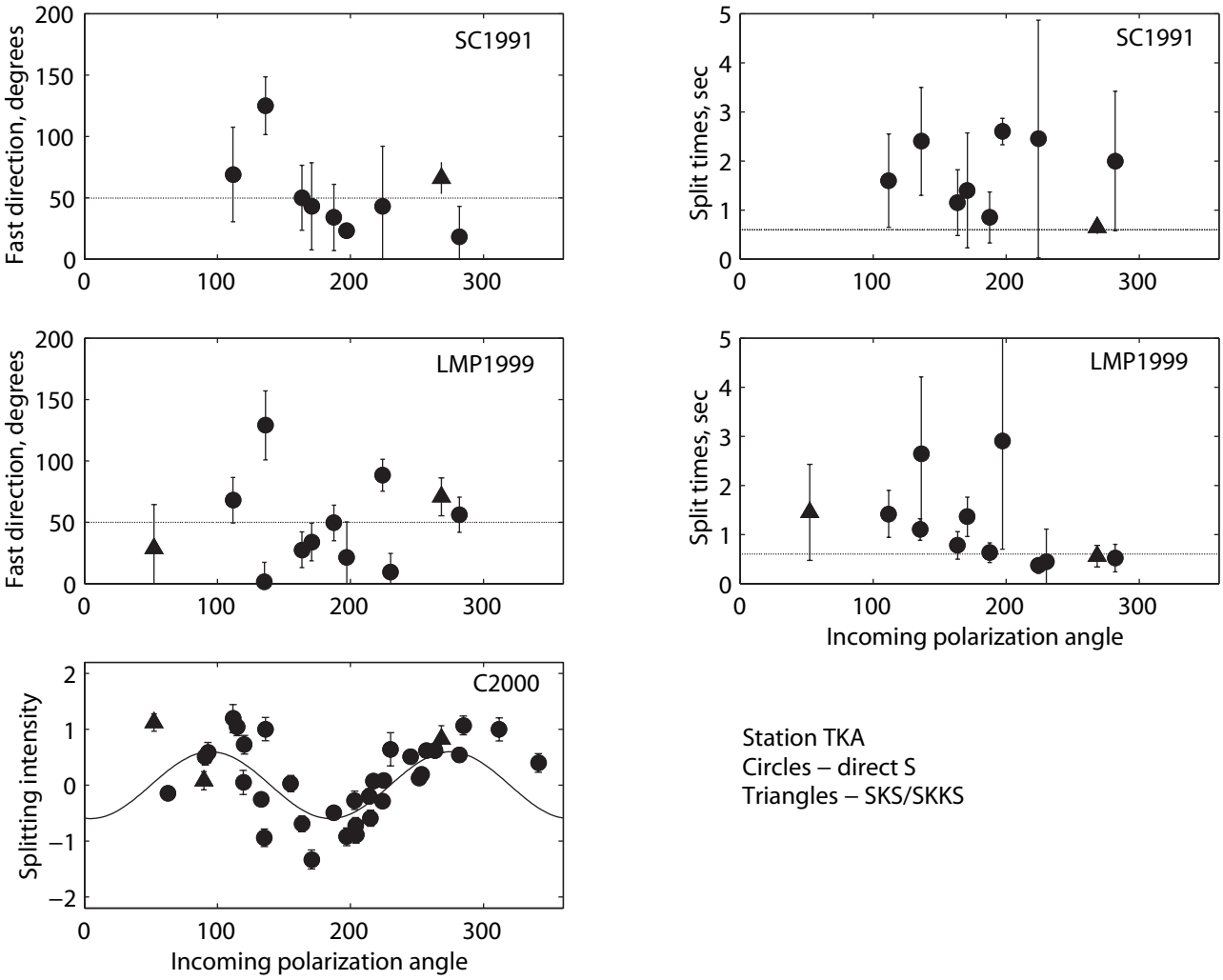
SC1991
Fast direction, degrees
Split times, sec
LMP1999
C2000
Splitting intensity
Incoming polarization angle
Station TKA
Circles – direct S
Triangles – SKS/SKKS

Figure 5

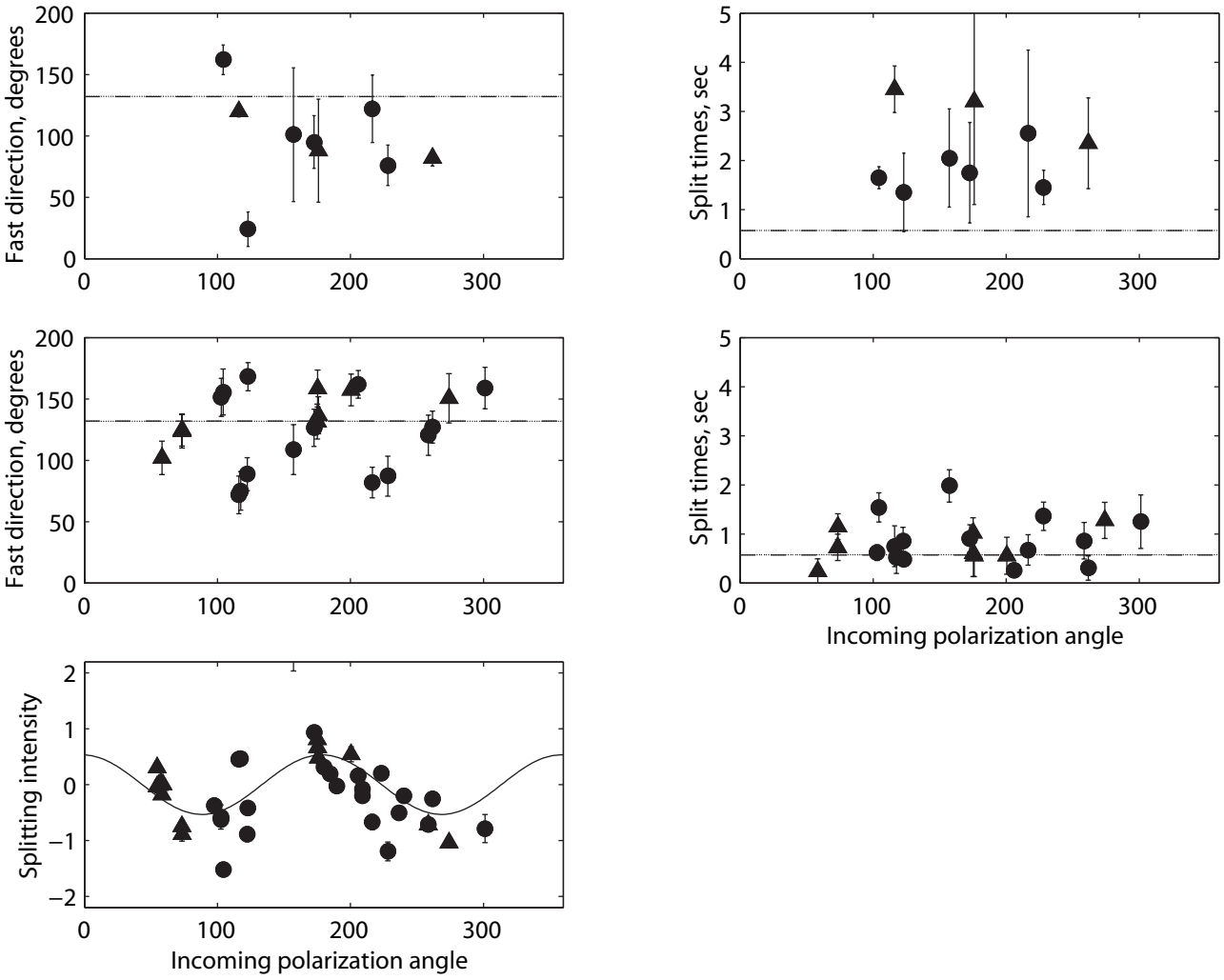
Fast direction, degrees
Split times, sec
Fast direction, degrees
Split times, sec
Splitting intensity
Incoming polarization angle
Incoming polarization angle

Figure 6

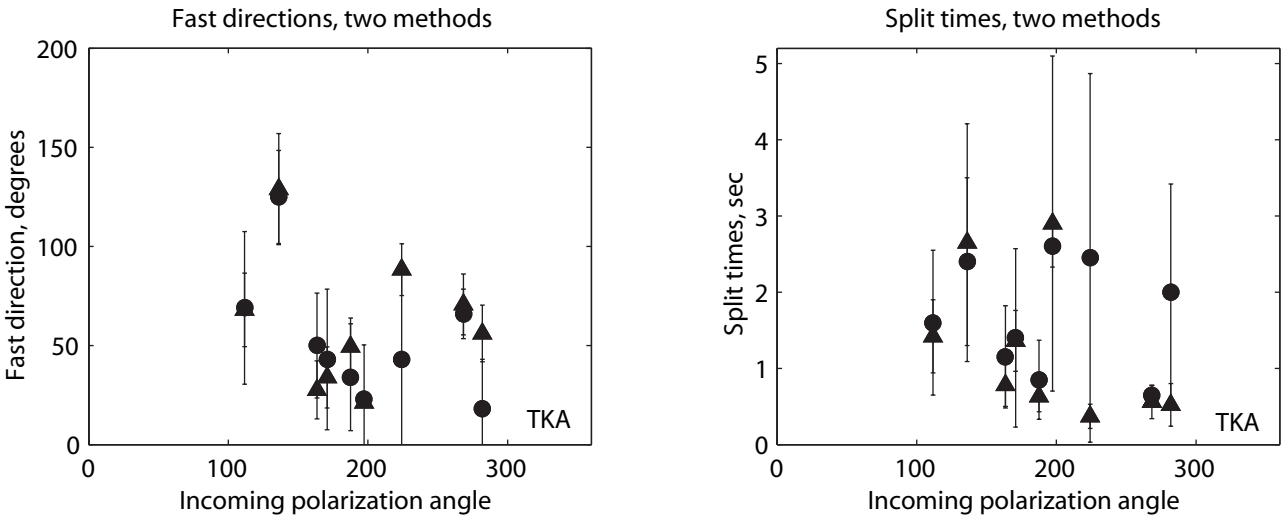
Fast directions, two methods
Fast direction, degrees
Incoming polarization angle
TKA
Split times, two methods
Split times, sec
Incoming polarization angle
TKA

Figure 7

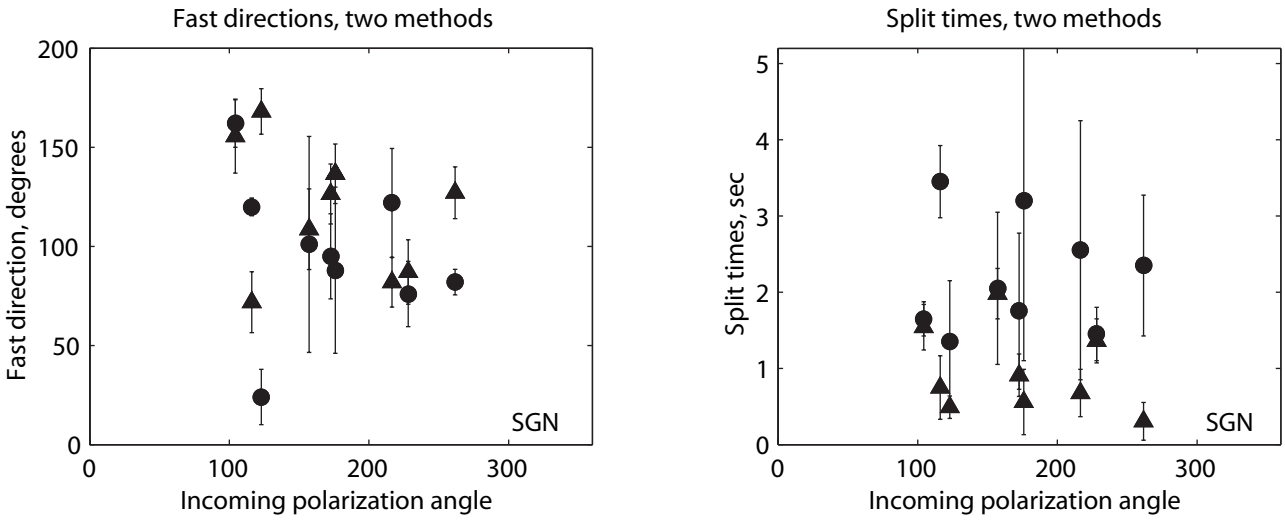
Fast directions, two methods
Fast direction, degrees
Incoming polarization angle
SGN
Split times, two methods
Split times, sec
Incoming polarization angle
SGN

Figure 8

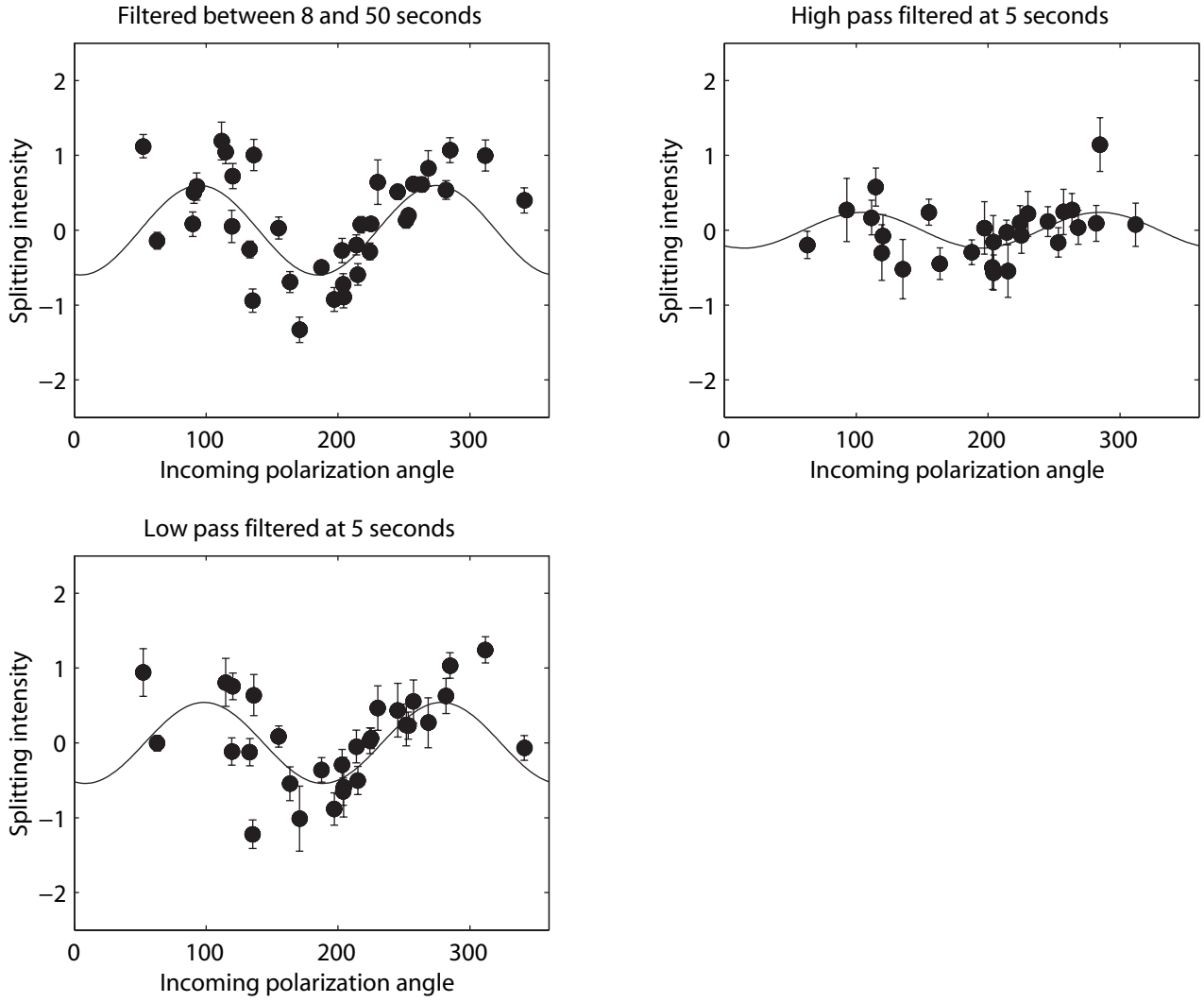
Filtered between 8 and 50 seconds
Splitting intensity
Incoming polarization angle
High pass filtered at 5 seconds
Splitting intensity
Incoming polarization angle
Low pass filtered at 5 seconds
Splitting intensity
Incoming polarization angle

Figure 9a

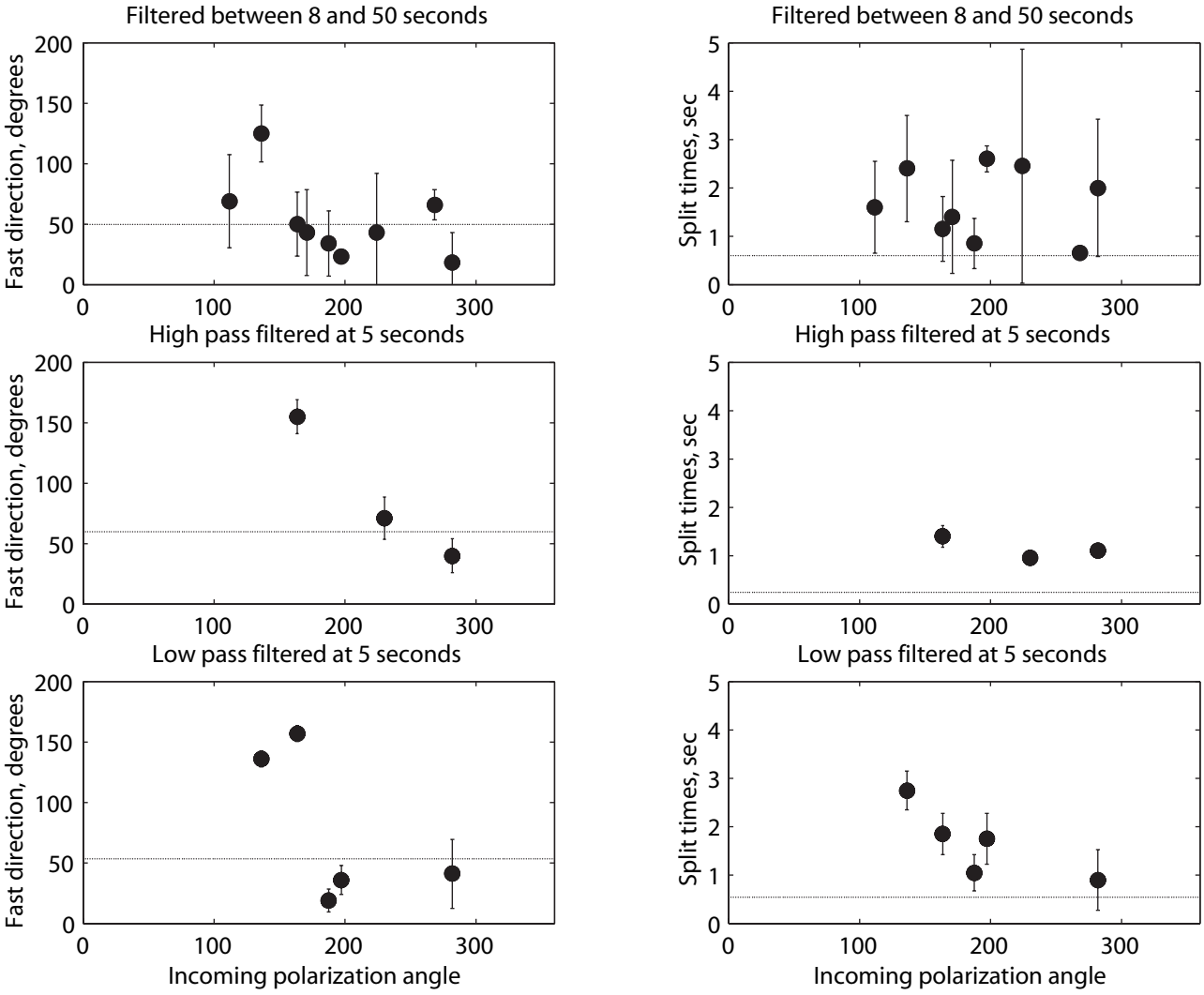
Filtered between 8 and 50 seconds
Fast direction, degrees
Split times, sec
High pass filtered at 5 seconds
Low pass filtered at 5 seconds
Incoming polarization angle
0
50
100
150
200
300
1
2
3
4
5

Figure 9b

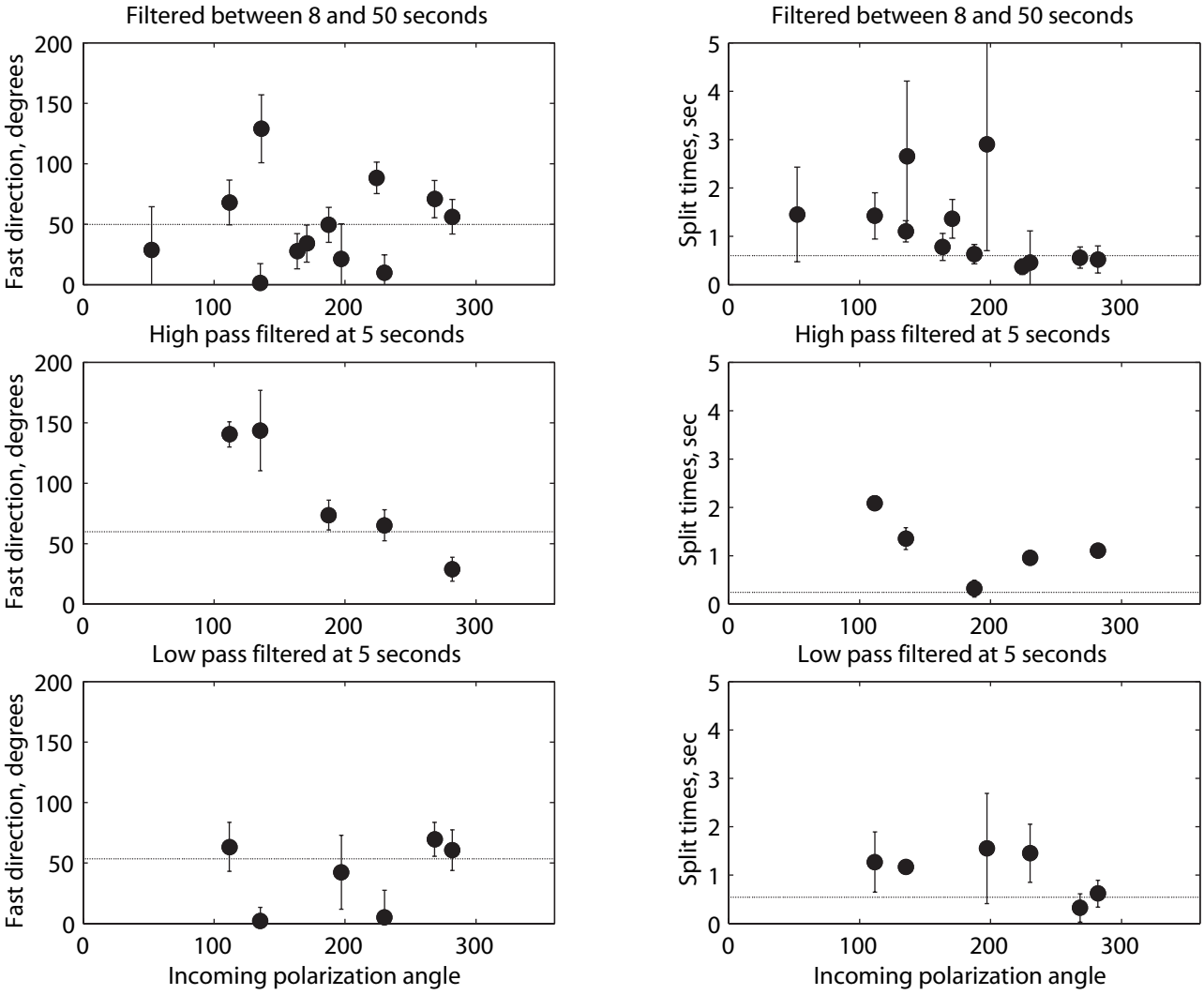
Filtered between 8 and 50 seconds
Fast direction, degrees
Split times, sec
High pass filtered at 5 seconds
Low pass filtered at 5 seconds
Incoming polarization angle
0
50
100
150
200
300
1
2
3
4
5

Figure 9c

Chapter 2

A teleseismic shear wave splitting data set for Japan[1]

Abstract

In this study, we utilize data from 64 broadband seismic stations of the Japanese *F*-net network to investigate the three-dimensional pattern of anisotropy in the subduction system beneath Japan. We have compiled a database of approximately 1900 high-quality splitting measurements, selected by visual inspection of over 25,000 records of *S*, *SKS*, and *SKKS* phases at *F*-net stations, covering a wide range of incidence angles, incoming polarization angles, and backazimuths. Analysis of the variations of measured splitting parameters with these parameters allows us to consider complexities in structure such as multiple anisotropic layers, dipping symmetry axes, and small-scale lateral variations in anisotropic properties. Here we focus on the presentation of the splitting measurements themselves; a detailed interpretation in terms of tectonics and mantle flow is beyond the scope of this paper.

In the southern part of the *F*-net array, along the Ryukyu arc, we find that fast directions are consistently trench-parallel, with splitting times of one second or more. Moving northward along the array, the measured splitting patterns become more complicated, with significant variations in apparent splitting parameters that indicate

[1] Published as: Long, M. D., van der Hilst, R. D., 2005b. Upper mantle anisotropy beneath Japan from shear wave splitting. Phys. Earth Planet. Inter. 151, 206-222.

complex anisotropic structure. Additionally, measured fast directions vary significantly over short length scales, and stations separated by less than 100 km often exhibit very different splitting behavior. This increase in complexity of anisotropic structure coincides geographically with the complicated slab morphology of the subducting Pacific plate. At stations on Hokkaido, to the north, and Kyushu, to the south, we see some evidence that the fast direction of anisotropy may rotate from trench-parallel close to the trench to subduction-parallel further away from the trench, which may correspond either to a change in stress conditions and/or volatile content, or to a change in flow regime.

1. Introduction

Elastic anisotropy in the Earth's mantle can manifest itself in the azimuthal dependence of body and surface wave propagation speed (Hess, 1964; Forsyth, 1975), a discrepancy between propagation speeds of Love and Rayleigh waves (e.g. Crampin, 1977), and shear wave splitting or birefringence (e.g. Savage, 1999). Seismic anisotropy is often assumed to have hexagonal symmetry (i.e., transverse isotropy) with an axis of symmetry that is either horizontal (i.e., azimuthal anisotropy) or vertical (i.e., radial anisotropy), but other orientations may, of course, occur. Seismic anisotropy in the upper mantle is a consequence of the strain-induced crystallographic or lattice preferred orientation (LPO) of intrinsically anisotropic mantle minerals, principally olivine. The relationships between deformation and LPO in olivine have been explored experimentally (e.g. Zhang and Karato, 1995) and theoretically (e.g. Tommasi et al., 2000; Kaminski and Ribe, 2001) and can also be inferred from petrographic examination of mantle-derived rocks (e.g. Christensen, 1984; Nicolas and Christensen, 1987). With known or assumed

relationships between tectonic processes and strain, on the one hand, and between strain and anisotropy (through LPO), on the other, observations of seismic anisotropy can provide us with information about causes, mechanisms, and consequences of deformation in Earth's interior (Silver, 1996). Shear wave splitting measurements are an especially powerful tool for characterizing anisotropy because birefringence is an unambiguous indicator of anisotropy (Babuska and Cara, 1991).

We aim to use shear wave splitting to investigate subduction-related processes - e.g., stress generation and accommodation of deformation, melt production and migration - in the upper mantle. These processes are still poorly understood and even the actual pattern of mantle flow above and below slabs of subducted lithosphere is not well known. Knowing the distribution of seismic anisotropy can help address these issues (e.g. Park et al., 2003). The presence of anisotropy in the upper mantle beneath subduction zones has been well established (e.g. Ando et al., 1983; Fischer and Yang, 1994; Hiramatsu and Ando, 1996; Fouch and Fischer, 1996; Iidaka and Obara, 1997; Fischer et al., 1998, 2000; Park and Levin, 2002). A diverse range of splitting behavior has been associated with different subduction zones. Both trench-parallel and trench-perpendicular fast directions have been inferred (e.g. Russo and Silver, 1994; Park and Levin, 2002), whereas at other stations above subduction zones no splitting is observed (Fischer et al., 1998).

Shear wave splitting measurements can provide a powerful tool for characterizing upper mantle deformation but their interpretation is particularly difficult in subduction zone settings. There is a diverse range of processes that could potentially affect the three-dimensional anisotropic structure of subduction zones, including corner flow in the mantle wedge induced by viscous coupling between the slab and wedge material, trench-

parallel flow in the mantle wedge (due to transpression) or beneath the slab (due to slab rollback), formation and migration of melt, flow around the slab edge, frozen lithospheric anisotropy in the slab, and anisotropic structure in the overriding plate. Additionally, new experimental studies suggest that the relationships between strain and resulting LPO can be dramatically altered by the presence of a small amount of water or other volatiles (Jung and Karato, 2001; Karato, 2004) or by the presence of melt (Holtzman et al., 2003). Subduction-associated processes, therefore, are likely to lead to anisotropic structures that are more complicated than the simple single-layer anisotropic models that are often assumed when interpreting splitting measurements. Various studies have explored the effects of more complicated anisotropic models on splitting measurements, such as multilayered anisotropy (Fryer and Frazer, 1984, 1987; Silver and Savage, 1994; Ozalaybey and Savage, 1994; Levin et al., 1999, 2000), dipping symmetry axes (Hartog and Schwartz, 2000; Chevrot, 2000; Chevrot and van der Hilst, 2003), and smooth variations in fast axis orientation with depth (Saltzer et al., 2000). However, the interpretation of shear wave splitting measurements in the presence of complicated three-dimensional anisotropic structure remains extremely difficult and non-unique.

Our long-term goal is to meet these challenges by a rigorous integration of seismological data analysis and geodynamical (flow) modeling. Japan, the geographical region of our primary interest, is well suited for such an approach. First, the region is very well instrumented because of the need for continuous monitoring of seismic and volcanic activity, and data from several broadband seismic networks are freely available. Second, it is fairly well located with respect to both global seismicity (especially for teleseismic events in the 40°-80° epicentral distance range, although azimuthal coverage

for events at 85º and beyond is considerably poorer) and local seismicity from slab earthquakes. Third, the slab morphology associated with the subduction of the Pacific and Philippine plates beneath Eurasia (Figure 1) is known from travel time tomography (e.g. Van der Hilst et al., 1991; Fukao et al., 1992) and seismicity (e.g. Engdahl et al., 1998; Gudmundsson and Sambridge, 1998).

As a first step toward achieving the long term goal we present here a large dataset of shear wave splitting measurements from *F*-net, a network of 64 broadband stations in Japan (Figure 1), and establish evidence for complex anisotropic structure in the upper mantle beneath the array. In the denser parts of the network the average station spacing is of the order of 70-80 km (equivalent to the station spacing envisioned for the USArray component of Earthscope). Our splitting database contains approximately 1900 measurements, with as many as 55 high-quality measurements for individual stations. We explore in detail the dependence of splitting on backazimuth, incoming polarization azimuth, and incidence angle. We address several specific questions. What are the characteristic splitting patterns at *F*-net stations, and what is the range of splitting behavior over the array? Over what spatial length scales does splitting behavior change or stay constant, and what can this tell us about different styles of deformation in the upper mantle? Are splitting patterns at *F*-net stations generally consistent with simple, single-layer anisotropic models, or do we see evidence for complexity in anisotropic structure beneath Japan? Do features of the splitting map for the *F*-net network correlate with tectonic features? What do our *F*-net splitting results tell us generally about interpreting splitting measurements in subduction zone environments?

2. Data and Methods

We utilize data from *F*-net (Figure 1), a network of 82 broadband stations that is administered by the Japanese **N**ational Research **I**nstitute for **E**arth Science and **D**isaster Prevention (NIED). We have processed data for a subset of 64 stations of the *F*-net array which were installed in or before 2001 and were collectively known as the FREESIA array. The first *F*-net stations were installed in early 1995. *F*-net data is made available on the web by NIED (www.fnet.bosai.go.jp). Despite relatively high levels of cultural noise in Japan and the proximity of many *F*-net stations to the ocean, the data quality for *F*-net stations is very high and we found only three stations (TYM, TTO, and IWT) with insufficient data quality to carry out a detailed splitting analysis.

We have selected recordings of teleseismic direct *S* phases for epicentral distances from 40°-80°, *SKS* from 85°-120°, and *SKKS* from beyond 105°. At some stations we have also analyzed local *S* phases from deep slab earthquakes. A map of events used in this study is shown in Figure 2. Coverage for *SKS* and *SKKS* is restricted to certain backazimuthal ranges, but backazimuthal coverage for direct *S* phases is adequate, and, in addition, there is abundant local seismicity. We consider splitting from these different types of shear wave phases together; these phases take very different raypaths through the mantle and/or core, but they sample the region beneath the stations in a very similar way. A justification for this approach, which has been followed by previous studies (e.g. Hartog and Schwartz, 2000), is contained in Section 4.1. For teleseismic *S* phases we restrict our search to deep (> 200km) events to reduce contamination from near-source anisotropy. For direct *S* phases the polarization vector of the incoming wave is determined directly from the seismogram by measuring the direction of maximum

polarization (Vidale, 1986). We apply a 4-pole Butterworth bandpass filter with corner frequencies at 0.02 Hz and 0.125 Hz to the data, and window around the phase of interest based on the predicted traveltimes from the iasp91 earth model (Kennett and Engdahl, 1991). Records were visually inspected for good signal-to-noise ratio and waveform clarity; we compared the shapes of the radial and transverse waveforms to ensure that energy on the transverse component conforms to expectations for anisotropy. A recording of an *SKS* arrival at station SGN in various stages of processing is shown in Figure 3.

In order to be able to recognize complex anisotropy better and obtain robust estimates of splitting parameters we use two complementary methods for estimating the shear wave splitting parameters φ and δt (the polarization direction of the fast shear arrival and the time separation between the orthogonal components, respectively). For a detailed explanation of the splitting methods used we refer to Long and van der Hilst (2005a), but for the sake of completeness we summarize them here. The cross-correlation method (Fukao, 1984, and others; we use the implementation due to Levin et al., 1999) yields an estimate of φ and δt from the horizontal components of a single seismogram by grid-searching for the inverse splitting operator that maximizes the similarity in the pulse shapes of the corrected horizontal seismogram components (which therefore maximizes their cross-correlation). The second method, due to Chevrot (2000), uses the variation of the amplitudes of the transverse components with incoming polarization angle (which for core-refracted phases such as *SKS* is equivalent to the backazimuth). For a homogenous layer of anisotropy with a horizontal axis of symmetry the amplitude of the transverse seismogram component T(t) is given by:

$$T(t) \approx -1/2\ (\delta t \sin 2\beta)\ R'(t),$$

where R'(t) is the time derivative of the radial waveform and β is the angle between the incoming polarization vector $\boldsymbol{p}$ and the fast direction φ. The ratio of the transverse amplitude to the amplitude of the time derivative of the radial component as a function of incoming polarization angle is known as the splitting vector: in the case of a single horizontal anisotropic layer we can retrieve (φ, δt) from the phase and amplitude of the sin(2θ) curve that best fits the observed splitting vector. If the anisotropy is more complex, the splitting vector would not show a simple sinusoidal behavior and the (φ, δt) determined with the cross-correlation method would depend on backazimuth (or $\boldsymbol{p}$ for direct waves). In this case the measured splitting parameters are merely "apparent" measurements and must be interpreted with complex anisotropy in mind.

3. Splitting Results

3.1 Splitting patterns at individual stations.

For each of the 64 *F*-net stations we have measured apparent splitting parameters as a function of incoming polarization angle. Because of the excellent data coverage, with some stations having as many as 55 good recordings, we are able to characterize the splitting patterns in great detail. For six stations (marked on Figure 1), which are representative of the wide range of splitting behavior present at *F*-net stations, we show in Figure 4 the results of both the Chevrot (2000) and the cross-correlation method. It is obvious from a visual inspection of Figure 4 that a wide range of splitting behavior is observed at *F*-net stations. For stations FUK and TKA (see Figure 1 for station locations) the Chevrot (2000) splitting vector is fit very well with a sin(2θ) curve, and the measured fast directions φ and split times δt obtained from the cross-correlation method show no

systematic variation (and little scatter) with incoming polarization azimuth. The average splitting parameters obtained with the cross-correlation method agree well with the (φ, δt) retrieved from the Chevrot (2000) splitting vector. At stations TMR and FUJ, however, the measured splitting patterns are strikingly different from the simple splitting behavior at FUK and TKA. Although there is ample evidence for splitting and, therefore, for anisotropy, significant variations in apparent splitting with incoming polarization angle are present in both the Chevrot (2000) and cross-correlation measurements. These observations suggest that the anisotropy beneath TMR and FUJ is complicated. The remaining two stations shown in Figure 4, SGN and HSS, exhibit splitting behavior that is somewhat in between the two endmember cases; at both of these stations there is significant variation in measured splitting parameters with incoming polarization azimuth, but a significant part of the splitting signal appears to be consistent with a simple anisotropic model, and it is possible to find average splitting parameters that explain the main features of the splitting pattern.

3.2 Geographical variations in splitting parameters.

We synthesize our database of over 1900 splitting measurements into a map of geographical variations of shear wave splitting for *F*-net. This map is shown in Figure 5, along with contours of Wadati-Benioff seismicity at 100 km intervals. We have somewhat arbitrarily divided the stations into four categories; I: splitting behavior consistent with a single horizontal anisotropic layer (e.g., FUK and TKA, Figure 4), II: splitting pattern deviates from a simple anisotropic model, but meaningful average splitting parameters can still be extracted (e.g., SGN and HSS, Figure 4), III: evidence of

anisotropy, but splitting pattern deviates strongly from the predictions of a simple model and complex anisotropic structure is very likely present (e.g., TMR and FUJ, Figure 4), and IV: data quality is insufficient. Category II can be thought of as an "intermediate" category between "simple" (Category I) and "complex" (Category III) stations. For stations in Category II we do compute average splitting parameters and we do expect them to have physical meaning, but we recognize that there is probably a slight deviation from a perfectly simple, homogeneous, single-layer anisotropic model. For example, it could imply an anisotropic layer with a slight dip, or a two-layer model where one layer is much thicker and/or more anisotropic than the other. We recognize that by computing average splitting parameters for Category II stations we are missing some subtle aspects of the anisotropy beneath the station. This is why we carefully distinguish between Category I and Category II stations and invest a greater degree of confidence in the average splitting parameters for Category I stations. For all stations in categories I and II the average fast direction is indicated on the splitting map (Figure 5). A summary of splitting behavior at all *F*-net stations can be found in the Appendix, both in table form (Table A1) and as a plot of circular histograms (rose diagrams) showing the distribution of measured fast directions at each station (Figure A1).

The splitting map for the *F*-net network exhibits several intriguing geographical variations. First, there is much variability in the character of splitting behavior from station to station, and in some regions shear wave splitting changes dramatically over lateral distances as small as 50 km. A Fresnel zone argument (e.g. Alsina and Snieder, 1995) would suggest that at least some of the observed signal has a shallow mantle origin. In the southernmost part of the array, along the Ryukyu arc, the fast directions are

consistently trench-parallel. Moving northward along the array into the central Kanto-Tokai region, the splitting behavior becomes more complicated and small-scale spatial variations become more pronounced. Both the measured fast directions and the character of splitting patterns vary rapidly over this part of the network, although many stations in the central part of the array exhibit a fast direction trending roughly NW-SE. In northern Honshu nearly all stations exhibit a higher degree of complexity than the stations in the southern part of the array, which coincides geographically with the complex morphology of the Marianas-Japan-Kuril slab compared to the simple morphology of the Philippine slab. In the northernmost part of the array, on Hokkaido, the fast directions seem to rotate from trench-parallel for stations vertically above the 100-km depth contour of the slab, to trench-perpendicular for stations located farther to the northwest of the trench.

4. Discussion

4.1 The range of splitting behavior at F-net stations: implications for deformation.

At several *F*-net stations we observe splitting patterns that are consistent with a single horizontal anisotropic layer, but most stations exhibit more complexity. Some of this complexity may be due double-layer anisotropy, e.g., beneath SGN. The range in splitting behavior observed at *F*-net stations argues for a range of possible anisotropic structures beneath the Japanese islands, and for a range of deformation styles or geometries. In some areas, most notably the Kanto-Tokai region where slab morphology is most complicated, stations that are separated by less than 70 km often exhibit totally different splitting behavior. This could be attributed to very shallow anisotropy, based on a Fresnel zone argument (Alsina and Snieder, 1995; Favier and Chevrot, 2003), or it

could be a consequence of lateral heterogeneity in anisotropic structure on very short length scales. In other areas, most strikingly along the Ryukyu arc, we observe splitting patterns that are remarkably consistent over ~700 km length scales. This geographic coherence in splitting behavior is likely a result of large-scale coherence of upper mantle flow patterns or other anisotropy-generating mechanisms.

4.2 Does splitting result primarily from upper mantle anisotropy?

Because shear wave splitting is a path-integrated measurement, without additional information it is impossible to deduce the location of the anisotropy along the path from a single measurement. We explain here why we neglect contributions from the crust, the lower mantle, and near-source structure.

First, we note that although the ray geometry for the different types of phases used (*S, SKS, SKKS)* are quite different, their raypaths through the anisotropic upper mantle beneath the array are nearly identical and they sample the anisotropic region in nearly the same way. It is probable that our measurements contain some signal from crustal anisotropy, as crustal rocks are often anisotropic and can frequently have intrinsic shear wave anisotropy approaching ~50% (e.g. Crampin, 1977). However, the split times attributed to crustal anisotropy are typically much smaller than those attributed to upper mantle anisotropy (Silver, 1996; Savage, 1999) due to the much shorter path lengths in the crust compared to those in the upper mantle. Kaneshima (1990) studied shear wave splitting due to crustal anisotropy in Japan and found split times less than 0.2 s, and typically less than 0.1 s. We typically see a much larger split time (e.g. 0.70 – 1.5 s) at *F*-

net stations, but we acknowledge that a small amount of contamination from crustal anisotropy is possible and, perhaps, likely.

Another possible source of contamination is a contribution from anisotropy in the lower mantle. We view this possibility as unlikely for two reasons. First, previous studies of mineral physics and seismological results (Meade et al., 1995; Niu and Perez, 2004) argue that most of the splitting of *SKS*-type phases, which travel from the core-mantle boundary to the surface on their receiver-side leg, can be attributed to upper mantle anisotropy beneath the receiver, with negligible contribution from D'', the lower mantle, and the transition zone. A more persuasive argument comes from the dataset itself. We have used a similar geographical distribution of events at each *F*-net station, and the rays traveling from a given event to each station in the network have similar (and long) path lengths in the lower mantle. If lower mantle anisotropy made a significant contribution to teleseismic shear wave splitting, then we would see a great deal of coherence among the shear wave splitting patterns at each station. Instead, we observe that stations separated by short distances (~ 100 km) often have completely different splitting patterns. This argues against a systematic contribution to the anisotropic signal from the lower mantle.

Next we consider possible contributions from near-source anisotropy. Because most of the phases in our dataset are direct *S* phases, this is a serious concern. In order to reduce the contamination by anisotropy in the shallow mantle near the source we restrict our data set to events with hypocenter depths greater than 200 km. However, anisotropy has been inferred to exist to depths as great as 400 km or perhaps deeper in subduction zone environments (e.g. Fouch et al., 1996; Fischer and Wiens, 1996). If anisotropy near the deep sources considered has a detectable effect on our splitting measurements, we

would expect 1) that this effect is similar for all stations of the array since the range of wave vectors associated with the deep events considered in our study is fairly small and 2) that omitting data from deep events would alter the inferred splitting parameters. We have investigated the possibility of both types of expression. First, we investigated for each deep earthquake the pattern of splitting parameters across the array. Only one deep event (beneath Tonga) produced a spatially coherent signal, with splitting of ~ 1.5 seconds and a roughly N-S fast direction. To reduce possible bias from near-source anisotropy from this event, we discarded data from this event. Any remaining long wavelength imprint due to distant source-side structure is unlikely to influence the character of the short wavelength variations of splitting parameters across the array. Second, we subdivided the set of deep events into four geographic regions and two depth ranges, and we inspected the effect on the splitting pattern at station HSS of omitting data from any of these source regions. The results of this test are presented in Figure 6. In general, removal of data from different groups of events does not significantly change the inferred splitting parameters for this station. Only one group of intermediate depth ($z <$ 400 km) events beneath the Fiji-Tonga region may induce some complexity to the splitting pattern (Figure 6), but even here the effect is small compared to the observed spatial changes in splitting parameters along the array. Finally, for stations in the Ryukyu arc we have measured splitting for both teleseismic and local slab events. These two types of measurements give very similar results, which precludes significant contamination from source-side or lower mantle anisotropy (see Figure 7).

We conclude, therefore, that most of the splitting signal we observe at *F*-net stations results from anisotropy located in the shallow mantle beneath the receivers, and

that contributions from the crust, the lower mantle, and near-source anisotropy for direct *S* phases are negligible. By implication, data from direct *S* and *SK(K)S* phases can be interpreted jointly for the purpose of our study.

4.3 Is anisotropy located primarily in the lithosphere or the asthenosphere?

The relative contributions of lithospheric and asthenospheric anisotropy have been hotly debated (see reviews by Silver, 1996 and Savage, 1999) and it is clear that in some continental regions contributions from both must be considered (e.g. Simons and van der Hilst, 2003). We cannot rule out contributions from the lithosphere, but for the current presentation of the results we assume that asthenospheric anisotropy contributes significantly to splitting observed at *F*-net. First, the magnitude of the splitting times for *F*-net stations (often larger than 1 second) may be difficult to explain with lithospheric anisotropy alone, but would be consistent with the large asthenospheric deformation that can be expected at subduction zones. Second, there is significant observational evidence for an asthenospheric component in subduction zones worldwide (e.g. Fischer et al., 1998; Fischer and Wiens, 1996; Fouch and Fischer, 1996; Smith and Fouch, 2005; Peyton et al., 2001, and others). Furthermore, for stations that are consistent with a simple anisotropic model (Figure 5) we expect that there is either little contribution from lithospheric anisotropy or that the lithospheric and asthenospheric fast directions are closely aligned. The complexity observed at other stations could be due to a lithospheric contribution, however, and in our future modeling of the splitting parameters both the lithospheric and asthenospheric contributions will be investigated more quantitatively.

4.4 Interpretation of *F*-net splitting in terms of tectonic features.

Perhaps the most striking feature of the *F*-net splitting map is the consistently trench-parallel fast directions along the Ryukyu arc (Figure 5). It is worth noting that both trench-perpendicular and trench-parallel fast directions associated with subduction zone anisotropy have been observed in different parts of the world (e.g. Fouch and Fischer, 1996; Smith et al., 2001; Park and Levin, 2002; Levin et al., 2004). Three possible mechanisms have been suggested to generate trench-parallel fast directions above a subduction zone: trench-parallel flow above the slab, due to transpression of the overlying mantle wedge (Mehl et al., 2003), trench-parallel flow beneath the slab due to slab rollback or a similar mechanism (Peyton et al., 2001) or corner flow in the mantle wedge induced by viscous coupling with the downgoing slab, along with the presence of an "exotic" deformation-induced LPO pattern (Jung and Karato, 2001; Holtzman et al., 2003).

In an attempt to determine which of the above possibilities is most plausible we measured splitting from local events beneath the Ryukyu stations and compared the observed splitting from local events to the teleseismic splitting patterns (Figure 7). While the usefulness of this comparison is limited by the number of local events located directly beneath Ryukyu stations, this comparison seems to rule out significant contributions from anisotropy beneath the slab. Additionally, it seems difficult to explain anisotropy in the mantle wedge with trench-parallel flow due to transpression, as the convergence direction at the Ryukyu arc is nearly perpendicular to the strike of the trench. Therefore, it seems that corner flow coupled with "unusual" LPO is the most likely mechanism for the trench-parallel fast directions in the southernmost part of the array.

A second striking feature in our dataset is the apparent rotation of the fast direction from trench-parallel close to the trench to trench-perpendicular farther inland – this is observed very clearly at Hokkaido stations and is also present in the transition from northern Ryukyu stations to southern Kyushu stations (Figure 5). It has been suggested by Karato (2004) that such a rotation could be associated with the spatial variations in water content and/or stress conditions. Karato (2004) hypothesized that the rotation can be explained by simple corner flow in the mantle wedge, in which the primary flow direction is trench-parallel, in combination with so-called "Type B" olivine LPO associated with high stress and/or high H_2O content (Jung and Karato, 2001) close to the trench. Farther away from the trench, either the mantle material is dehydrated or the prevailing stress conditions are lower, and a "Type A" olivine LPO pattern is established. An alternate hypothesis is that the rotation is associated with complicated flow patterns in the upper mantle, perhaps associated with the kink in the Pacific slab beneath Hokkaido and associated with the confluence of the Pacific and Philippine slabs beneath southern Kyushu. Without further modeling we cannot distinguish between these two hypotheses but we note that the rotation from trench-parallel fast directions close to the trench to trench-perpendicular away from the trench that we observe in our *F*-net dataset has been observed in other subduction systems (e.g. Smith et al., 2001; Margheriti et al., 1996; Nakajima and Hasegawa, 2004), although the opposite trend has also been observed (Levin et al., 2004).

A third striking feature of our splitting dataset is the character of splitting patterns at stations in northern Honshu (Figure 5). The stations in northern Honshu and southernmost Hokkaido exhibit splitting patterns that are more complicated than a simple

anisotropic model would allow; however, the patterns at these stations are coherent over long spatial length scales (shown in Figure 8). The splitting patterns obtained using the Chevrot (2000) method exhibit significant departure from a simple sin(2θ) variation; in fact, a sin(θ) periodicity seems to dominate the signal. This may indicate the presence of a dipping axis of anisotropic symmetry (Chevrot, 2000; Chevrot and van der Hilst, 2003), but more detailed forward modeling is needed to confirm this interpretation. The presence of a dipping axis of symmetry would be consistent with the dominant tectonic feature beneath this group of stations, the westward-dipping Pacific slab.

Finally, we emphasize that in the region under study a rapid spatial variation in observed splitting patterns is usually correlated with complexity in slab morphology. In locations where the slab morphology is simple, such as along the Ryukyu arc or beneath northern Honshu, the splitting behavior is generally consistent among stations separated by several hundred kilometers. Sections of the array where splitting behavior changes rapidly between stations separated by ~70 km or less, such as the Kanto-Tokai region, or where splitting behavior at individual stations is usually more complicated than a simple anisotropic model would allow, such as Hokkaido, are generally located above areas of complicated slab morphology (Figure 5). This correspondence provides support for the idea that complicated slab morphology may induce complex upper mantle flow patterns, which in turn manifest themselves as rapid spatial variations in shear wave splitting behavior.

4.5 Implications for other subduction zones.

Our investigation has shown that the majority of *F*-net stations exhibit variations in measured splitting parameters with backazimuth and/or incoming polarization direction that are inconsistent with a simple anisotropic model. We emphasize the danger of interpreting a single splitting measurement at one of these stations in terms of mantle anisotropy. For stations with complicated splitting patterns, the splitting parameters inferred from a single *SK*(*K*)*S* or teleseismic *S* wave arrival can be misleading and the interpretation must be based on of a large number of measurements covering a range of backazimuths and/or incoming polarization azimuths. At *F*-net stations, complicated splitting patterns at individual stations are commonplace; in fact, stations that exhibit splitting patterns consistent with a simple anisotropic model are the exception rather than the rule. It seems likely that complex splitting is common in other subduction zones and in other tectonically complicated regions. Therefore, caution should be exercised when interpreting a single splitting measurement in terms of upper mantle anisotropy at stations that overlie complex tectonic structure.

4.6 Comparison with previous studies

Two recent studies have investigated the splitting of local *S* phases due to upper mantle anisotropy at Japanese stations. Smith and Fouch (2005) used data from local slab events beneath a subset of the *F*-net stations, while Nakajima and Hasegawa et al. (2004) exploited data from shallow and intermediate-depth earthquakes measured at short-period stations of the Hi-net array, which is also operated by NIED. A direct comparison of local

and teleseismic splitting is difficult, but we find several points of agreement between the main features of our dataset and these two studies.

The work of Smith and Fouch (2005) focused on a subset of the *F*-net network and covered the area from roughly 32° to 36° N and 134° to 138° W (see Figure 1). Their dataset covers events with hypocentral depths ranging from approximately 25 km to nearly 500 km. The three main features of their dataset that are consistent with our work are as follows. First, they find fast directions that trend consistently NW-SE at a group of stations in the southern Kanto-Tokai region (OHS, KNY, and NAA). We find similar NW-SE fast directions at stations KNY and NAA, as well as nearby stations HKW and KNM. Secondly, they identify a region to the southwest of the NW-SE trending fast directions where fast directions trend approximately perpendicular, to the SW-NE. This is consistent with our results for stations TGA and ISI in this region. Finally, Smith and Fouch (2005) note a consistent increase in the measured splitting time with increasing hypocenter depth, with the largest split times (associated with events from 400-500 km depth) of approximately 1 s. Although we lack such depth resolution, their results for deep events are quite consistent with the average split times we obtain from teleseismic events at the stations in their study region, which range from ~ 0.6 s to ~ 1.0 s.

The work of Nakajima and Hasegawa (2004) focuses on a region beneath the southern part of Tohuku, covering the area from roughly 36° to 39° N and 138° to 142° E. The station density for the Hi-net network is far higher than for *F*-net; there are only 9 *F*-net stations located in the Nakajima and Hasegawa (2004) study area compared to approximately 75 Hi-net stations. Moreover, they only consider data from relatively shallow earthquakes, and thus presumably sample the crust and lithosphere only.

Notwithstanding these differences, we can make a few observations. First, the Nakajima and Hasegawa (2004) study reveals a striking rotation of fast directions from trench-parallel closer to the trench to trench-parallel farther away from the trench, which is similar to the results obtained in the present study for other areas. This pattern is difficult to discern in our *F*-net results for the southern Tohuku region, perhaps due to the paucity of stations. At the four *F*-net stations in this region for which we obtained reliable fast directions we identified a SW-NE trending fast direction (trench-parallel) for station CHS and NW-SE trending fast direction (trench-perpendicular) at stations HRO, ONS, and KZK. This is consistent with the results of Nakajima and Hasegawa (2004). Secondly, we note that the split times we obtained for stations in this region for teleseismic phases (~ 0.5 - 0.9 s) are considerably larger than the highest split times obtained by Nakajima and Hasegawa (2004) (0.1 – 0.4 s). This discrepancy highlights the greater sensitivity to crustal anisotropy in the Nakajima and Hasegawa dataset.

5. Future work

We emphasize that the interpretations of the data presented in this paper should be considered as preliminary. We have assembled a large dataset for shear wave splitting and have thoroughly investigated the dependence of measured values for (φ, δt) on parameters such as incoming polarization azimuth, but the interpretation of splitting parameters is difficult and inherently non-unique, especially in the presence of complex anisotropic structure. However, we believe that our dataset affords us a chance to characterize more quantitatively the three-dimensional structure of the upper mantle. By bringing to bear more sophisticated forward (numerical modeling of geodynamic

processes in the mantle wedge and beneath the slab) and inverse (the inversion of shear wave splitting measurements for three-dimensional anisotropic structure) techniques, we will more fully exploit the splitting dataset we have assembled.

6. Summary

We have assembled and processed a large database of teleseismic shear wave (*S, SKS,* and *SKKS*) splitting measurements for the broadband *F*-net array in Japan. For each station we analyzed records covering a wide range of incoming polarization azimuths and incidence angles, and we looked for variations in measured splitting parameters that could be indicative of complex anisotropic structure. Most of the *F*-net stations exhibit splitting behavior that is more complicated than a simple, homogenous, single-layer anisotropic model would allow. We observe two endmember scenarios for geographical variations in splitting behavior. In some parts of the array, most notably the Ryukyu arc, we observe splitting behavior that is consistent between stations over a distance of approximately 700 km. In other parts of the array, most notably the Kanto-Tokai region, splitting behavior changes rapidly, with stations separated by as little as 70 km exhibiting completely different splitting patterns. We cannot rule out a lithospheric contribution but our observations seem most consistent with significant complexity in anisotropic structure in the asthenospheric upper mantle beneath much of Japan. Our observations allow several preliminary interpretations in terms of tectonic processes, but the long-term goal of this work is to combine geodynamical modeling and inversion of shear wave splitting measurements to obtain a quantitative model of the three-dimensional anisotropic structure beneath Japan.

7. Appendix

Here we provide a summary of our splitting measurements at all stations. In Figure A1, we plot circular histograms (rose diagrams) showing the distribution of fast directions measured with the cross-correlation method. For all stations in Category I and II, the average fast direction measured with the Chevrot (2000) method is shown with a gray line. Table A1 provides station coordinates for all stations as well as best-fitting splitting parameters (φ, δt) for stations in Categories I and II.

8. Acknowledgements

The authors thank the Japanese National Research Institute for Earth Science and Disaster Prevention for making *F*-net data available and easily accessible, Sebastien Chevrot for assistance with data processing and for providing his splitting codes, and Bill Menke for making his cross-correlation code freely available. The comments of an anonymous reviewer greatly improved the manuscript. This research was supported by NSF grant EAR-0337697 and by an NSF Graduate Research Fellowship awarded to M.D.L.

Figure Captions

Figure 1. a. Station map for *F*-net, along with relevant tectonic features. Circles indicate the locations of *F*-net stations as of mid-2002. The locations of trenches (solid lines) and slab contours at 100 km intervals (dotted lines) are shown, after Gudmundsson and Sambridge (1998) and Engdahl et al. (1998). Arrows indicate the directions of plate motions, and rectangles indicate the study areas of Nakajima and Hasegawa (2004) (top) and Smith and Fouch (2005) (bottom). b. The locations of all *F*-net stations mentioned by name in the text.

Figure 2. A map of events used in this study, March 1995 – May 2004.

Figure 3. a. A raw, unfiltered seismogram at station SGN, with the expected arrival times for *SKS*(ac)*, SKS*(df), *SKKS,* and *Sdiff* from the iasp91 earth model shown. b. The record has been bandpass filtered between 0.02 Hz and 0.125 Hz. A clear *SKS* arrival can be seen. c. The seismogram has been windowed around the *SKS* phase and the radial (bottom) and transverse (middle) components are shown. In the top trace, the transverse component is overlain with the time derivative of the radial component. As expected, the shape of the transverse component matches the derivative of the radial component. Vertical bars indicate the time window used in the splitting analysis.

Figure 4. The results of the splitting analysis using the Chevrot (2000) method (A) along with measured fast directions B) and split times (C) using the cross-correlation method, for station TKA. In panels D-F, and G-I, we show the results for stations SGN and TMR, respectively. In panels J-L we display the Chevrot (2000) results only for stations FUK, HSS, and FUJ. All error bars are 2σ. All plots of the Chevrot splitting vector include a rose diagram (inset) showing the distribution of fast directions found with the cross-correlation method. Gray bars on the rose diagram indicate the best fit from the Chevrot (2000) method. Direct *S* phases are marked with a circle; core-refracted phases are marked by a triangle. Each plot shows the relevant splitting parameter plotted against the incoming polarization angle, which is equivalent to the backazimuth for *SK*(*K*)*S* phases. For direct *S* phases, the polarization angle (0°-180°) was measured directly from the seismogram. Measured polarization angles for events with a backazimuth in the range 90°-270° were then adjusted by adding 180°, so that events with similar polarizations but widely different polarizations will plot 180° apart. This convention makes the splitting patterns easier to visualize, but in no way changes their interpretation.

Figure 5. a. A map of the types of splitting behavior observed at F-net stations. At stations marked with a black square, the splitting behavior is Category I (see text) and is consistent with a simple anisotropic model. Category II stations are marked with a black triangle. At stations marked with a gray circle, the splitting behavior is Category III and is inconsistent with a simple model. Category IV stations, for which the data quality is poor, are marked with an open diamond. b. A map of fast directions at *F*-net stations. We plot a fast direction for all Category I and Category II stations.

Figure 6. a. A map of the event distribution for station HSS, subdivided into regions used in the hypothesis testing described in section 4.1. Direct *S* events are indicated with circles; black circles indicate events deeper than 400 km, and gray circles indicate events between 200 and 400 km depth. *SK*(*K*)*S* events are marked with diamonds. b. The Chevrot (2000) splitting vector for station HSS. The splitting intensities for intermediate-depth events in the New Hebrides-Tonga-Kermadec subduction zone are plotted with gray triangles; all other events are plotted with black circles.

Figure 7. a. The combined teleseismic splitting vector for all Ryukyu arc stations is shown with gray circles. The dark line indicate the best $\sin(2\theta)$ fit to the teleseismic splitting data. Also shown are the splitting results for 9 local slab events; these results are plotted in black. b. For clarity, the individual teleseismic splitting results have been removed and only local events are shown. The $\sin(2\theta)$ fit is the same as shown in (a). Events with hypocenter depths between 50 and 100 km are plotted as triangles; those deeper than 100 km are plotted as squares. All deep slab events are consistent with as much splitting (or more) than the average teleseismic splitting, while shallower slab events show little or no splitting. These results suggest that anisotropy is concentrated in the deeper part of the superslab mantle.

Figure 8. The splitting vectors for five northern Honshu stations (IYG, GJM, KSN, KSK, and SBT) are plotted with different symbols and shading. Although the splitting patterns

are clearly inconsistent with a simple anisotropic model, they are coherent over long length scales.

Figure A1. Rose diagrams showing the distribution of fast directions measured with the cross-correlation method at 55 *F*-net stations. For stations in Categories I and II, the best-fitting fast direction found with the Chevrot (2000) method is marked with a gray line. For station locations, categorizations, and best-fitting splitting parameters, see Table 1. Stations with poor data quality (IWT, TTO, and TYM) are not shown on this figure; rose diagrams for stations TKA, SGN, TMR, FUJ, FUK, and HSS are shown in Figure 4.

Table A1. Station coordinates for F-net stations, along with best-fitting splitting parameters for all Category I and Category II stations.

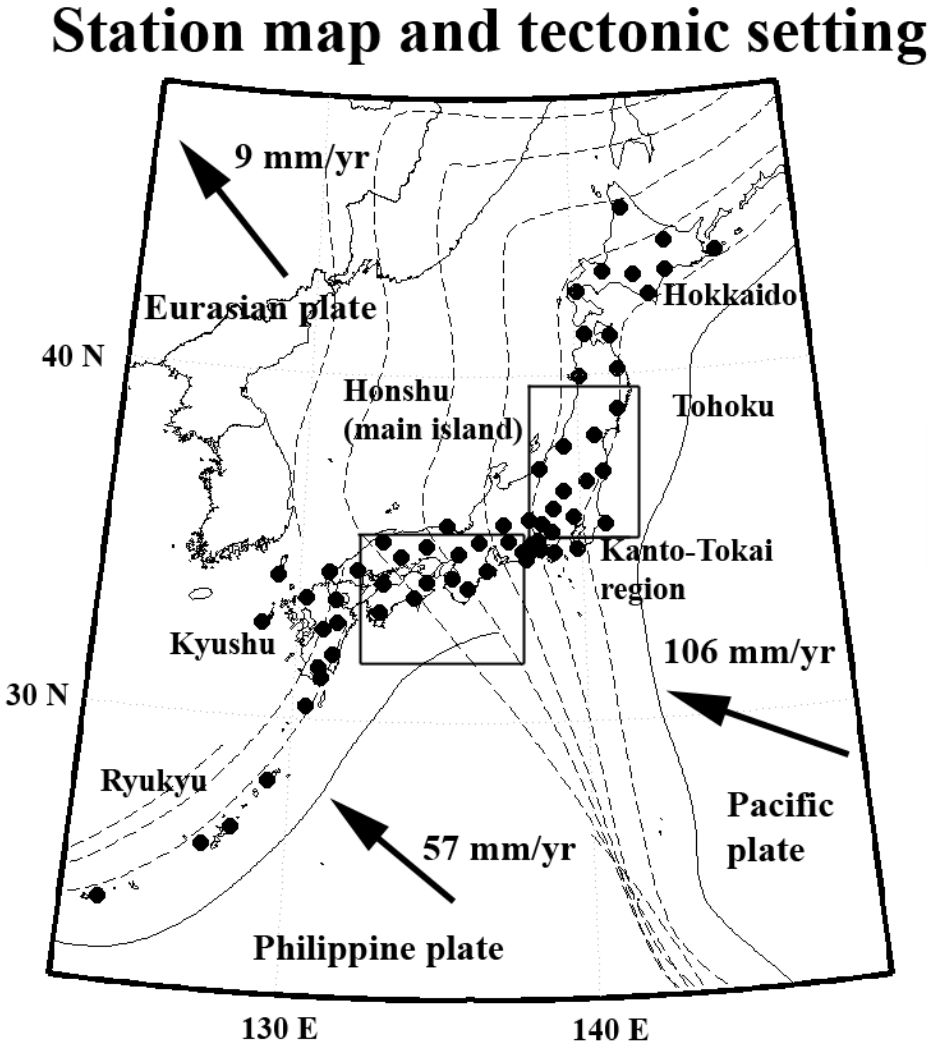
Station map and tectonic setting
9 mm/yr
Eurasian plate
Hokkaido
40 N
Honshu
(main island)
Tohoku
Kanto-Tokai
region
Kyushu
106 mm/yr
30 N
Ryukyu
Pacific
plate
57 mm/yr
Philippine plate
130 E
140 E

Figure 1a

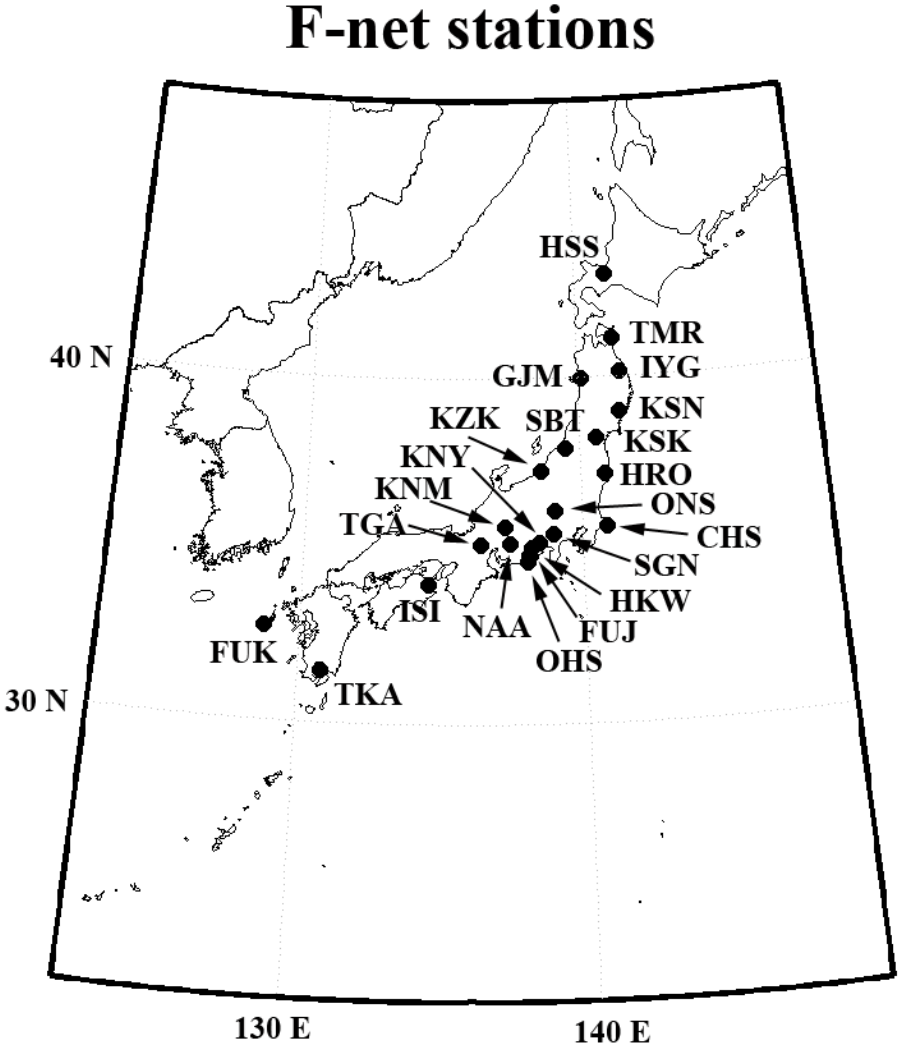
F-net stations
HSS
TMR
IYG
GJM
KSN
KZK
SBT
KSK
KNY
HRO
KNM
ONS
TGA
CHS
SGN
HKW
ISI
NAA
FUJ
OHS
FUK
TKA
40 N
30 N
130 E
140 E

Figure 1b

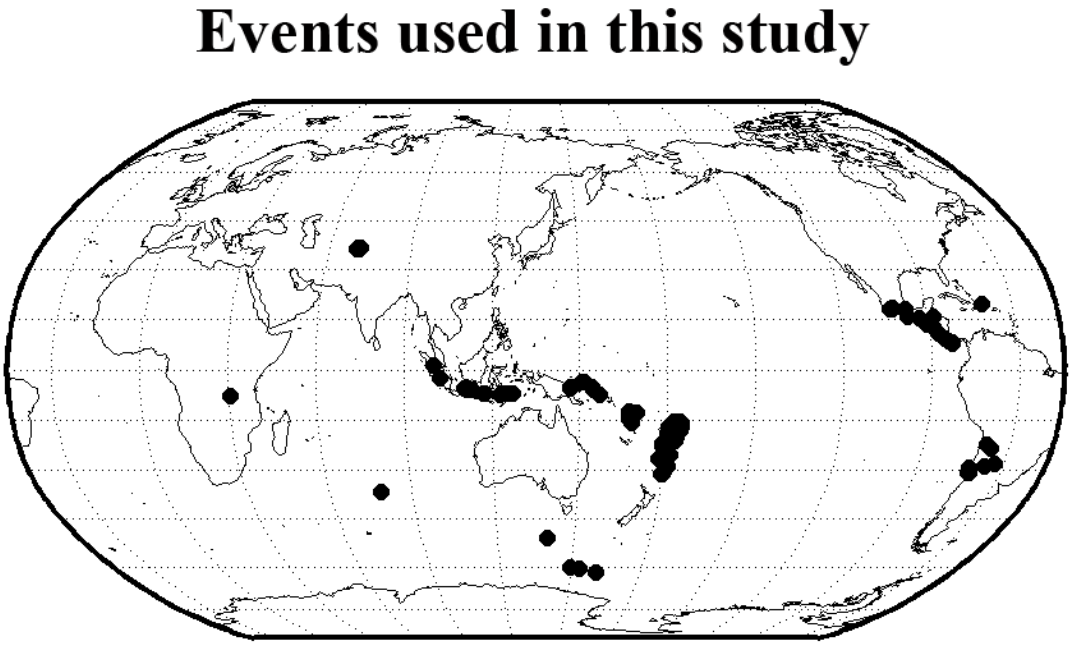

Figure 2

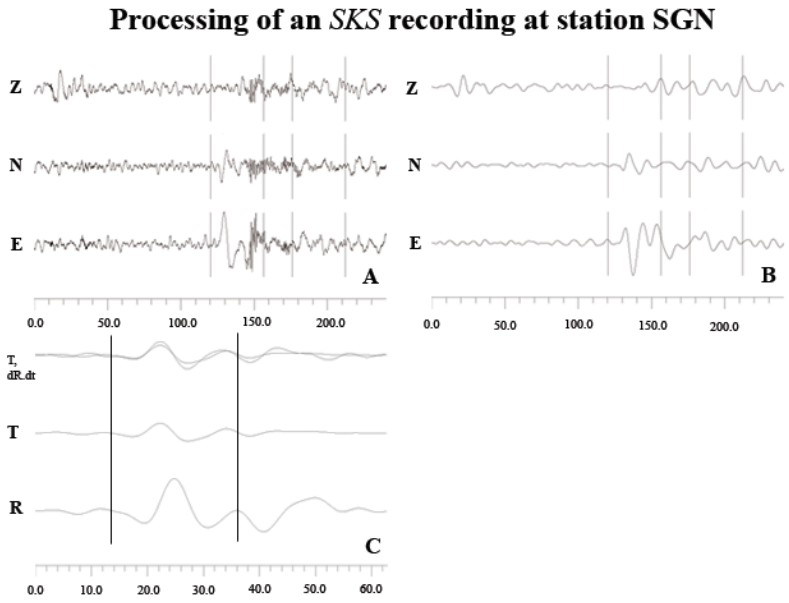
Processing of an *SKS* recording at station SGN
Z
N
E
A
0.0
50.0
100.0
150.0
200.0
Z
N
E
B
0.0
50.0
100.0
150.0
200.0
T,
dR.dt
T
R
C
0.0
10.0
20.0
30.0
40.0
50.0
60.0

Figure 3

Splitting patterns at 6 F-net stations

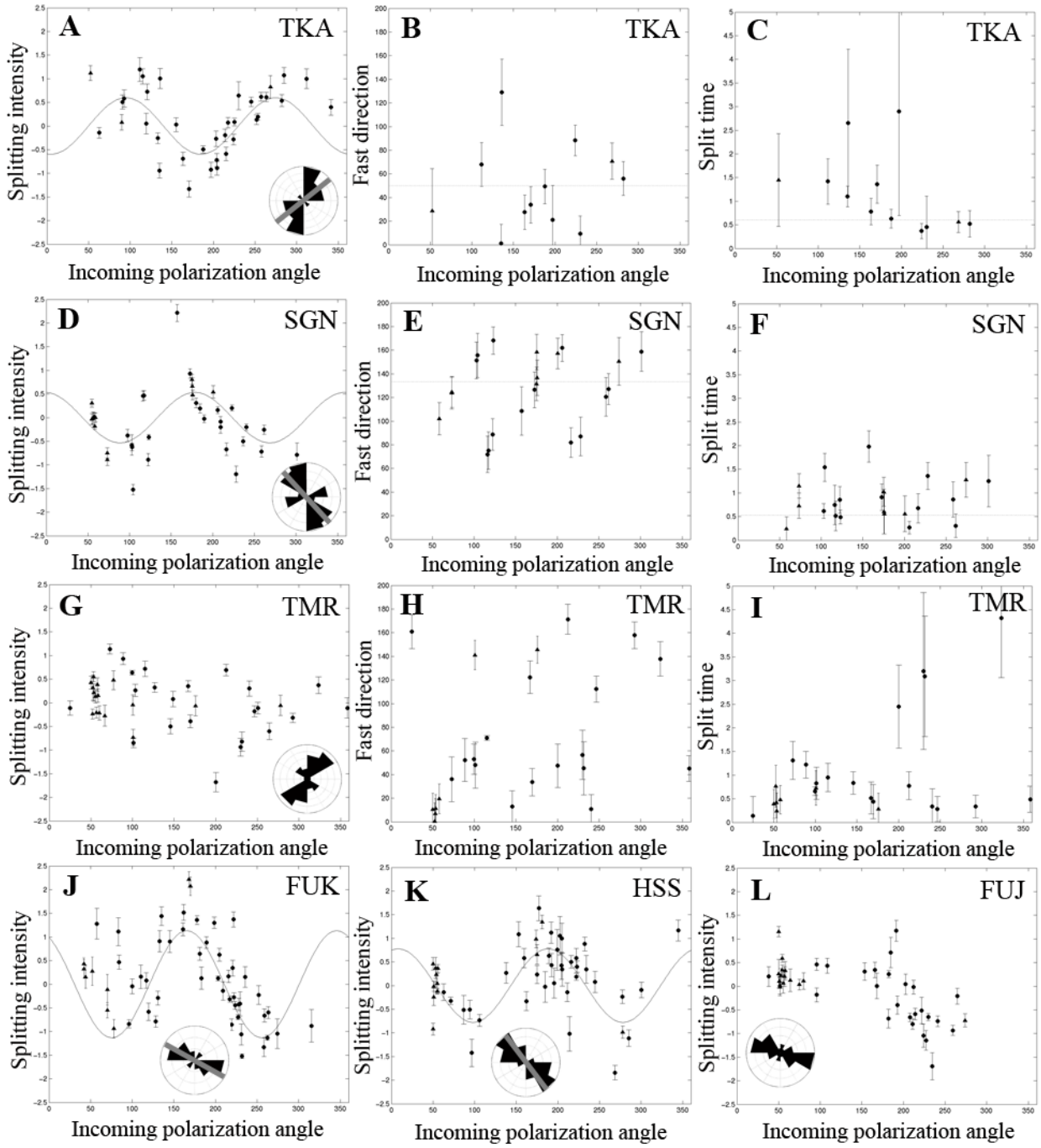

Figure 4

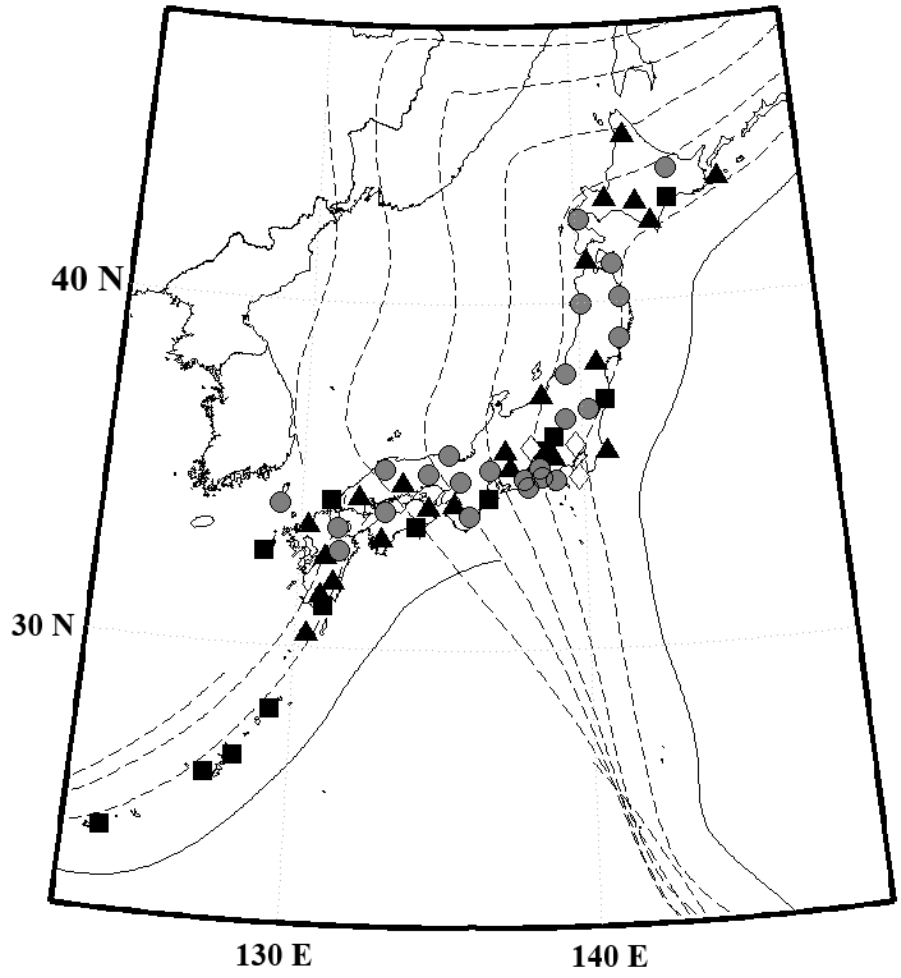

Figure 5a

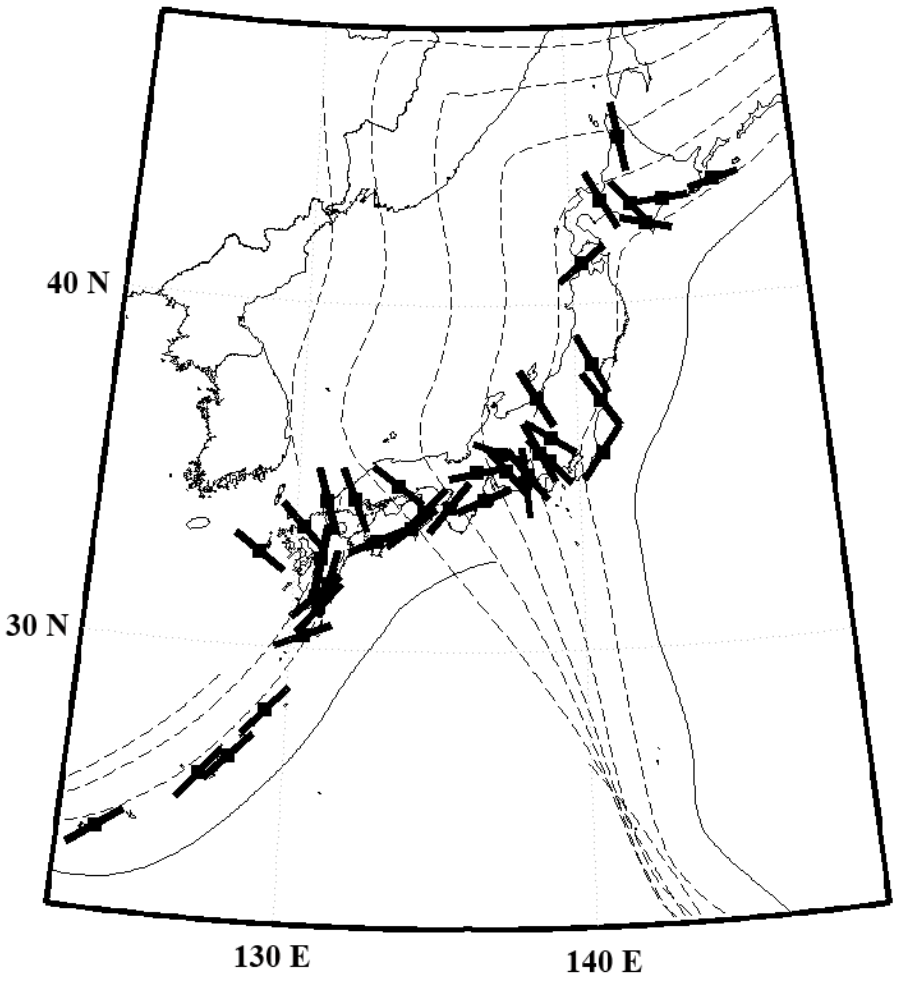

Figure 5b

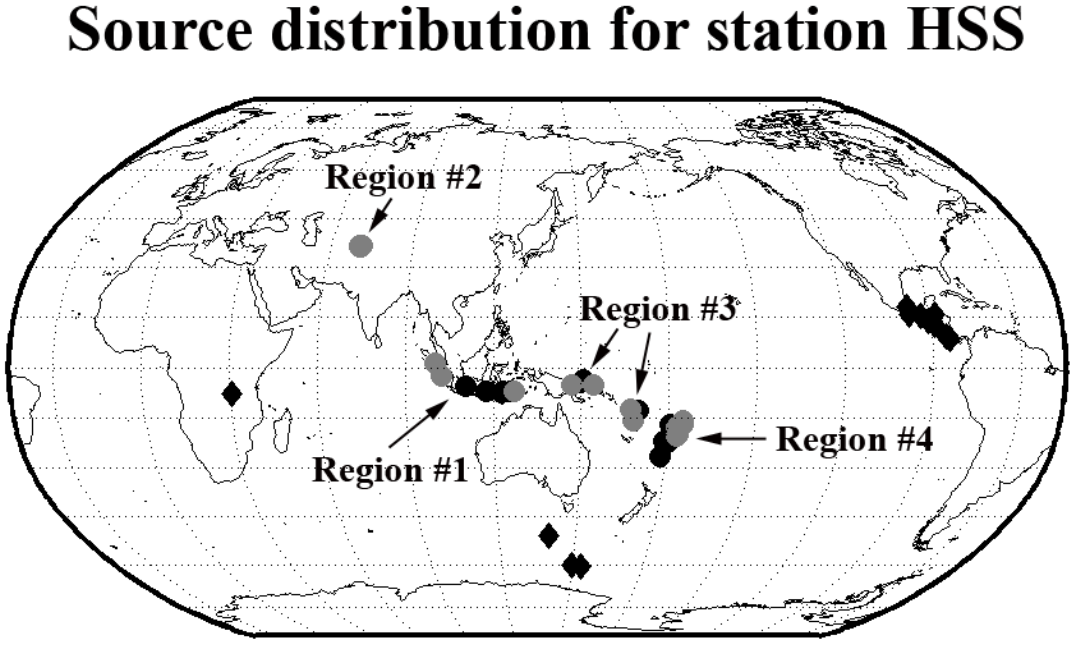
Source distribution for station HSS
Region #2
Region #3
Region #4
Region #1

Figure 6a

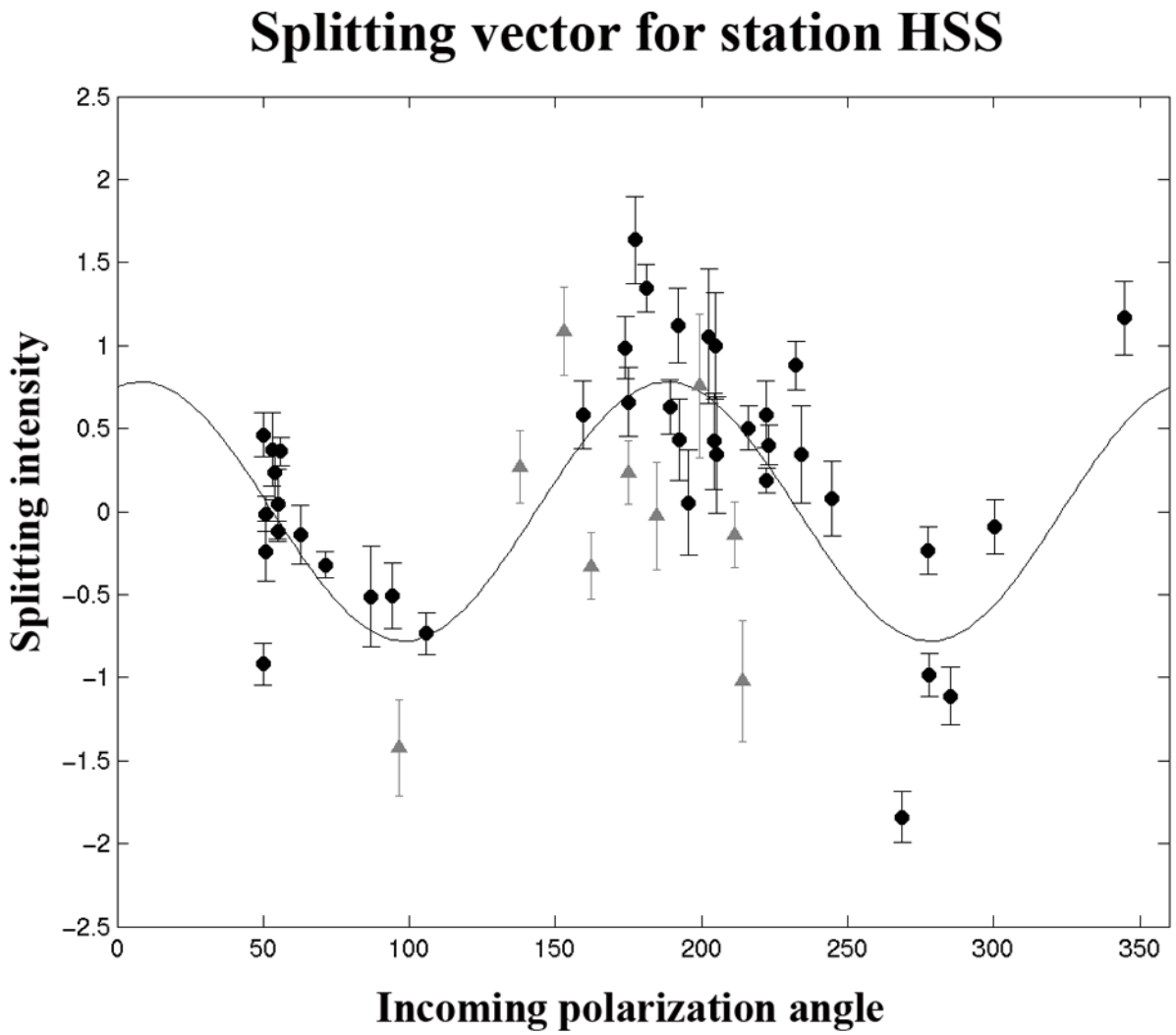
Splitting vector for station HSS
Splitting intensity
Incoming polarization angle
2.5
2
1.5
1
0.5
0
−0.5
−1
−1.5
−2
−2.5
0
50
100
150
200
250
300
350

Figure 6b

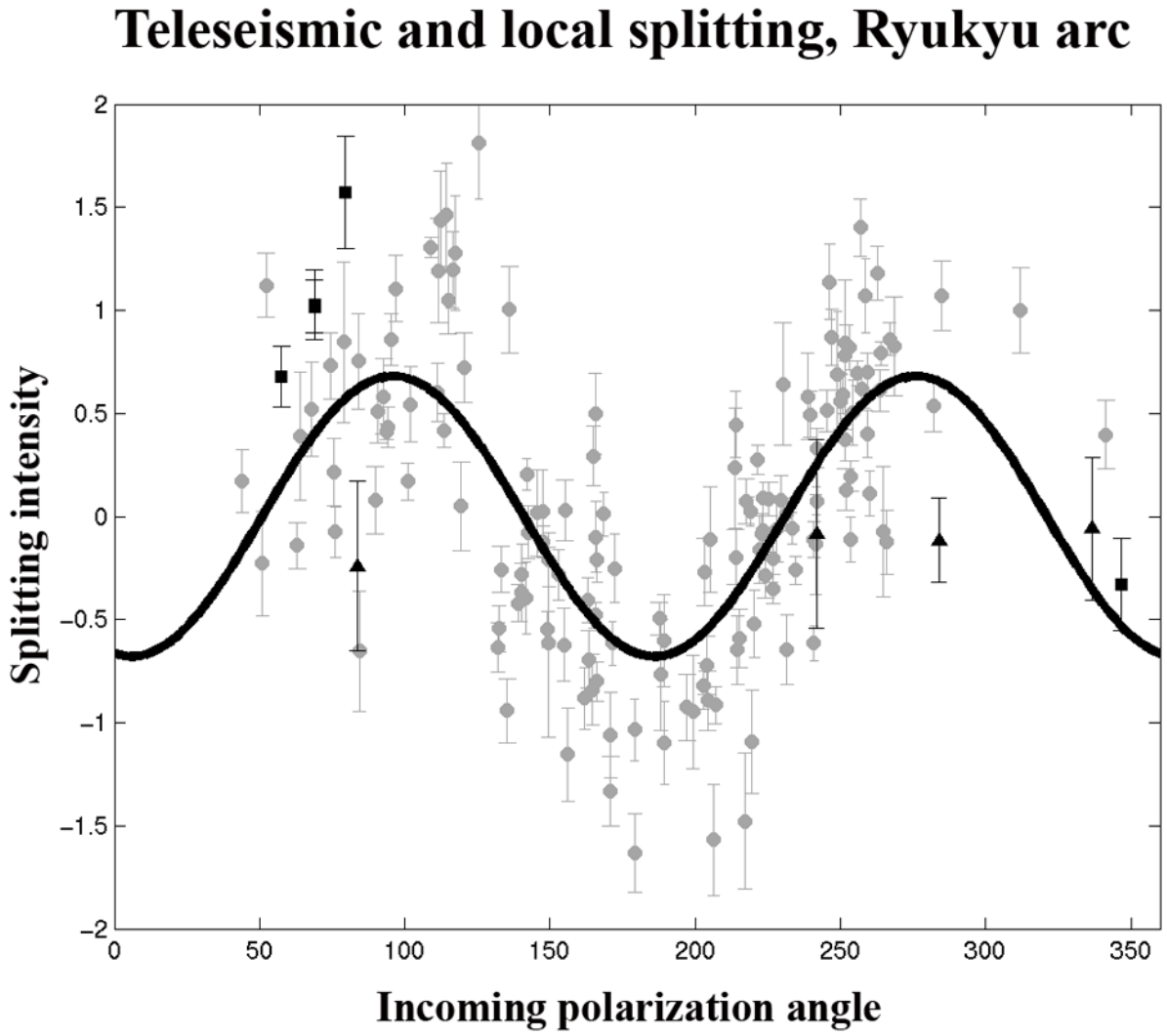
Teleseismic and local splitting, Ryukyu arc
Splitting intensity
Incoming polarization angle
2
1.5
1
0.5
0
−0.5
−1
−1.5
−2
0
50
100
150
200
250
300
350

Figure 7a

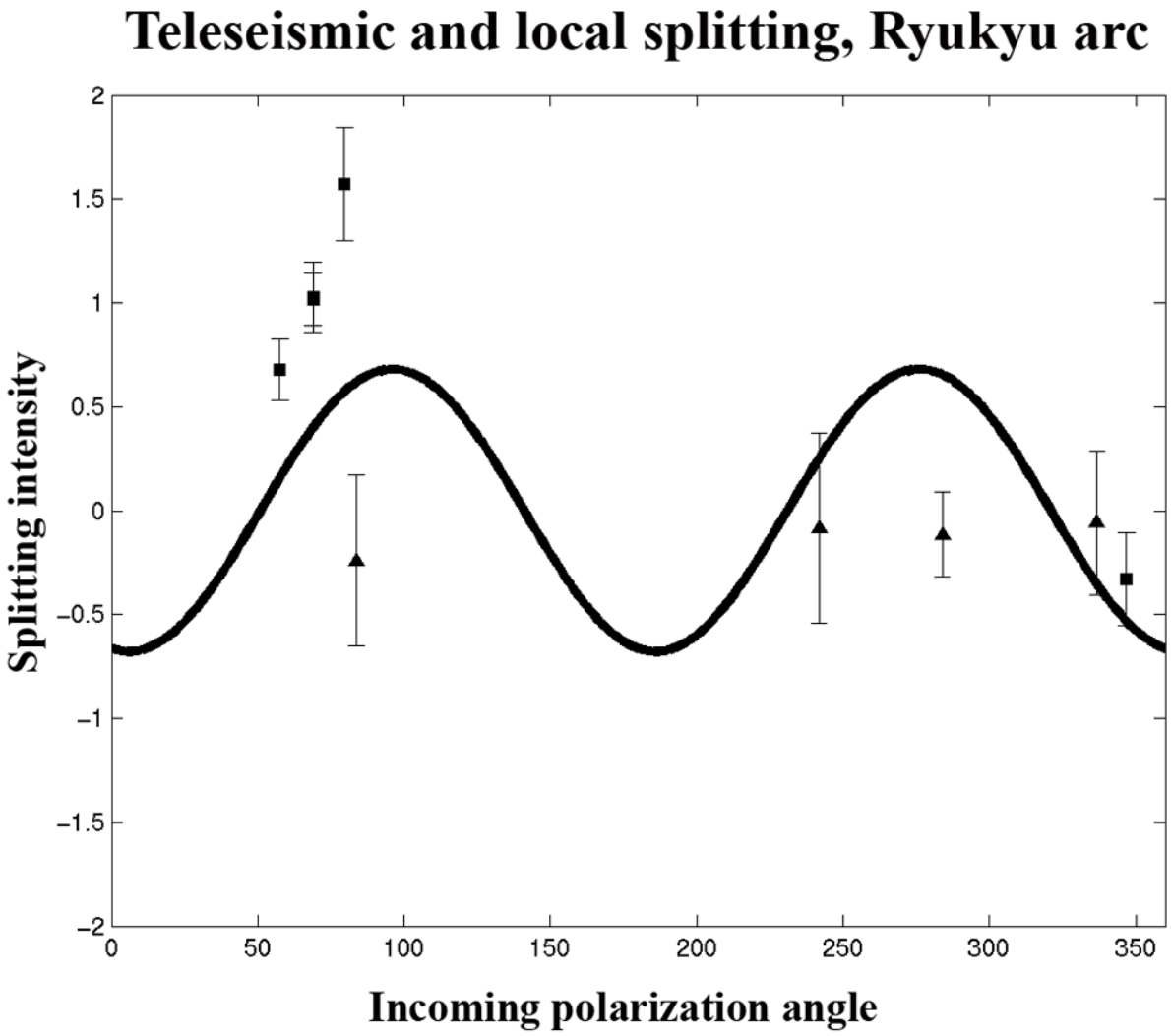
Teleseismic and local splitting, Ryukyu arc
Splitting intensity
Incoming polarization angle
2
1.5
1
0.5
0
−0.5
−1
−1.5
−2
0
50
100
150
200
250
300
350

Figure 7b

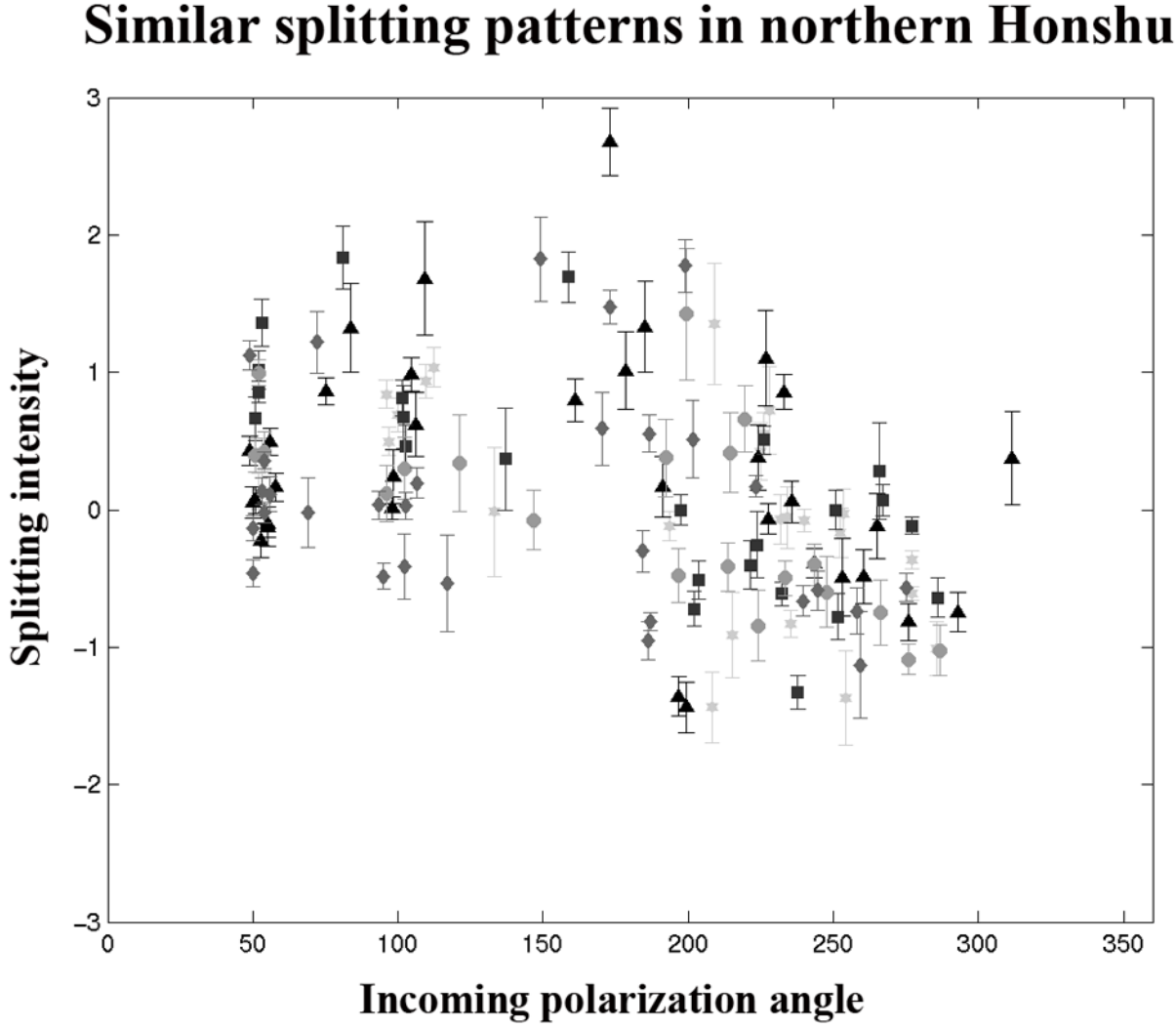
Similar splitting patterns in northern Honshu
Splitting intensity
Incoming polarization angle
3
2
1
0
−1
−2
−3
0
50
100
150
200
250
300
350

Figure 8

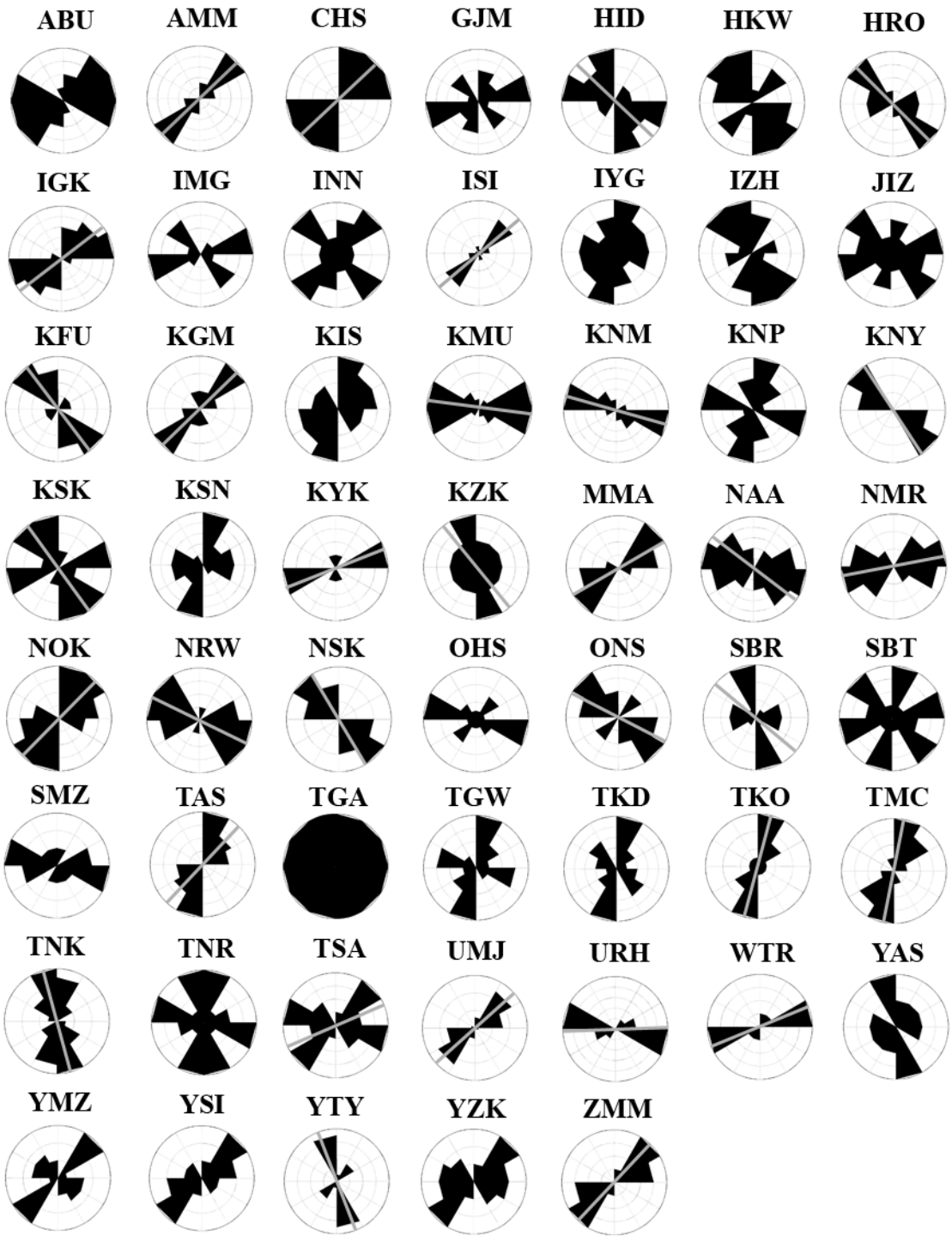
ABU
AMM
CHS
GJM
HID
HKW
HRO
IGK
IMG
INN
ISI
IYG
IZH
JIZ
KFU
KGM
KIS
KMU
KNM
KNP
KNY
KSK
KSN
KYK
KZK
MMA
NAA
NMR
NOK
NRW
NSK
OHS
ONS
SBR
SBT
SMZ
TAS
TGA
TGW
TKD
TKO
TMC
TNK
TNR
TSA
UMJ
URH
WTR
YAS
YMZ
YSI
YTY
YZK
ZMM

Figure A1

Station Name	Lat	Lon	φ, deg	δt, sec		Station Name	Lat	Lon
Category I						**Category III**		
AMM	28.15	129.30	46	0.65		ABU	34.86	135.57
FUK	32.71	128.76	-59	1.13		ASI	36.65	139.42
HRO	37.22	140.88	-46	0.38		FUJ	35.23	138.42
IGK	24.41	124.18	53	1.10		GJM	39.95	140.12
KFU	35.75	138.57	-34	0.79		HKW	35.09	138.14
KGM	26.75	128.22	47	0.58		IMG	42.39	140.14
ONS	36.15	138.98	-64	0.78		INN	33.47	131.31
TAS	31.19	130.91	45	0.75		IYG	40.12	141.59
TKA	31.51	130.79	52	0.63		IZH	34.13	129.21
UMJ	33.57	134.04	56	0.78		JIZ	34.91	139.00
URH	42.93	143.67	87	0.68		KIS	33.86	135.89
WTR	34.37	136.58	70	0.56		KNP	43.76	143.71
YTY	34.28	131.04	-20	0.73		KSN	38.97	141.53
ZMM	26.23	127.31	45	0.55		OHS	34.68	138.01
Category II						SBT	37.97	139.45
CHS	35.70	140.86	43	0.73		SMZ	34.99	138.52
HID	42.82	143.41	-50	0.28		TGA	35.18	136.34
HSS	42.96	141.23	-37	0.78		TGW	33.97	132.93
ISI	34.06	134.46	50	0.33		TKD	32.81	131.39
KMU	42.24	142.97	-79	0.59		TMR	41.10	141.39
KNM	35.72	137.18	-74	1.10		TNR	34.91	137.89
KNY	34.87	138.07	-31	0.26		YAS	35.65	135.16
KSK	38.25	140.59	-34	0.41		YMZ	36.92	140.25
KYK	30.37	130.41	71	0.37		YSI	35.19	132.89
KZK	37.30	138.52	-38	0.34		YZK	35.09	134.46
MMA	41.16	140.41	59	0.38		**Category IV**		
NAA	35.22	137.37	-48	0.39		IWT	35.93	139.74
NMR	43.37	145.75	80	0.72		TTO	35.83	138.12
NOK	34.14	135.35	45	0.45		TYM	34.97	139.84
NRW	34.76	133.53	-64	1.09				
NSK	34.34	132.00	-30	0.39				
SGN	35.51	138.95	-48	0.54				
SBR	33.50	130.26	-49	0.38				
TKO	31.89	131.23	16	0.33				
TMC	32.60	130.92	11	1.40				
TNK	44.78	142.08	-13	0.54				
TSA	33.17	132.82	71	0.27				

Table A1

Chapter 3

A local shear wave splitting data set for the Ryukyu Arc[1]

Abstract

We present shear wave splitting measurements from local slab earthquakes at eight seismic stations of the Japanese *F*-net array located in the Ryukyu Arc. We obtained high-quality splitting measurements for 70 event-station pairs and found that the majority of the measured fast directions were parallel to the strike of the trench and perpendicular to the convergence direction. Splitting times for individual measurements ranged from 0.25 seconds to 2 seconds; most values were between 0.75 and 1.25 seconds. Both the fast directions and the split times were similar to results for teleseismic *S(K)KS* and *S* wave splitting at the same stations, which suggests that the anisotropy is located in the mantle wedge above the slab. We considered several mantle deformation scenarios that would result in predominantly trench-parallel fast directions, and concluded that for the Ryukyu subduction system the most likely explanation for the observations is corner flow in the mantle wedge combined with B-type olivine fabric. In this model, the flow direction in the wedge is perpendicular to the trench, but the fast axes of olivine crystals tend to align perpendicular to the flow direction, resulting in trench-parallel shear wave splitting.

[1] In press as: Long, M. D., van der Hilst, R. D., 2006. Shear wave splitting from local events beneath the Ryukyu Arc: Trench-parallel anisotropy in the mantle wedge. Phys. Earth Planet. Inter., in press.

1. Introduction

Observations of seismic anisotropy in the Earth's upper mantle, such as measurements of shear wave birefringence or splitting, are an important tool for characterizing the style and geometry of tectonic deformation. The measurement and interpretation of shear wave splitting for phases that traverse the upper mantle has shed light on past and present deformation processes in a variety of tectonic settings: for example, mid-ocean ridges (Wolfe and Solomon, 1998), rift zones (Kendall et al., 2005), continental collisions (Flesch et al., 2005; Lev et al., 2006), strike-slip faults (Özaleybey and Savage, 1995; Ryberg et al., 2005), regions of mantle upwelling (Walker et al., 2001; Xue and Allen, 2005), and stable cratonic regions (Fouch et al., 2004). Shear wave splitting associated with upper mantle anisotropy has also been found to be nearly ubiquitous in subduction zone settings (Ando et al., 1983; Russo and Silver, 1994; Fouch and Fischer, 1996; Sandvol and Ni, 1997; Fischer et al., 1998; Smith et al., 2001; Anderson et al., 2004, Currie et al., 2004), but the interpretation of shear wave splitting measurements in subduction zones is difficult and non-unique.

There are many processes that can contribute to subduction zone anisotropy, including corner flow in the mantle wedge, flow beneath the slab of subducted lithosphere, flow around the slab edge, the generation and migration of melt, and anisotropic structure in the slab itself or in the overriding plate (for an overview, see Park and Levin, 2002). Because of the ambiguity of which processes are contributing to the observed anisotropy, and because shear wave splitting is a path-integrated measurement with generally poor depth resolution, the interpretation of shear wave splitting

measurements in subduction zone settings is still an area of controversy. In particular, the interpretation of fast splitting directions that are parallel to the trench (that is, perpendicular or at a large angle to the convergence direction) is a matter for some debate.

Both trench-parallel and trench-perpendicular fast directions have been observed in subduction zone settings (for a detailed review, see Wiens and Smith, 2003), but trench-parallel fast directions seem to be more common and have been observed or inferred in New Zealand (Marson-Pidgeon et al., 2001), the Aleutians (Yang et al., 1995; Mehl et al., 2003), Japan (Fouch and Fischer, 1996), and Tonga (Fischer and Wiens, 1996), among other regions. These observations of trench-parallel fast directions contradict the predictions of simple corner-flow models for flow in the mantle wedge, in which viscous coupling between the downgoing slab and the overlying wedge material induces flow that is parallel to the convergence direction (e.g., Fischer et al., 2000). However, new laboratory results have shown that when olivine aggregates are deformed under high-stress, low-temperature, water-rich conditions, the fast axes of individual olivine crystals tend to align 90° from the flow direction (Jung and Karato, 2001). These B-type olivine fabrics, in conjunction with trench-perpendicular flow in the mantle wedge, may explain trench-parallel fast directions in some regions (Karato, 2003; Kneller et al, 2005). It is not clear, however, if the stresses, temperatures, and volatile concentrations needed to produce B-type olivine fabric are relevant to large volumes of the mantle wedge.

In a study of teleseismic shear wave splitting at stations of the broadband *F*-net array in Japan, Long and van der Hilst (2005b) reported consistently trench-parallel fast

directions in the Ryukyu arc, with split times between 0.65 – 1.2 seconds. However, the depth extent and location of the anisotropy could not be robustly determined because the study focused mainly on measurements of *SKS, SKKS,* and teleseismic *S* phases. Here, we report the results of a follow-up study of splitting from local slab events at Ryukyu arc stations (see Figure 1 for station locations and tectonic setting). The comparison of shear wave splitting in local and teleseismic arrivals allows us to isolate contributions from anisotropy in the mantle wedge. The depth constraint on anisotropy thus provided can help discriminate among the various hypotheses for explaining subduction zone anisotropy.

2. Tectonics of the Ryukyu Arc

We summarize the geological evolution and tectonic setting of the Ryukyu arc after overviews by Taira (2001) and Schellart et al. (2002). The Ryukyu Arc (Figure 1) is associated with the subduction, initiated at ~55 Ma, of the Philippine plate beneath Eurasia at a relative rate of ~55 mm/yr. The convergence direction is to the northwest and the trench strikes generally NE-SW, so that along most of the arc there is little or no obliquity in subduction direction (e.g., McCaffrey, 1996). Rifting in the backarc, bounded by the Okinawa Trough to the northwest, started in the late Miocene (Schellart et al., 2002; Letouzey and Kimura, 1985). Slab rollback rates are generally small along most of the arc, with a rate of (southeastward) trench migration of less than 10 mm/yr (Heuret and Lallemand, 2005; Yu and Kuo, 1996; Mazzotti, 1999). However, toward the southernmost part of the arc, where the strike of the trench changes from NE-SW to nearly E-W, there is an increase in subduction obliquity and in the rate of slab rollback.

The part of the Ryukyu arc near Taiwan has been studied extensively (e.g., Kao et al., 2000) but the tectonic setting here is more complicated than in the center of the arc and there is no consensus on how deformation is accommodated.

The morphology of the subducting Philippine slab has been studied using earthquake hypocenter locations (Engdahl et al., 1998; Gudmundsson and Sambridge, 1998) and seismic tomography of the western Pacific (e.g., Widiyantoro et al., 1999; Gorbatov and Kennett, 2003; Lebedev and Nolet, 2003; Li et al., 2006), although the slab is generally not well resolved at shallow depths (above ~ 300 km) by the data used in the tomographic inversions. The slab dips at approximately 45° to the northwest, and the dip remains nearly constant along the strike of the trench. The maximum depth of the seismogenic zone decreases from ~ 300 km in the south to ~ 250 km in the north (Gudmundsson and Sambridge, 1998). For studies of the crustal structure of the Ryukyu arc and the adjacent oceanic regions we refer to Iwasaki et al. (1990) and Wang et al. (2004). Analyses of earthquake focal mechanisms and fault geometries (e.g., McCaffrey, 1996; Fournier et al., 2001; Kubo and Fukuyama, 2003) suggest the existence of localized regions of arc-parallel extension along the arc, but it is unclear to what degree, if any, extension in the crust is coupled to deformation in the mantle.

3. Data and Methods

We have analyzed data from the eight southernmost stations of *F*-net (Figure 1), a network of 82 broadband seismic stations in Japan (www.fnet.bosai.go.jp). With the exception of station YNG, which was not installed until mid-2002, we previously investigated teleseismic shear wave splitting at each of these stations (Long and van der

Hilst, 2005b). Among the *F*-net stations throughout Japan, Ryukyu arc stations exhibited some of the largest split times, generally around 1 s or more. Long and van der Hilst (2005b) observed backazimuthal variations in observed splitting patterns, presumably indicating complex anisotropy, at the majority of *F*-net stations, but the Ryukyu stations exhibited splitting patterns consistent with a simple anisotropic model (that is, a single anisotropic layer with a horizontal axis of symmetry).

To understand the origin of the anisotropic signal better we investigate if splitting from events located in the slab itself can help distinguish between anisotropy in the mantle wedge and anisotropy within or beneath the slab of subducted lithosphere. We selected intermediate (70-300 km) depth earthquakes occurring between July 1999 and May 2005. We searched for events at a small distance (1°-2°) from each station location to facilitate the interpretation of the results and to ensure that all shear phases arrive within the angular window defined by the critical P-S conversion angle at the free surface. Figure 2 depicts the locations of the events and stations used in this study, as well as the approximate raypaths for both the local *S* phases and the teleseismic raypaths from Long and van der Hilst (2005b).

After identifying candidate events for analysis, *S* wave arrivals with high signal-to-noise ratios were selected by visual inspection of the waveforms. Before this inspection we applied two different bandpass filters: one with corner frequencies of 0.02 and 0.125 Hz, which is the same as used in Long and van der Hilst (2005b), and one with corner frequencies of 0.1 and 1 Hz, similar to the filter used in Levin et al. (2004). Most events had significant energy in one band or the other, but not both. Most *S* arrivals from the local events had more energy in the higher frequencies, but we report splitting results

for both the high- and the low-frequency bandpass (0.02-0.125 Hz) because the latter can be more easily compared to the teleseismic splitting reported in Long and van der Hilst (2005b).

Once clear *S* wave arrivals were identified in the data, we applied the cross-correlation method to estimate splitting parameters (Ando et al., 1983; Fukao, 1984). This method grid-searches for the fast direction φ and split time δt that corrects the horizontal seismogram components to the two most nearly identical pulse shapes. We use an implementation of the cross-correlation algorithm described by Levin et al (1999). Long and van der Hilst (2005a) evaluated the performance of several shear wave splitting methods at Japanese stations and found that this method was generally stable and robust even for complex tectonic regions. We visually checked the corrected particle motion diagrams to ensure near-linearity, and the contour plots of the cross-correlation coefficient for each potential pair of splitting parameters were inspected to ensure the best-fitting (φ, δt) values were well-constrained. We calculated formal errors based on the formulation of Levin et al. (1999). An example of a splitting analysis for a recording at station IGK is shown in Figure 3.

4. Results

In the high frequency band we obtained a total of 34 well-constrained splitting measurements at the eight stations considered in this study, along with 8 well-constrained null measurements (clear *S* arrivals with no discernable splitting). In the low frequency band we obtained 19 measurements and 9 nulls. We list all measurements in table form as Table 1. Individual measurements of fast direction φ and split time δt in each frequency

band are plotted in Figure 4, along with average teleseismic splitting from Long and van der Hilst (2005b).

A striking feature of the low-frequency data set (Figure 4a) is the preponderance of fast directions that are parallel or sub-parallel to the strike of the trench, which is in agreement with splitting in the teleseismic data. About two-thirds of the fast directions measured in the low frequency band were found to be within 20° of the strike of the trench. Notable exceptions to this trend include measurements made at the two southernmost stations in the array, YNG and IGK, where there is a great deal of scatter in the measurements, and a few measurements at station ZMM. In the high-frequency band the directions are more variable: compared to measurements as low frequency, we observe more fast directions that are nearly perpendicular or oblique to the strike of the trench (Figure 4b), and only a slim majority of the measured high-frequency fast directions (53%) is within 20° of trench-parallel. We suggest two possible reasons for the increased scatter. First, a Fresnel zone argument (Alsina and Snieder, 1995) would imply that the low-frequency measurements are sensitive to a larger anisotropic volume than the high-frequency measurements. Therefore, the low-frequency measurements may tend to "smooth out" small-scale anisotropic heterogeneity that may exist in the mantle wedge whereas the short period data would be more sensitive to it. Second, it has been proposed that for vertically stratified anisotropic structures (for example, crustal anisotropy overlying an anisotropic upper mantle) higher-frequency measurements may be biased toward near-surface structure (Clitheroe and van der Hilst, 1998; Saltzer et al., 2000). Long and van der Hilst (2005b) examined the possibility of crustal contamination in the *F*-net teleseismic shear wave splitting dataset and concluded that an anisotropic signal

from the crust, while small, is probably present. It is thus possible that crustal anisotropy contributes to the scatter in our high-frequency splitting measurements.

There is also a noticeable increase in scatter in the southernmost part of the array (stations YNG and IGK) compared to stations located further north. This may be due to a change in crustal anisotropy. However, scatter in the low-frequency data (where we expect the crustal contribution to be much smaller) increases also. Instead, we attribute the increased scatter in the south to more complex anisotropy, which may reflect a southward increase in tectonic complexity. At the southernmost part of the arc the subduction direction in this region becomes oblique to the trench, which causes trench-parallel stretching (Lallemand et al., 1999). Additionally, there may be deformation associated with flow around the slab edge with the transition from subduction at the southern Ryukyu trench to collision in Taiwan (Kao et al., 2000). We focus on the more consistently trench-parallel fast directions observed to the north.

Measured split times range from 0.25 s, which is near the lower detection limit, up to approximately 2 s, with most δt values between 0.75-1.25 s. This range of δt values is similar to the range of splitting times observed at Ryukyu stations for teleseismic phases (Long and van der Hilst, 2005b). Along with the similarity of the polarization directions this suggests that the two data sets sample the same source of anisotropy. Figure 5 shows observed split time with respect to event depth: there is no systematic dependence of split time on earthquake depth, either for the entire dataset (Figure 5a) or for the trench-parallel measurements only (Figure 5b). This suggests that most ray paths accumulate a similar split time, regardless of the event focal depth, and, therefore, that the anisotropy is concentrated in the shallower portions of the mantle wedge. If this

interpretation is correct a highly anisotropic medium is likely needed to generate the fairly large split times observed. Even if we allow for a contribution from the crust and (thin) lithosphere we would attribute 1 s or more of splitting to a mantle layer of perhaps 60-100 km, which suggests anisotropy up to about 10%.

In general, we find that measurements at low frequencies tend to yield higher split times than measurements at high frequencies (Figure 5). Similar observations have been made by, for example, Long and van der Hilst (2005b) and Marson-Pidgeon and Savage (1997), but other studies have found different frequency effects, including significant splitting at high frequencies and little splitting at low frequencies (Clitheroe and van der Hilst, 1998; Özalaybey and Chen, 1999) and frequency dependent fast directions with no frequency dependence in split times (Fouch and Fischer, 1998). In our study, high-frequency measurements reflect anisotropy in the mantle wedge but a bias towards near-surface anisotropy (Saltzer et al., 2000) may produce smaller delay times (and increased scatter) than measurements made at lower frequencies.

The low- and high-frequency data sets both suggest that there is significant heterogeneity of anisotropic structure, but two first-order conclusions can be drawn from them. First, there is firm evidence for significant anisotropy in the mantle wedge above the subducting Philippine slab beneath the Ryukyu arc. Both the fast directions and split times from local shear waves are remarkably consistent with the teleseismic splitting reported by Long and van der Hilst (2005b). Specifically, even though the teleseismic and local raypaths sample different parts of the mantle wedge (see Figure 2), with the teleseismic raypaths sampling the forearc corner of the wedge (as well as the slab itself and the subslab mantle) and the local raypaths sampling the backarc, the character of the

anisotropy sampled by these two data sets seems to be similar. While we cannot rule out a contribution to splitting of teleseismic phases from within or beneath the subducting slab, the similarity between the teleseismic and local splitting patterns argues that the teleseismic phases are probably sampling significant anisotropy in the wedge itself. Second, although there is significant scatter, the majority of the fast directions measured in this study are parallel to the trench. This argues for significant trench-parallel anisotropy in the wedge beneath much of the Ryukyu arc, with the possible exception of the two southernmost stations.

5. Models for trench-parallel fast directions

Several hypotheses have been proposed to explain trench-parallel fast directions in subduction zone settings. Russo and Silver (1994) invoked trench-parallel flow beneath the subducting slab associated with slab rollback to explain trench-parallel fast directions in South America. Smith et al. (2001) suggested that trench-parallel fast directions in the Lau Basin result from trench-parallel flow around the slab edge of infiltrating material from the Samoan plume. In subduction zones where the convergence direction is oblique to the strike of the trench, or where there is significant strike-slip motion in the backarc, there may be significant trench-parallel shear in the mantle wedge and a simple corner flow model may not be appropriate (e.g., Hall et al., 2000); this may explain trench-parallel fast directions in such systems. In regions where the morphology of the downgoing slab is complicated, three-dimensional flow patterns in the asthenospheric mantle probably become important, and complex three-dimensional flow may explain trench-parallel fast directions in some subduction systems.

The relative simplicity of the tectonic setting at the Ryukyu arc compared to most subduction zones limits the range of plausible explanations for trench-parallel fast directions in this region. The convergence direction at the Ryukyu arc is perpendicular to the trench (see Figure 1) except at the southernmost part of the arc, where the strike of the trench rotates from NE-SW to E-W. This implies that transpression in the mantle wedge due to oblique subduction can be ignored as a possible mechanism for trench-parallel fast directions at most Ryukyu stations. The geometry of the Philippine slab beneath Ryukyu as inferred from seismicity (Engdahl et al., 1998; Gudmundsson and Sambridge, 1998) is fairly simple and is well-described by a two-dimensional model with a slab dip of about 45° (again, with the exception of the southernmost part of the slab). This simple slab morphology tends to argue for a simple flow regime, at least in the interior part of the arc. Finally, although the location of the Ryukyu trench is not completely stationary, along most of the trench the rate of trench migration due to slab rollback is slow compared to a global compilation of trench motions (Heuret and Lallemand, 2005; Yu and Kuo, 1996; Mazzotti, 1999) and the effects of slab rollback on mantle flow patterns are presumably much smaller than for most subduction zones.

In order to explain the predominantly trench-parallel fast directions at the Ryukyu arc stations, we consider several different scenarios for mantle flow and anisotropy generation that are consistent with generally trench-parallel directions. We note that at the southernmost part of the arc a mechanism other than those discussed here may be responsible for the observed anisotropy, such as flow around the slab edge. We emphasize also that although the majority of observed fast directions are trench-parallel, we also found a significant minority of trench-perpendicular or intermediate

measurements. Ideally, any successful model for Ryukyu arc anisotropy should be able to explain this subset of measurements as well. In this section we consider four possible scenarios for Ryukyu anisotropy: trench-parallel flow in the mantle wedge, corner flow in the mantle wedge with B-type olivine fabric, shape-preferred orientation of melt pockets, and frozen lithospheric and/or crustal anisotropy that is unrelated to present-day deformation processes.

5.1 Trench-parallel flow in the mantle wedge

Trench-parallel flow beneath the subducting plate has been invoked to explain trench-parallel fast directions in South America (Russo and Silver, 1994; Anderson et al., 2004) and Kamchatka (Peyton et al., 2001); however, we reject such a mechanism here because our local splitting measurements suggest that the trench-parallel anisotropy in the Ryukyu arc has its origin in the mantle wedge, that is, above the plate. Instead, we consider the possibility of trench-parallel flow in the wedge itself. In order to invoke such a model, we must identify a mechanism that would result in consistently trench-parallel flow over a fairly long distance (approximately 800 km along the arc), with trench-parallel strains dominating the mantle wedge flow field. Because we observe trench-parallel fast directions at stations located approximately 100 km from the trench in the interior of the arc (most noticeably station KGM; see Table S1), a mechanism such as flow around the edges of the slab is probably insufficient. Conder et al. (2002) proposed a model for flow associated with decompression melting in the mantle wedge and suggested that in some arc systems, corner flow may act in concert with trench-parallel flow. It has been suggested (James Conder, Washington University, personal

communication) that elevated temperatures in the interior of the mantle wedge lead to a dramatic reduction in viscosity that may form hot, low-viscosity channels whose flow regime is decoupled from the rest of the wedge and the downgoing slab. If such low-viscosity channels form, and if a pressure gradient is applied across the length of the arc, this may drive trench-parallel flow along the arc in a localized channel. A source for such a pressure gradient is somewhat difficult to envision for Ryukyu, however, as the rate of slab rollback is small and appears to be fairly constant over most of the length of the arc (Heuret and Lallemand, 2005). A series of laboratory experiments by Buttles and Olson (1998) investigated the formation of anisotropy due to flow in subduction zones, and they suggested that for systems with simultaneous slab rollback and down-dip motion, fast directions in the wedge should be dominated by the down-dip motion of the slab, and that large amounts of rollback are needed to produce trench-parallel anisotropy anywhere in the system. Therefore, it is difficult to find a mechanism that would produce significant, dominant trench-parallel flow in the Ryukyu mantle wedge, and we conclude that this is an unlikely model to explain the observed trench-parallel splitting. However, this scenario cannot be completely ruled out, and further three-dimensional modeling may clarify the relative importance of trench-parallel and perpendicular flow in subduction systems with slow rollback rates such as Ryukyu.

5.2 Corner flow with B-type olivine fabric

An alternate model for the Ryukyu arc system combines trench-perpendicular corner flow in the mantle wedge (resulting in trench-perpendicular flow directions) with B-type olivine fabric to produce trench-parallel fast splitting directions. This hypothesis

for subduction zone anisotropy originated with Jung and Karato (2001), who conducted laboratory experiments on olivine aggregates with significant water content (200-1200 ppm) deformed at high differential stresses (> 300 MPa) and found that slip along the [001] direction was enhanced at these conditions, such that the fast axes of individual olivine crystals tended to be aligned 90° from the shear direction. Examples of B-type fabric in mantle-derived rocks have since been documented by Mizukami et al. (2004) in samples from the Higashi-akaishi peridotite body in southwest Japan, just northeast of the Ryukyu arc. Subsequent modeling work by Kneller et al. (2005) indicates that B-type fabric conditions may occur in part of the mantle wedge. They find that the forearc mantle may have conditions that favor a B-type fabric (and therefore trench-parallel splitting), and they predict a rapid transition to trench-perpendicular fast directions (associated with A-, C-, or E-type olivine fabric) toward the backarc. The B-type fabric hypothesis has been invoked to explain a transition from trench-parallel splitting in the forearc to trench-perpendicular splitting in the backarc elsewhere in Japan; Nakajima and Hasegawa (2004) observed this apparent rotation at stations located in northern Honshu.

Can the B-type fabric model explain the trench-parallel splitting we observe in Ryukyu? Unfortunately, the *F*-net station distribution is limited to stations located on the volcanic islands themselves, so we do not have good sampling across the entire forearc and backarc region. It is clear from the teleseismic splitting results of Long and van der Hilst (2005b) that there is significant trench-parallel anisotropy in the forearc mantle, which is consistent with the Kneller et al. model. However, the local raypaths examined in this study clearly sample a significant volume of backarc mantle (Figure 2). Kneller et al. (2005) envision a transition from trench-parallel to trench-perpendicular fast

directions located at the volcanic front for a generic subduction zone model. However, we also observe trench-parallel fast directions for rays that sample a larger part of the backarc (see Figure 4). Our observations could perhaps be reconciled with the models of Kneller et al. if a slight change in their model parameters (such as water content, temperature structure of the incoming and overriding plates, rheological parameters, and the degree of coupling between the slab and the overlying wedge) could move the trench-parallel/trench-perpendicular transition further into the backarc, or if the B-type fabric can exist for a larger range of physical and compositional parameters than inferred experimentally by Jung and Karato (2001). Only a slight shift in this transition point would be required to explain our observations with the B-type model, especially if the anisotropy we observe is generally located on the near-surface portion of the raypaths. It is not immediately obvious what change(s) in model parameters would be required to move the transition point farther into the backarc; we are currently undertaking a detailed comparison of splitting observations in Japan with the models of Kneller et al. (2005), and further modeling of B-type fabric may also be required to elucidate this point. It also remains to be demonstrated through modeling and experiments that a region of B-type fabric in the mantle wedge can produce split times on the order of the ~ 1.5 s or more that we observe. We note, finally, that some of the measured trench-perpendicular and intermediate fast directions are not inconsistent with the B-type fabric hypothesis if raypaths sample trench-perpendicular fast directions further into the backarc, or if they sample the transition from B- to A-, C-, or E-type fabric regimes.

5.3 Shape-preferred orientation (SPO) of melt pockets

We also considered the possibility that anisotropy in the Ryukyu wedge arises not from lattice preferred orientation due to dislocation creep in olivine, but from shape preferred orientation of melt structures. The contribution of aligned melt to anisotropy in the mantle has been examined by Kendall (1994) for the case of a mid-ocean ridge, by Kendall and Silver (1998) and Moore et al. (2004) for the D'' region, and by Fischer et al. (2000) for a subduction zone. Fischer et al. (2000) considered a model in which melt-filled cracks align 20° - 30° from the maximum deviatoric compressive stress, following the experimental results of Zimmerman et al. (1999), and concluded that melt-filled cracks could result in trench-parallel splitting. However, melt production in subduction zones is likely restricted to a thin column of vertical melt transport (see, for example, Gaetani and Grove, 2003) and therefore anisotropy due to aligned melt structures would have to be concentrated in a small zone directly beneath the stations to explain both the teleseismic and local splitting for Ryukyu. It is unlikely a very small volume of SPO-induced anisotropy can explain the large split times (up to 2 seconds, with an average δt of about 1 second) observed in this study. Also, it is unclear what processes control the geometry of melt migration in subduction zones, and where (or whether) aligned melt cracks or sheets are likely to form. We therefore conclude that the melt hypothesis is unlikely for Ryukyu, but further work on the aligned melt hypothesis is needed to rule out this possibility completely.

5.4 Frozen anisotropy in the lithosphere and/or crust

Finally, we examined the hypothesis that the splitting we observe is due to frozen anisotropy in the lithosphere or crust and is unrelated to present-day deformation processes. Some contribution to the observed signal from the crust is likely in this splitting dataset, but anisotropy in the crust cannot explain the observed δt values up to nearly 2 s. The crustal thickness in the Ryukyu arc, ~ 35-40 km (Taira, 2001), is insufficient to explain such large splitting, and observed crustal splitting times in Japan average about 0.2 s (Kaneshima, 1990). It has been demonstrated that both lithospheric and asthenospheric contributions to anisotropy are important in many regions (e.g., Fouch et al., 2000; Simons et al., 2002; Simons and van der Hilst, 2003; Fischer et al., 2005; Waite et al., 2005), although splitting measurements in subduction zone settings are nearly always interpreted in terms of flow in the asthenosphere (e.g., Fischer et al., 1998, 2000; Smith et al., 2001; Anderson et al., 2004). The lithosphere beneath the Ryukyu arc stations is likely to be thin, due to thermal erosion associated with mantle wedge flow (e.g., Conder et al., 2002), and it is unlikely that the lithosphere is thick enough to explain the large split times. A second line of argument against primarily lithospheric anisotropy comes from the data itself. As argued in Long and van der Hilst (2005b), for *F*-net stations with simple teleseismic splitting patterns, such as the Ryukyu arc stations, we expect little or no contribution from the lithosphere, or that the fast directions in the lithosphere and the asthenosphere are closely aligned. Therefore, although we cannot completely rule out a contribution from the lithosphere, the anisotropic signal we observe is probably dominated by present-day deformation and flow in the asthenosphere.

5.5 The most plausible model for Ryukyu anisotropy

All of the models considered here have some weaknesses when considered in the context of the Ryukyu arc splitting dataset. However, we conclude that the most likely explanation for the trench-parallel anisotropy in the wedge is a model that combines corner flow in the wedge with a B-type olivine fabric. Although we observe trench-parallel fast directions farther into the backarc than predicted by early modeling work on the B-type hypothesis (Kneller et al., 2005), we think it is possible that our splitting results can be reconciled with such models by an adjustment of model parameters or scaling relations of laboratory results. The B-type fabric model may also be consistent with the minority of trench-perpendicular and intermediate fast directions observed in part of the dataset if the associated raypaths sample regions of the backarc mantle that are dominated by A-, C-, or E-type fabric, or if they sample the transition region between the fabric regimes. There is also likely a small amount of splitting signal from anisotropy in the crust, which may explain the increased scatter in the high-frequency splitting dataset.

If the B-type fabric hypothesis is, indeed, the correct explanation for the trench-parallel fast directions we observe in Ryukyu, then our results suggest that the physical range in which B-type fabric can develop may be larger than that suggested by the modeling results of Kneller et al. (2005) and/or the laboratory results of Jung and Karato (2001). New experimental data on olivine fabrics in pressure-temperature-water content space (e.g. Katayama and Karato, 2006), observations of B-type fabric in natural rocks (e.g. Skemer et al, 2006), and models of strain accumulation in the proposed B-type fabric regime should shed further light on the viability of the B-type fabric hypothesis. It has not yet been demonstrated, however, that B-type fabrics can indeed develop over the

large region that the Ryukyu splitting observations would require. Additionally, models must demonstrate that sufficient strains can be accumulated in the B-type fabric-dominated regime to produce the relatively large split times that we observe in this study.

6. Summary

We measured shear wave splitting from local events in the Ryukyu arc and compared these measurements to a previously published set of teleseismic splitting observations at the same stations. We obtained 70 high-quality measurements and found that a majority of fast directions lie within 20° of the strike of the trench, although a significant minority exhibit φ values that are trench-perpendicular or intermediate. The local splitting trends are similar to the teleseismic splitting observed by Long and van der Hilst (2005b). From these observations, we infer that there is significant trench-parallel anisotropy in the Ryukyu mantle wedge. After exploring several plausible explanations for this observation, we favor a model in which anisotropy develops due to strain associated with corner flow in the mantle wedge, and B-type olivine lattice preferred orientation dominates.

7. Acknowledgements

We acknowledge the Japanese National Research Institute for Earth Science and Disaster Prevention as the source for the data used in this study. We thank James Conder, Martijn de Hoop, Brad Hager, Tim Grove, Stéphane Rondenay, and Wiki Royden for useful discussions, and Sara Pozgay for her comments on an early draft of this

manuscript. We thank Vadim Levin and an anonymous reviewer for their thoughtful and helpful reviews. This work was supported by NSF grant EAR-0337697.

Figure Captions

Figure 1. Tectonic setting of the Ryukyu arc and station locations (black circles). Colors represent topography and seafloor bathymetry from Smith and Sandwell (1997). Large black arrow shows the convergence direction at the trench. Velocities of the Philippine plate relative to Eurasia (from the HS3-Nuvel1A model, Gripp and Gordon, 2002) and seafloor ages quoted in Heuret and Lallemand (2005) are shown at three locations along the arc.

Figure 2a. Map view of raypaths for local events analyzed in this study (black) and teleseismic events (gray) analyzed in Long and van der Hilst (2005b). The black dotted line indicates the location of the trench; gray dotted lines are slab contours at 100 km intervals from Gudmundsson and Sambridge (1998).

Figure 2b. Three-dimensional sketch of local (black) and teleseismic (gray) raypaths in the upper mantle, looking north along the Ryukyu arc. Raypaths are approximated as straight lines. Local events are marked with open circles.

Figure 3a. Uncorrected particle motion (top) and seismogram components (bottom) for a typical high-frequency *S* arrival at station IGK. Vertical bars on the horizontal traces indicate the window used in the splitting analysis.

Figure 3b. Corrected particle motion (top) and seismogram components (middle) for the best-fitting φ and δt values (46° and 0.45 seconds, respectively). In the bottom panel, a contour plot of the cross-correlation values is shown. The pair of splitting parameters that maximizes the cross-correlation is marked with a white star.

Figure 4a. Fast directions measured in the low frequency band (0.02-0.125 Hz). Individual measurements are plotted as black bars at the midpoint of the raypath. Gray bars plotted at the station locations represent the average teleseismic fast directions from Long and van der Hilst (2005b). Bars have *not* been scaled to the split time in order to emphasize the better-constrained fast directions; bars scaled to the split time are shown in Figure 4c.

Figure 4b. Similar to Figure 4a, for fast directions measured in the high frequency band (0.1 – 1 Hz).

Figure 4c. High-frequency measurements are plotted in gray; low-frequency measurements are plotted in black. The length of each bar has been scaled by the split time δt.

Figure 4d. Null measurements made in the low- (black crosses) and high- (dark gray crosses) frequency bands, plotted at the midpoint of the raypath. Nulls are distributed geographically throughout the arc. The orientation of the crosses correspond to the

direction of incoming polarization of the shear wave and the direction 90° from the incoming polarization azimuth.

Figure 5a. Plot of measured split time vs. event depth for high-frequency (circles) and low-frequency (triangles) measurements. Error bars are 2σ.

Figure 5b. Plot of measured split time vs. event depth, for trench-parallel fast directions only.

Table 1. Results of all splitting measurements reported in this study, for high-frequency and low-frequency bandpass filters. 2σ formal errors on the fast direction φ and split time δt are reported; errors were calculated using the formulation of Levin et al. (1999). Each measurement is classified as null (N), trench-parallel (∥), trench-perpendicular (⊥), or oblique (O). For null measurements, we also list the initial polarization direction of the shear wave, in lieu of the fast direction.

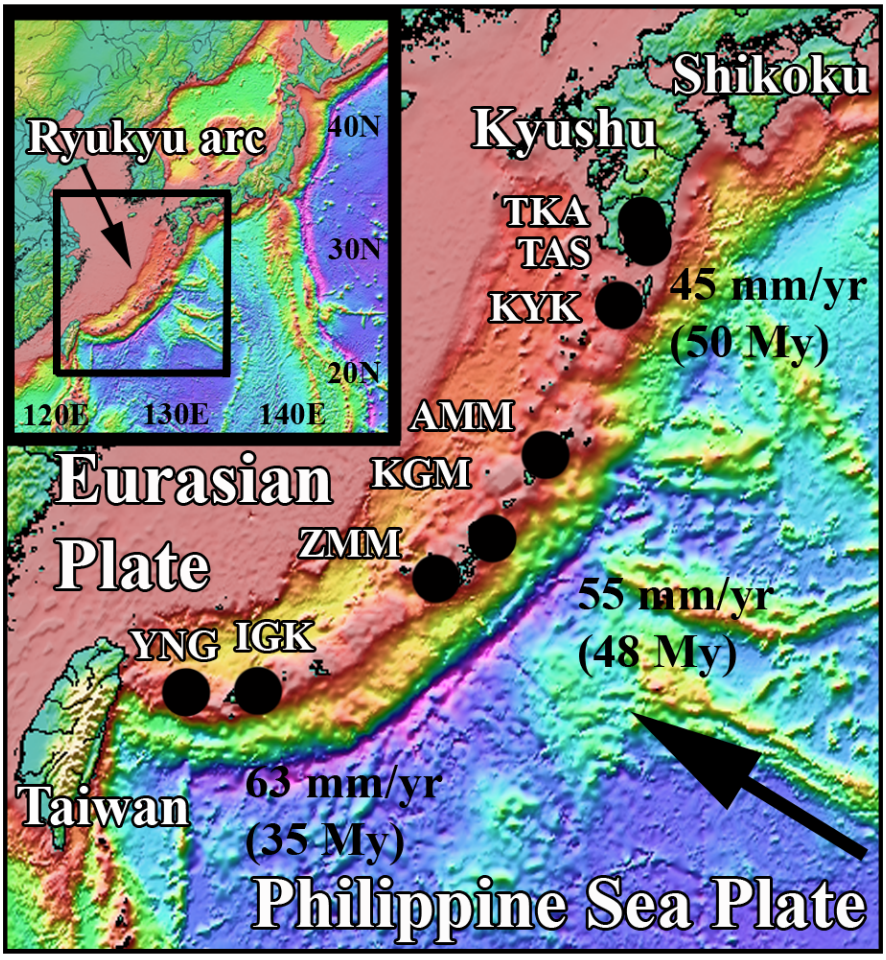
Ryukyu arc
40N
30N
20N
120E
130E
140E
Shikoku
Kyushu
TKA
TAS
KYK
45 mm/yr
(50 My)
AMM
KGM
ZMM
Eurasian
Plate
55 mm/yr
(48 My)
YNG
IGK
Taiwan
63 mm/yr
(35 My)
Philippine Sea Plate

Figure 1

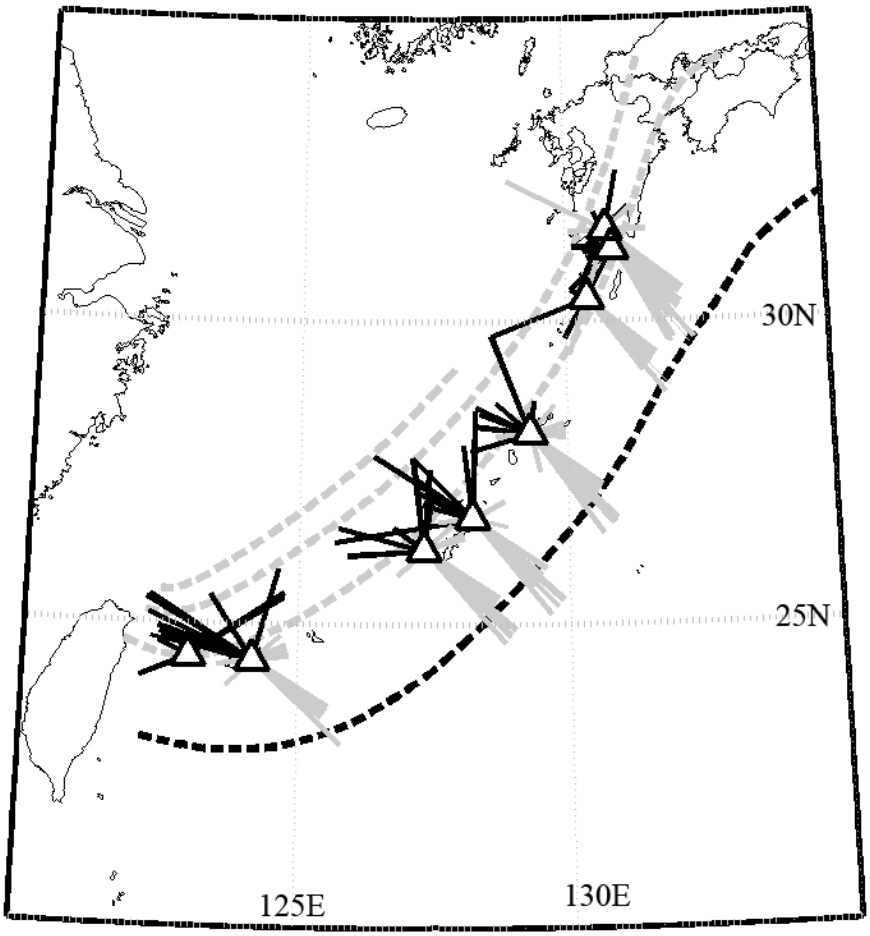

Figure 2a

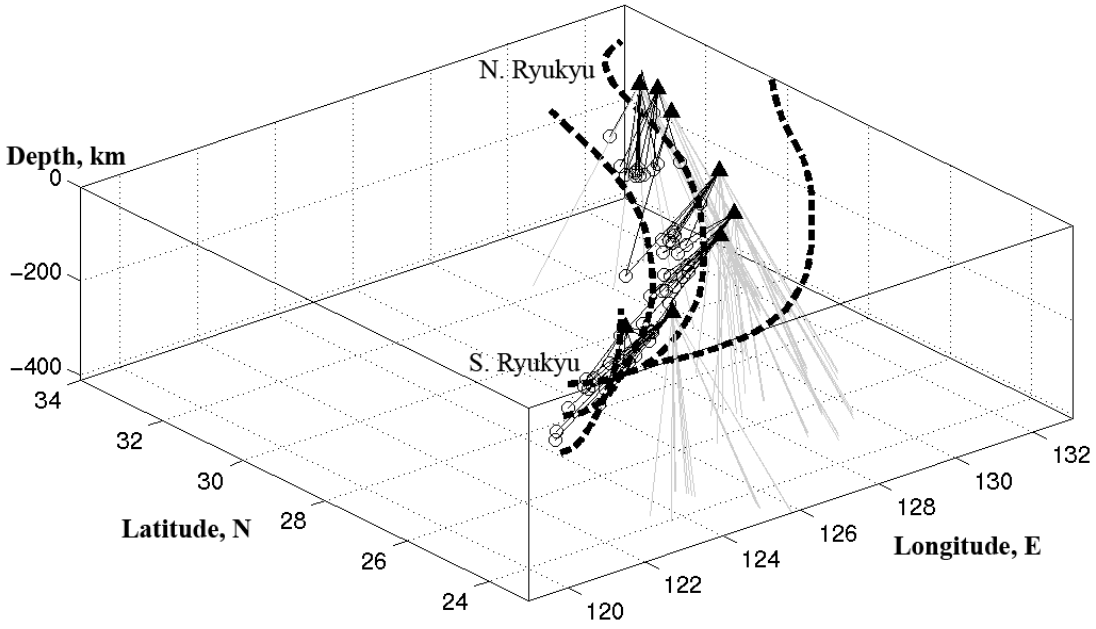
N. Ryukyu
S. Ryukyu
Depth, km
0
−200
−400
34
32
30
28
26
24
Latitude, N
120
122
124
126
128
130
132
Longitude, E

Figure 2b

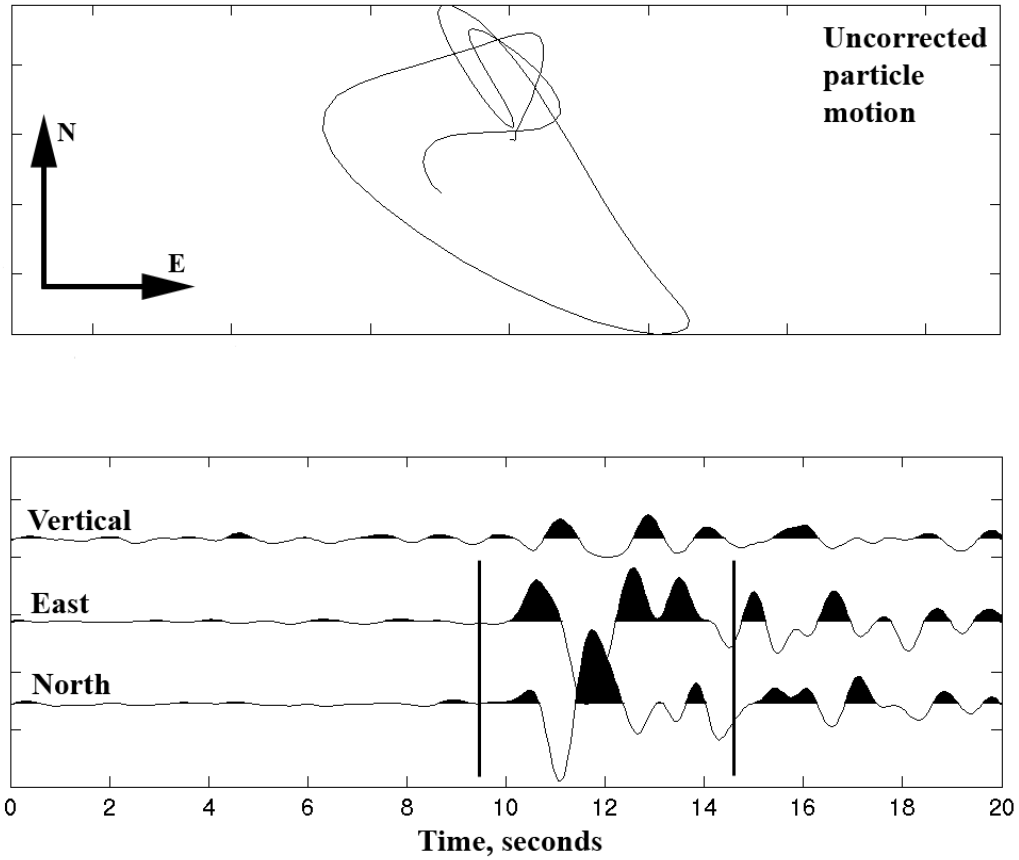
Uncorrected
particle
motion
N
E
Vertical
East
North
0
2
4
6
8
10
12
14
16
18
20
Time, seconds

Figure 3a

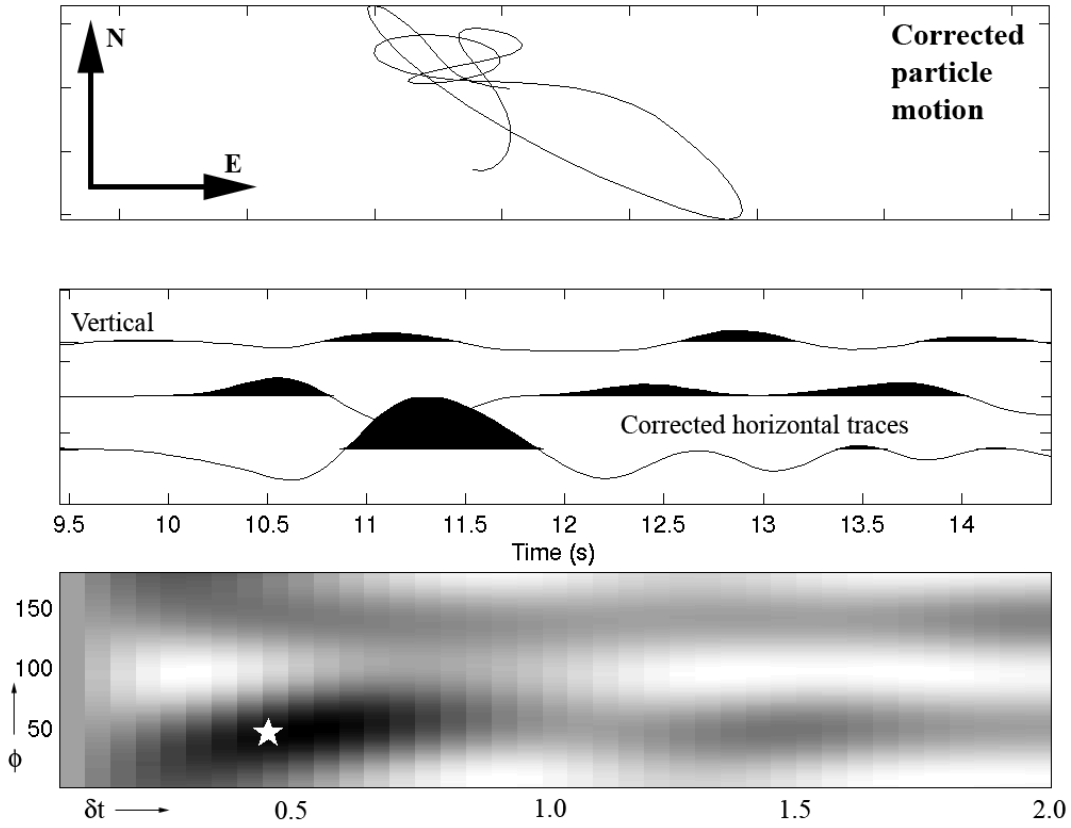
N
E
Corrected particle motion
Vertical
Corrected horizontal traces
9.5
10
10.5
11
11.5
12
12.5
13
13.5
14
Time (s)
150
100
50
ϕ
δt
0.5
1.0
1.5
2.0

Figure 3b

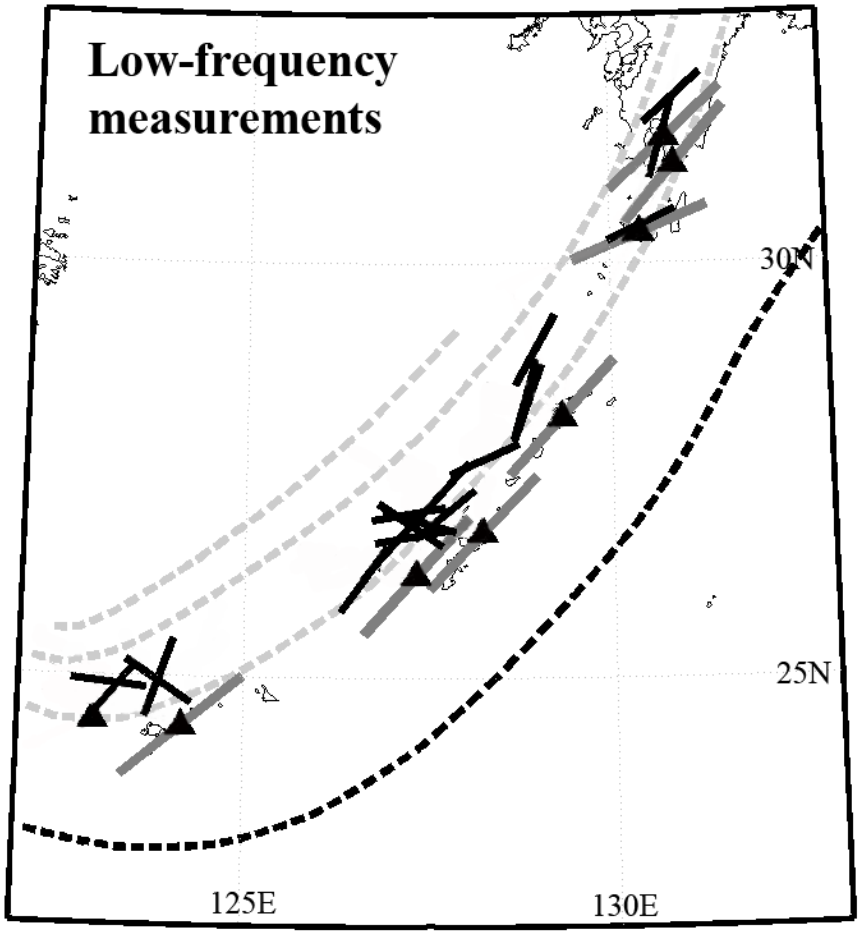

Figure 4a

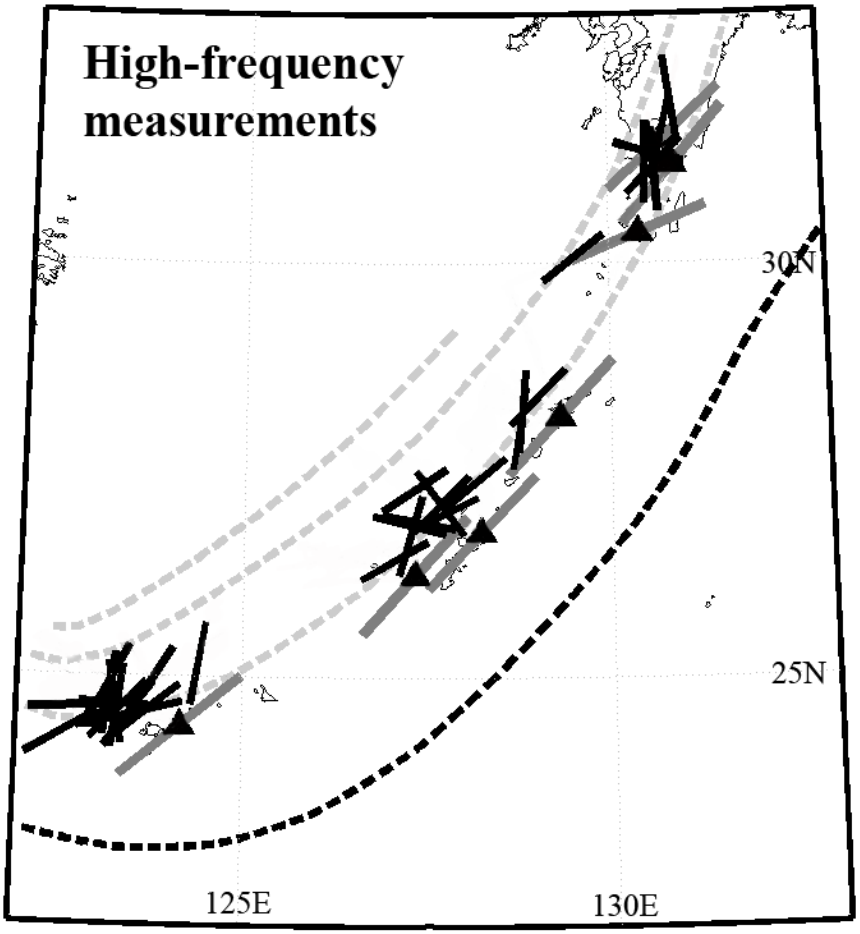

Figure 4b

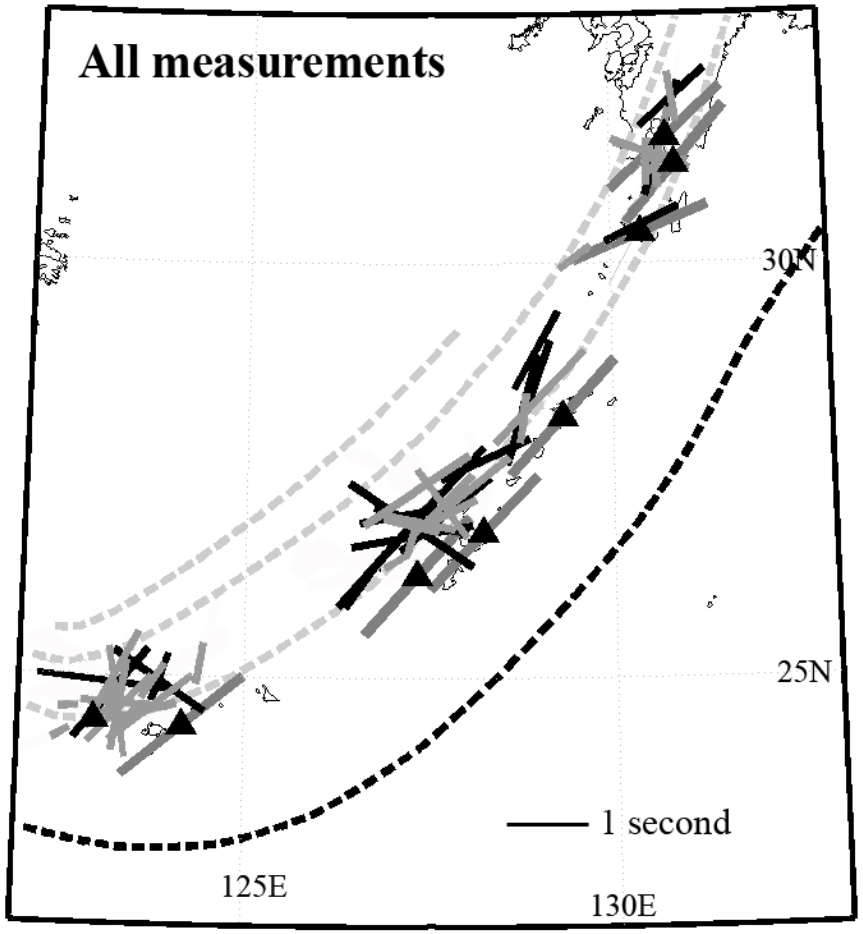

Figure 4c

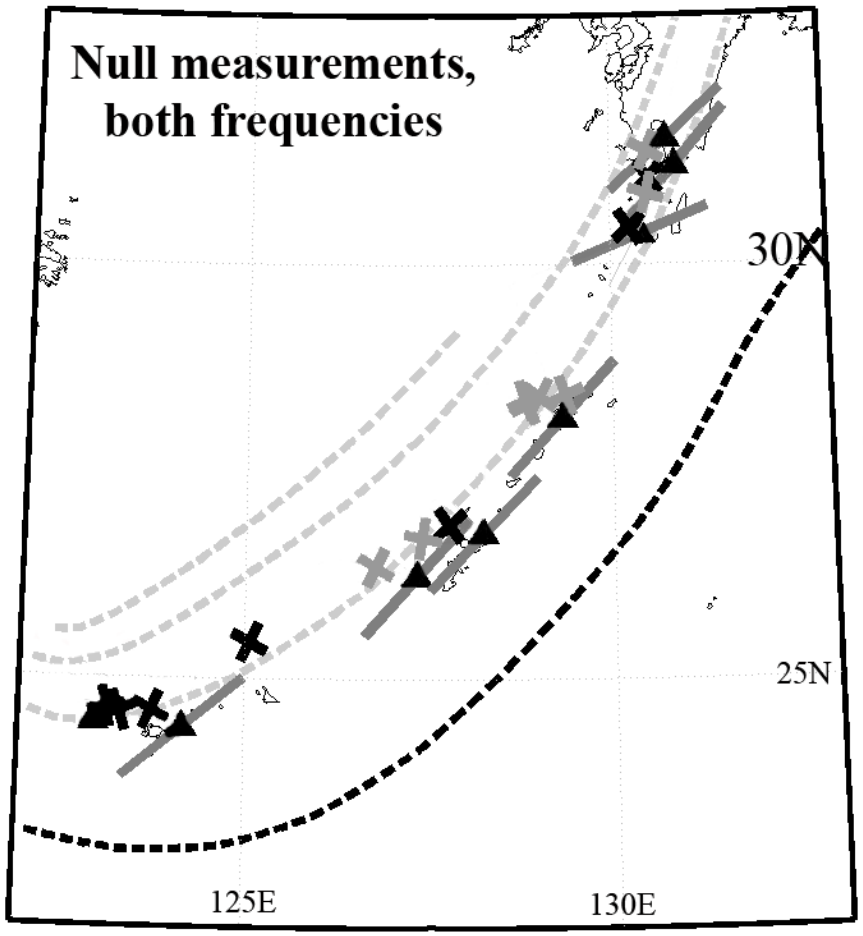

Figure 4d

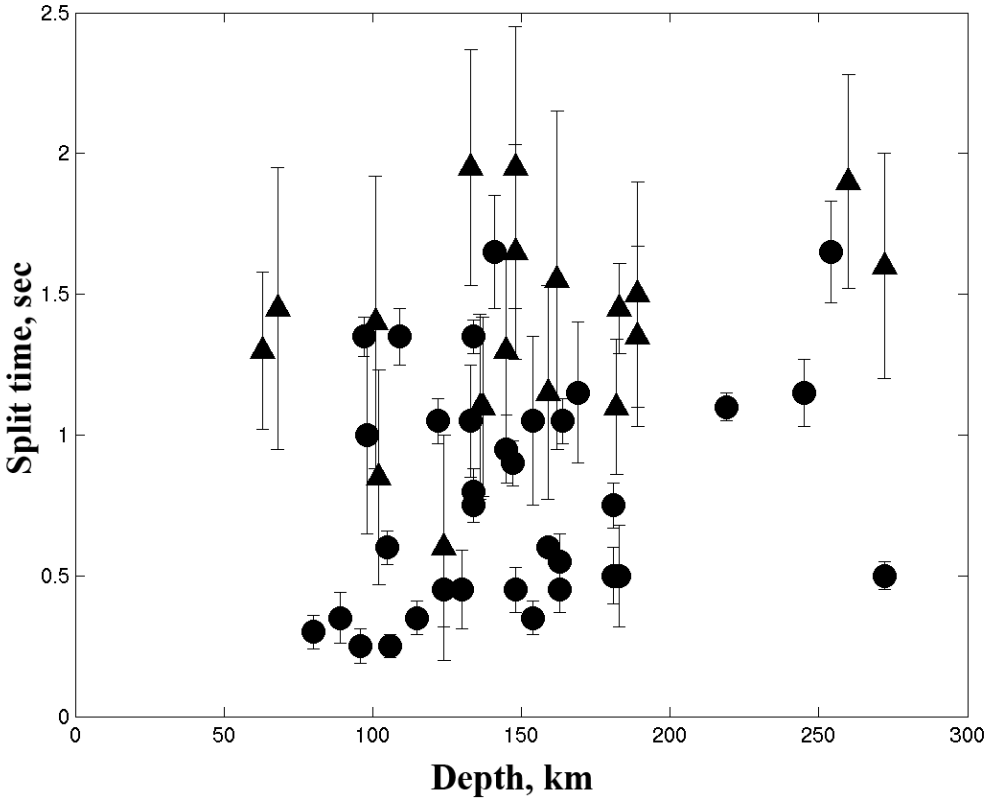

Figure 5a

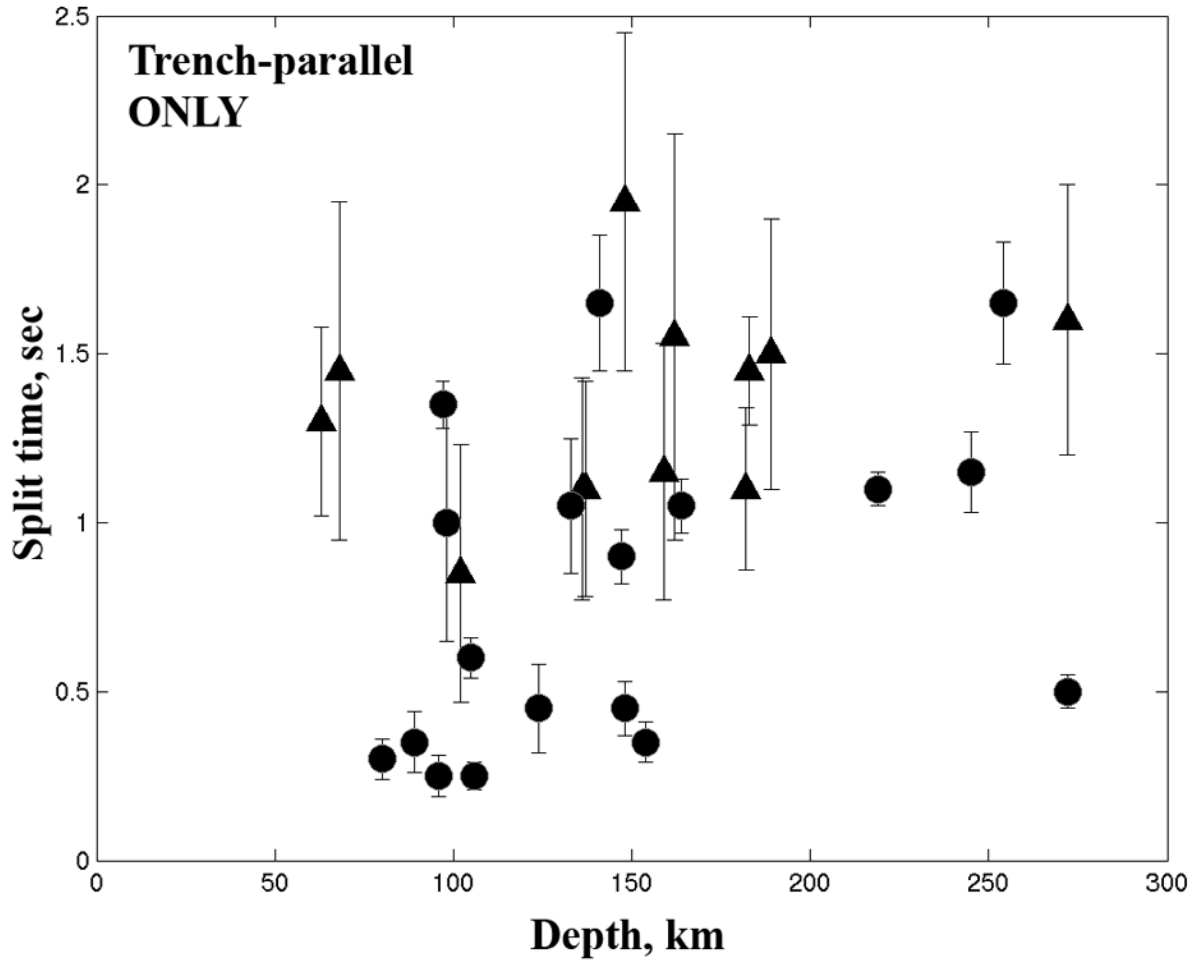
Trench-parallel
ONLY
Split time, sec
Depth, km
0
0.5
1
1.5
2
2.5
0
50
100
150
200
250
300

Figure 5b

Event	Station	Depth, km	φ, °	dφ, 2σ	δt, sec	dδt, 2σ	Class
Hi-freq							
1999.196	AMM	136	N - 68				N
2000.212	AMM	130	6	18	0.45	0.14	O
2001.303	AMM	136	N - 70				N
2002.061	AMM	141	48	20	1.65	0.20	‖
2002.142	AMM	135	N - 33				N
2003.163	AMM	115	11	15	0.35	0.06	O
2004.295	AMM	95	N - 158				N
2000.148	IGK	245	30	14	1.15	0.12	‖
2000.206	IGK	124	46	14	0.45	0.13	‖
2000.315	IGK	109	77	14	1.35	0.10	O
2001.153	IGK	134	9	14	0.80	0.08	O
2002.239	IGK	219	35	12	1.10	0.05	‖
2002.259	IGK	183	9	20	0.50	0.18	O
2002.277	IGK	134	170	11	1.35	0.06	O
2002.322	IGK	181	11	18	0.50	0.10	O
2003.214	IGK	105	64	9	0.60	0.06	‖
2005.059	IGK	80	39	15	0.30	0.06	‖
2005.143	IGK	97	54	20	1.35	0.07	‖
2000.100	KGM	133	55	22	1.05	0.20	‖
2000.274	KGM	164	48	20	1.05	0.08	‖
2002.289	KGM	254	59	14	1.65	0.18	‖
2003.071	KGM	147	67	15	0.9	0.08	‖
2001.250	KYK	272	56	14	0.50	0.05	‖
2002.173	TAS	154	49	13	0.35	0.06	‖
2002.190	TAS	163	176	11	0.45	0.08	O
2002.298	TAS	121	N - 15				N
2003.204	TAS	163	2	16	0.55	0.10	O
2004.061	TAS	181	15	14	0.75	0.08	O
2000.016	TKA	169	108	17	1.15	0.25	O
2000.093	TKA	159	170	6	0.60	0.03	O
2002.173	TKA	154	103	21	1.05	0.30	O
2002.279	TKA	170	N - 25				N
2002.338	YNG	98	93	22	1.00	0.35	‖
2003.214	YNG	106	87	14	0.25	0.04	‖
2003.234	YNG	96	61	24	0.25	0.06	‖
2002.205	ZMM	110	N - 100				N
2003.061	ZMM	145	100	15	0.95	0.12	O
2003.071	ZMM	148	18	14	0.45	0.08	‖
2004.242	ZMM	134	102	10	0.75	0.06	O
2004.258	ZMM	122	140	19	1.05	0.08	⊥
2004.262a	ZMM	98	N - 29				N
2004.305	ZMM	89	63	18	0.35	0.09	‖

Lo-freq							
1999.196	AMM	137	22	21	1.10	0.32	‖
2001.205	AMM	272	33	18	1.60	0.40	‖
2001.303	AMM	136	18	18	1.10	0.33	‖
2000.206	IGK	125	N - 159				N
2001.328	IGK	260	95	17	1.90	0.38	O
2002.259	IGK	183	42	14	1.45	0.16	‖
2005.143	IGK	98	N - 26				N
2000.117	KGM	163	45	17	1.30	0.28	‖
2000.180	KGM	108	N - 51				N
2002.283	KGM	162	68	24	1.55	0.60	‖
2003.048	KGM	189	46	18	1.50	0.40	‖
2003.071	KGM	148	54	12	1.95	0.5	‖
2002.298	KYK	121	N - 142				N
2002.298	TAS	121	N - 15				N
2003.190	TAS	68	68	15	1.45	0.50	‖
2004.061	TAS	182	20	17	1.10	0.24	‖
2000.093	TKA	159	53	14	1.15	0.38	‖
2001.008	TKA	116	N - 47				N
2003.250	YNG	124	21	25	0.60	0.40	⊥
2004.010	YNG	101	121	22	1.4	0.52	O
2005.143	YNG	98	N - 169				N
2003.048	ZMM	189	81	15	1.35	0.32	O
2003.061	ZMM	145	104	18	1.30	0.33	O
2003.071	ZMM	148	81	22	1.65	0.38	O
2004.242	ZMM	133	121	16	1.95	0.42	⊥
2004.262a	ZMM	98	N - 29				N
2004.262b	ZMM	102	39	13	0.85	0.38	‖
2005.054	ZMM	162	N - 27				N

Table 1

Chapter 4

Two-dimensional numerical modeling of subduction zone anisotropy[1]

Abstract

We present a series of two-dimensional finite element models of viscous flow in the mantle wedge induced by a subducting lithospheric plate. We use a kinematically defined slab geometry approximating subduction of the Philippine Sea Plate beneath Eurasia. Through numerical modeling, we explore the effects of different rheological and thermal constraints (e.g. a low-viscosity region in the wedge corner, power-law vs. Newtonian rheology, the inclusion of thermal buoyancy forces, and a temperature-dependent viscosity law) on the velocity and finite strain field in the mantle wedge. From the numerical flow models, we construct models of anisotropy in the wedge by calculating the evolution of the finite strain ellipse and combining it with appropriate elastic constants for transversely isotropic mantle material. We then predict shear wave splitting for stations located above the model domain using approximate expressions derived from (anisotropic) perturbation theory, and compare the predictions to about 500 previously published shear wave splitting measurements from seventeen stations of the broadband F-net array located in southwestern Japan. We find that although the use of different model parameters can have a fairly large effect on the character of the finite

[1] In preparation as: Long, M. D., de Hoop, M. V., Hager, B. H., van der Hilst, R. D., 2006a. Two-dimensional modeling of subduction zone anisotropy and applications to southwestern Japan. To be submitted to Geophys. J. Int.

strain field, the effect on the average splitting parameters is not as striking. However, the details of the predicted splitting patterns at individual stations for different models are dramatically different, and rigorous analysis of the detailed splitting patterns will likely allow us to discriminate among different rheological models for flow in the mantle wedge. The splitting observed in southwestern Japan agrees well with the predictions of trench-perpendicular flow in the mantle wedge with B-type olivine fabric dominating in a region from the wedge corner to about 150 km from the trench.

1. Introduction

Subduction zones, regions where slabs of dense oceanic lithosphere descend into the deeper mantle, are among the most complicated tectonic environments on the Earth, and even first-order aspects of their structure and dynamics are not well understood (Stern, 2002). For example, the pattern of flow that is induced in the mantle wedge due to viscous coupling with the downgoing slab, flow around the slab edge, or the forces associated with slab rollback are in general not well characterized for subduction systems. One tool for probing the geometry of deformation associated with subduction is the measurement of shear wave splitting, a consequence of seismic anisotropy. Anisotropy in the upper mantle can arise when mantle material, composed of individual anisotropic mineral crystals, is subjected to strain and develops a lattice preferred orientation (LPO). If the relationships among deformation, LPO, anisotropy, and shear wave splitting are known or assumed, then measurements of shear wave splitting at seismic stations located above subduction zones can shed light on the style of mantle deformation associated with subduction.

Upper mantle anisotropy related to deformation in subduction zone environments has been well-documented in a variety of regions (e.g. Ando et al., 1983; Fischer et al., 1998; Smith et al., 2001; Anderson et al., 2004; Currie et al., 2004; Anglin and Fouch, 2005; Long and van der Hilst, 2005b, 2006); however, the interpretation of shear wave splitting measurements in the context of a subduction zone is not straightforward. The character of splitting observations varies greatly from region to region (see Wiens and Smith, 2003, for a review), and because there are many different processes that could potentially contribute to anisotropy (Park and Levin, 2002), the interpretation of splitting observations is difficult and non-unique. For example, both trench-parallel (e.g. Russo and Silver, 1994; Gledhill and Gubbins, 1996; Anderson et al., 2004; Peyton et al., 2001) and trench-perpendicular (e.g. Fischer and Yang, 1994; Currie et al., 2004) fast directions have been observed in different regions. Several studies have noted a rotation in the fast splitting direction from trench-parallel close to the trench to trench-perpendicular farther from the trench (Margheriti et al., 1996; Smith et al., 2001; Nakajima and Hasegawa, 2004; Long and van der Hilst, 2005b), although the opposite trend has also been observed (Levin et al., 2004). This diversity, along with the complexity of splitting patterns measured at individual stations (e.g. Helffrich et al., 2002; Long and van der Hilst, 2005b; Pozgay et al., 2006), is difficult to explain with a simple model for anisotropy. In contrast, the consistently ridge-normal fast directions observed at oceanic spreading centers are relatively well understood and well-explained by a simple model (e.g. Wolfe and Solomon, 1998).

A promising approach toward a rigorous interpretation of shear wave splitting measurements is to compare them with the predictions of numerical and experimental

flow models and thus narrow the class of plausible models that can explain a given dataset. This approach has been taken for both global- and regional-scale problems (e.g. Becker et al., 2003; Behn et al., 2004) as well for the specific problem of subduction zone deformation (Fischer et al, 2000; Hall et al., 2000; Blackman and Kendall, 2002). Much progress has been made recently on the problem of modeling subduction zone deformation (see van Keken, 2003 for a review). Various numerical modeling studies have employed both kinematically (Hall et al., 2000; Rupke et al., 2004) and dynamically (Kincaid and Sacks, 1997; Billen et al., 2003) driven slabs. Recent modeling studies have explored the effect of temperature-dependent viscosity (Eberle et al., 2002), a low-viscosity wedge (Billen and Gurnis, 2001), and significant back-arc spreading (Conder et al., 2002) on the pattern of flow in the mantle wedge. The effects of dehydration reactions and fluid release on the dynamics of the wedge have also been explored through numerical modeling studies (van Keken et al., 2000; Rupke et al., 2004; Arcay et al., 2005). The three-dimensional pattern of flow associated with phenomena such as slab rollback has mainly been explored through laboratory studies (Buttles and Olson, 1998; Funiciello et al., 2003, 2006; Kincaid and Griffiths, 2004). Finally, the possible presence of B-type olivine fabric in the mantle wedge, which would cause fast splitting directions to be oriented perpendicular to the prevailing flow direction (Jung and Karato, 2001; Karato, 2003), has been explored recently using numerical models (Kneller et al., 2005).

In this study, we compare the predictions from a suite of two-dimensional numerical subduction zone models with shear wave splitting measurements from seventeen broadband stations in southwestern Japan. These stations, located on islands in the Ryukyu Arc and on the islands of Kyushu and southernmost Honshu, overlie the

subduction of the Philippine plate beneath Eurasia. We previously examined the splitting of teleseismic shear phases at sixteen of these stations (Long and van der Hilst, 2005b) and noted a change from generally trench-parallel fast directions close to the trench to generally trench-perpendicular fast directions further away from the trench. We also evaluated the splitting of direct *S* phases from events originating in the Philippine slab (Long and van der Hilst, 2006) and found evidence for significant trench-parallel anisotropy in the mantle wedge for eight stations in the Ryukyu Arc. Here, we predict shear wave splitting for a total of 460 teleseismic raypaths and 28 local raypaths that correspond to the measurements of Long and van der Hilst (2005b, 2006) and compare those predictions to the observed splitting.

We address four specific goals. First, with two-dimensional flow models for the Ryukyu subduction zone, we evaluate the effects of different rheological and thermal constraints. Second, we calculate the distribution of finite strain, predict shear wave splitting for each of the flow models, and compare the model predictions to splitting measurements due to Long and van der Hilst (2005b, 2006). This allows us to identify the model that is most consistent with the observed shear wave splitting, which in turn allows us to make inferences about the style of deformation in this region. Third, we test whether a two-dimensional model of the flow field associated with subduction beneath southwestern Japan yields predictions that are broadly consistent with the observed splitting, which would support the use of a two-dimensional approximation. Finally, we discuss how flow models can be integrated with an inversion of the observed splitting intensities for anisotropic structure (Long et al., 2006b).

2. Description of splitting dataset

We use data from 17 stations of the broadband F-net array (http://www.fnet.bosai.go.jp); the station locations and names, along with the geometry of the subducting Philippine Sea plate, are shown in Figure 1a. Splitting parameters for teleseismic *SKS*, *SKKS*, and direct *S* phases were measured at 16 of these stations by Long and van der Hilst (2005b); splitting from local events beneath the eight southernmost stations in the array was investigated by Long and van der Hilst (2006). Raypaths for the teleseismic and local phases measured in these studies are shown in map view in Figure 1b, and Figure 1c shows average teleseismic splitting parameters and local splitting for individual events. We note that many of the stations exhibit splitting that varies with incidence angle or backazimuth/incoming polarization azimuth, which is characteristic of underlying anisotropic structure that is more complicated than a simple, single horizontal layer of anisotropy (e.g. Silver and Savage, 1994; Saltzer et al., 2000; Schulte-Pelkum and Blackman, 2003).

Long and van der Hilst (2005b, 2006) measured splitting parameters using two different techniques: the cross-correlation method used by, among others, Ando et al., (1983), Fukao (1984), and Levin et al. (1999), and the multichannel method described by Chevrot (2000). In this paper we use the splitting intensities measured using the Chevrot (2000) method as a basis for comparison between the model predictions and the splitting observations. For our purposes, this method has two distinct advantages: first, the splitting function (the variations in measured splitting intensities with incoming polarization azimuth) facilitates the investigation of backazimuthal variations in splitting resulting from complex anisotropic structure such as a dipping axis of symmetry. Second,

the splitting intensity accrued along incremental sections of the raypath can simply be summed to predict the total intensity observed at the surface. The latter is not true in the case of the splitting parameters (φ, δt) measured using the cross-correlation technique. The inverse splitting operator $\mathbf{\Gamma}^{-1}$, which rotates and shifts the horizontal components of an individual seismogram to correct for the effect of splitting, is not commutative (Silver and Savage, 1994). Therefore, the splitting intensity is a more convenient quantity to work with when evaluating splitting due to complex anisotropic structures (see also Favier and Chevrot, 2003; Favier et al., 2004; Chevrot et al., 2004).

The most striking features of the splitting map shown in Figure 1c are the preponderance of trench-parallel fast directions measured at stations located close (less than 150 km) to the trench and the apparent change in orientation of the fast directions from trench-parallel to trench-perpendicular at stations located farther in the backarc. Our previous analysis (Long and van der Hilst, 2006) of splitting from local events at Ryukyu Arc stations yielded fast directions and split times that were very similar to the observed teleseismic splitting, suggesting that both types of measurements reflect anisotropy in the mantle wedge above the slab. Long and van der Hilst (2006) concluded that the most likely explanation for the observed splitting is trench-perpendicular corner flow in the mantle wedge combined with a B-type olivine fabric that results in a fast direction of anisotropy 90° from the prevailing flow direction (Jung and Karato, 2001; Karato, 2003).

Here we test such a model against the detailed splitting patterns observed at F-net stations in southwestern Japan. Our approach takes the strain field and geometry of anisotropy obtained from purely two-dimensional flow models. In contrast to other models which include B-type olivine fabric (Kneller et al., 2005), our modeling approach

does not incorporate a physical basis for the B-type fabric regime; rather, we invoke a change in olivine fabric where the splitting data seem to require it. The measurements due to Long and van der Hilst (2005b, 2006) are well-suited to such an approach: the geographical distribution and spacing of F-net stations provide favorable raypath coverage across much of the mantle wedge (Figure 1b), and the good data coverage in backazimuth, incoming polarization azimuth, and incidence angle allows us to evaluate and discriminate among complex anisotropic models.

3. Flow modeling framework

We implement a series of two-dimensional models for a kinematically defined downgoing slab using the ConMan finite element code for incompressible flow. In the most basic model, flow in the mantle wedge is driven only by viscous coupling between the downgoing slab and the overlying mantle material. The slab dip is fixed at 45° to be roughly consistent with the geometry of the subducting Philippine Sea plate as deduced from seismicity (Gudmundsson and Sambridge, 1999; Engdahl et al., 1998) and seismic tomography (Nakamura et al., 2003; Li et al., 2006; see Figure 2). We impose velocity boundary conditions that are consistent with plate motions.

For viscous flow in an incompressible medium, the ConMan finite element code (King et al., 1990) solves the coupled system of equations for the conservation of momentum, mass, and energy while enforcing an incompressibility constraint using a penalty function. Following the notation of King et al. (1990), these equations are given by:

$$\nabla \cdot (\eta(T,x,z) \nabla u) = -\nabla p + R_a T \hat{k} \qquad (1)$$

$$\nabla \cdot u = 0 \tag{2}$$

$$\frac{\partial T}{\partial t} = u \cdot \nabla T + \nabla^2 T, \tag{3}$$

which are the equations of momentum, continuity, and energy, respectively. Here u represents velocity, T is temperature, p is pressure, t is time, $\dot{\varepsilon}$ is strain rate, and $\hat{k}$ is the unit vector in the vertical direction. The viscosity η is a function of temperature and of position (x,z). All of the dimensional material properties are combined in the dimensionless Rayleigh number, R_a,

$$R_a = \frac{g\alpha\Delta T d^3}{\kappa\eta_0}, \tag{4}$$

where g is the gravitational acceleration, α the thermal expansivity, ΔT the temperature drop across the model box, d the depth of the model box, κ the thermal diffusivity, and η_0 is the (dynamic) reference viscosity. All parameters are nondimensionalized for use in the ConMan input, but hereinafter we refer to their dimensional values.

We solve this system of equations using a regular grid of 80 elements in the horizontal direction and 40 elements in the vertical direction, closely following the approach of Hall et al. (2000). A sketch of the model geometry is shown in Figure 3. We model flow in the mantle between 50 km and 900 km depth; each model block is 21.25 km square. We impose kinematic boundary conditions consistent with the convergence speed at the Ryukyu arc (~ 50 mm/yr; Gripp and Gordon, 2002) at nodes along the top right of the model box and at nodes within the 100 km thick downgoing slab. Other nodes along the top of the model domain are pinned (that is, u_x,u_z=0) . Nodes along the bottom of the model domain are also pinned, except for a line of eight nodes (Figure 3) that allow material to leave the model domain. We define a 30-fold increase in the reference

viscosity η_0 at a depth of 660 km in our models; the downgoing slab is assigned a reference viscosity of 100 times the ambient upper mantle material.

For models that include the effects of thermal buoyancy, we assign an isothermal boundary condition at the top of the model box of T_{top} = 950K, which corresponds to a depth of 50 km. The temperature at the bottom, T_{bottom}, is kept at 1838K. The initial temperature profile is defined to follow the mantle geotherm given by Stacey (1992). The incoming slab material is given a fixed temperature at the top of the model domain; this temperature increases linearly from $T_{slab,left}$ = 950K to $T_{slab,right}$ = 1250K. This is designed to mimic the increase in temperature with depth of the lithospheric slab material as it begins its descent into the mantle. We use a thermal diffusivity $\kappa = 10^{-6}$ m/s^2 and a length scale of 1000 km. We implement a temperature-dependent viscosity law after the approach of Eberle et al. (2002). Temperature-dependent viscosity $\eta(T)$ is generally written in the form of the Arrhenius equation (e.g. Conrad and Hager, 1999; Kohlstedt et al., 1995):

$$\eta(T) = n_0 \exp\left(\frac{E_a}{RT} - \frac{E_a}{RT_0}\right), \tag{5}$$

where η_0 is the reference viscosity, E_a is the activation energy, T_0 is the reference temperature, and R is the gas constant. Following Eberle et al. (2002), we use values that correspond to an activation energy of ~ 500 kJ/mol, and a reference (normalizing) temperature of 1673K; this corresponds to a decrease of four orders of magnitude in viscosity when the temperature increases from 1343K to 1673K.

Non-Newtonian rheologies are implemented in the following manner (King and Hager, 1999): the stress-strain relationship is given by

$$\dot{\varepsilon} = A(\frac{\sigma}{\sigma_0})^n \ , \tag{6}$$

where σ and σ_0 are the stress and reference stress, respectively, n is the power law exponent, and A is given by

$$A = \frac{\sigma_0}{\eta_0 \exp[(E_a + E_V P)/kT]} \ . \tag{7}$$

Here E_V is the activation volume and k is the Boltzmann constant. The effective viscosity is defined by

$$\eta_{eff} = \frac{\sigma}{2\dot{\varepsilon}} , \tag{8}$$

and two different forms of the effective viscosity can be defined, one based on stress and one based on strain:

$$\eta_{eff}^{(strain)} = \frac{\sigma_0}{2A^{\frac{1}{n}}\dot{\varepsilon}^{(1-\frac{1}{n})}} , \tag{9}$$

$$\eta_{eff}^{(stress)} = \frac{\sigma_0^n}{2A\sigma^{(n-1)}} \ . \tag{10}$$

It is numerically efficient and stable to combine the two effective viscosity formulation into one geometric average, in the form (King, 1991)

$$\eta_{eff} = [\eta_{eff}^{(stress)}]^x [\eta_{eff}^{(strain)}]^{(1-x)} , \tag{11}$$

where x is a weighting factor. In our models, we use values of $n = 3$ and $x = 1/3$.

We present five models in this paper. In the most basic model, hereinafter referred to as Model A, flow is driven only by viscous coupling between the downgoing slab and the ambient mantle. In subsequent models, we add increasing complexity. Model B explores the effect on the flow pattern of adding a low-viscosity region (a viscosity

reduction of two orders of magnitude) in the corner of the mantle wedge (e.g. Billen and Gurnis, 2001). Model C uses a power-law rheology instead of a Newtonian (linear) rheology; this model was calculated using the Adina finite element code. With Model D we explore the effects of temperature and thermal buoyancy on the modeled flow and strain fields. Model E illustrates the effect of a temperature-dependent viscosity law. Finally, we compute a model that is a modification of Model E; this is designed to demonstrate the feasibility of using constraints on the geometry of anisotropy obtained from, for example, tomographic inversions, as input parameters for numerical flow models; this is a key component of our combined inversion/flow modeling approach (Long et al., 2006b).

After obtaining steady-state velocity fields for each model, we trace streamlines through the velocity field and calculate the evolution of the finite strain along each streamline. (For the non-steady state models that include temperature effects, we run the model until a nearly steady-state velocity field is achieved, and use this velocity field in subsequent calculations.) Here we follow the approach of Hall et al. (2000), which is based on Malvern (1969) and McKenzie (1979). In this framework, the rate of change of the finite deformation gradient tensor **F** is defined as

$$\dot{\mathbf{F}} = \mathbf{L}\mathbf{F} \tag{12}$$

where **L** is the velocity gradient tensor. McKenzie (1979) gives a time-centered finite difference solution to equation (12) in the form

$$\frac{\mathbf{F}^{n+1} - \mathbf{F}^{n}}{\Delta t} = \frac{\mathbf{L}\left(\mathbf{F}^{n+1} + \mathbf{F}^{n}\right)}{2} \tag{13}$$

where Δt is the time increment between steps. The deformation gradient tensor is related to finite strain through the relation given by Malvern (1969):

$$\mathbf{B}^{-1} = (\mathbf{F}^{-1})^{\mathrm{T}}\,\mathbf{F}^{-1}, \tag{14}$$

where $\mathbf{B}^{-1}$ is the Cauchy deformation tensor. The eigenvalues and eigenvectors of $\mathbf{B}^{-1}$ then give us the principal axes and lengths of the two-dimensional strain ellipsoid; the stretch ratio of deformed length to undeformed length in the direction of the maximum strain is given by

$$r = \frac{1}{\sqrt{\lambda_{\max}}}, \tag{15}$$

where λ is the eigenvalue associated with the maximum finite strain direction.

We emphasize that there are several restrictive approximations involved in our modeling approach. We assume that flow in subduction zone is well-described by a two-dimensional model and that the flow field is controlled by the downdip motion of the slab. We also assume that the slab is well-described everywhere by a 45° dip angle. Subsequent work on fully three-dimensional flow models for this region may clarify the relative importance of flow out of the two-dimensional plane considered here. However, the objective of the work described here is to identify anisotropic models based on a two-dimensional approximation that are consistent with the shear wave splitting observed at the surface.

4. Flow modeling results

Velocity vectors, streamlines, and finite strain ellipse orientations for the simple viscous coupling model (Model A) are shown in Figure 4. The solution for this model agrees well with models by, e.g., Fischer et al. (2000) and Hall et al. (2000), and with the analytical solution for corner flow (Turcotte and Schubert, 1982). For the more complex models, we find differences in the details of the velocity fields and in the resulting finite

strain fields. For example, Model B (with a viscosity reduction of two orders of magnitude in the corner of the wedge) and Model C (with a non-Newtonian, power-law rheology with n = 3) produce subtle differences in the flow field when compared with Model A. In Figure 5, we show streamlines for Models B and C compared with the streamlines for Model A. The differences in the velocity field and streamlines are subtle for most regions of the mantle wedge, but are most pronounced in the wedge corner.

Model D (Figure 6), which includes the effects of thermal buoyancy forces, produces a velocity field that is quite similar to Model A. However, when we add a temperature-dependent viscosity law to the model (Model E), a flow field is produced that is strikingly different from that of Model D. The velocities and temperature field for Model E are shown in Figure 7. In this model, material flows sharply upwards in the wedge corner as hot, buoyant material erodes the colder, stiffer material above it. Further away from the wedge corner, a cold, stiff layer up to ~ 100 km thick that does not participate in the flow field develops. This is similar to the behavior observed by, for example, Eberle et al. (2002) for a temperature-dependent viscosity law. We calculate the evolution of the finite strain ellipse along streamlines in the mantle wedge for Models A-E; this is shown in Figure 8. The details of the finite strain field vary from model to model, but the most dramatic change in the strain field is occurs due to the temperature-dependence of viscosity (i.e. model E).

5. Comparison of model predictions with splitting observations for F-net

In order to map the finite strain distributions into anisotropy and shear wave splitting predictions, we make additional assumptions about the relationships among

strain, anisotropy, and splitting. In our calculations we follow, for example, Fischer et al. (2000) and Hall et al. (2000) and use the orientation and length of the maximum elongation of the finite strain ellipse (FSE) as a proxy for anisotropy. The incorporation of a more detailed treatment of the development of olivine LPO into our models, such as that undertaken by Kaminski and Ribe (2001, 2002), Blackman and Kendall (2002), Kaminski et al. (2004), and Lassak et al. (2006), among others, is beyond the scope of this paper but will be considered in future research. We also assume that the observed splitting is due to anisotropy in the mantle wedge itself; anisotropy within and beneath the slab is ignored in this treatment. This assumption is warranted on the basis of our previous work comparing local and teleseismic splitting at Ryukyu Arc stations (Long and van der Hilst, 2006).

To calculate splitting parameters from the flow models, we trace the evolution of the finite strain ellipse along streamlines throughout the mantle wedge region beginning at the base of the upper mantle (z = 410 km). In this way, we calculate the angle from the horizontal and the stretch ratio of maximum finite strain for each element in our model space. The distribution of stretch ratios and the dip of the FSE from the horizontal for Model A are shown in Figure 9. For the data of Long and van der Hilst (2005b, 2006) we then trace rays using the 1-D iasp91 velocity model (Kennett and Engdahl, 1991) as a background. For each of the 488 raypaths in the dataset, we use the known station and event locations, backazimuths, and ray parameters to trace rays through a "pseudo 3-D" model. Our isotropic background S velocities from iasp91 depend only on the depth z; the distribution of finite strain is 2-D and depends only on depth z and horizontal distance from the trench x. The ray positions, however, are calculated in three dimensions based

on both the backazimuth and the ray parameter. The positions of all the raypaths used in the comparison, projected into the x-z plane of the flow model, are shown in Figure 10 along with the angular sampling of each model block; in this way we can visualize how well our splitting dataset samples the flow model space.

We calculate splitting in depth increments that correspond to the element size in our flow models (21.25 km). For each depth increment, we calculate the incremental splitting using the equations derived in Chevrot and van der Hilst (2003) for shear wave propagation in a transversely isotropic medium with a dipping axis of symmetry. Briefly, their approach uses anisotropic perturbation theory (after, for example, Jech and Pšenčík, 1989; Farra, 2001) to derive approximate expressions for quasi-*S* velocities and polarizations in a weakly anisotropic medium with a dipping axis of symmetry. Chevrot and van der Hilst (2003) find that in the presence of a dipping symmetry axis, the polarizations of the quasi-*S* waves vary with backazimuth, with the deviation angle between the axis of symmetry and the apparent polarization given by

$$\alpha = \arctan\left(\frac{\sin\varphi}{\frac{\tan\theta_c}{\tan\theta} - \cos\varphi}\right), \tag{16}$$

where θ_c is the angle that the symmetry axis makes with the z axis (closely related to the dip of the symmetry axis θ_0) and θ and φ are the incidence angle and azimuth, respectively, of the incoming shear wave. The apparent fast direction for each splitting increment can therefore be predicted from this relation. The approximate velocities of the two quasi-*S* waves are given by

$$VI = \sqrt{\frac{C_{44}}{\rho}}\left(A_0 + A_1\cos\varphi + A_2\cos 2\varphi\right) \tag{17}$$

$$V2 = \sqrt{\frac{C_{44}}{\rho}}\left(B_0 + B_1 \cos\varphi + B_2 \cos 2\varphi + B_3 \cos 3\varphi + B_4 \cos 4\varphi\right), \tag{18}$$

where C_{44} is an elastic constant of the material, ρ is the density, and A_0, A_1, A_2, B_0, B_1, B_2, B_3, and B_4 are all functions of θ_0, θ, and the elastic constants C_{ij} of the material, expressed as combinations of the Thomsen parameters ε, δ, and γ (Thomsen, 1986; Mensch and Rasolofosaon, 1997). From these expressions, given in Chevrot and van der Hilst (2003), we calculate the apparent splitting parameters φ and δt for each depth increment. We then calculate the predicted splitting intensity s for that depth increment, using (Chevrot, 2000)

$$s = \delta t \sin\left[2(\varphi - \varphi_0)\right], \tag{19}$$

where φ_0 is the azimuth of the apparent fast axis. The total splitting intensity for each raypath is found by summing the splitting intensities calculated for each depth increment.

We approximate the anisotropic medium using elastic constants for a transversely isotropic mantle (TIM) described in Chevrot and van der Hilst (2003); a similar approach was used by Hartog and Schwartz (2000). The elastic constants were obtained by averaging the elastic tensor of single-crystal olivine (Kumazawa and Anderson, 1968) around the a-axis with an isotropic reference mantle in the ratio of 1/3 to 2/3. We then assume that the fast axis of the TIM aligns with the maximum FSE in our flow model. We further assume that once a stretch ratio of 3 has been achieved along a streamline, the LPO pattern has saturated and the splitting associated with TIM is used. For stretch ratios of less than 3, we scale the predicted split time linearly with the amount of strain; this approximates the effect of non-steady state, weaker LPO for stretch ratios less than 3.

We predict splitting for each of the 488 raypaths in our splitting dataset for each of the finite strain distributions calculated from Models A-E. In Figure 11, we show the data and model comparison for Model A at four selected *F*-net stations (AMM, FUK, IGK, and TAS; see Figures 1a and 10a for station locations). Except for station FUK, which is located ~ 400 km from the trench, the model fit is quite poor. This is not unexpected; the best-fitting fast directions at stations AMM, IGK, and TAS are all nearly trench-parallel, and we do not expect a two-dimensional corner flow-type model to be able to match trench-parallel fast directions. Following the arguments in Long and van der Hilst (2006), we invoke a B-type fabric mechanism in the corner of the mantle wedge. A sketch of the raypaths that is color-coded by the type of measurement (trench-parallel, trench-perpendicular, or intermediate/complicated), shown in Figure 12, gives us an indication of where in the model the observations seem to require B-type fabric. We therefore "flip" the LPO, and therefore the fast direction of anisotropy, by 90° in a triangular region extending ~ 150 km from the trench.

In Figure 13 we show the splitting data and model predictions for each of the same four stations for the strain field derived from Model A, with a B-type fabric region in the mantle wedge. The fit at stations AMM, IGK, and TAS is clearly better; the model now predicts splitting that is consistent with the trench-parallel fast directions observed at those stations. The fit for station FUK remains unchanged, as none of the raypaths associated with this station sample the region where we have "flipped" the LPO to B-type.

In Figures 11 and 13, we show the splitting predictions for strain fields derived from Model A. When we examine the predictions for Model E, which produces a strain

field that is markedly different from Model A, we find that the detailed splitting patterns at most stations are also substantially different. Figure 14 shows the observed and predicted splitting at the same four stations for Model E, modified to include the same B-type region in the wedge corner. We find that details of the splitting predictions are different, and the fit to the measured splitting is slightly better. However, the visual character of the splitting patterns is not drastically different, and the *average* splitting parameters that we would predict for most stations are not much different from those for Model A (Figure 13). These observations are borne out when we examine the model predictions at station TKA for four different flow models (Models A, B, D, and E, with a B-type fabric region) (Figure 15). All of the model predictions fit the observations fairly well, but the details of the splitting patterns for different models are substantially different. This suggests that the *average* shear wave splitting observed at the surface, while generally consistent with the predictions of our flow models, is not very sensitive to the details of the model parameters used; it appears that average measured splitting parameters cannot be easily used as an indicator of rheological properties in the mantle wedge. However, because the detailed splitting patterns at each station are substantially different for different models, a dense dataset with good sampling at individual stations (such as that of Long and van der Hilst, 2005b, 2006) would be sensitive to the pattern of anisotropy of the wedge, and therefore to the rheological properties that control the geometry. This gives us confidence that we can interpret the detailed splitting patterns we observe in southwestern Japan in terms of the 2-D anisotropic geometry in the mantle wedge.

6. Discussion

Our 2-D flow modeling approach ignores the possible effects of flow around the slab edge or flow induced by effects such as slab rollback or back-arc extension. Because the rollback rate of the Ryukyu trench is slow compared to the downdip motion of the slab (Heuret and Lallemand, 2005; Yu and Kuo, 1996; Mazzotti, 1999), Long and van der Hilst (2006) argued that the flow field is likely dominated by convergence-parallel flow and that three-dimensional flow effects are likely small. It is necessary to invoke the B-type olivine fabric hypothesis (Jung and Karato, 2001; Karato, 2003) in order to reconcile the trench-parallel fast directions we observe in southwestern Japan with a two-dimensional flow model that neglects three-dimensional effects. We do acknowledge that there are outstanding questions about the applicability of B-type fabrics observed in the laboratory to the Earth's mantle; studies have questioned whether the physical and chemical conditions needed to produce B-type fabric are present in large volumes of the mantle wedge (e.g. Kaminski, 2002). However, recent (Kneller et al., 2005) and ongoing modeling studies are examining in detail whether the stress, strain, and hydration conditions needed to produce B-type fabric are in fact achieved in large portions of the wedge corner. There is a growing body of evidence from experimental (Jung and Karato, 2001; Katayama and Karato, 2006), petrographic (Mizukami et al., 2004; Skemer et al., 2006), observational (Nakajima and Hasegawa, 2004; Long and van der Hilst, 2006; Nakajima et al., 2006) and modeling (Lassak et al., 2006; Kneller et al., 2006) studies that B-type fabric may indeed be important in certain regions of the mantle wedge.

We have identified a suite of models that incorporate B-type fabric in the mantle wedge and are consistent with the observed splitting. However, we emphasize that the

approach we have taken to identifying the region dominated by B-type fabric is driven by the splitting observations; we do not attempt to predict the B-type fabric region, and our models do not contain or describe the "physics" of the olivine fabric transition. A complementary approach is taken by Kneller et al. (2005); their models incorporate laboratory results for olivine rheology (Katayama and Karato, 2006) and LPO development (Jung and Karato, 2003; Katayama et al., 2004) and predict the region of the wedge in which the B-type fabric should dominate. We are currently undertaking a detailed comparison of our splitting dataset with these and similar models and preliminary work indicates that the results we obtain with our more data-driven approach are quite consistent with such models (Kneller et al., 2006).

We have produced a series of models that match the splitting observations across the mantle wedge very well. This provides support to the hypothesis favored by Long and van der Hilst (2006): the observed splitting can be produced with a 2-D model that invokes trench-perpendicular flow coupled to the downdip motion of the slab with a region of B-type olivine fabric in the corner of the wedge. However, although we match the broad features of the splitting patterns at most stations fairly well with this model, we are still unable to match the details of the splitting patterns observed at each of the 17 stations examined. Part of this mismatch may be due to along-strike variations in slab geometry, flow field, and the resulting anisotropy, which our 2-D modeling approach cannot account for. However, much of the mismatch between the observed and predicted splitting is likely due to incorrect or inadequate aspects of the 2-D forward models themselves. Therefore, we plan to invert the mismatch between predicted splitting and

splitting observations to obtain the best possible 2-D model for anisotropy beneath southwestern Japan.

The two models considered in this study that best match the splitting observations are Model A, which is isothermal, and Model E, which includes a temperature-dependent viscosity. It appears from the splitting patterns in Figures 13-14 that the fit for Model E may be slightly better than the fit for Model A, although in evaluating the fits there is likely some tradeoff between the geometry of the strain field and the elastic parameters used in creating the anisotropic model. The temperature-dependent viscosity law used in Model E is likely to be more physically realistic (e.g. Kelemen et al. 2003), and the high temperatures in the shallow regions of the wedge corner predicted by this and similar models is more consistent with petrologic evidence (Elkins Tanton et al., 2001). In any case, the direct inversion of our shear wave splitting data set should provide tighter constraints on the geometry of anisotropy than can be provided by forward modeling alone, and this work should help to discriminate further between the possible models.

7. Outlook

In a future study the models produced here will be used as starting models in a formal inversion approach, in which we invert the mismatch between observed and predicted splitting intensities for an updated 2-D anisotropic structure. This work is currently in progress (Long et al., 2006b). An advantage to using the results of numerical flow models as starting models for an inversion is their adaptability and their potential use in an iterative inversion framework. If we can obtain new constraints on the geometry of anisotropy in certain regions of the mantle wedge from the inversion of shear wave

splitting intensities, then we can in turn incorporate that information as additional constraints in an updated flow model. Perturbing the numerical models of flow in the wedge with additional constraints obtained from the inversion should allow us to produce a model that comes even closer to predicting the observed splitting, and to provide better constraints on the likely character of anisotropy in regions of the wedge that are not as well-sampled by the raypath geometry (Figure 10).

There are two possible approaches for integrating constraints from the inversion and from the flow models. The first approach involves the imposition of additional kinematic velocity constraints into an updated flow model. In regions of the model where the inversion is well-resolved and where we obtain high-confidence estimates of the local geometry of the anisotropy (and therefore of the strain field), we can insert consistent kinematic velocity constraints into a perturbed flow model. The difficulty with such an approach, however, is that translating the local geometry of anisotropy into velocity constraints is not straightforward. The geometry of the finite strain ellipse at any point in the model depends on the strain history along a streamline that passes through that point. Because of this dependence of local strain geometry on the strain history, it is not immediately obvious what velocity constraints will produce the desired strain geometry. However, if we restrict ourselves to perturbing the flow field only for certain regions of the model that are very well-resolved by the inversion, it should be possible to experiment with velocity constraints and obtain the sought-after strain orientation. Although this *ad hoc* approach will require some experimentation to find appropriate velocity constraints, it should allow us to produce updated models that bring us closer to the optimal solution. These updated models can then be used as new starting models for

an updated inversion, and this process can be iterated until a final solution is converged upon.

A second approach to integrating inversion constraints with the flow modeling framework involves a second, direct inversion for the appropriate flow modeling parameters that come closest to matching the strain geometry we retrieve from (well-resolved areas of) the splitting inversion. In such an approach, we would obtain partial derivatives of the two anisotropic parameters that describe the model at each point (dip θ_0 and anellipticity ε_A; see Long et al., 2006b) with respect to the flow model parameters of interest (for example, activation energy E_a in the temperature-dependent viscosity law, or the power n in the non-Newtonian rheology law). These partial derivatives can be obtained numerically by varying the parameter of interest slightly from its initial value, running the flow model again, and calculating the change in finite strain orientation and magnitude. Such an approach would yield partial derivatives (for example, $\frac{\partial \theta_0}{\partial E_a}$ and $\frac{\partial \varepsilon_A}{\partial E_a}$) at each point in the model, and these sensitivities could be used to invert the anisotropic parameter values for the most appropriate flow model parameter value(s). These values can then be used in an updated flow model, which can be used as a new starting model for the splitting intensity inversion; this process can be iterated to find a best solution. An example of a calculation of partial derivatives of anisotropic parameters with respect to E_a is shown in Figure 16. This method has an advantage over the velocity constraint approach in that the sensitivities are straightforward to compute, while appropriate velocity constraints must be found using a somewhat *ad hoc* approach. However, it is not clear how stable an inversion for best-fitting flow parameters would be, particularly because of the limited seismic illumination in the wedge. Both of these

approaches hold promise for incorporating the constraints from the splitting intensity inversion into our flow modeling framework, and deciding which one is most appropriate and can best integrate the inversion and flow modeling methodologies will be the subject of future work.

8. Summary

We have computed velocity and finite strain fields for a suite of two-dimensional numerical models of flow in the mantle wedge associated with a downgoing slab. Combining these models with assumptions about the relationship between maximum finite strain and the resulting anisotropy allows us to predict shear wave splitting. We have applied this technique to southwestern Japan, using flow model boundary conditions appropriate for the subduction of the Philippine Sea plate beneath Eurasia and comparing the model splitting predictions to a shear wave splitting dataset for seventeen broadband stations located in the Ryukyu Arc, Kyushu, and southernmost Honshu. We draw the following conclusions: 1) We are able to identify flow models that are consistent with the observed splitting, which suggests that the flow field can be approximated with a 2-D modeling approach. 2) The splitting intensity introduced by Chevrot (2000) provides a natural and visually intuitive way of comparing splitting observations with the model predictions. 3) The *average* predicted splitting parameters are relatively insensitive to the details of the finite strain field, and therefore to the parameters used in the flow models. However, the details of the splitting patterns predicted for different models are dramatically different. Rigorous analysis of the details of splitting patterns for dense splitting datasets, such as the dataset of Long and van der Hilst (2005b, 2006), has the

potential to discriminate among different rheological models for flow in the mantle wedge. 4) In order to explain the observed splitting, we must invoke a region of B-type olivine fabric in the wedge corner, extending ~ 150 km into the backarc. This is consistent with other, complementary modeling studies of B-type fabric in the mantle wedge (e.g. Kneller et al., 2005, 2006). The flow modeling framework presented here yields starting models that are suitable for inverting splitting observations for anisotropic structure, and constraints obtained from an inversion approach can be incorporated into subsequent updates to the flow field; we have outlined two possible tactics for this integration.

Figure Captions

Figure 1a. Station locations and tectonic setting. Locations of the seventeen broadband F-net stations used in this study are shown as triangles. Dotted lines indicate slab contours from Gudmundsson and Sambridge, 1998. The trench is shown with a black line, and slab contours at 100-km intervals are shown with gray lines. The black arrow indicates the convergence direction at the Ryukyu arc. The location of the tomographic cross-section shown in Figure 2 is shown as a thick black line.

Figure 1b. Map view of raypaths for the splitting measurements used in this study. Black lines indicate the upper mantle portion of teleseismic raypaths (*SKS*, *SKKS*, and direct *S*) Gray lines indicate raypaths for events originating within the Ryukyu slab.

Figure 1c. Summary of average fast splitting directions from Long and van der Hilst (2005b, 2006). The orientation of each bar corresponds to the fast polarization direction. Average splitting parameters for teleseismic measurements are plotted in black at the station locations. Stations with complicated teleseismic splitting patterns for which there is no physically meaningful average (Category III in Long and van der Hilst, 2005b) are marked with a green circle. Teleseismic splitting was not investigated at station YNG (marked with a blue circle). Individual low-frequency local splitting measurements are plotted in black at the midpoint of the ray.

Figure 2. Cross-section through the tomographic P velocity model of Li et al. (2006) between the surface and the base of the transition zone. The location of the cross-section is shown on Figure 1a. The color bar scale ranges from +2% (blue) to -2% (red) perturbations to the ak135 reference model. Earthquake hypocenters from the EHB data set (Engdahl et al., 1998) are plotted as white circles; the dashed black line represents the 410 km discontinuity.

Figure 3. Sketch of finite element model setup. The model domain consists of 80 horizontal elements and 40 vertical elements. We model depths between 50 km and 900 km, after Hall et al. (2000). There is a 30-fold increase in viscosity at the 660-km discontinuity. The Ryukyu slab is modeled as a continuous, kinematically-defined feature down to the 660 km discontinuity with a constant dip of 45°. At the top of the model domain, nodes to the left of the slab (thick black line) are pinned; nodes to the right of the slab (thick gray line) are given a constant plate velocity. Nodes within the slab are given a prescribed velocity consistent with the plate velocity at the top of the model. At the bottom of the model domain, most nodes are pinned (thick black lines), with a small section allowed to move freely, such that material is allowed to leave the model domain.

Figure 4. a. Velocity field for the basic model setup (model A). The portion of the model corresponding to depths between 50 km and 660 km is shown. Arrows correspond to velocities at individual nodes. Axis labels correspond to the depths (z) and horizontal coordinates (x) in km. b. Streamlines traced through the velocity field displayed in (a). Alternating colors are for clarity. c. Finite strain ellipses calculated for model A along the

streamlines shown in (b). Finite strain ellipses are shown as colored bars, with the orientation and length of the bar corresponding to the orientation and strength of the maximum finite strain direction.

Figure 5. Streamlines for basic viscous model, a model with a low-viscosity region in the wedge corner, and a model with a nonlinear rheology. a. Streamlines for model A (blue) and model B (red) for the same starting positions. b. Streamlines for model A (blue) and model C (green) for the same starting positions. Axis labels correspond to the depths (z) and horizontal coordinates (x) in km.

Figure 6. Time snapshots of the temperature field associated with a downgoing slab. The time series covers approximately 17 Myr of subduction; each time step therefore represents about 2.1 Myr. Axis labels correspond to the depths (z) and horizontal coordinates (x) in km.

Figure 7. Temperature field and model velocities in the wedge corner for a model with a temperature-dependent viscosity. Axis labels correspond to the depths (z) and horizontal coordinates (x) in km.

Figure 8a-e. Finite strain ellipses (FSE) in the mantle wedge for the models (A-E) investigated in this study. Contrasting colors are for clarity. Axis labels correspond to the depths (z) and horizontal coordinates (x) in km.

Figure 9. a. Color representation of the magnitude of the maximum finite strain field for Model A. Color bar goes from stretch ratios of 0 (blue) to stretch ratios of 5 or greater (red). b. Color representation of the angle of the maximum finite strain ellipse with the horizontal for Model A. Near-horizontal angles are shown in green; the color scale goes from angles of 90 degrees counterclockwise from horizontal (red) to 90 degrees clockwise from horizontal (blue). Axis labels correspond to the depths (z) and horizontal coordinates (x) in km.

Figure 10. a. Sketch of raypaths in the splitting dataset projected onto the 2-D model plane. The distribution of finite strain in the wedge for Model A is shown. Station locations are marked with a black triangle and station names are shown. Gray lines indicate the portion of the model space shown in (b). b. Color representation of the number of incidence angle bins sampled by the raypaths in the southwestern Japan splitting dataset for each model block. For each block, the number of 15° wide incidence angle bins covered by the dataset was sampled. The regions with the best coverage are sampled by three different ranges of incidence angles. Axis labels correspond to the depths (z) and horizontal coordinates (x) in km.

Figure 11a-d. Comparison of splitting observations (black circles) and model predictions (green triangles) for Model A (with no B-type fabric) at 4 stations (AMM, IGK, FUK, TAS). The best-fitting $\sin(2\theta)$ curve to the observed splitting is shown in black. Splitting intensities (y axis) are plotted with respect to incoming polarization azimuths (x axis).

Figure 12. Cross-sectional plot of all teleseismic raypaths in this study, color-coded by type of observation. Rays associated with near trench-parallel fast directions are shown in red; rays associated with near trench-perpendicular fast directions are shown in light blue. Rays associated with stations for which the measured splitting is complex (Category III stations in Long and van der Hilst, 2005b) are shown in dark blue. The finite strain distribution for Model A is shown. Axis labels correspond to the depths (z) and horizontal coordinates (x) in km.

Figure 13a-d. Comparison of splitting observations (black circles) and model predictions (green triangles) for Model A (includes B-type fabric regime) at 4 stations (AMM, IGK, FUK, and TAS). The best-fitting sin(2θ) curve to the observed splitting is shown in black. Splitting intensities (y axis) are plotted with respect to incoming polarization azimuths (x axis).

Figure 14a-d. Comparison of splitting observations (black circles) and model predictions (green triangles) for Model E (includes B-type fabric regime) at 4 stations (AMM, IGK, FUK, and TAS). The best-fitting sin(2θ) curve to the observed splitting is shown in black. Splitting intensities (y axis) are plotted with respect to incoming polarization azimuths (x axis).

Figure 15a-d. Comparison of splitting observations and model predictions for four models (Models A, B, D, E) at station TKA. Splitting intensities (y axis) are plotted with respect to incoming polarization azimuths (x axis).

Figure 16. a-b. Strain field for Model E (a) and a similar model with activation energy equal to 0.5 times the activation energy for Model E (b). c-d. Partial derivatives of anisotropic parameters θ_0 (c) and ε_A (d) with respect to the activation energy E_a. Derivatives were calculated numerically by changing the value of E_a in the model, solving the resulting strain field, and calculating the change in the anisotropic parameters at each point.

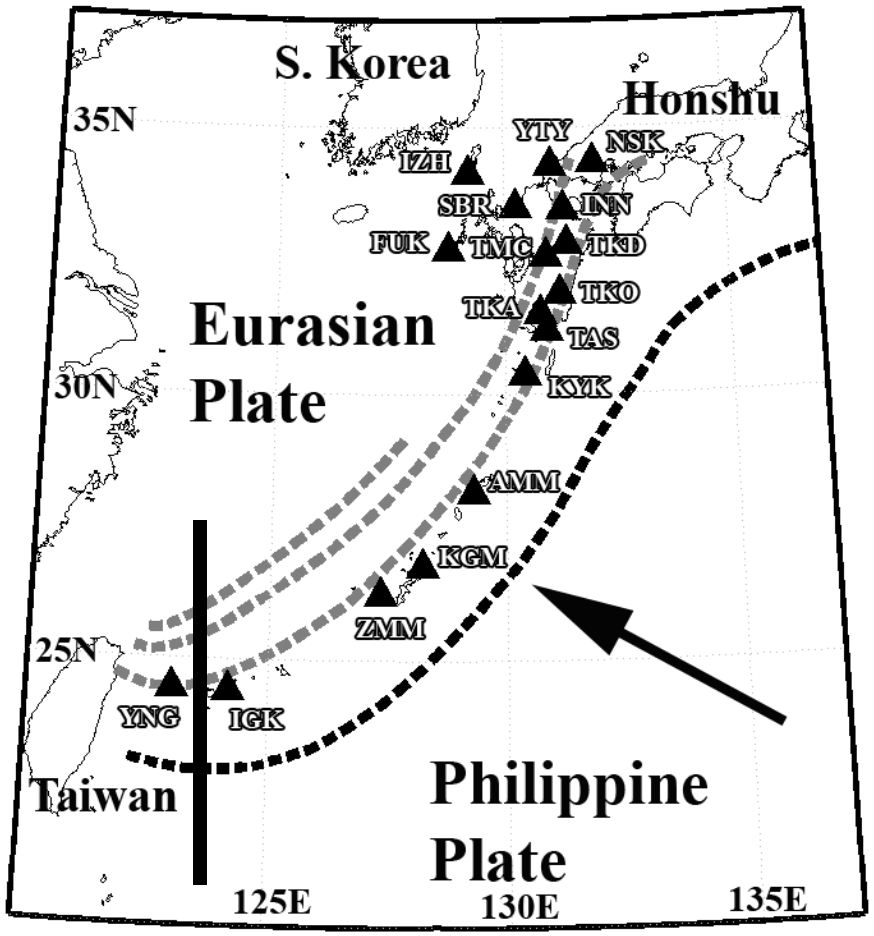
S. Korea
Honshu
35N
YTY
NSK
IZH
SBR
INN
FUK
TMC
IKD
TKO
TKA
TAS
KYK
Eurasian
Plate
30N
AMM
KGM
ZMM
25N
YNG
IGK
Taiwan
Philippine
Plate
125E
130E
135E

Figure 1a

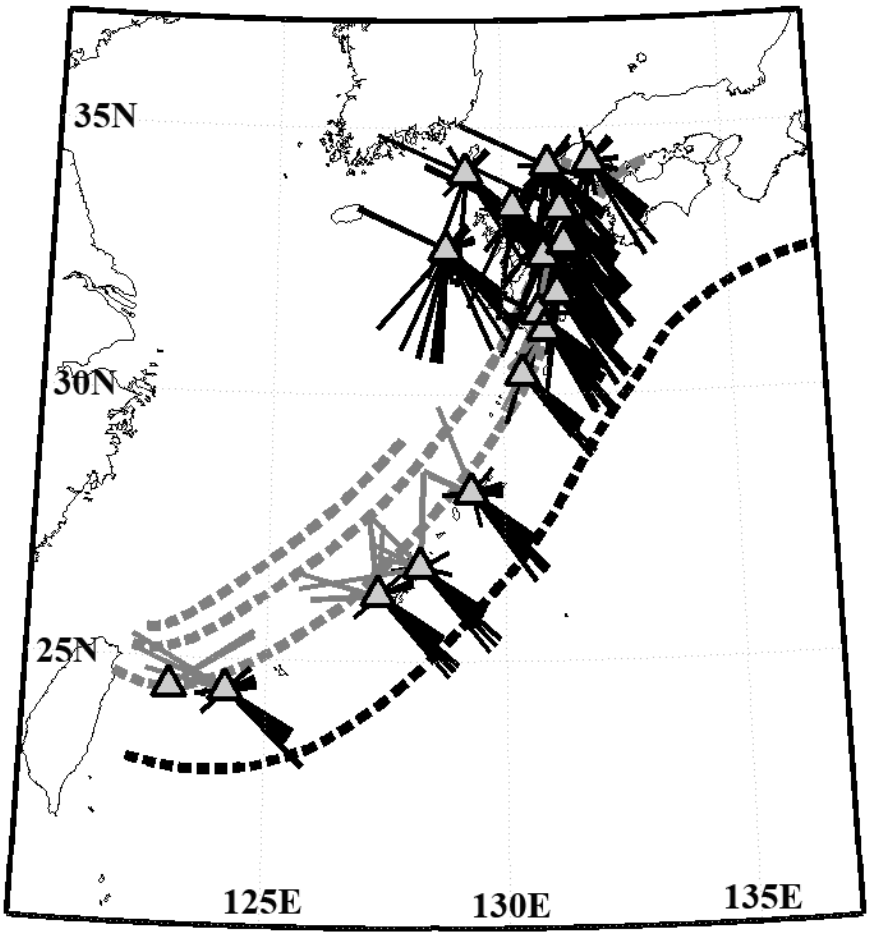

Figure 1b

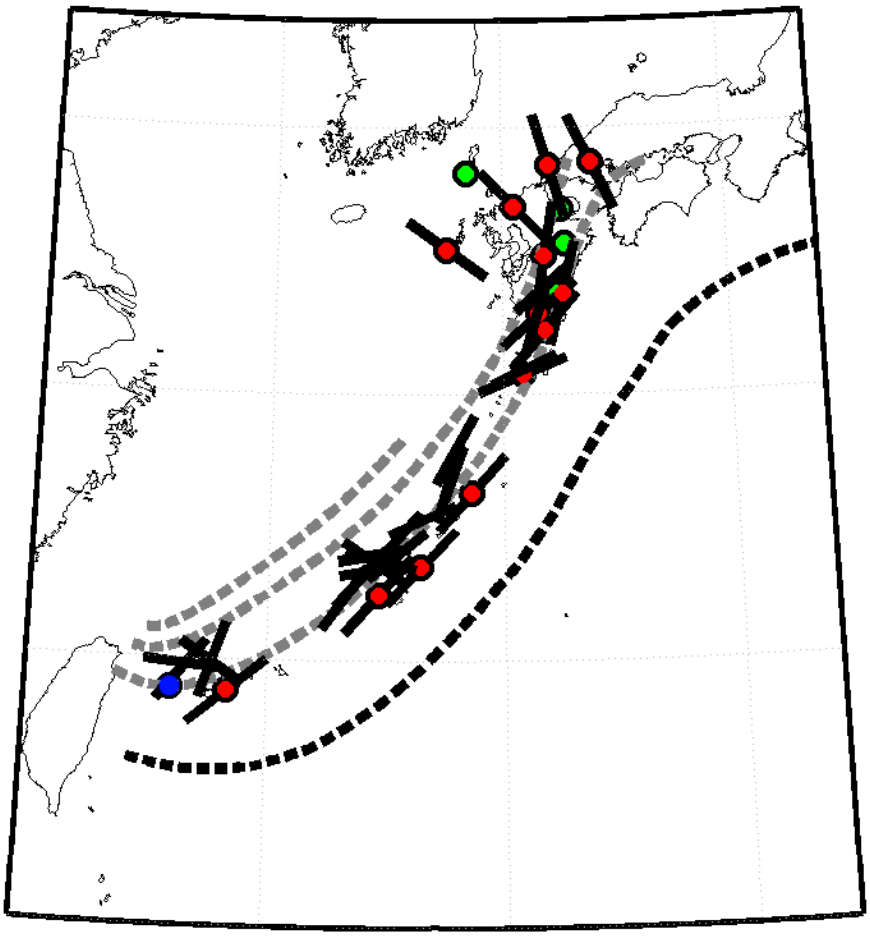

Figure 1c

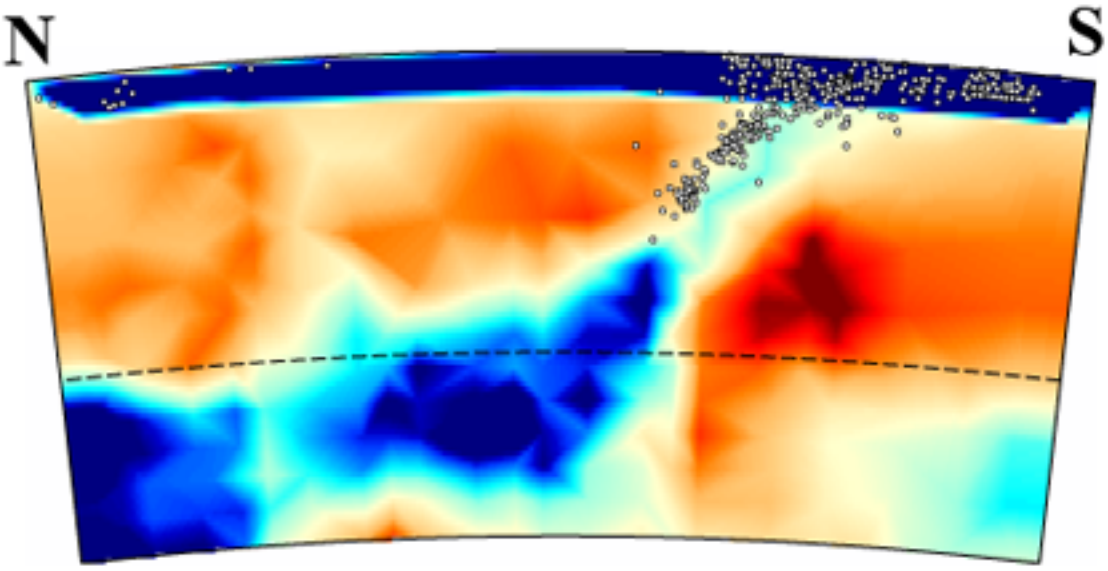

Figure 2

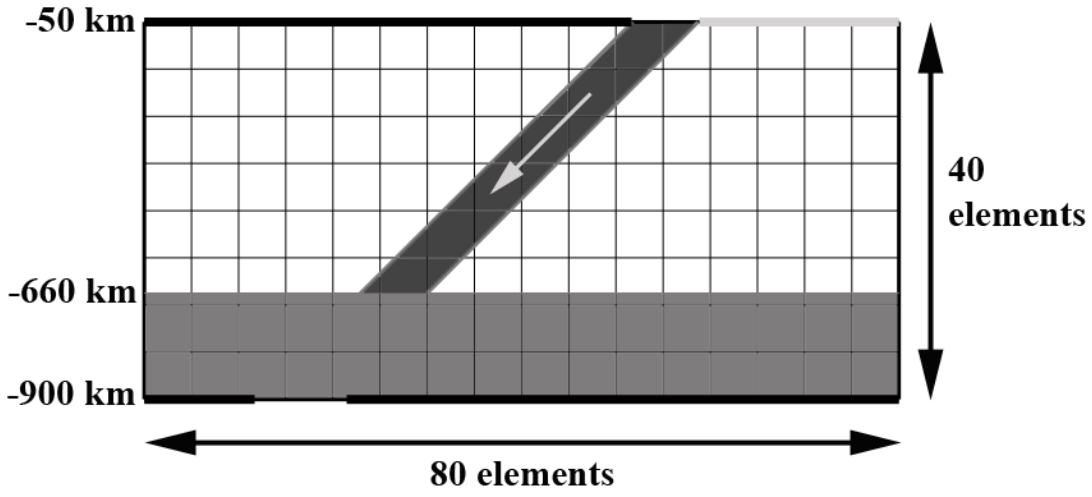

Figure 3

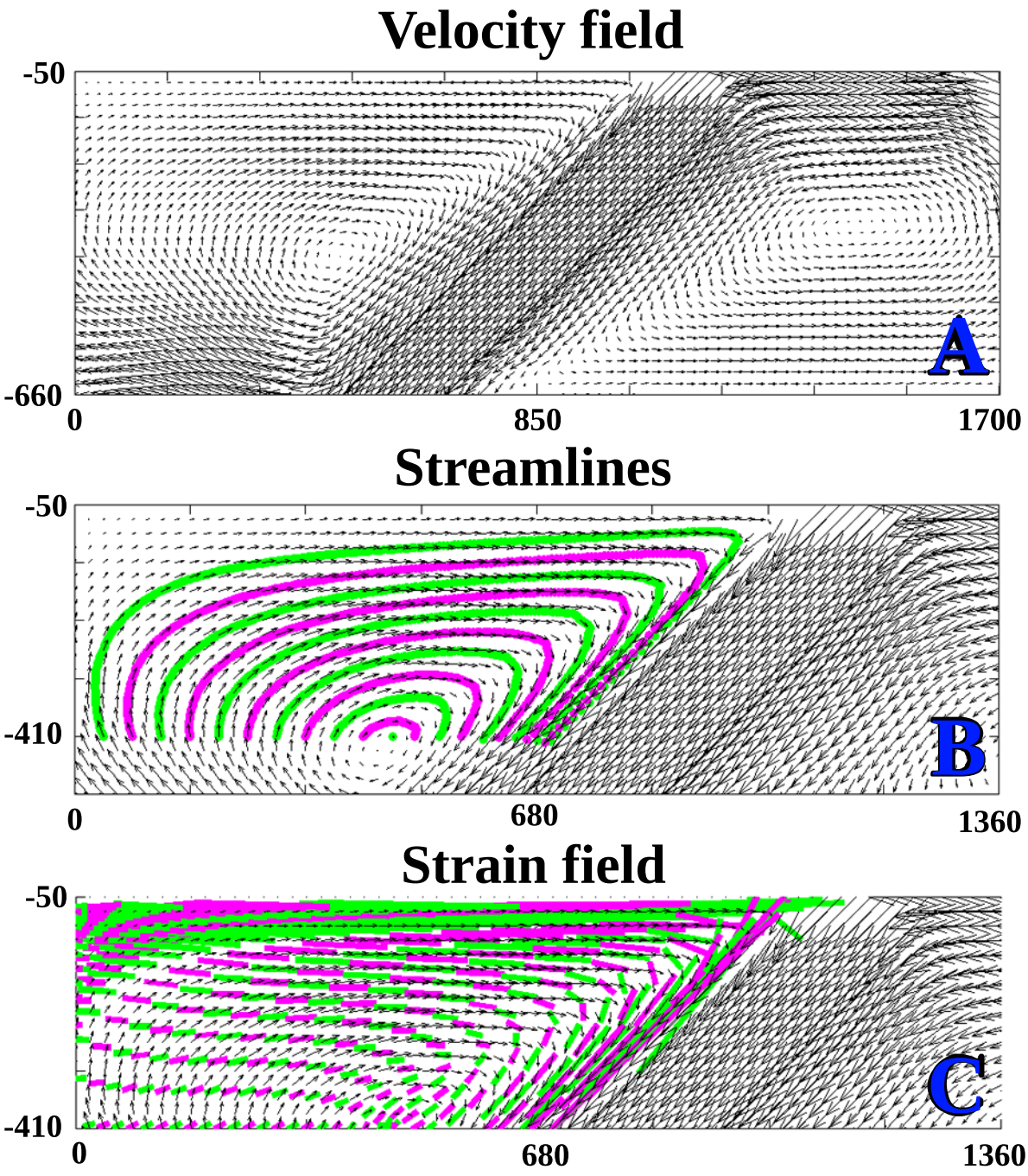
Velocity field
-50
-660
0
850
1700
A
Streamlines
-50
-410
0
680
1360
B
Strain field
-50
-410
0
680
1360
C

Figure 4

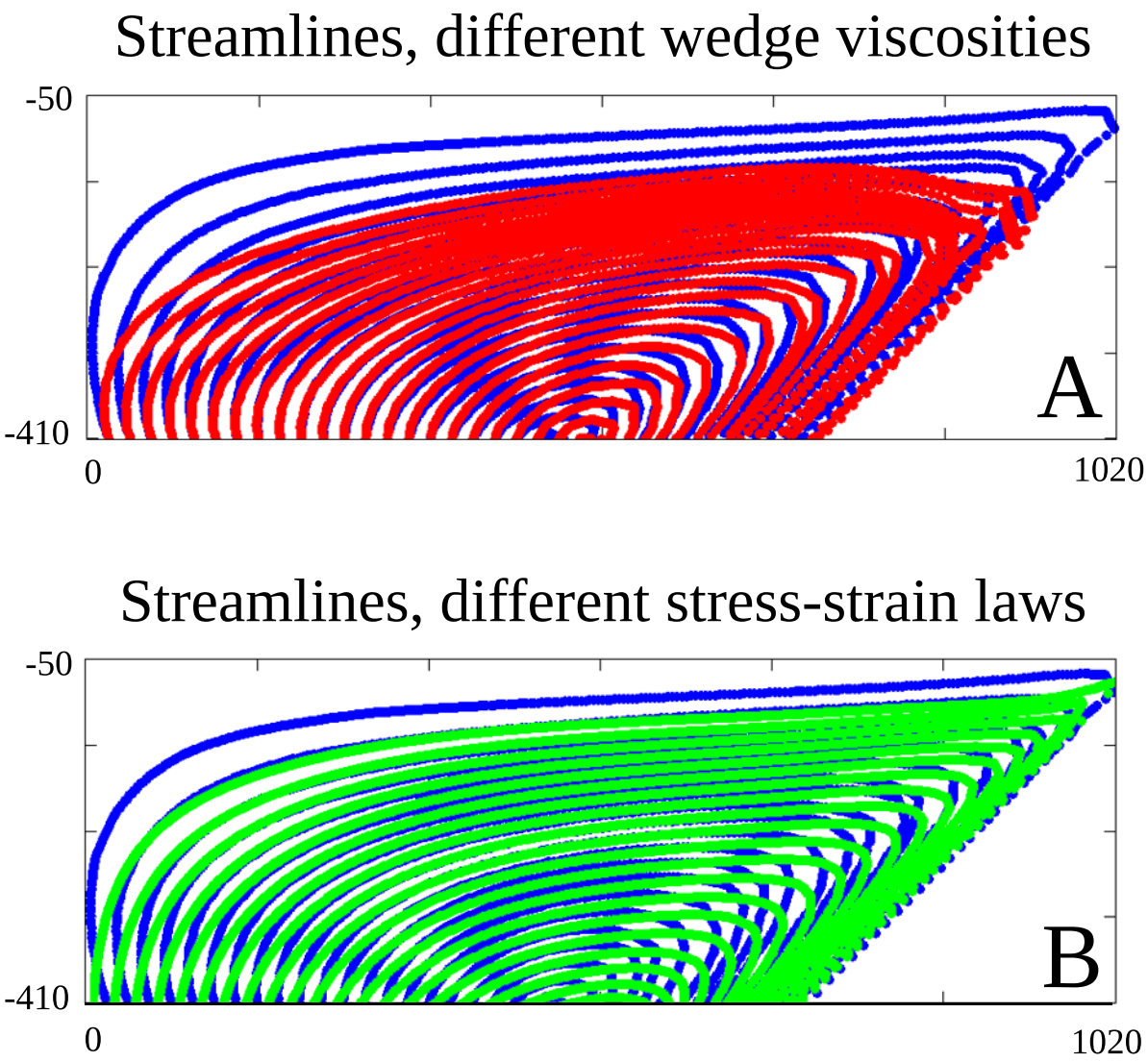
Streamlines, different wedge viscosities
-50
-410
0
1020
A
Streamlines, different stress-strain laws
-50
-410
0
1020
B

Figure 5

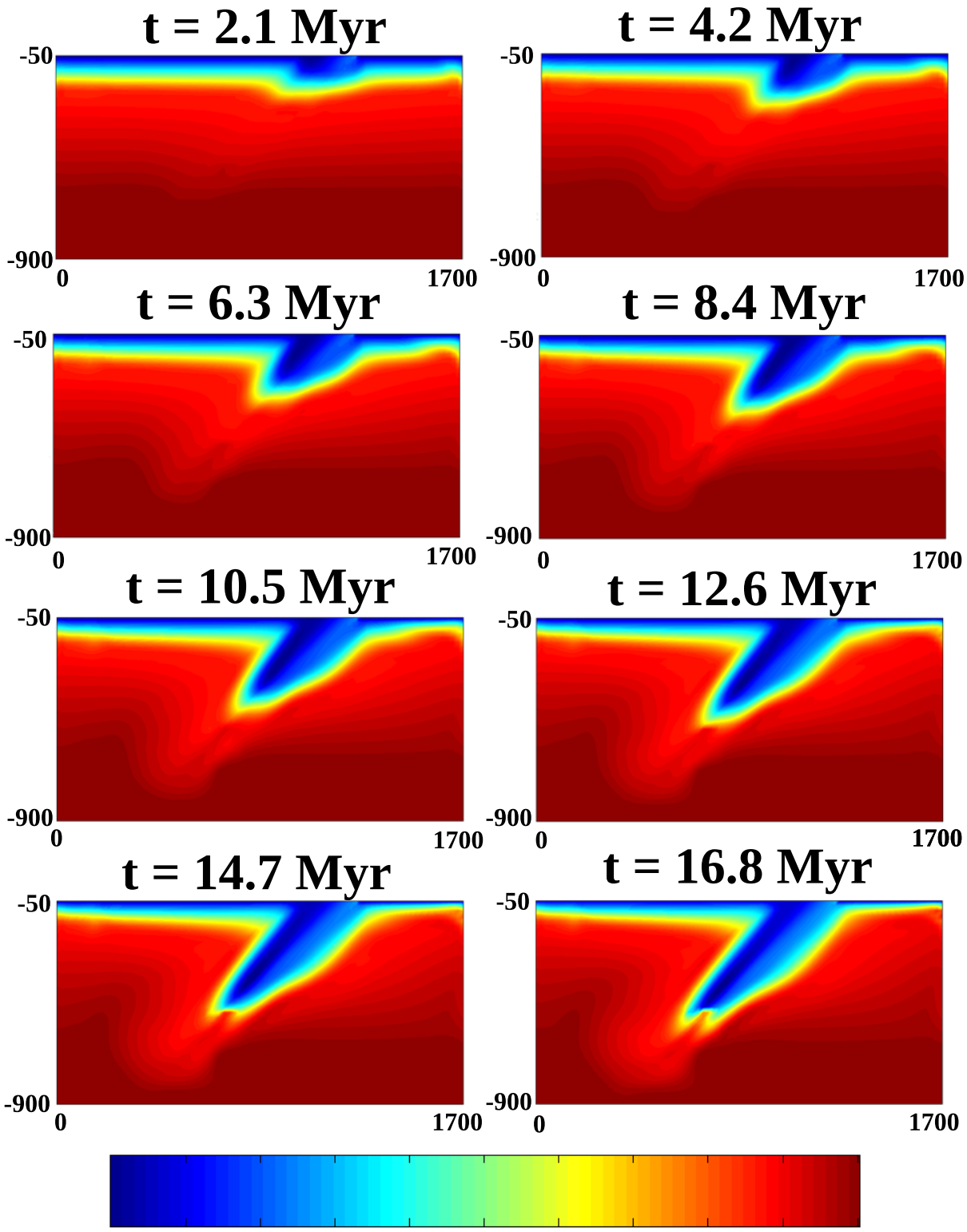
t = 2.1 Myr
t = 4.2 Myr
t = 6.3 Myr
t = 8.4 Myr
t = 10.5 Myr
t = 12.6 Myr
t = 14.7 Myr
t = 16.8 Myr
-50
-900
0
1700
950K
1700K

Figure 6

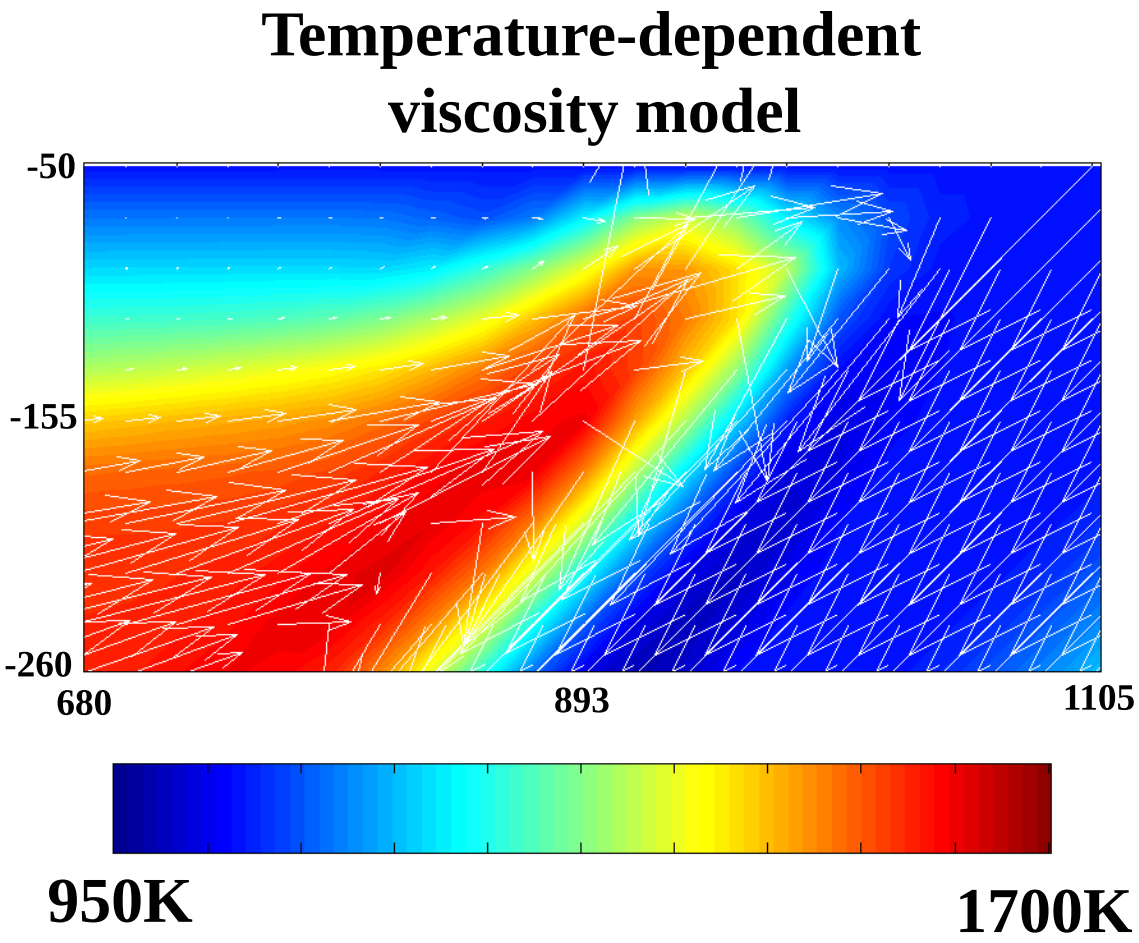
Temperature-dependent
viscosity model
-50
-155
-260
680
893
1105
950K
1700K

Figure 7

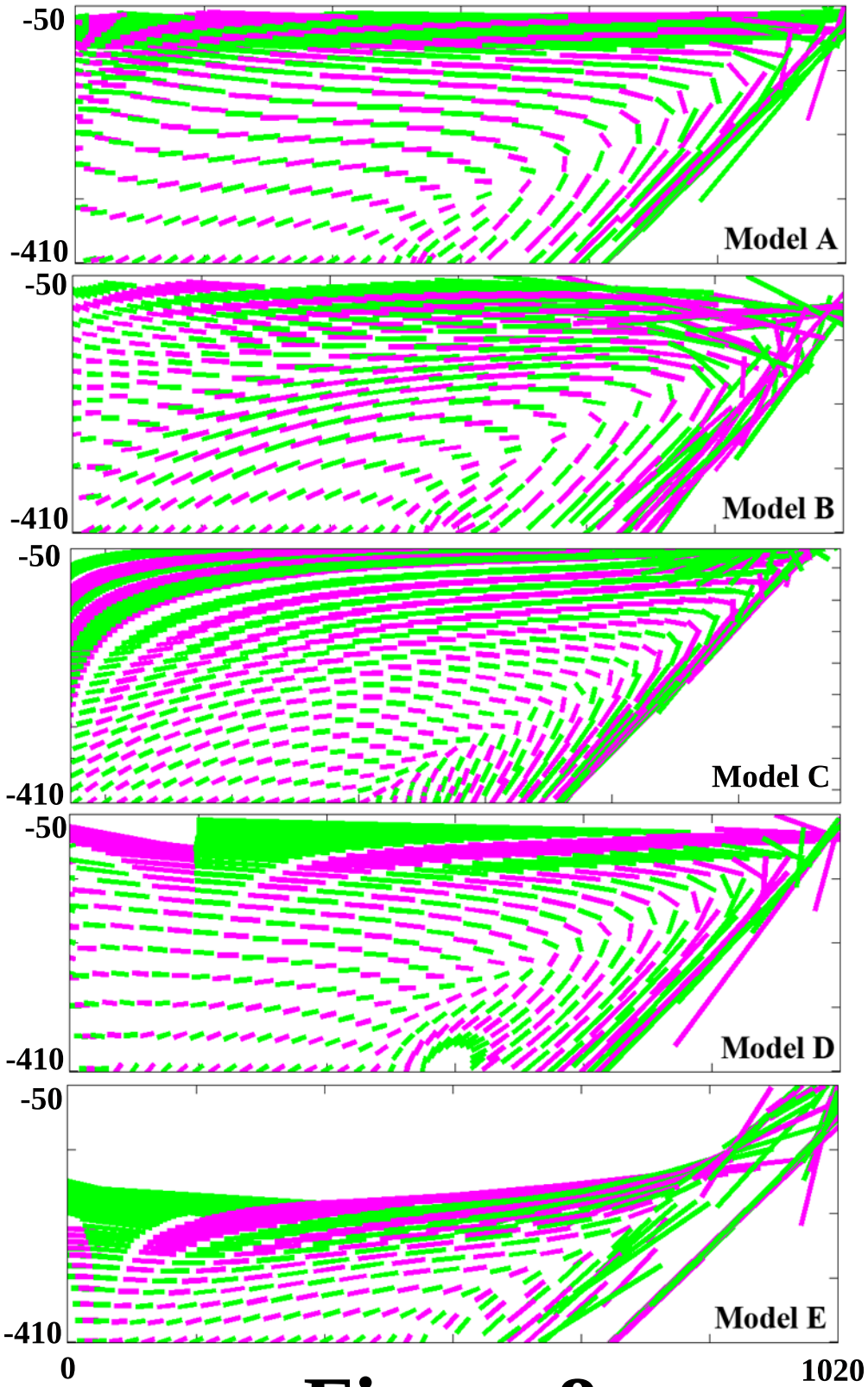
-50
-410
Model A
-50
-410
Model B
-50
-410
Model C
-50
-410
Model D
-50
-410
Model E
0
1020

Figure 8

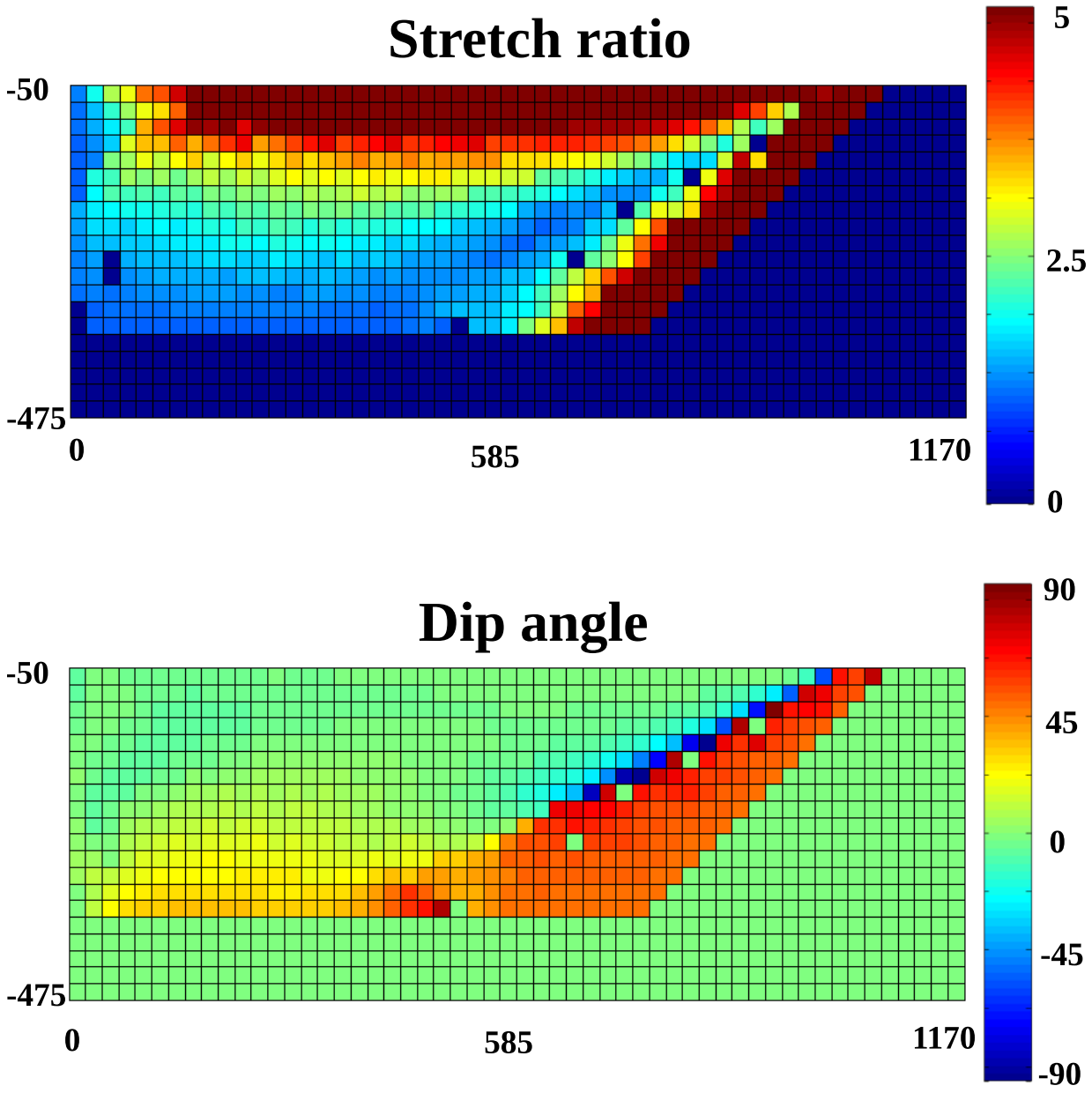
Stretch ratio
-50
-475
0
585
1170
5
2.5
0
Dip angle
-50
-475
0
585
1170
90
45
0
-45
-90

Figure 9

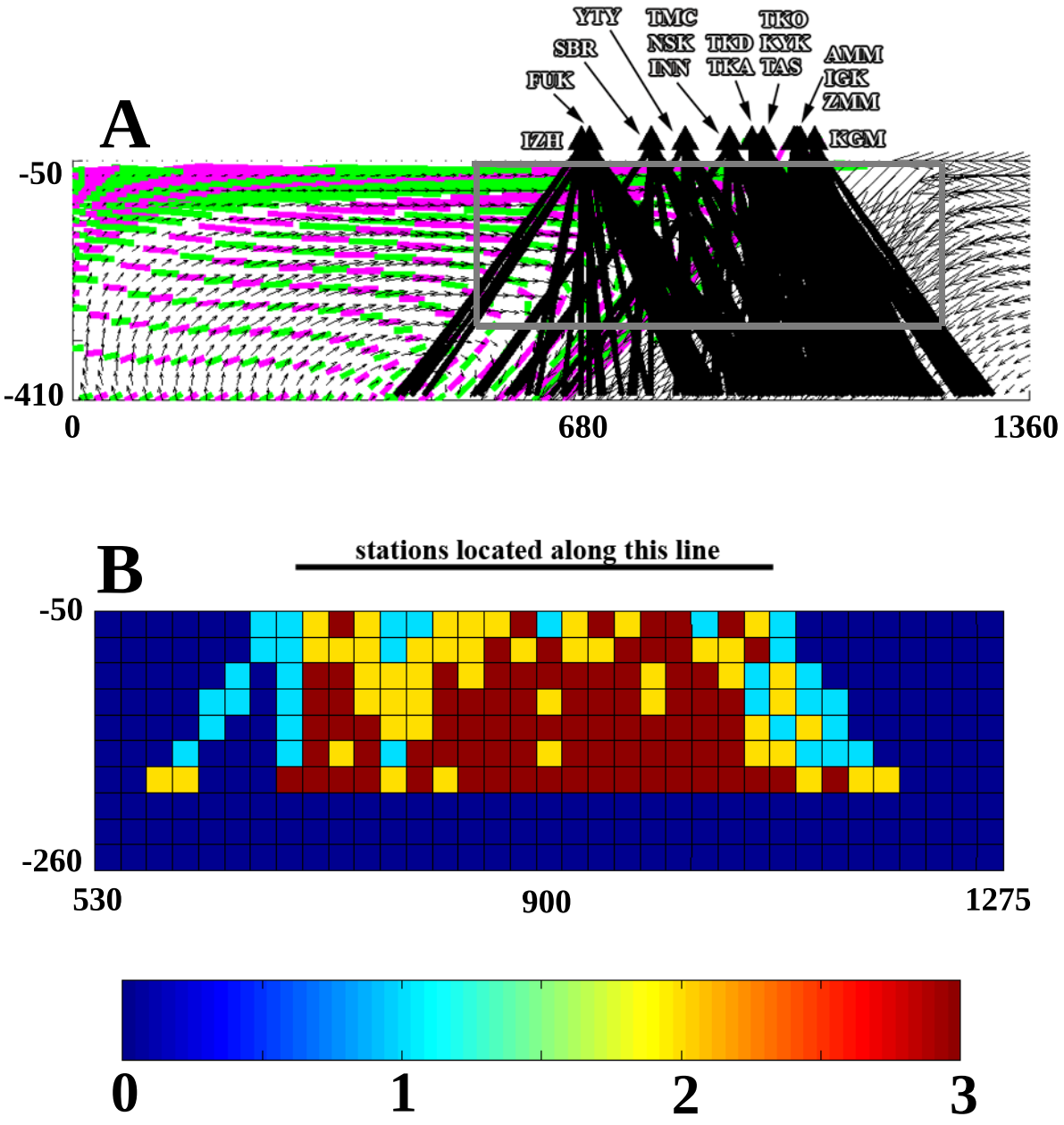
A
YTY
TMC
TKO
SBR
NSK
TKD
KYK
AMM
FUK
INN
TKA
TAS
IGK
ZMM
IZH
KGM
-50
-410
0
680
1360
B
stations located along this line
-50
-260
530
900
1275
0
1
2
3

Figure 10

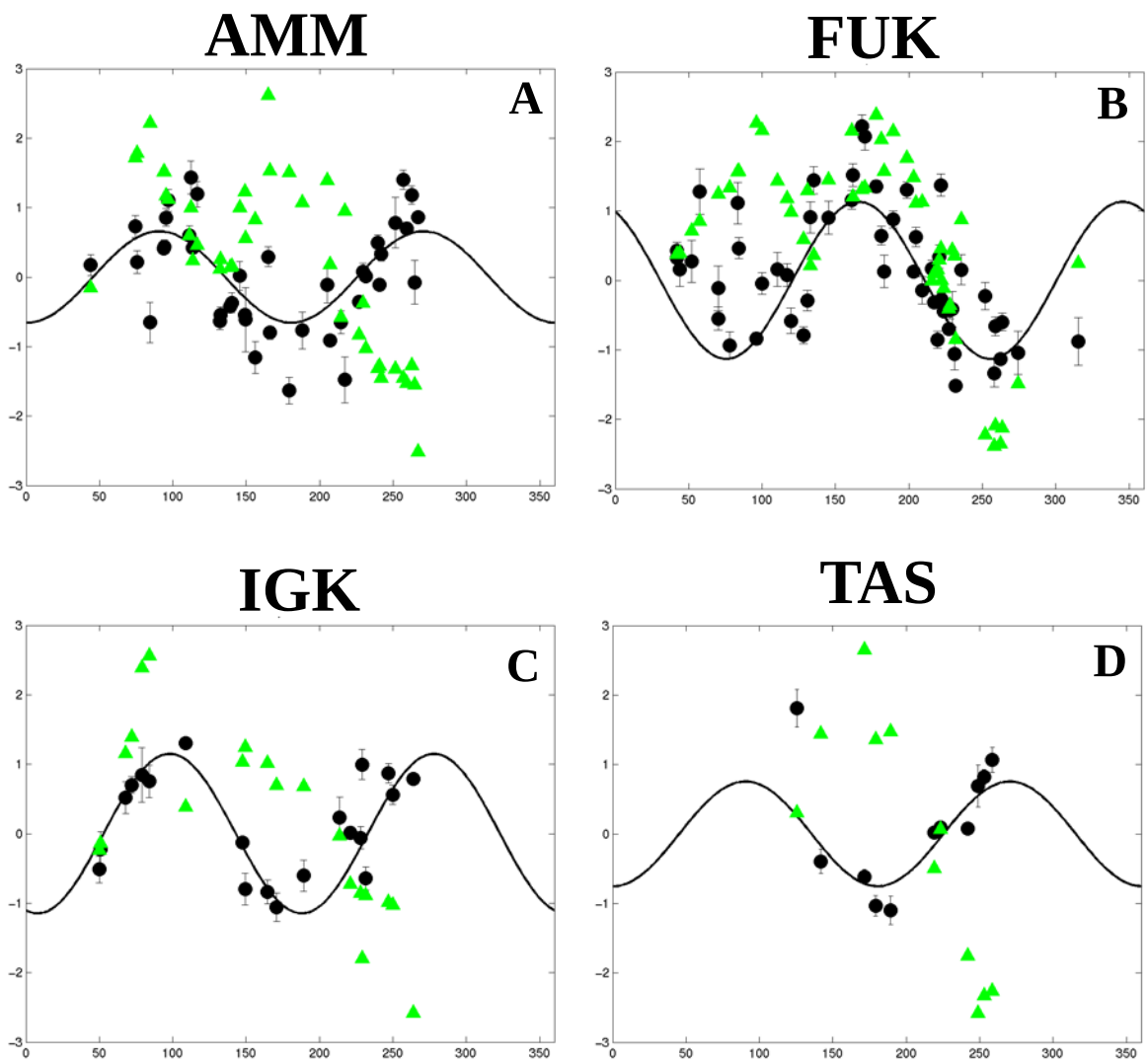

MODEL A

Figure 11

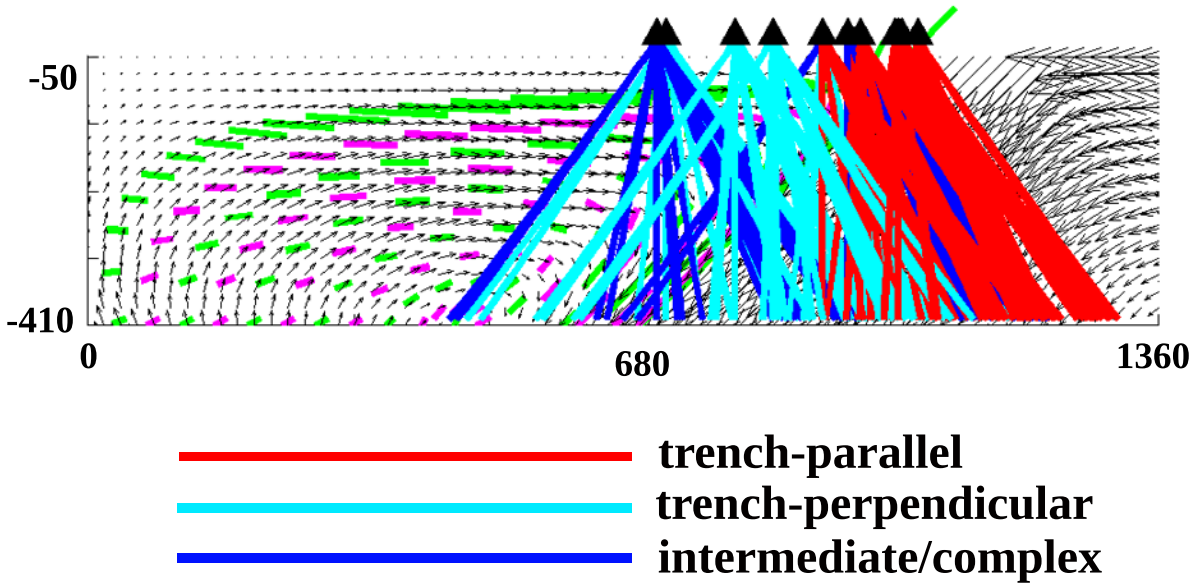
-50
-410
0
680
1360
trench-parallel
trench-perpendicular
intermediate/complex

Figure 12

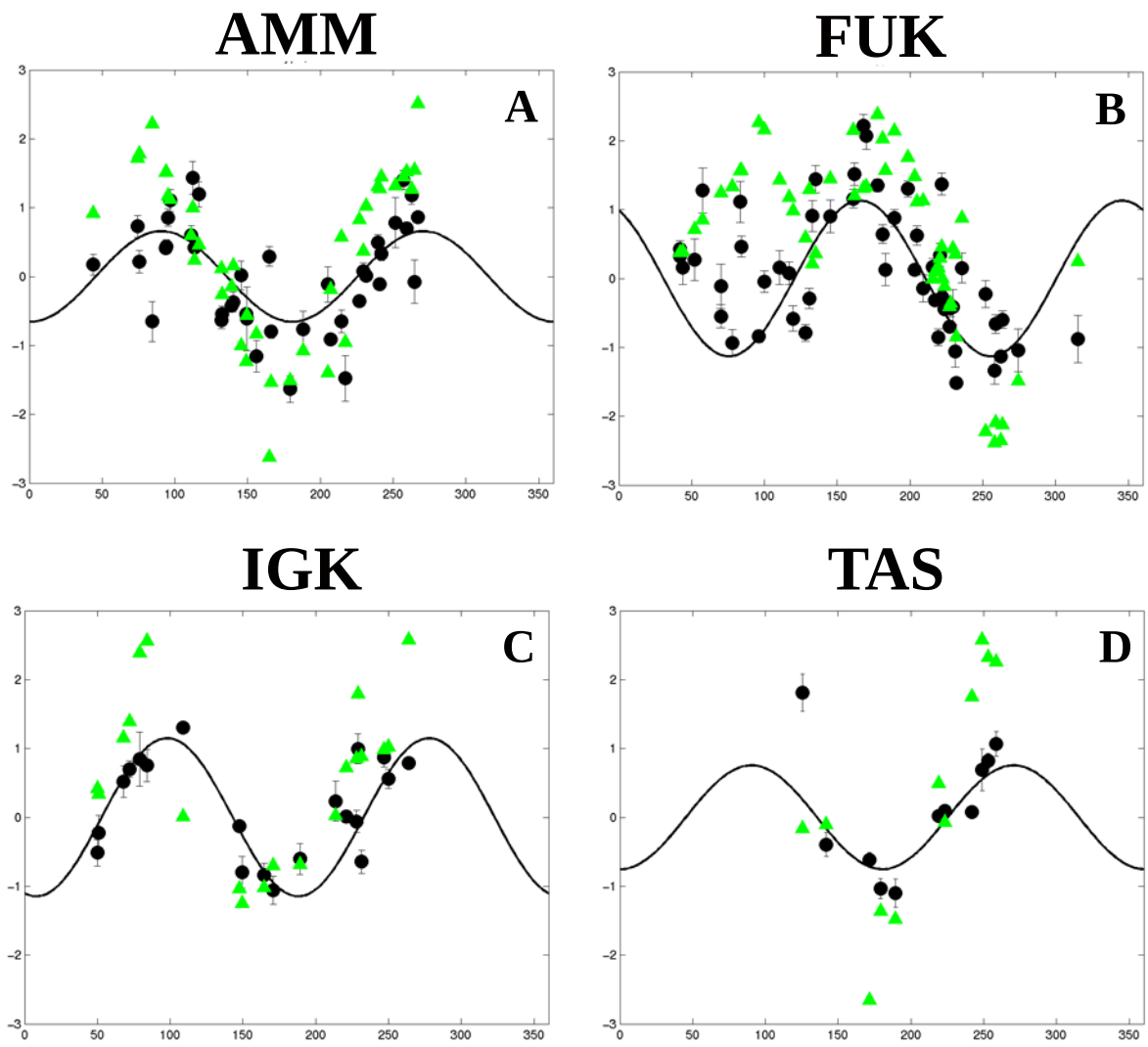

MODEL A,
w/ B-type fabric

Figure 13

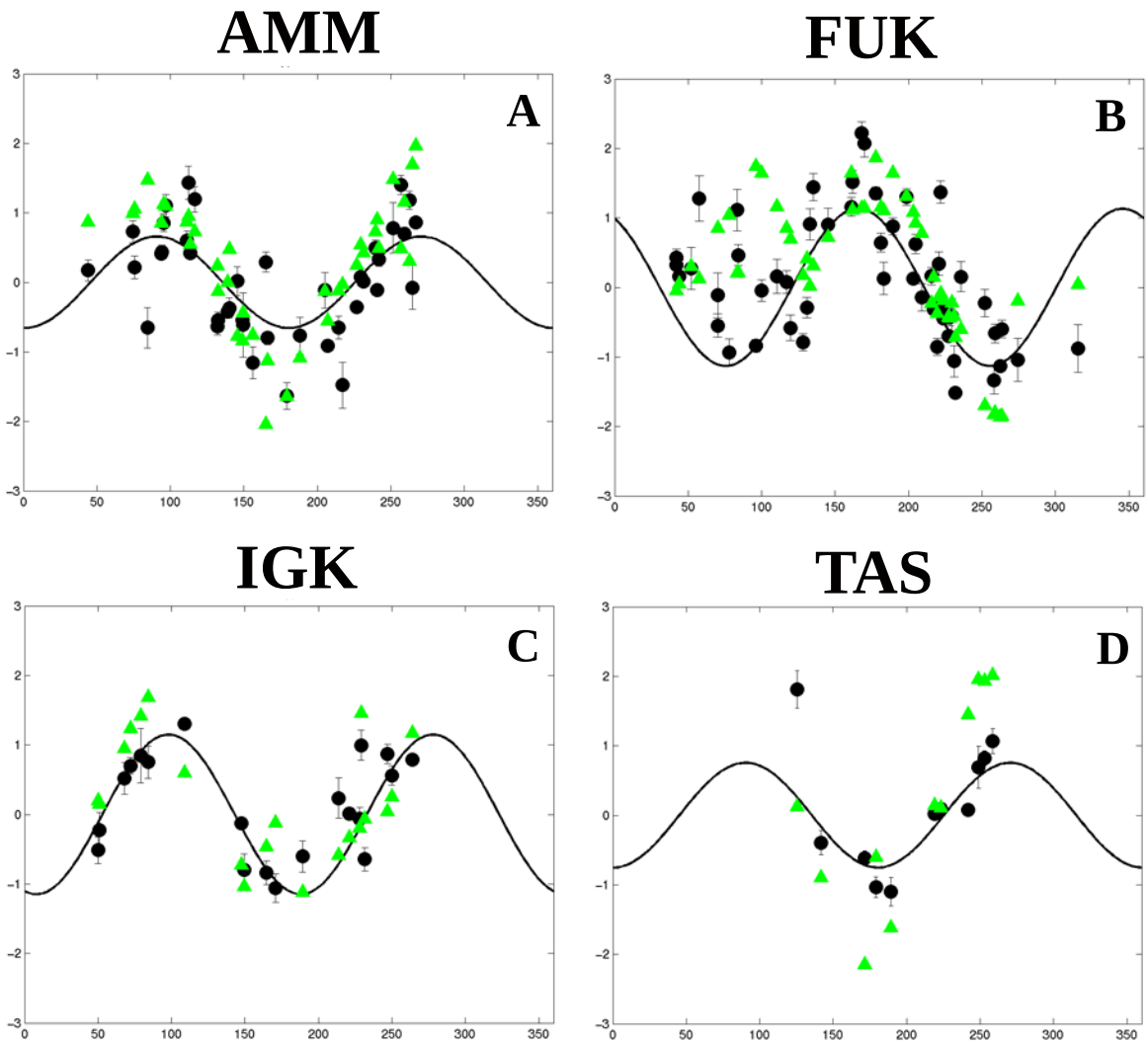

MODEL E,
w/ B-type fabric

Figure 14

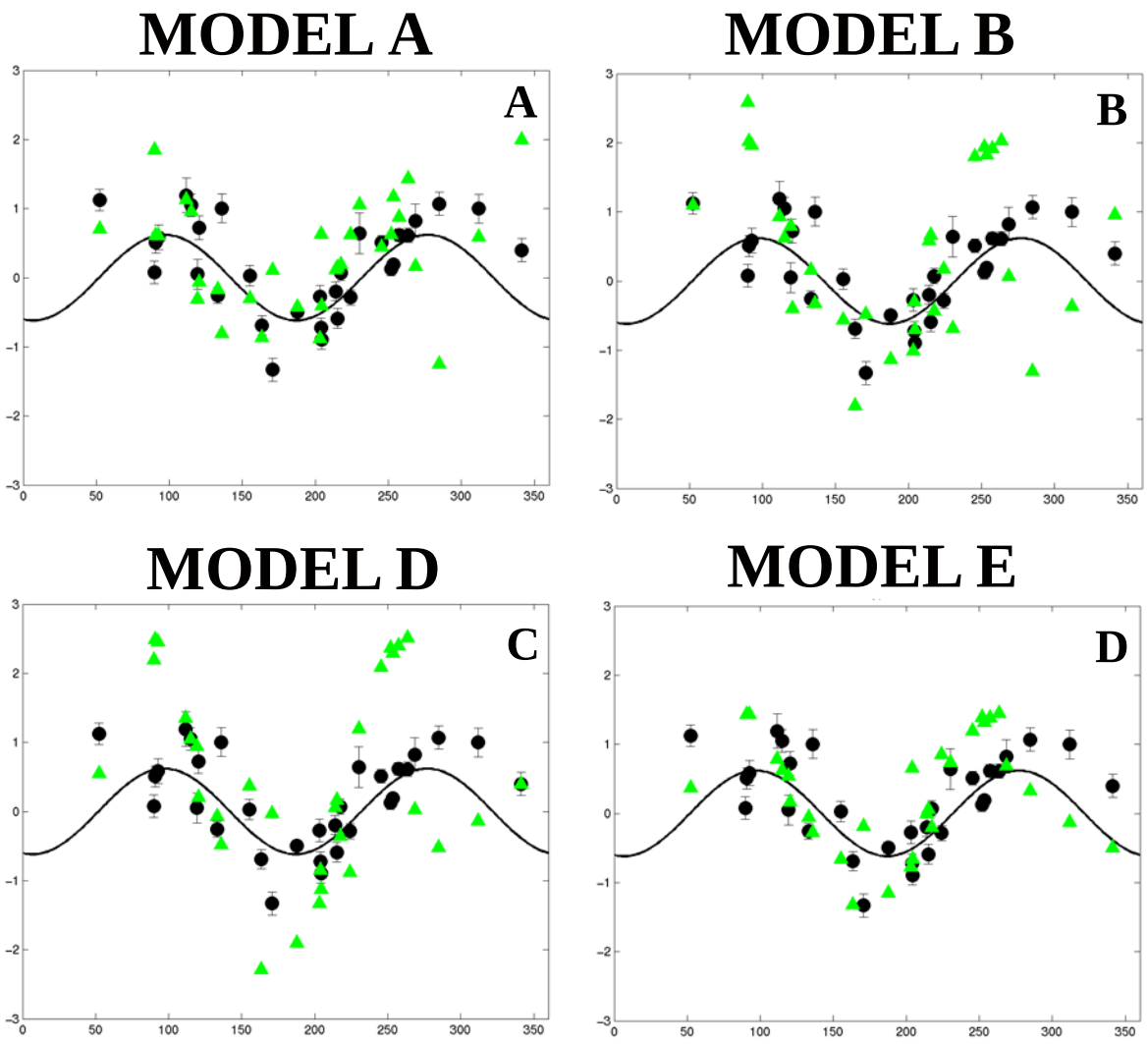

STATION TKA,
Models A,B,D,E
w/ B-type fabric

Figure 15

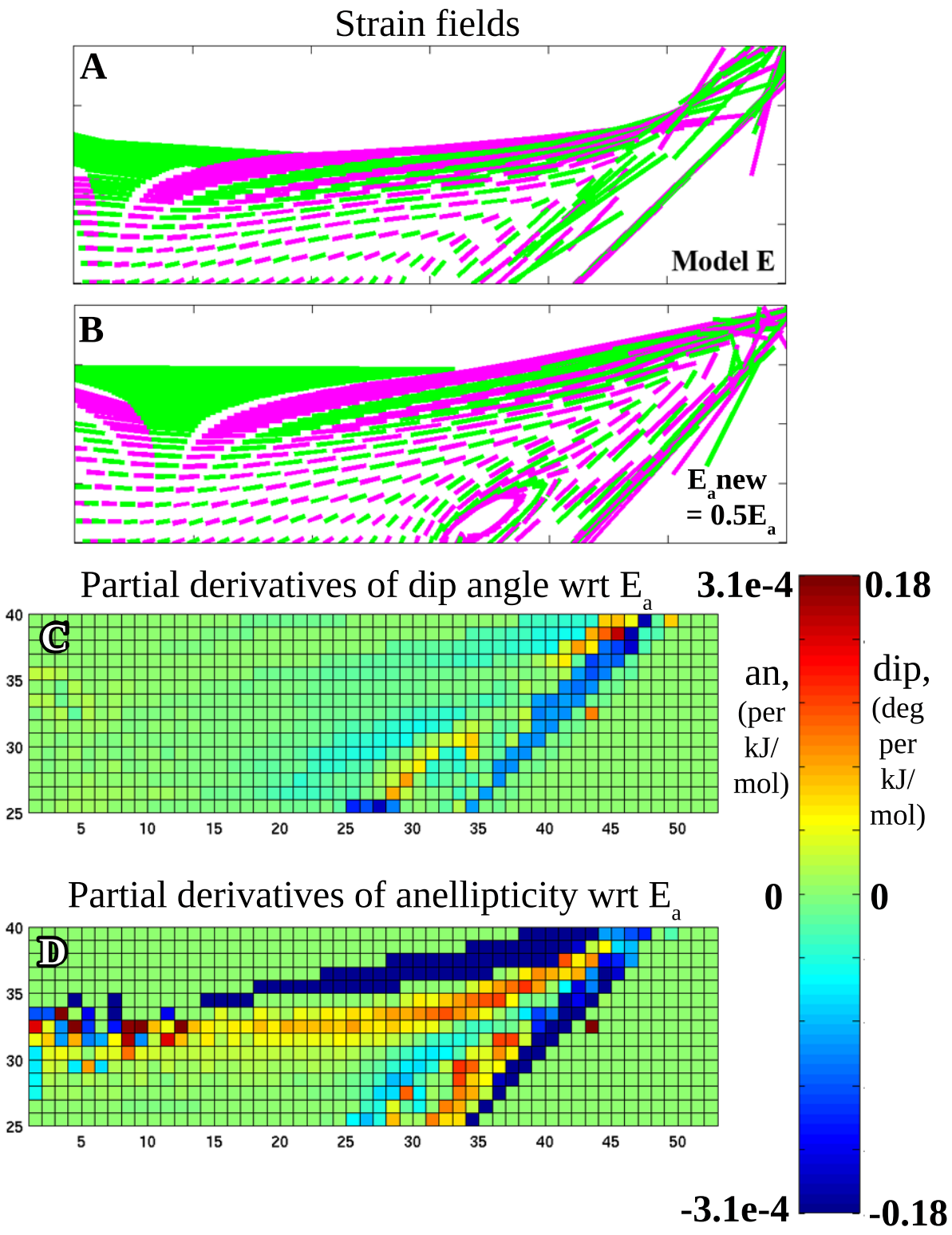
Strain fields
A
Model E
B
E_a new
= 0.5E_a
Partial derivatives of dip angle wrt E_a
C
Partial derivatives of anellipticity wrt E_a
D
3.1e-4
0.18
an, (per kJ/ mol)
dip, (deg per kJ/ mol)
0
0
-3.1e-4
-0.18

Figure 16

Chapter 5

Inversion of shear wave splitting intensities for anisotropic structure[1]

Abstract

We develop a theoretical framework for the tomographic inversion of shear wave splitting intensities and apply this framework to a set of previously published teleseismic splitting measurements at stations located in southwestern Japan. We use a 2.5-D geometrical setup in which the anisotropic model is invariant in one horizontal direction. This type of geometry is appropriate for modeling upper mantle anisotropy associated with a subducting lithospheric slab if the trench-slab system is approximately 2-D. We use the Born approximation for anisotropic elastic media under the assumption of weak anisotropy to derive expressions for finite-frequency sensitivity kernels for two anisotropic parameters: the dip θ_0 of the symmetry axis with respect to the horizontal plane, and the anellipticity parameter ε_A. Sensitivities for each parameter are calculated with respect to a starting model for anisotropy beneath the Ryukyu arc obtained from a 2-D numerical flow modeling study. The observed splitting intensities are then inverted for an updated anisotropic model using the LSQR implementation of the conjugate gradient method. In this paper we compute examples of sensitivity kernels corresponding to splitting observations from the southwestern Japan data set, present a very preliminary

[1] In preparation as: Long, M. D., de Hoop, M. V., van der Hilst, R. D., Hager, B. H., 2006b. Inversion of shear wave splitting intensities for anisotropic structure and coupling with numerical flow models. To be submitted to J. Geophys. Res.

inversion result for anisotropic structure beneath the Ryukyu arc, and discuss strategies for integrating constraints obtained from the inversion with geodynamical models of subduction-induced flow in the mantle wedge.

1. Introduction

Since the pioneering work of Hess (1964), measurements of seismic anisotropy in the upper mantle have provided us with information on the geometry of deformation and flow patterns associated with tectonic processes. Seismic anisotropy in the upper mantle is generally understood to arise when an aggregate of mantle rock, composed of intrinsically anisotropic crystals of (mainly) olivine, is subjected to strain and develops a lattice preferred orientation (LPO) (e.g. Christensen, 1984; Zhang and Karato, 1995). Because of this link between deformation and the resulting anisotropy, measurements of anisotropy provide a very important tool for probing the geometry of deformation and flow in the upper mantle and other regions of the Earth's interior. One unambiguous indicator of anisotropy is the splitting or birefringence of shear waves that traverse the upper mantle. Early studies of shear wave splitting by, among others, Kosarev et al. (1979), Ando et al. (1984), and Fukao (1984) established the promise of this method, and it is now commonly used and to detect and interpret upper mantle anisotropy (see Silver, 1996, and Savage, 1999, for reviews).

Shear wave splitting measurements have been made in a variety of tectonic settings, but the interpretation of splitting in the context of a subduction zone is particularly challenging (e.g. Park and Levin, 2002; Wiens and Smith, 2003). Many first-order aspects of the structure, dynamics, and flow patterns in subduction zones are poorly

understood (e.g. Stern, 2002), and the measurement and interpretation of shear wave splitting can potentially illuminate many of these phenomena. However, splitting datasets in subduction zone regions are often sparse, the measurements lack depth resolution because of their near-vertical paths through the upper mantle, and their interpretation in terms of anisotropic structure is non-unique. Many studies have found evidence for anisotropy associated with subduction zone deformation (e.g. Fouch and Fischer, 1996; Fischer et al., 1998; Smith et al., 2001; Currie et al., 2004; Anderson et al., 2004; Pozgay et al., 2006), but the signals are often complicated. For example, Long and van der Hilst (2005b, 2006) measured splitting at Japanese stations and found complicated splitting patterns that are consistent with complex anisotropy beneath the array. In part because of such complexity, the interpretation of these measurements remains difficult and controversial. An additional complication arises when the possible presence of B-type olivine fabric that has been observed in the laboratory (Jung and Karato, 2001) and in mantle-derived rocks (Mizukami et al., 2004; Skemer et al., 2006) is considered. In regions dominated by the B-type fabric regime, the fast axis is oriented ~ 90° from the prevailing flow direction. B-type fabric has been invoked to explain trench-parallel splitting in subduction zone settings (Karato, 2003; Lassak et al., 2006), and Long and van der Hilst (2006) argued that the most likely model for anisotropy beneath southwestern Japan takes the form of corner flow with B-type fabric dominating a region of the mantle wedge extending ~ 150 km from the trench.

One promising approach is to compare the observed splitting patterns with predictions from numerical models of flow induced in the upper mantle due to the subducting lithospheric slab. In a companion paper (Long et al., 2006a; hereinafter Paper

I), we assessed a suite of two-dimensional models describing the subduction of the Philippine Sea plate beneath southwestern Japan and compared the splitting predicted from those models to the observations of Long and van der Hilst (2005b, 2006). The predictions are generally consistent with the observed splitting, although this forward modeling approach is not able to reproduce the detailed features of the observed splitting patterns. An alternative approach involves the formal inversion of splitting parameters. Here we use the best forward model from Paper I as a starting model to develop and apply a framework for inverting measured shear wave splitting intensities for anisotropic structure in the upper mantle beneath southwestern Japan.

Tomographic inversion of shear wave splitting measurements is not often attempted. First, there is the difficulty in assembling datasets with sufficient ray coverage. Seismic arrays with dense spatial coverage are required in order to obtain good ray coverage in the upper mantle, and permanent instruments or long deployment times are generally needed to obtain sufficient measurements over a range of backazimuths and incidence angles. It should be noted that many regions are not favorably located with respect to global seismicity; in such regions, it is difficult or impossible to obtain a diverse set of measurements. Second, even for dense, long-running, favorably located arrays, the problem of inverting for laterally varying general anisotropy, everywhere described by 21 independent elastic parameters, is vastly non-unique and under-determined (e.g. Foss et al., 2005). A few previous studies have addressed the problem of inverting shear wave splitting measurements for anisotropic structure. In an exploration seismology setting, for example, several workers have used splitting data from vertical seismic profile (VSP) experiments to invert for anisotropy (e.g. Esmersoy, 1990;

MacBeth, 1991). Other studies of anisotropy for exploration-scale problems (Zheng, 2004; Yang et al., 2005) have inverted shear wave polarization and delay time data for anisotropic parameters, but in these models the anisotropic parameters were not allowed to vary laterally. A similar approach to determining anisotropic parameters for continental lithosphere was taken by Šílený and Plomerová (1996), using both shear wave splitting parameters and *P* wave travel time residuals. Ryberg et al. (2005) inverted shear wave splitting measurements for a single *SKS* arrival across a dense seismic array using a coarse block model and a parameter space search approach.

We aim to overcome the challenges inherent in an anisotropic inversion scheme in two ways. First, we take advantage of a permanent, dense broadband seismic array (the Japanese F-net array, see Long and van der Hilst, 2005b) that allows us to construct a high-quality set of shear wave splitting measurements with good ray coverage in the upper mantle. Second, we use numerical flow modeling (Paper I) to obtain a physically-based 2-D starting model that best fits the splitting observations. The integration of seismic imaging and flow modeling - through the overlaying of the tomographic resolution operator with the flow modeling solution - allows us to identify models that are both consistent with the splitting data and physically plausible. Additionally, it allows us to make inferences about the likely geometry of anisotropy even in areas where the ray coverage is poor; we can use the constraints obtained from the inversion in regions with good resolution as input into an updated flow model and therefore interpolate/extrapolate across regions of the model with poor resolution.

The research described here has four specific goals. First, we develop a theoretical framework for the inversion of teleseismic shear wave splitting intensities. The

development of this inversion framework uses the Born approximation and anisotropic ray perturbation theory (e.g. Farra 1989, 2001; Jech & Pšenčík 1989) to derive finite-frequency sensitivity kernels for the splitting intensity, a metric developed by Chevrot (2000). Second, we apply this inversion framework to a subset of the teleseismic shear wave splitting dataset of Long and van der Hilst (2005b) to obtain a model of upper mantle anisotropy beneath southwestern Japan. Third, we describe a strategy for coupling the results of the tomographic inversion with numerical models of subduction-related upper mantle deformation. The fourth, long-term goal of this work is to interpret our coupled tomographic imaging and flow modeling results in terms of mantle flow and tectonic processes associated with the subduction of the Philippine Sea plate beneath Eurasia at the Ryukyu arc. In this paper, we focus on the theoretical development and computation strategies for splitting intensity sensitivity kernels, the discretization and parameterization scheme, and the inversion strategy and resolution considerations. We also present an initial inversion result for upper mantle structure beneath southwestern Japan, but at this stage the results of the inversion implementation must be considered very preliminary.

2. Theory: shear wave splitting intensity kernels in 2.5-D

The aim of our study is the inversion of teleseismic shear wave splitting observations measured at broadband stations in southwestern Japan. In this section, we develop the theory that describes the splitting intensity sensitivity kernels for this application. A list of symbols and notation used in the derivation can be found in Appendix A. The development of the splitting kernels is similar to that in Favier and

Chevrot (2003) and Chevrot et al. (2004), but we use different assumptions about the geometry of the anisotropic medium and a different set of parameters to describe the anisotropy. A detailed comparison of our formulation with the kernels developed by Favier and Chevrot (2003) is contained in Appendix B. Our treatment also makes use of the framework for 2.5-D parameter inversion in anisotropic media developed by Foss et al. (2005). A sketch of the geometry of the problem is shown in Figure 1.

The coordinate system is chosen so that the model geometry does not vary in the x_2 direction. We associate the direction of initial polarization of the incoming shear wave with the radial displacement u^R; that is, we assume that the shear wave is initially polarized in the (q)SV direction and that all the energy recorded on the transverse component arises from the anisotropic perturbation to the elastic constants $\delta\boldsymbol{c}$. We invoke four additional assumptions in our derivation of the splitting kernel. First, we assume that the problem is described by a 2.5-D approximation and that (x_1,x_3) are the coordinates of the symmetry plane. Second, we assume weak anisotropy, as defined by Thomsen (1986). Third, we assume that the split time δt is much less than the characteristic period T_0 of the data; for our splitting dataset ($T_0 \approx$ 8-12 sec) and typical split times for upper mantle anisotropy (~ 2 sec, e.g. Savage, 1999) this should be a robust assumption. Fourth, we assume that some degree of anisotropy exists everywhere in the model region; we do not treat the case of degenerate quasi-*S* polarizations.

2.1 Perturbation in 2.5-D and the weak anisotropy approximation

2.1.1 The unperturbed field: Green's functions

The geometrical ray approximation (GRA) to the Green's functions is a causal, short-period approximate solution, G_{in}, to the elastic wave equation, in the frequency domain given by

$$\rho(\mathbf{x})\omega^2 G_{in} + \partial_j (c_{ijkl}(\mathbf{x})\partial_l G_{kn}) = -\delta_{in}\delta(\mathbf{x}-\mathbf{x}^s),\ i,j,k,l,n = 1,2,3, \tag{1}$$

where ω is angular frequency and the position vector is denoted by $\mathbf{x} = (x_1, x_2, x_3)$; $\rho(\mathbf{x})$ and $c_{ijkl}(\mathbf{x})$ are the density and stiffness tensor, respectively; both are smooth functions of $\mathbf{x}$. The Kronecker delta, δ_{in}, generates the force in the canonical directions (n=1,2,3), operative at the source at position $\mathbf{x}^s$, through the delta function δ. The Green's function is a sum over the different wave modes, where each term is of the form

$$G_{ip}(\mathbf{x},\omega,\mathbf{x}^s) = A(\mathbf{x},\mathbf{x}^s)h_i^s(\mathbf{x})h_p(\mathbf{x}^s)\exp[\mathrm{i}\omega T(\mathbf{x},\mathbf{x}^s)], \tag{2}$$

in which $T(\mathbf{x}, \mathbf{x}^s)$ is the travel time along the ray connecting $\mathbf{x}$ with $\mathbf{x}^s$. (We do not explicitly indicate the mode of propagation; we treat the modes of propagation separately.) In (2), h_i^s and h_p are components of the unit polarization vectors, where the superscript s indicates explicitly that this polarization vector is associated with the ray originating at $\mathbf{x}^s$. $A(\mathbf{x},\mathbf{x}^s)$ is the amplitude, which becomes complex in the presence of caustics, and which can be written in the form (Červený, 2001)

$$A(\mathbf{x},\mathbf{x}^s) = \frac{\exp[-\mathrm{i}\frac{\pi}{2}\kappa(\mathbf{x},\mathbf{x}^s)\operatorname{sgn}\omega]}{4\pi[\rho(\mathbf{x})v^s(\mathbf{x})\rho(\mathbf{x}^s)v(\mathbf{x}^s)]^{1/2}\,|\det\mathbf{Q}_2(\mathbf{x},\mathbf{x}^s)|^{1/2}}. \tag{3}$$

Here, $v^s(\mathbf{x})$ and $v(\mathbf{x}^s)$ are the phase velocities at $\mathbf{x}$ and $\mathbf{x}^s$, respectively, evaluated in the direction of the slowness vectors associated with the ray connecting these points. The relative geometrical spreading, $|\det\mathbf{Q}_2(\mathbf{x},\mathbf{x}^s)|^{1/2}$, is given by

$$[Q_2]^{-1}_{ij}(\mathbf{x},\mathbf{x}^s) = -\frac{\partial^2 T(\mathbf{x},\mathbf{x}^s)}{\partial q_i^s \partial q_j}, \; i,j = 1,2, \tag{4}$$

where q_j and q_i^s are local phase-related coordinates in the plane normal to the slowness vectors at $\mathbf{x}^s$ and $\mathbf{x}$, respectively; $\kappa(\mathbf{x},\mathbf{x}^s)$ is the KMAH index and counts the caustics that the ray encounters between $\mathbf{x}^s$ and $\mathbf{x}$.

Due to the symmetry arising in the 2.5-D approximation, we may choose one of the wave front coordinates, (q_1,q_2), to coincide with the out-of-plane direction: we choose $q_2 = x_2$. The first wave front coordinate, q_1, is chosen in-plane (i.e., $q_1=x_1$). Thus, in the 2.5-D reduction, $\frac{\partial T(\mathbf{x},\mathbf{x}^s)}{\partial q_1^s}$ and $\frac{\partial T(\mathbf{x},\mathbf{x}^s)}{\partial q_1}$ are even functions in x_2, so that $\frac{\partial^2 T(\mathbf{x},\mathbf{x}^s)}{\partial q_1^s \partial x_2} = \frac{\partial^2 T(\mathbf{x},\mathbf{x}^s)}{\partial x_2^s \partial q_1} = 0.$ In these wave front coordinates, the relative geometrical spreading matrix in equation (4) becomes a diagonal matrix,

$$\mathbf{Q}_2(\mathbf{x},\mathbf{x}^s) = \begin{bmatrix} \dfrac{1}{\dfrac{\partial^2 T(\mathbf{x},\mathbf{x}^s)}{\partial q_1^s \partial q_1}} & 0 \\ 0 & \dfrac{1}{\dfrac{\partial p_2}{\partial x_2}} \end{bmatrix} = \begin{bmatrix} Q_2^{\parallel}(\mathbf{x},\mathbf{x}^s) & 0 \\ 0 & Q_2^{\perp}(\mathbf{x},\mathbf{x}^s) \end{bmatrix}, \tag{5}$$

where $Q_2^{\parallel}(\mathbf{x}, \mathbf{x}^s)$ and $Q_2^{\perp}(\mathbf{x}, \mathbf{x}^s)$ are the in-plane and out-of-plane relative geometrical spreading factors, respectively, and p_2 is the second component of the slowness vector $\mathbf{p}$. This structure implies that the relative geometrical spreading in equation (3) factors into an in-plane and out-of-plane component,

$$|\det \mathbf{Q}_2(\mathbf{x},\mathbf{x}^s)|^{1/2} = |Q_2^{\parallel}(\mathbf{x},\mathbf{x}^s) Q_2^{\perp}(\mathbf{x},\mathbf{x}^s)|^{1/2}. \tag{6}$$

The out-of-plane geometrical spreading $Q_2^{\perp}$ can be expressed as

$$Q_2^{\perp}(\mathbf{x},\mathbf{x}^s) = \frac{x_2}{p_2} = \int_{\mathbf{ray}} \frac{V_2}{p_2}\,\mathrm{d}t\,, \tag{7}$$

where V_2 is the second component of the group velocity **V**, and the integral is along the ray parameterized by the travel time t connecting **x** with $\mathbf{x}^s$. The integrand V_2/p_2 remains finite when both V_2 and p_2 tend to zero (in accordance with the 2.5-D approach, where $p_2 = 0$, $V_2 = 0$). Closed-form expressions for the integrand for transversely isotropic media can be found in Ettrich et al. (2002), equation (19).

Furthermore, we introduce the amplitude, $A^{\parallel}(\mathbf{x},\mathbf{x}^s)$, expressed in terms of the in-plane geometrical spreading only,

$$A^{\parallel}(\mathbf{x},\mathbf{x}^s) = \frac{\exp[-\mathrm{i}\frac{\pi}{2}\kappa(\mathbf{x},\mathbf{x}^s)\operatorname{sgn}\omega]}{4\pi[\rho(\mathbf{x})v^s(\mathbf{x})\rho(\mathbf{x}^s)v(\mathbf{x}^s)]^{1/2}\,|\,Q_2^{\parallel}(\mathbf{x},\mathbf{x}^s)\,|^{1/2}}\,. \tag{8}$$

The incident wave asymptotic representation reads

$$u_0(\mathbf{x}^r,\omega,\mathbf{x}^s) = -W^s(\omega)h_i^s(\mathbf{x}^r)p_r^s(\mathbf{x}^s)M_{rp}(\mathbf{x}^s)G_{ip}(\mathbf{x}^r,\omega,\mathbf{x}^s) \tag{9}$$

if the equivalent body force is given by

$$f_j(\mathbf{x},t) = -M_{ij}(\mathbf{x}^s)\partial_t\delta(\mathbf{x}-\mathbf{x}^s)H(t-t^s), \quad t^s := 0, \tag{10}$$

consistent with the far field approximation, and subject to the replacement of $\partial_t H(t)$ by $W^s(t)$. Here, M_{ij} is the moment tensor. Consistent with the 2.5-D approximation ($p_2 = 0$), the 2-component f_2 disappears from the analysis. In our application, we restrict the unperturbed polarizations (h_i^s) to quasi-SV (qSV) components.

2.1.2 The Born approximation

We invoke the *single-scattering* or *Born approximation* in which the scattered wavefield is thought of as the combination of a background wavefield (associated with a

smooth background elastic medium) and a scattered wavefield associated with a linear perturbation to the background medium (Cohen and Bleistein, 1977; Bleistein and Cohen, 1979). The 2.5-D Born modeling formula is derived from the 3-D Born formula by a stationary phase argument integrating over the out-of-plane coordinate (x_2). From now on, we let $\mathbf{x} = (x_1, x_3)$. The stationary phase argument involves the stationarity condition

$$\partial_{x_2}(T(\mathbf{x}^s, \mathbf{x}) + T(\mathbf{x}, \mathbf{x}^r)) = p_2^s + p_2^r = 0, \tag{11}$$

where $\mathbf{p}^s = (p_1^s, p_2^s, p_3^s)$ and $\mathbf{p}^r = (p_1^r, p_2^r, p_3^r)$ are the slowness vectors associated with the source and receiver ray, respectively. We consider in-plane scattering only, when $p_2^s = p_2^r = 0$; for shear waves this is an additional assumption.

The medium parameters are represented by a sum of a smooth background, ρ and c_{ijkl}, and a smooth perturbation, δc_{ijkl}. The perturbations extend cylindrically out of the x_1-x_3 symmetry plane (Figure 1).

We write u_{mn}, that is, the m^{th} component of the perturbed wave field due to a body force in the n-direction, as

$$\begin{aligned} u_{mn}(\mathbf{x}^s, \mathbf{x}^r, t) \approx \sum_{i \in I} \sqrt{\frac{i}{2\pi}} \int\int_{\mathbf{R}} h_m^r(\mathbf{x}^r) \omega^{3/2} \rho(\mathbf{x}) \frac{A^{\parallel}(\mathbf{x}^s, \mathbf{x}) A^{\parallel}(\mathbf{x}, \mathbf{x}^r)}{\mathcal{L}^{\perp}(\mathbf{x}^r, \mathbf{x}, \mathbf{x}^s)} \\ \cdot \mathbf{w}^T(\mathbf{x}^r, \mathbf{x}, \mathbf{x}^s) \delta \mathbf{c}(\mathbf{x}) \exp[\mathrm{i}\omega(T^{(i)}(\mathbf{x}^r, \mathbf{x}, \mathbf{x}^s) - t)] h_n^s(\mathbf{x}^s) \, \mathrm{d}\omega \, \mathrm{d}x. \end{aligned} \tag{12}$$

Here, $T^{(i)}$ is the refracted travel time given by

$$T^{(i)}(\mathbf{x}^r, \mathbf{x}, \mathbf{x}^s) = T(\mathbf{x}^s, \mathbf{x}) + T(\mathbf{x}, \mathbf{x}^r). \tag{13}$$

(NB the superscript (i) on $T^{(i)}$ is needed when the refracted travel time is multivalued due to caustics. In that case i labels the branches. Hereinafter, the sum over the different travel time branches will be suppressed and assumed implicit.) We note that although we restrict the unperturbed polarization to SV only, we consider contributions to the

scattered field from both SV and SH; therefore, we sum the perturbation described in equation (12) over both polarizations.

The refracted out-of-plane geometrical spreading is given by

$$\mathcal{L}^{\perp}(\mathbf{x}^{\mathrm{r}}, \mathbf{x}, \mathbf{x}^{\mathrm{s}}) = | Q_2^{\perp}(\mathbf{x}^s,\mathbf{x}) + Q_2^{\perp}(\mathbf{x},\mathbf{x}^r)|^{1/2}. \tag{14}$$

The medium perturbations are collected in the matrix $\delta\mathbf{c}(\mathbf{x})$ and the radiation patterns in $\mathbf{w}(\mathbf{x}^r,\mathbf{x},\mathbf{x}^s)$. With the equivalent body force above,

$$\delta u(\mathbf{x}^r, \omega, \mathbf{x}^s) = -W^s(\omega) h_i^r(\mathbf{x}^r) p_r^s(\mathbf{x}^s) M_{rp}(\mathbf{x}^s) M_{rp}(\mathbf{x}^s) U_{ip}(\mathbf{x}^r, \omega, \mathbf{x}^s), \tag{15}$$

where U_{ip} is the Fourier transform of u_{ip}. In our application, the polarization (h_i^r) is either qSV or qSH.

In the 2.5-D approximation, with $p_2^s = p_2^r = 0$, the polarizations of qP and qSV waves satisfy $h_2 = 0$. The polarization of qSH is given by (0,1,0). We use superscript "*T*" for a component in the direction of qSH, and superscript "*R*" for a component in the direction of qSV.

2.1.3 Medium perturbations and radiation patterns

With (x_1, x_3) the plane of symmetry, the stiffness tensor is given by

$$[c_{ijkl}] = \begin{bmatrix} c_{1111} & c_{1122} & c_{1133} & 0 & c_{1113} & 0 \\ c_{1122} & c_{2222} & c_{2233} & 0 & c_{2213} & 0 \\ c_{1133} & c_{2233} & c_{3333} & 0 & c_{3313} & 0 \\ 0 & 0 & 0 & c_{2323} & 0 & c_{2312} \\ c_{1113} & c_{2213} & c_{3313} & 0 & c_{1313} & 0 \\ 0 & 0 & 0 & c_{1223} & 0 & c_{1212} \end{bmatrix}. \tag{16}$$

This representation allows transversely isotropic (TI) media tilted in the (x_1,x_3)-plane, as well as TI media with symmetry axes aligned with the x_2-axis.

The medium perturbations are collected in a 13 × 1 matrix:

$$\delta\mathbf{c}(\mathbf{x}) = \left\{ \frac{\delta c_{ijkl}(\mathbf{x})}{\rho(\mathbf{x})} \right\}. \tag{17}$$

We restrict the indices of δc_{ijkl} to the 13 independent components of the stiffness tensor (equation 16); this representation is similar to the parameters in Chapman and Pratt (1992). With higher symmetry, such as isotropy, the matrix reduces accordingly. The radiation pattern matrix is defined similarly as a 13 × 1 matrix (Burridge et al., 1998):

$$\mathbf{w}(\mathbf{x}^r, \mathbf{x}, \mathbf{x}^s) = \left\{ h_i^s(\mathbf{x}) p_j^s(\mathbf{x}) h_k^r(\mathbf{x}) p_l^r(\mathbf{x}) \right\}, \tag{18}$$

where the indices follow those of the stiffness matrix in the order defined by the matrix or inner product $\mathbf{w}^T(\mathbf{x}^r,\mathbf{x},\mathbf{x}^s)\delta\mathbf{c}(\mathbf{x})$ in equation (12). Since the out-of-plane slowness will be zero ($p_2^s = p_2^r = 0$), we see from equation (18) that the contribution vanishes if $j,l = 2$ in δc_{ijkl}; the sensitivity is therefore restricted to 7 independent parameters.

2.1.4 The weak anisotropy approximation

We apply a rotation to u to obtain, at $\mathbf{x}^r$, $u^R = u_0^R + \delta u^R$, that is, a projection of u onto the qSV polarization, and $u^T = u_0^T + \delta u^T$, that is, the projection of u onto the qSH polarization. Under the assumption of weak anisotropy (Thomsen 1986), all of the anisotropy is described by the contrast δc_{ijkl} and is hence accounted for by the Born approximation. This assumption implies that u_0^R represents the SV polarized wave in the isotropic background.

The elastic parameters are assumed to be supported, that is, defined (and finite), in a localized region right beneath the receivers (in our application, we assume that the anisotropy is located in the upper mantle above the 410 km discontinuity). The

teleseismic sources are far away from this region. Incident shear waves are selected to be SV polarized, and therefore $u_0^T \equiv 0$.

2.2 The cross-correlation splitting intensity criterion

The splitting detection criterion is derived from the cross-correlation criterion in wave-equation tomography (e.g. de Hoop and van der Hilst, 2005a). However, instead of comparing per event, at any given station, modeled data with observed data, one compares the ^{R} component with the ^{T} component of the observed trace. Hence, we consider $\partial_t \mathrm{C}(u^R, u^T)(t)$, where C(t) denotes the time-correlation function. C(t) is written (e.g. de Hoop and van der Hilst, 2005a)

$$C(t) = \int_{\mathbf{R}} u^R(t') u^T(t+t')\,\mathrm{d}t'. \tag{19}$$

Because $u_0^T \equiv 0$, up to leading order

$$\partial_t \mathrm{C}(u^R, u^T)(t) \cong \partial_t \mathrm{C}(u_0^R, \delta u^T)(t). \tag{20}$$

With δt the split time, let $\partial_t \mathrm{C}(u^R, u^T)(\delta t) = 0$. The assumption that $\delta t << T_0$, which is commonly invoked in studies of teleseismic shear wave splitting due to upper mantle anisotropy (e.g. Silver and Chan, 1988, 1991), allows us to define the simpler splitting intensity measure (Chevrot, 2000):

$$\mathrm{S} = -N_{s,r}^{-1} \partial_t \mathrm{C}(u^R, u^T)(0), \quad \mathrm{S} = \mathrm{S}[\delta \mathbf{c}](\mathbf{x}^s, \mathbf{x}^r). \tag{21}$$

Here,

$$N_{s,r} = \int |\,\partial_t u^R\,|^2\,\mathrm{d}t \approx \int \left|\partial_t u_0^R\right|^2 \mathrm{d}t \tag{22}$$

represents the normalized radial component energy. Again, in the perturbed transverse component we consider contributions from both the scattered SV and SH wave fields and therefore sum over the SV and SH polarizations. We now write

$$H\delta\mathbf{c} = -\partial_t \, \mathrm{C}(u_0^R, \delta u^T)(0), \tag{23}$$

with the operator H introduced below. The 'mismatch' criterion yields $\varepsilon = \frac{1}{2}\int\int |\, \mathrm{S} - N_{s,r}^{-1} H\delta\mathbf{c}\,|^2 \, \mathrm{d}\,\mathbf{x}^s \, \mathrm{d}\,\mathbf{x}^r$. Again, we assume that the splitting arises entirely from perturbation about the isotropic case. We write the image

$$N_{s,r}^{-1} H\delta\mathbf{c}(\mathbf{x}^s, \mathbf{x}^r) = \int \mathcal{K}(\mathbf{x}^s, \mathbf{x}^r; \mathbf{x}) \delta\mathbf{c}(\mathbf{x}) \, \mathrm{d}\,\mathbf{x} \,. \tag{24}$$

In (23), $\mathcal{K}$ is the sensitivity kernel, which we will derive below.

2.3 The sensitivity kernel

Assuming that there exists anisotropy everywhere in the model region (that is, there are no isotropic regions) allows us to refrain from treating the case of degenerate quasi-*S* polarizations. Substituting equation (12) into (23) and using Parseval, then we obtain

$$\begin{aligned} H\delta\mathbf{c}(\mathbf{x}^s, \mathbf{x}^r) &= \int \overline{\hat{u}_0^R} \, \mathrm{i}\,\omega \delta\hat{u}^T \, \mathrm{d}\,\omega \\ &= \int \left\{ \int \begin{array}{l} \mathrm{i}\,\omega^{5/2} \rho(\mathbf{x}) \dfrac{A^{\|}(\mathbf{x}^s, \mathbf{x}) A^{\|}(\mathbf{x}, \mathbf{x}^r)}{\mathcal{L}^{\perp}(\mathbf{x}^r, \mathbf{x}, \mathbf{x}^s)} \dfrac{\overline{A_0^{\|}(\mathbf{x}^r, \mathbf{x}^s)}}{|\, Q_{0;2}^{\perp}(\mathbf{x}^r, \mathbf{x}^s)\,|^{1/2}} \\ M_{rp}(\mathbf{x}^s) h_{0;p}^s(\mathbf{x}^s) p_{0;r}^s(\mathbf{x}^s) M_{r'p'}(\mathbf{x}^s) h_{p'}^s(\mathbf{x}^s) p_{r'}^s(\mathbf{x}^s) \,|\, W^s(\omega)\,|^2 \\ \exp[\mathrm{i}\,\omega(T(\mathbf{x}^r, \mathbf{x}, \mathbf{x}^s) - T_0(\mathbf{x}^r, \mathbf{x}^s))] \, \mathrm{d}\,\omega \mathbf{w}^T(\mathbf{x}^r, \mathbf{x}, \mathbf{x}^s) \end{array} \right\} \delta\mathbf{c}(\mathbf{x}) \, \mathrm{d}\,\mathbf{x}. \\ &= \int \mathcal{K}(\mathbf{x}^s, \mathbf{x}^r; \mathbf{x}) \delta\mathbf{c}(\mathbf{x}) \, \mathrm{d}\,\mathbf{x} \end{aligned} \tag{25}$$

To facilitate the computation of the kernel $\mathcal{K}$ we make two further approximations. When the source is far away from the support of the perturbation in elastic parameters $\delta\mathbf{c}$, the take-off directions of the perturbed and unperturbed rays are very close: that is,

$$p_r^s(\mathbf{x}^s) \approx p_{0;r}^s(\mathbf{x}^s), \quad h_p^s(\mathbf{x}^s) \approx h_{0;p}^s(\mathbf{x}^s). \tag{26}$$

For the (in-plane) relative geometrical spreading we can then write

$$\frac{1}{|Q_2^{\parallel}(\mathbf{x}^s,\mathbf{x})|^{1/2}|Q_2^{\parallel}(\mathbf{x},\mathbf{x}^r)|^{1/2}} \approx \frac{1}{|Q_2^{\parallel}(\mathbf{x}^r,\mathbf{x})|^{1/2}} \frac{1}{|Q_{0;2}^{\parallel}(\mathbf{x}^r,\mathbf{x}^s)|^{1/2}}, \tag{27}$$

while

$$\frac{1}{|Q_2^{\perp}(\mathbf{x}^s,\mathbf{x})+Q_2^{\perp}(\mathbf{x},\mathbf{x}^r)|^{1/2}} \approx \frac{1}{|Q_2^{\perp}(\mathbf{x}^s,\mathbf{x})|^{1/2}} \approx \frac{1}{|Q_{0;2}^{\perp}(\mathbf{x}^r,\mathbf{x}^s)|^{1/2}}. \tag{28}$$

Furthermore, if the distance from the source to the image point is much greater than the distance from the image point to the receiver, that is, $|\mathbf{x} - \mathbf{x}^s| >> |\mathbf{x}^r - \mathbf{x}|$, we can suppress the occurrence of caustics near the receiver to obtain

$$\frac{A^{\parallel}(\mathbf{x}^s,\mathbf{x})A^{\parallel}(\mathbf{x},\mathbf{x}^r)}{\mathcal{L}^{\perp}(\mathbf{x}^r,\mathbf{x},\mathbf{x}^s)} \approx A^{\parallel}(\mathbf{x}^r,\mathbf{x}) \frac{[\rho(\mathbf{x}^r)v^s(\mathbf{x}^r)]^{1/2}}{[\rho(\mathbf{x})v^s(\mathbf{x})]^{1/2}} \frac{A_0^{\parallel}(\mathbf{x}^r,\mathbf{x}^s)}{|Q_{0;2}^{\perp}(\mathbf{x}^r,\mathbf{x}^s)|^{1/2}}. \tag{29}$$

The energy factor is given by the inner product

$$\begin{aligned} N_{s,r} &= \int \overline{\hat{u}_0^R}\,\omega^2 \hat{u}_0^R \,\mathrm{d}\omega \approx \frac{|A_0^{\parallel}(\mathbf{x}^r,\mathbf{x}^s)|^2}{|Q_{0;2}^{\perp}(\mathbf{x}^r,\mathbf{x}^s)|} \\ &[M_{rp}(\mathbf{x}^s)h_{0;p}^s(\mathbf{x}^s)p_{0;r}^s(\mathbf{x}^s)]^2 \int \omega^2 |W^s(\omega)|^2 \,\mathrm{d}\omega. \end{aligned} \tag{30}$$

With these approximations, we can now proceed to write the expression for $\mathcal{K}$. The gradient of ε yields the image $\int \mathcal{K}(\mathbf{x}^s,\mathbf{x}^r;\mathbf{x})\,\mathrm{S}(\mathbf{x}^s,\mathbf{x}^r)\,\mathrm{d}\mathbf{x}^s\,\mathrm{d}\mathbf{x}^r$, with sensitivity kernel

$$\begin{aligned} \mathcal{K}(\mathbf{x}^s,\mathbf{x}^r;\mathbf{x}) \approx &\left[\int \omega^2 |W^s(\omega)|^2 \,\mathrm{d}\omega\right]^{-1} \sqrt{\frac{\mathrm{i}}{2\pi}} \int \mathrm{i}\omega^{5/2} \rho(\mathbf{x}) \frac{[\rho(\mathbf{x}^r)v^s(\mathbf{x}^r)]^{1/2}}{[\rho(\mathbf{x})v^s(\mathbf{x})]^{1/2}} \\ &A^{\parallel}(\mathbf{x}^r,\mathbf{x})|W^s(\omega)|^2 \exp[\mathrm{i}\omega(T(\mathbf{x}^r,\mathbf{x},\mathbf{x}^s) - T_0(\mathbf{x}^r,\mathbf{x}^s))\,\mathrm{d}\omega \mathbf{w}^T(\mathbf{x}^r,\mathbf{x},\mathbf{x}^s). \end{aligned} \tag{31}$$

In equation (31), all of the parameters (slownesses, polarizations, densities, travel times, geometrical spreading) pertaining to the ray path are computed for each station/event pair; we assume a reasonable frequency spectrum $|W^s(\omega)|^2$ for teleseismic shear waves. We remark, finally, that two different strategies may be employed to estimate $\delta \boldsymbol{c}$ by inversion of the splitting observations. One can use equation (24), thereby directly solving the linearized equation (e.g. Stork and Clayton, 1991), for instance with the LSQR algorithm (Paige and Saunders, 1982). Alternatively, one can carry out local optimization with ε. These are, in effect, two different ways of accounting for the same matrix, or system of normal equations. The resolution properties of the inverse problem are derived from

$$\exp[\mathrm{i}\,\omega(\delta T(\mathbf{x}^r,\mathbf{x},\mathbf{x}^s) - \delta T(\mathbf{x}^r,\mathbf{x},\mathbf{x}^s)\,|\,W^s(\omega)\,|^2\;\psi(\mathbf{x}^s,\mathbf{x}^r). \tag{32}$$

Here, $\psi = 1$ where there is a source-receiver pair.

3. Application to southwestern Japan

3.1 Data

The metric for our shear wave splitting measurements comes from the multichannel method introduced by Chevrot (2000). The splitting intensity (equation (21)) is the ratio of the energy on the transverse horizontal component to energy on the time derivative of the radial component, and it is measured for each incoming shear wave at a given seismic station. A detailed comparison of the splitting intensity measure with other methods of measuring shear wave splitting parameters can be found in the appendix to Chevrot et al. (2004); an evaluation of the performance of different splitting measurement methods for broadband Japanese stations is discussed in Long and van der

Hilst (2005a). In our inversion scheme we wish to avoid restrictive assumptions about the geometry of anisotropy beneath the station. Therefore, instead of obtaining average splitting parameters (φ, δt) from the splitting vector at individual stations (see Appendix B), we treat each estimation of splitting intensity S as an individual measurement.

We use the splitting intensities from the teleseismic shear wave splitting data measured by Long and van der Hilst (2005b). In this study we consider data from 16 southern stations of the broadband Japanese F-net array (www.fnet.bosai.go.jp); see Figure 2. In Paper I, we also considered splitting observations from local slab events measured at low frequencies and we included teleseismic splitting from a range of backazimuths. In the inversion, however, we restrict our sensitivity kernel computation and parameter estimation to a 2.5-D framework, and only consider distant sources. Also, because we assume that the anisotropic model is invariant in the direction parallel to the trench and perpendicular to the direction of subduction, we eliminate splitting observations from rays that do not come in nearly parallel (< 20°) to the plane of the model. With a maximum deviation angle of 20° from the model plane, all *SKS* and *SKKS* observations can be used in the inversion (the incidence angle for a typical *SKS* arrival is ~ 10°, and ~ 20° for *SKKS*). Fortunately, the distribution of global seismicity suits this approach well for stations located in southwestern Japan; teleseismic direct *S* phases from events in the Tonga-Fiji and Hindu Kush regions come in nearly perpendicular to the Ryukyu trench. We use a total of 431 splitting intensity measurements in the inversion. A map view showing station locations and the upper mantle portions of all ray paths is shown in Figure 2.

3.2 A 2-D starting model from a numerical flow modeling study

We previously considered a variety of models for the inferred anisotropy (Long and van der Hilst, 2006) and concluded that a model involving trench-perpendicular corner flow in the mantle wedge best fit the splitting observations and the constraints from geodetic observations of the plate motions (e.g. Heuret and Lallemand, 2005). Therefore, we treat the geometry of the Ryukyu subduction zone and our station geometry as a 2.5-D problem (Figure 3). We assume that the anisotropy in the mantle wedge is controlled by flow induced by viscous coupling with the downgoing lithospheric slab and that all of this motion is contained in a plane perpendicular to the strike of the trench. Furthermore, we assume that the anisotropic structure is invariant in the direction of the strike of the trench. This allows us to "collapse" the two-dimensional station geometry shown in Figure 3 onto a one-dimensional line above the plane of the model; the station coordinates can then be expressed in terms of the station's distance from the trench.

Although they are consistent with the results of our previous work (Long and van der Hilst, 2006; Paper I), our assumptions about the 2-D geometry of the flow field and the resulting anisotropy are restrictive. In particular, we ignore the effects of any three-dimensional flow induced by along-strike changes in slab morphology or by trench migration and slab rollback. We also recognize that in the 2.5-D framework the inclusion of stations located on Kyushu and southern Honshu (Figure 2) may be problematic as they raise some questions about possible effects of flow around the slab edge or contributions to anisotropy from the subducting Pacific plate to the north. However, it is

necessary to include them because these station locations extend much further into the backarc than stations located in the Ryukyu island arc and greatly improve the resolution.

As a starting model for the inversion we use the results of numerical flow modeling: Paper I considered a range of 2-D flow models with a kinematically defined downgoing lithospheric slab and various rheological and temperature constraints. For each steady-state velocity field obtained from these models we calculated the evolution of finite strain along streamlines that started at the 410 km discontinuity. For each finite strain model (Models A-E), we traced rays through the iasp91 velocity model (Kennett and Engdahl, 1991) and calculate the incremental and total splitting intensity along each ray using the predictions from ray perturbation theory for a dipping transversely isotropic medium (Chevrot and van der Hilst, 2003). The two most dramatically different strain fields are associated with model A (in which flow in the mantle wedge is driven only through viscous coupling between the downgoing slab and the overlying wedge material) and model E (a model which includes the effects of thermal buoyancy and a temperature-dependent viscosity), and there are corresponding differences in the predicted splitting intensities for the two models.

The best-fitting flow models include a region of B-type fabric that extends ~ 150 km from the trench; in this region, the fast axis of anisotropy is oriented 90° from the plane of the flow model (that is, in the x_2-x_3 plane). In our initial inversion approach, we do not solve for the azimuth of the fast direction in the horizontal plane; we fix the orientation according to the starting model and compute the sensitivity kernels accordingly. We can then experiment with the horizontal position of the presumed fabric transition in order to obtain the best-fitting model. Here, we present preliminary inversion

results using Model A as a starting model. The distribution of finite strain in the mantle wedge, the values of the dip parameter θ_0 and the anellipticity ε_A, and the distributions of the A-type and B-type fabric regions for starting Model A are shown in Figure 4.

3.3 Discretization and parameterization

The model domain is divided into a grid with block sizes of 21.25 km x 21.25 km. This is the same grid spacing used in our finite element models (Paper I). We compute the sensitivity kernels and solve the anisotropic parameters in each model block. The area of the model space with significant ray coverage is 35 blocks (~640 km) wide and 15 blocks (~320 km) deep. At each point in the model, we describe the local geometry of the anisotropy with three parameters: θ_0, ε_A, and α. The dip parameter θ_0 denotes the angle between the axis of symmetry of the transversely isotropic medium and the horizontal plane. The anellipticity parameter ε_A is a measure of the strength of anisotropy. When relating the anisotropic parameters to finite strain we assume that a maximum anellipticity value is reached once the finite strain reaches a value of 3; for smaller finite strain values, we assume that ε_A scales linearly with the amount of strain. This is compatible with experimental constraints on lattice preferred orientation development in olivine (e.g. Zhang and Karato, 1995). The anellipticity is a combination of the elastic tensor components, namely

$$\varepsilon_A \equiv \frac{(c_{11}-c_{55})(c_{33}-c_{55})-(c_{13}+c_{55})^2}{(c_{11}-c_{55})(c_{33}-c_{55})}, \tag{33}$$

as given by Schoenberg and de Hoop (2000). For our starting model, we pick a maximum value for ε_A ($\varepsilon_{A_{MAX}}$ = 0.15) that corresponds to the transversely isotropic mantle (TIM)

elastic constants used by Chevrot and van der Hilst (2003), Hartog and Schwartz (2000), and Paper I. The parameter α describes the orientation of the symmetry axis in the horizontal plane. In our 2.5-D approximation, we allow the symmetry axis to coincide with the x_1-x_3 plane or with the x_2-x_3 plane; no intermediate orientations are permitted. A symmetry axis in the x_2-x_3 plane corresponds to areas of the model where the B-type olivine fabric dominates, as described in section 4.2. The parameter α is specified in the starting model, but in our initial inversion runs we do not allow the value of α to vary from its initial values. Therefore, our inversion scheme solves for two independent anisotropic parameters, θ_0 and ε_A, in each model block.

In order to derive and compute sensitivity kernels for our two chosen anisotropic parameters we express each term in the perturbed elastic tensor $\delta\mathbf{c}$ in terms of θ_0 and ε_A. We begin with reduced 6 x 6 matrix describing the elastic tensor for a transversely isotropic medium (e.g. Thomsen, 1986):

$$c_{ij} = \begin{bmatrix} c_{11} & c_{11}-2c_{66} & c_{13} & 0 & 0 & 0 \\ c_{11}-2c_{66} & c_{11} & c_{13} & 0 & 0 & 0 \\ c_{13} & c_{13} & c_{33} & 0 & 0 & 0 \\ 0 & 0 & 0 & c_{55} & 0 & 0 \\ 0 & 0 & 0 & 0 & c_{55} & 0 \\ 0 & 0 & 0 & 0 & 0 & c_{66} \end{bmatrix}, \tag{34}$$

which contains the 5 independent elastic parameters needed to describe a TI medium. Following Zhu and Dorman (2000) and Okaya and McEvilly (2003), we rotate the elastic tensor in the (x_1-x_3) or (x_2-x_3) plane, depending on the strike of the symmetry axis. For the case of $\alpha = 0$ (the fast symmetry axis is parallel to the trench, as in the B-type fabric regime), the 6 x 6 rotation matrix is given by

$$R_1 = \begin{bmatrix} \cos^2\theta_0 & 0 & \sin^2\theta_0 & 0 & 2\sin\theta_0\cos\theta_0 & 0 \\ 0 & 1 & 0 & 0 & 0 & 0 \\ \sin^2\theta_0 & 0 & \cos^2\theta_0 & 0 & -2\cos\theta_0\sin\theta_0 & 0 \\ 0 & 0 & 0 & \cos\theta_0 & 0 & -\sin\theta_0 \\ -\cos\theta_0\sin\theta_0 & 0 & \cos\theta_0\sin\theta_0 & 0 & \cos^2\theta_0 - \sin^2\theta_0 & 0 \\ 0 & 0 & 0 & \sin\theta_0 & 0 & \cos\theta_0 \end{bmatrix} \quad (35)$$

and the properly rotated elastic constant matrix is given by RCR^T. As discussed in section 2.1.3, the geometry of our problem allows us to gain sensitivity to only 7 independent elastic constants. These rotated elastic constants can be collected into the vector $\mathbf{c}'$:

$$\mathbf{c}' = \begin{bmatrix} c'_{11} \\ c'_{13} \\ c'_{33} \\ c'_{44} \\ c'_{15} \\ c'_{35} \\ c'_{55} \end{bmatrix}. \quad (36)$$

The corresponding radiation pattern matrix also reduces to 7 independent entries:

$$\mathbf{w}^T(\mathbf{x}^r, \mathbf{x}, \mathbf{x}^s) = \begin{bmatrix} h_1^s(\mathbf{x})p_1^s(\mathbf{x})h_1^r(\mathbf{x})p_1^r(\mathbf{x}) \\ h_1^s(\mathbf{x})p_1^s(\mathbf{x})h_3^r(\mathbf{x})p_3^r(\mathbf{x}) \\ h_3^s(\mathbf{x})p_3^s(\mathbf{x})h_3^r(\mathbf{x})p_3^r(\mathbf{x}) \\ h_2^s(\mathbf{x})p_3^s(\mathbf{x})h_2^r(\mathbf{x})p_3^r(\mathbf{x}) \\ h_1^s(\mathbf{x})p_1^s(\mathbf{x})h_1^r(\mathbf{x})p_3^r(\mathbf{x}) \\ h_3^s(\mathbf{x})p_3^s(\mathbf{x})h_1^r(\mathbf{x})p_3^r(\mathbf{x}) \\ h_1^s(\mathbf{x})p_3^s(\mathbf{x})h_1^r(\mathbf{x})p_3^r(\mathbf{x}) \end{bmatrix}. \quad (37)$$

We obtain the following expressions for the rotated elastic parameters:

$$c'_{1111} = c'_{11} = (2c_{13} + 4c_{55})\sin^2\theta_0\cos^2\theta_0 + c_{11}\cos^4\theta_0 + c_{33}\sin^4\theta_0. \quad (38)$$

$$c'_{1133} = c'_{13} = (c_{11} + c_{33} - 4c_{55})\sin^2\theta_0\cos^2\theta_0 + c_{13}\cos^4\theta_0 + c_{13}\sin^4\theta_0. \quad (39)$$

$$c'_{3333} = c'_{33} = (2c_{13} + 4c_{55})\sin^2\theta_0\cos^2\theta_0 + c_{11}\sin^4\theta_0 + c_{33}\cos^4\theta_0. \quad (40)$$

$$c'_{3313} = c'_{35} = (c_{33} - c_{13})\cos^3\theta_0 \sin\theta + (c_{13} - c_{11})\sin^3\theta_0 \cos\theta_0 - 2c_{55}\cos^3\theta_0 \sin^3\theta_0. \quad (41)$$

$$c'_{2323} = c'_{44} = c_{55}\cos^2\theta_0 + c_{66}\sin^2\theta_0. \quad (42)$$

$$c'_{1113} = c'_{15} = (c_{13} - c_{11})\cos^3\theta_0 \sin\theta_0 - (c_{13} + c_{33})\sin^3\theta_0 \cos\theta_0 + 2c_{55}\cos^3\theta_0 \sin^3\theta_0. \quad (43)$$

$$c'_{1313} = c'_{55} = (c_{11} + c_{33} - 2c_{55})\cos^2\theta_0 \sin^2\theta_0 + c_{55}\cos^4\theta_0 + c_{55}\sin^4\theta_0. \quad (44)$$

Finally, in these equations we can substitute for the elastic constants c_{11}, c_{13}, c_{33}, and c_{55} expressions in terms of the anellipticity ε_A, according to equation (33). For the case where α = 90° (fast axis is perpendicular to the trench), the process is similar but the rotation matrix is given by

$$R_2 = \begin{bmatrix} 0 & 1 & 0 & 0 & 0 & 0 \\ \cos^2\theta_0 & 0 & \sin^2\theta_0 & 0 & 2\cos\theta_0 \sin\theta_0 & 0 \\ \sin^2\theta_0 & 0 & \cos^2\theta_0 & 0 & -2\cos\theta_0 \sin\theta_0 & 0 \\ \cos\theta_0 \sin\theta_0 & 0 & -\sin\theta_0 \cos\theta_0 & 0 & \sin^2\theta_0 \cos^2\theta_0 & 0 \\ 0 & 0 & 0 & \cos\theta_0 & 0 & -\sin\theta_0 \\ 0 & 0 & 0 & -\sin\theta_0 & 0 & -\cos\theta_0 \end{bmatrix}. \quad (45)$$

Now that we have expressed the rotated stiffness matrix as a function of the chosen anisotropic parameters θ_0 and ε_A, we can linearize the relationships to obtain derivatives of the stiffness tensor components with respect to θ_0 and ε_A. Following de Hoop et al. (1999, equations (52) and (54)), we write the partial derivatives

$$\delta c_1 = \frac{\partial c}{\partial \varepsilon_A}\delta\varepsilon_A \quad (46)$$

$$\delta c_2 = \frac{\partial c}{\partial \theta_0}\delta\theta_0, \quad (47)$$

where c represents a nonzero component of the stiffness tensor. The total perturbation in the stiffness tensor component can then be written

$$\delta c = \delta c_1 + \delta c_2 = \frac{\partial c}{\partial \varepsilon_A}\delta\varepsilon_A + \frac{\partial c}{\partial \theta_0}\delta\theta_0 . \quad (48)$$

In this way, the perturbed elastic constant vector $\delta\mathbf{c}$ can be obtained by linearizing the perturbations to each anisotropic parameter c and calculating the (local) derivatives of the elastic constants with respect to each. In practice, we numerically evaluate the derivatives of each component of the properly rotated elastic tensor with respect to each parameter for each point in the model space. The derivatives with respect to ε_A are computed over the range ε_A = 0 (isotropy) to ε_A = 0.15 (TIM). The derivatives with respect to the symmetry axis dip are evaluated locally with respect to the starting model; therefore, we compute the derivatives about the local starting value of θ_0.

3.4 Ray aspects of kernels and computation scheme

We compute the sensitivity $\mathcal{K}$ for θ_0 and ε_A at each point **x** in the model using equation (31). For use in the inversion, the sensitivities for each event-station pair in the splitting intensity dataset are calculated using a grid spacing equal to the block size of the model. We also calculate sensitivities on a finer grid to visualize their properties better. A schematic diagram of the sensitivity kernel calculation is shown in Figure 5. For each scattering point **x** in the model, we calculate the unit slowness vectors **p** and the unit polarization vector **h** for the two segments (source-scatterer and scatterer-receiver) of the perturbed ray; the vectors $\mathbf{p}^r$, $\mathbf{p}^s$, $\mathbf{h}^r$, and $\mathbf{h}^s$ are used to form the radiation pattern vector **w** according to equation (18). We calculate the in-plane geometrical spreading between the scattering point **x** and the receiver position $\mathbf{x}^r$. The isotropic background shear velocities $v(\mathbf{x})$ and mass densities $\rho(\mathbf{x})$ are taken from the 1-D iasp91 model (Kennett and Engdahl, 1991) and a 1-D density model (Montagner and Kennett, 1995), respectively. The travel

time difference between the unperturbed and perturbed rays, $T(\mathbf{x}^r, \mathbf{x}, \mathbf{x}^s)$-$T_0(\mathbf{x}^r, \mathbf{x}^s)$, are calculated with respect to the iasp91 shear velocity model. In practice, the slowness vectors, traveltime differences, and geometrical spreading $A^{\|}(\mathbf{x}^r, \mathbf{x})$ are calculated from a 2-D ray tracing code. The frequency spectrum of the incident shear wave is approximated as

$$|W^s(\omega)|^2 = \frac{\omega^2\tau^2}{4\pi} e^{-\omega^2\tau^2/8\pi^2}, \quad (49)$$

where τ is the characteristic period of the wave. Here we follow the approach of Favier and Chevrot (2003) and approximate the spectrum as the second derivative of a Gaussian; this is appropriate for *SKS*-type phases where the records have been deconvolved from the radial component waveform (this preprocessing step was used by Chevrot, 2000, and followed by Long and van der Hilst, 2005b). We use a characteristic period of τ = 8 sec for direct *S* phases, τ = 10 sec for *SK*(*K*)*S* phases. The integrals over frequency in equation (31) are numerically calculated using the trapezoidal rule over a frequency range from 0.02 Hz to 0.125 Hz; this is the frequency range used to bandpass filter the shear wave data (Long and van der Hilst, 2005b). Finally, the partial derivatives of $\delta\mathbf{c}$ with respect to the anisotropic parameters θ_0 and ε_A with respect to the local starting model are numerically calculated as described in section 3.3 at each scattering point **x**.

In Figures 6-8 we show examples of sensitivity kernels $\mathcal{K}(\theta_0)$ and $\mathcal{K}(\varepsilon_A)$ calculated for shear arrivals in our splitting dataset. In Figure 6, we show a series of kernels for four different ray paths: a direct *S* arrival at station FUK, an *SKS* arrival at station YTY, and two direct *S* arrivals from opposite backazimuths at station TKA. We calculate the sensitivity at scattering points **x** located on a fine grid (~ 4 km grid spacing). The kernels are calculated with respect to a homogenous starting model where the symmetry axis dip

θ_0 is everywhere zero. The kernels display the familiar oscillatory behavior (e.g. Hung et al., 2000; Chevrot et al., 2004; de Hoop and van der Hilst, 2005a); because the kernels are 2-D, the sensitivity is nonzero along the ray theoretical path. Figure 7 displays kernels for the same four ray paths calculated with respect to the starting model shown in Figure 4b-d. The "imprint" of the starting model on the sensitivity kernels can clearly be seen in Figure 7, because the partial derivatives of the perturbed elastic tensor $\delta\mathbf{c}$ are calculated with respect to the starting model. In Figure 8, we show the sensitivity kernels for a different *SKS* arrival at station YTY calculated on both the fine grid (~ 4 km grid spacing) and for a grid spacing equivalent to that used in the flow model and the inversion scheme. In general, the kernels are similar to the 2-D sensitivity kernels in Favier and Chevrot (2003), except that we allow for nonvertical incidence and a nonhomogenous starting model in which the dip of the symmetry axis is allowed to vary.

We emphasize that the differences between the kernels shown in Figures 6 and 7 demonstrate the importance of using kernels computed in a realistic heterogeneous background model (see also de Hoop and van der Hilst, 2005a,b). The local values of the partial derivatives $\frac{\partial c}{\partial \varepsilon_A}$ and $\frac{\partial c}{\partial \theta_0}$, and therefore the local sensitivity to the anisotropic parameters, depend strongly on the starting model. We also point out that the kernel computation should be performed iteratively; if the inversion is repeated using an updated starting model, the sensitivity kernels should be re-computed and updated kernels used in the inversion.

Once we have calculated sensitivities for each of the shear arrivals in the splitting dataset, we can predict the splitting that would be observed at the surface for the starting model used in the kernel calculation. This forward calculation takes into effect finite

frequency effects, which are considerable for the fairly long periods studied by Long and van der Hilst (2005b). The predicted splitting intensity for a given source-receiver pair is written

$$\delta S(\mathbf{x}^s, \mathbf{x}^r) = \int \mathcal{K}(\mathbf{x}^s, \mathbf{x}^r; \mathbf{x}) \delta \mathbf{c}(\mathbf{x}) \, \mathrm{d}\mathbf{x} \,. \tag{50}$$

We integrate over the model area by summing the contribution to the splitting intensity at each grid point, computed by multiplying the sensitivity at that point (times the area of the grid block) and the model perturbations ($\delta\theta_0$ and $\delta\varepsilon_A$) over all points **x** in the model. In Paper I we predicted splitting for different strain models derived from numerical flow calculations using the ray theoretical framework of Chevrot and van der Hilst (2003); the finite-frequency forward calculation should be more accurate than the previous ray theoretical calculation. We predict splitting for the entire data set; a plot of the contribution at each model block to the total splitting intensity observed at the surface is shown in Figure 9. This visualization of the total contribution to the observed splitting reflects the distribution of sensitivity in the model space and the distribution of anisotropy in the starting model. A plot of observed and modeled splitting intensities at four F-net stations is shown in Figure 10.

3.5 Inversion strategies and resolution considerations

We calculate sensitivities for each of the two anisotropic parameters on our 15 x 35 model grid for each of the 431 shear arrivals in the splitting intensity dataset. These sensitivities are then used to construct the normal equations for the inversion. We solve for a total of 15 x 35 x 2 unknowns in the inversion. The data vector **d** contains the 431 splitting intensity observations, the model vector **m** contains the 1050 unknowns, and the

431 x 1050 sensitivity matrix **K** is constructed from the sensitivity kernels. When both norm and gradient damping are applied, the inversion aims to minimize the quantity $|| \mathbf{Km} - \mathbf{d} ||^2 + \lambda_1 || \mathbf{Lm} ||^2 + \lambda_2 || \mathbf{m} ||^2$, where λ_1 and λ_2 are weights for the damping and **L** is a smoothing operator. We use the iterative LSQR method (Paige and Saunders, 1982) to solve the normal equations. LSQR yields the estimate $\langle \delta \mathbf{m} \rangle$, corresponding with

$$\langle \delta \mathbf{m} \rangle = \langle \mathbf{K}^* \mathbf{K} \rangle^{-1} \mathbf{K}^* \mathbf{d}; \tag{51}$$

the resolution is described by the operator

$$\mathbf{R} = \langle \mathbf{K}^* \mathbf{K} \rangle^{-1} \mathbf{K}^* \mathbf{K}, \ \langle \delta \mathbf{m} \rangle = \mathbf{R} \delta \mathbf{m}, \tag{52}$$

if $\delta \mathbf{m}$ were the "true" model. **R** reveals the cross-coupling between estimated parameters, as well as the linear combinations of parameters that can be resolved. In Figure 11, we show the total sensitivity to each parameter at each model point; this type of visualization gives an indication of which areas of the model are well-resolved.

4. Preliminary results

4.1 Inversion result

Figure 12 shows a first, preliminary inversion result for anisotropic structure beneath the Ryukyu arc from shear wave splitting intensity measurements made at F-net stations. The starting model used in the inversion is the same model used in the construction of the sensitivity kernels (Figure 4). We compute the predicted splitting intensities for this starting model (see Figure 10) and subtract the corresponding observed splitting intensities to form our data vector $\mathbf{d} = (\boldsymbol{S}_{model} - \boldsymbol{S}_{obs})$. We then solve the inversion system using LSQR for a change to the starting model. To obtain our initial model, we applied norm damping with a weight of $\lambda_2 =$ 0.8; this tends to minimize the amplitude of

the solution. The models that we obtain for both θ_0 and ε_A are extremely rough; we have not yet applied gradient damping to our inversion solution. Gradient damping tends to minimize the differences between adjoining model blocks and thus produces a smoother model. Although the inversion result shown in Figure 12 must be considered as extremely preliminary, one remarkable feature of the model is the small change in anellipticity in regions that correspond to the subducting slab and the subslab mantle. In our starting model, these regions were isotropic, and the inversion result suggests that the data indeed do not require anisotropy within and beneath the slab. This tends to support the inference of Long and van der Hilst (2006) that most of the observed splitting at Ryukyu arc stations can be explained by anisotropy in the mantle wedge and that significant anisotropy in the slab itself is not required by the observations.

4.2 Strategies for iteration with flow modeling constraints

A key component of this work is the proposed integration of constraints from geodynamical modeling with constraints obtained from shear wave splitting measurements. We have used an anisotropic model derived from our previous flow modeling study as a starting point for computing the sensitivity kernels and as a starting model in the inversion. We also aim to integrate constraints obtained from our inversion results back into the flow modeling framework. In this way, we use constraints from the solution of equations that govern viscous flow in the mantle associated with a subducting plate to inform our choice of starting model for the inversion, and we use constraints on anisotropic structure obtained from the inversion of splitting observations to perturb the flow models. This coupling between the methods of geodynamical flow modeling with

the inversion of seismic data should allow us to converge on a model for anisotropy that is compatible with both our model of the physical processes that govern flow in subduction zones, and with the splitting observations that make up our data set.

Two possible strategies for integrating constraints obtained from the inversion into the flow modeling framework are outlined in detail in Paper I. Briefly, one method relies on the addition of kinematic velocity constraints into the flow model that produce a strain field that is consistent with the inverse model for certain well-resolved areas of the model. An alternative approach involves changing the parameters used in the flow models to obtain numerical estimates of local derivatives of the strain (anisotropy) parameters with respect to flow model parameters. Constraints on anisotropy obtained from the seismological inversion can then, in turn, be inverted for the best possible combination of flow model parameters that would produce the inferred anisotropic structure. Either approach could lend itself to an iterative strategy in which the splitting tomography result is used to obtain a perturbed flow model that better matches the splitting observations, and the tomographic inversion is then re-run using the perturbed flow model as a starting model.

It is important to note that for either strategy, the operator that describes the resolution of the inversion plays a crucial role in incorporating inversion constraints into the flow model. We wish to avoid mapping poorly resolved regions of the inversion into the updated flow model. We can therefore use the resolution (see Figure 11) to choose regions of the model where the update of the flow modeling is meaningful. We can set a resolution threshold that defines the regions of the model that are sufficiently well-resolved to use in the flow model update, and ignore poorly resolved regions. This

incorporation of constraints from well-resolved regions to perturb the flow field and obtain a better estimate for the anisotropy in regions that are poorly resolved in the inversion can be thought of as a physically-based regularization method; this framework allows us to obtain reasonable constraints on anisotropy even in areas that are not well illuminated by the seismic data set.

5. Outlook, discussion, and concluding remarks

In this paper we have described a theoretical framework for shear wave splitting intensity tomography and a computational strategy for obtaining finite-frequency sensitivity kernels for a carefully chosen combination of anisotropic parameters. We have presented example kernels for several event-station pairs represented in our southwestern Japan data set, discussed the implementation of the inversion scheme itself, and presented a very preliminary inversion result based on a starting model from our previous flow modeling study. There are several steps that need to be taken in order to obtain a more robust inversion result, which can then be used to solve for an updated flow model that is more consistent with the seismological constraints. First, we plan to thoroughly test our inversion scheme using a synthetic starting model and synthetic data. Second, a variety of damping schemes must be tested, and we plan to experiment with gradient damping in order to obtain a smoother model. Third, a wider variety of starting models needs to be tested. We previously investigated a range of two-dimensional flow models and predicted dramatically different splitting parameters for models with different rheological parameters. In particular, we found that models that utilize a temperature-dependent viscosity law (Model E) resulted in strain fields that are quite different from an

isothermal model in which flow is driven purely by viscous coupling between the slab and the overlying mantle (Model A). In this paper we have used Model A as our starting model for the kernel computation and the inversion. Further testing of other strain models as starting models is required. Third, we must test a range of models for the B-type fabric regime to obtain the best possible inversion result, as the position of the transition between A- and B-type olivine fabric is not a free parameter in the inversion. Finally, more thorough consideration of the resolution issues and more thorough resolution testing is required in order to identify regions of the inversion that are well-resolved enough to translate into additional constraints on updated flow models.

Although further work remains in order to obtain a robust inversion result and to integrate inversion constraints into our flow modeling framework, in this paper we have presented a framework for inverting teleseismic shear wave splitting measurements from a dense array of broadband stations for anisotropic structure and applied it to a data set from southwestern Japan. Shear wave splitting data sets are usually too sparse to interpret without making severely restrictive assumptions about the geometry of anisotropy beneath the stations, and the interpretation of such data sets is non-unique and controversial. In this paper and in preceding studies (Long and van der Hilst, 2005a,b, 2006; Long et al., 2006a) we have assembled and described a dense splitting dataset, established physically plausible anisotropic models based on geodynamical considerations, and described a framework for inverting splitting intensities for anisotropic structure and integrating these constraints with a flow modeling framework. This cross-disciplinary approach has already yielded a great deal of insight into the distribution of seismic anisotropy and tectonic deformation associated with subduction in

the upper mantle beneath Japan. Further work aimed towards obtaining the most robust inversion result possible and explicitly integrating it with geodynamical modeling constraints should further illuminate the mechanisms and consequences of anisotropy and deformation in the upper mantle beneath Japan, and contribute to our understanding of the structure, dynamics, and flow patterns associated with subduction zones.

6. Appendix A: Symbols and notation

Symbol	Description
t	time
T_0	dominant period of incoming shear wave
$\mathbf{x} = (x_1, x_2, x_3)$	position vector
$\rho(\mathbf{x})$	density
$c_{ijkl}(\mathbf{x})$	stiffness tensor
ω	angular frequency
$\mathbf{x}^s$	source position
$\mathbf{x}^r$	receiver position
$G_{in}(\mathbf{x}, \omega, \mathbf{x}^s)$	Green's function in the frequency domain
$T(\mathbf{x}, \mathbf{x}^s)$	travel time along ray connecting $\mathbf{x}$ with $\mathbf{x}^s$
$\mathbf{h}^s$ ($\mathbf{h}^r$)	unit polarization vector associated with source (receiver) ray
$A(\mathbf{x}, \mathbf{x}^s)$	amplitude of ray connection $\mathbf{x}$ with $\mathbf{x}^s$
$v(\mathbf{x})$	phase velocity
$\lvert \det \mathbf{Q}_2(\mathbf{x}, \mathbf{x}^s) \rvert^{1/2}$	relative geometrical spreading
(q_1, q_2)	local wave front coordinates
$\kappa(\mathbf{x}, \mathbf{x}^s)$	KMAH index along ray connecting $\mathbf{x}$ with $\mathbf{x}^s$
$\mathbf{Q}_2$	relative geometrical spreading matrix
$Q_2^{\parallel}(\mathbf{x}, \mathbf{x}^s)$	in-plane relative geometrical spreading factor
$Q_2^{\perp}(\mathbf{x}, \mathbf{x}^s)$	out-of-plane relative geometrical spreading factor
$\mathbf{V} = (V_1, V_2, V_3)$	group velocity vector
$A^{\parallel}(\mathbf{x}, \mathbf{x}^s)$	amplitude with in-plane geometrical spreading only
$f_j(\mathbf{x}, t)$	equivalent body force
M_{ij}	moment tensor
$\mathbf{p}^s$ ($\mathbf{p}^r$)	slowness vector associated with source (receiver) ray
δc_{ijkl}	smooth, compactly supported perturbation to elastic tensor
u_{mn}	m-component of perturbed wave field due to a body force in the n-direction (time domain)
U_{mn}	Fourier transform of u_{mn} (frequency domain)
$T^{(i)}(\mathbf{x}^r, \mathbf{x}, \mathbf{x}^s)$	refracted travel time given by $T(\mathbf{x}^s, \mathbf{x}) + T(\mathbf{x}, \mathbf{x}^r)$

$\mathcal{L}^{\perp}(\mathbf{x}^{\mathrm{r}}, \mathbf{x}, \mathbf{x}^{\mathrm{s}})$	refracted out-of-plane geometrical spreading
$\delta\mathbf{c}(\mathbf{x})$	matrix of medium perturbations
$\mathbf{w}(\mathbf{x}^{\mathrm{r}}, \mathbf{x}, \mathbf{x}^{\mathrm{s}})$	radiation patterns
δu	perturbation to wavefield
R	superscript indicating component in direction of qSV
T	superscript indicating component in direction of qSH
$u^R = u_0^R + \delta u^R$	projection of u onto qSV polarization direction
$u^T = u_0^T + \delta u^T$	projection of u onto qSH polarization direction
C	time-correlation function
$\mathrm{S} = \mathrm{S}[\delta\mathbf{c}](\mathbf{x}^{\mathrm{s}}, \mathbf{x}^{\mathrm{r}})$	splitting intensity measure
$N_{s,r} = \int \lvert \partial_t u^R \rvert^2 \, \mathrm{d}t$	normalized radial component energy
$\lvert W^s(\omega) \rvert^2$	frequency spectrum of incident wave
ε	mismatch between observed and predicted splitting intensities
$\mathcal{K}(\mathbf{x}^{\mathrm{s}}, \mathbf{x}^{\mathrm{r}}; \mathbf{x})$	sensitivity kernel
β	isotropic shear wave speed
θ_0	dip parameter
ε_A	anellipticity parameter
R_1	rotation matrix in the x_1-x_3 plane
R_2	rotation matrix in the x_2-x_3 plane
τ	characteristic period of incoming shear wave
$\gamma_{\mathrm{c}}, \gamma_{\mathrm{s}}$	anisotropic perturbation parameters of Favier and Chevrot (2003)
α	initial polarization azimuth of unperturbed SV phase
φ_0	azimuth of fast direction in the horizontal plane
λ_1, λ_2	weights for gradient and norm damping, respectively

7. Appendix B: Behavior of the splitting intensity and kernels

Following Chevrot (2000) and Chevrot et al. (2004), the splitting intensity s, obtained by projecting the transverse component waveform onto the radial component derivative, is written as

$$S = -2\frac{\int_{-\infty}^{\infty} -i\omega u_T(\omega) u_R^{0*}(\omega) d\omega}{\int_{-\infty}^{\infty} \omega^2 \, \lvert u_R^{0*}(\omega) \rvert^2 \, d\omega}, \qquad \text{(A1)}$$

which is our expression (20). The *splitting function* refers to the dependence of the splitting intensity on the incoming polarization azimuth; the *splitting vector* then refers to

the sample of the splitting function obtained at different incoming polarization azimuths for a given (limited) data set at a single seismic station.

Under certain assumptions, the average splitting parameters of the medium can be retrieved from the splitting vector. For example, if the anisotropy beneath the station is contained in a single, homogenous anisotropic layer with a horizontal axis of symmetry, then the splitting function for shear phases with vertical incidence takes the form (Chevrot, 2000)

$$s = \delta t \sin[2(\varphi - \varphi_0)], \tag{A2}$$

where φ is the azimuth of the fast symmetry axis, φ_0 the incoming polarization azimuth of the wave, and δt the delay time accumulated between the fast and slow components. A detailed comparison of the splitting intensity measure with other methods of measuring shear wave splitting parameters can be found in the appendix to Chevrot et al. (2004); an evaluation of the performance of different splitting measurement methods for broadband Japanese stations is discussed in Long and van der Hilst (2005b).

Favier and Chevrot (2003) have developed expressions that describe 2-D and 3-D Fréchet kernels for the splitting intensity in a homogenous anisotropic medium with a horizontal axis of symmetry. They parameterize the medium using two anisotropic perturbation parameters γ_c and γ_s, which are related to the anisotropic parameter γ of Thomsen (1986) and Mensch and Rasolofosaon (1997). The expressions they derive for the sensitivity kernels are in fact equivalent to framework derived above and expressed in equation (31), although we make fewer assumptions about the geometry of the anisotropic medium, we restrict ourselves to the 2.5-D case, and we parameterize the anisotropic medium differently. Our expression for the sensitivity kernel in equation (31)

is a generalization of the treatment in Favier and Chevrot (2003) with the following differences in notation. They express the splitting intensity perturbation δS in the following form:

$$\delta S(\mathbf{r}_0;\mathbf{r}) = -\gamma \frac{1}{4\pi\beta^2}\frac{2\omega_0}{r} F(\theta,\varphi,\alpha,\varphi_0) \frac{2\int_{-\infty}^{\infty} \omega^3 \mid u_R(\omega)\mid^2 \sin[\frac{\omega(r+z_0-z)}{\beta}]\,\mathrm{d}\,\omega}{\int_{-\infty}^{\infty} \omega^2 \mid u_R(\omega)\mid^2 \,\mathrm{d}\,\omega}. \quad \text{(A3)}$$

We, following from equation (31), express the splitting intensity due to an elastic perturbation $\delta\boldsymbol{c}$ in the form

$$\delta S(\mathbf{x}^s,\mathbf{x}^r) = \mathcal{K}(\mathbf{x}^s,\mathbf{x}^r;\mathbf{x})\delta\mathbf{c}(\mathbf{x}) \cong \left[\int \omega^2 \mid W^s(\omega)\mid^2 \mathrm{d}\,\omega\right]^{-1} \sqrt{\frac{\mathrm{i}}{2\pi}} \int \mathrm{i}\,\omega^{5/2} \rho(\mathbf{x})$$
$$\frac{[\rho(\mathbf{x}^r)v^s(\mathbf{x}^r)]^{1/2}}{[\rho(\mathbf{x})v^s(\mathbf{x})]^{1/2}} A^{\parallel}(\mathbf{x}^r,\mathbf{x}) \mid W^s(\omega)\mid^2 \exp[\mathrm{i}\,\omega(T(\mathbf{x}^r,\mathbf{x},\mathbf{x}^s) - T_0(\mathbf{x}^r,\mathbf{x}^s))\,\mathrm{d}\,\omega. \quad \text{(A4)}$$
$$\mathbf{w}^T(\mathbf{x}^r,\mathbf{x},\mathbf{x}^s)\,\delta\mathbf{c}$$

The differences in notation are as follows: we denote the source and scatterer position, respectively, with $\mathbf{x}^s$ and $\mathbf{x}$; their convention utilizes $\mathbf{r}_0$ and $\mathbf{r}$. Our expression for the radiation patterns, $\mathbf{w}^T(\mathbf{x}^r,\mathbf{x},\mathbf{x}^s)$, is equivalent to their function $F(\theta,\varphi,\alpha,\varphi_0)$ normalized by β^2, the square of the isotropic shear wave speed. Their work assumes that the perturbation in anisotropy is completely described by a perturbation in c_{44}: therefore our $\delta\boldsymbol{c}$ is equivalent to their $\gamma = \frac{-\delta c_{44}}{c_{44}}$, multiplied by $\beta^2\rho$ (because $\beta = \sqrt{\frac{c_{44}}{\rho}}$). We write the geometrical spreading as $\rho(\mathbf{x})A^{\parallel}(\mathbf{x}^r,\mathbf{x})$; due to the homogenous model and resulting raypath geometry used in Favier and Chevrot (2003), their expression for the geometrical spreading simplifies to $\frac{1}{4\pi\beta r}$. The ratio of densities and isotropic velocities

$\frac{[\rho(\mathbf{x}^r)v^s(\mathbf{x}^r)]^{1/2}}{[\rho(\mathbf{x})v^s(\mathbf{x})]^{1/2}}$ that appears in our kernel expressions simplifies to 1 in the case of a homogeneous layer, as assumed in Favier and Chevrot (2003). Finally, we write the unperturbed radial component as $W^s(\omega)$, while they use u^R, and we write the travel time difference between the perturbed and unperturbed rays as $T(\mathbf{x}^r,\mathbf{x},\mathbf{x}^s)-T_0(\mathbf{x}^r,\mathbf{x}^s)$, while for their geometry this expression can be written simply as $\frac{r+z_0-z}{\beta}$. The only substantial difference between our expression (34) and their expression (33) is the extra $\omega^{3/2}$ factor in the frequency integral that appears in our 2.5-D case. The differences between 2-D and 3-D kernels are discussed in the appendix to Favier and Chevrot (2003); they also note the $\omega^{5/2}$ frequency dependence in the integral. In their approach, this $\omega^{5/2}$ term means that the integral can no longer be evaluated analytically and numerical integration is needed; in our computational approach, we have assumed a narrow frequency band so the frequency terms may be taken outside the integral.

We now demonstrate that the result in equation (A3) can be obtained from our expression for the perturbed transverse component derived in Section 2. As before,

$$\delta u^T(\mathbf{x}^s,t,\mathbf{x}^r)\approx\sqrt{\frac{\mathrm{i}}{2\pi}}\int\!\!\int_R\omega^{3/2}\rho(\mathbf{x})\frac{A^{\|}(\mathbf{x}^s,\mathbf{x})A^{\|}(\mathbf{x},\mathbf{x}^r)}{\mathcal{L}^-(\mathbf{x}^r,\mathbf{x},\mathbf{x}^s)}$$
$$\cdot\,\mathbf{w}^T(\mathbf{x}^r,\mathbf{x},\mathbf{x}^s)\delta\mathbf{c}(\mathbf{x})\exp[\mathrm{i}\omega(T(\mathbf{x}^r,\mathbf{x},\mathbf{x}^s)-t)]h_p^s(\mathbf{x}^s)p_r^s(\mathbf{x}^s)M_{rp}(\mathbf{x}^s)\,\mathrm{d}\omega\,\mathrm{d}\mathbf{x}. \tag{A5}$$

We use the approach outlined in Appendix A of de Hoop and van der Hilst (2005a) and obtain the travel time shift predicted by ray perturbation theory. We find that

$$\delta u^T(\mathbf{x}^s,t,\mathbf{x}^r)\approx\partial_t u_0^R(\mathbf{x}^s,t,\mathbf{x}^r)(-)\delta T(\mathbf{x}^r,\mathbf{x}^s) \tag{A6}$$

where

$$\delta T(\mathbf{x}^r, \mathbf{x}^s) = -\frac{1}{2}\int_{t=0}^{T(\mathbf{x}^r, \mathbf{x}^s)} (-)\mathbf{w}^T(\mathbf{x}^r, \mathbf{x}(t), \mathbf{x}^s)\delta\mathbf{c}(\mathbf{x}(t))\,\mathrm{d}t\,. \tag{A7}$$

Here, $\mathbf{x}(t)$ is the ray connecting $\mathbf{x}^r$ with $\mathbf{x}(0)=\mathbf{x}^s$. This is the fundamental generalization of Favier and Chevrot (2003), equation (27). Indeed, we can compute $\delta T(\mathbf{x}^r, \mathbf{x}^s)$ for a homogenous transversely isotropic layer with symmetry axis in the horizontal plane (HTI) for a vertical (straight) ray connection $\mathbf{x}^r$ with $\mathbf{x}^s$, with $\delta c_{44} \neq 0$, with radiation pattern

$$\mathbf{w}^T(\mathbf{x}^r, \mathbf{x}(t), \mathbf{x}^s) \rightarrow \sin[2(\alpha - \varphi_0)] \tag{A8}$$

(see equation (19) in Favier and Chevrot, 2003). We note, also, that δt in their equation (27) is not the actual split shear travel time and is just an alternative parameter revealing the maximum split time. In general, if we wish to replace the model domain by a homogenous "matching" layer, we need to replace the sinusoid by the integrated linear combination of radiation patterns:

$$\left(\frac{1}{2}\int_{t=0}^{T(\mathbf{x}^r, \mathbf{x}^s)} \mathbf{w}^T(\mathbf{x}^r, \mathbf{x}(t), \mathbf{x}^s)\,\mathrm{d}t\right)\delta\mathbf{c}\,. \tag{A9}$$

Figure Captions

Figure 1. Geometry of the problem setup. The coordinates are chosen so that the anisotropic model is invariant in one horizontal direction (x_2). The medium is considered to be anisotropic above the 410 km discontinuity and isotropic everywhere else. The incoming shear wave is considered to be SV polarized; the quasi-SH energy observed on the transverse component (δu^T) arises solely from the anisotropic perturbation $\delta\mathbf{c}$.

Figure 2. Map view of the southernmost stations of the F-net array. Gray dashed lines indicate the surface projection of the slab contours at 100 km intervals; the dashed black line represents the position of the trench. The large arrow represents the direction of convergence. The upper mantle portions of the teleseismic shear wave raypaths used in this study are shown as thin gray lines. The symbol at each station represents the categorization of Long and van der Hilst (2005a); Category I stations are marked with a square, Category II stations with a triangle, and Category III stations with a circle. Thick black bars at Category I & II stations show the best-fitting average fast direction φ. The easternmost station, marked with a diamond, was not examined by Long and van der Hilst (2005a), but local splitting measurements from this station (Long and van der Hilst, 2006) were used to construct the starting model for the inversion.

Figure 3. A 3D sketch of the model and station geometry. Colors represent the strain field from the starting anisotropic model from Paper I. The model is invariant in the x_2 direction. The two-dimensional station geometry (circles) is then collapsed onto a one-dimensional line above the starting model.

Figure 4. a. Distribution of finite strain ellipses in the mantle wedge for Model A from Paper I, the starting model used for the inversion. The vertical and horizontal coordinates are given in km. The black box outlines the area of the flow model that is considered in the inversion. b. Distribution of the dip parameter θ_0 in the starting model for the region corresponding to the black box in (a). The horizontal and vertical element numbers are shown. c. Magnitude of the maximum finite strain (stretch ratio) in the starting model. The color scale saturates at a stretch ratio of 5. d. Distribution of A- and B-type olivine fabric in the starting model. The B-type fabric regime is shown in red.

Figure 5. Schematic diagram of the sensitivity kernel computation. The sensitivity is computed with respect to the starting model shown in Figure 4 at each scattering point **x**.

Figure 6a-d. Examples of sensitivity kernels for parameters ε_A (top) and θ_0 (bottom) for four shear arrivals in the splitting dataset. a. An *SKS* phase (backazimuth = 47°) recorded at station YTY. b. A direct *S* phase from an event in Tonga (backazimuth = 128°, incoming polarization direction = 91°) recorded at station TKA. c. A direct *S* phase from an event in the the Hindu Kush region (backazimuth = 293°, incoming polarization direction = 312°) recorded at station TKA. d. A direct *S* phase from an event in Tonga (backazimuth = 128°, incoming polarization direction 120°) recorded at station FUK. All sensitivities are given in s/m^2 and are calculated with respect to a homogenous anisotropic model with a horizontal symmetry axis.

Figure 7a-d. Sensitivity kernel examples for the same four event-station pairs as in Figure 6, but here the sensitivities are computed with respect to the starting model in Figure 4. All sensitivities are given in s/m^2.

Figure 8. a. Sensitivity kernels for an *SKS* wave (backazimuth = 107°) recorded at station YTY and computed on a grid five times finer than the grid spacing of the starting model. Note the differences in sensitivity with Figure 7a; these differences are due to the differences in backazimuth, and therefore in incoming polarization directions, between the two *SKS* waves. The sensitivities are given in s/m^2. b. Same as (a), but the sensitivities are computed on a coarser grid. Here the grid spacing is equal to the grid spacing of the starting model.

Figure 9. Total contribution to the predicted splitting observed at the surface calculated using finite-frequency sensitivity kernels and the starting model shown in Figure 4. At each point in the model, we sum the absolute values of each splitting intensity contribution for all rays in the dataset. The resulting plot reflects the distribution of parameter sensitivities as well as the anisotropic structure of the starting model. Because only the mantle wedge is anisotropic in the starting model, the contribution to the splitting intensity for the slab and underlying mantle is zero.

Figure 10. Observed and predicted splitting at stations KYK, NSK, TAS, and TKD. The splitting intensity is plotted with respect to incoming polarization azimuth. Observations are shown with black circles; the predicted splitting is shown with green triangles.

Figure 11. Total sensitivity for the anisotropic parameters ε_A (a) and θ_0 (b). At each point in the model, we sum the absolute values of the sensitivity for the entire dataset. Resolution is good in regions with high total sensitivity (red) and poor in regions shown in blue.

Figure 12. Preliminary inversion result for ε_A (a) and θ_0 (b). Colors represent the departure from the parameter values in the starting model at each point. We recover changes of ±15° in dip and up to ~ 0.3 in anellipticity. The thick black line represents the position of the top of the subducting slab in the starting model. The roughness in the recovered image is due to the lack of gradient damping in our preliminary inversion setup.

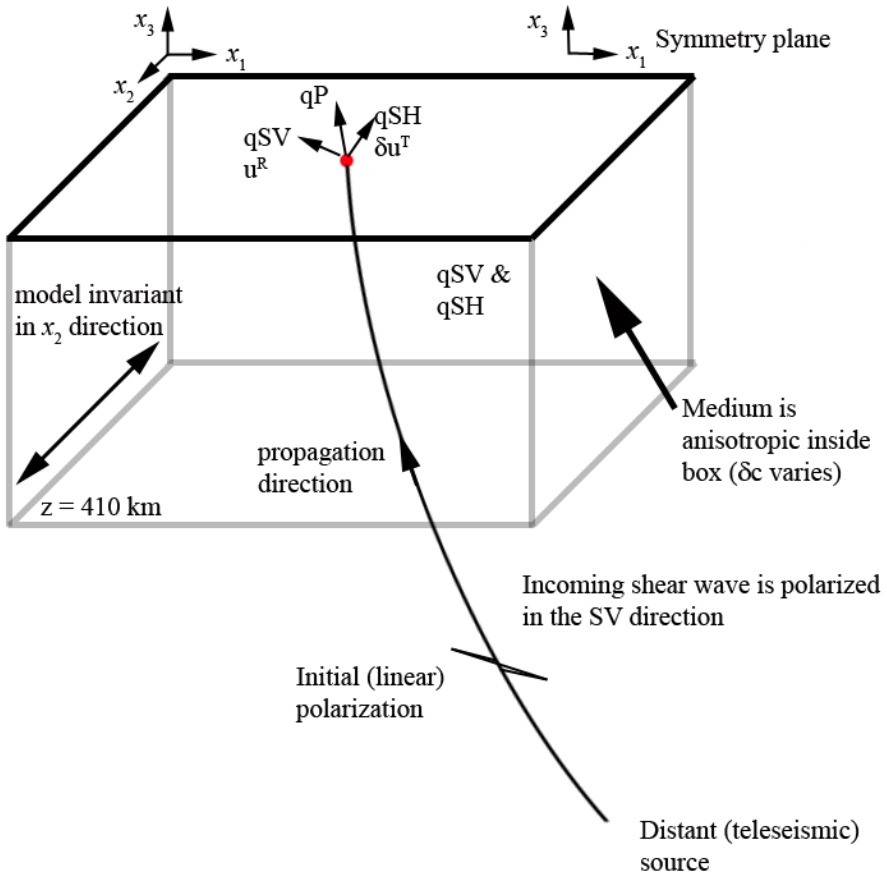
x_3
x_1
x_2
x_3
x_1
Symmetry plane
qP
qSH
δu^T
qSV
u^R
qSV &
qSH
model invariant
in x_2 direction
Medium is
anisotropic inside
box (δc varies)
propagation
direction
z = 410 km
Incoming shear wave is polarized
in the SV direction
Initial (linear)
polarization
Distant (teleseismic)
source

Figure 1

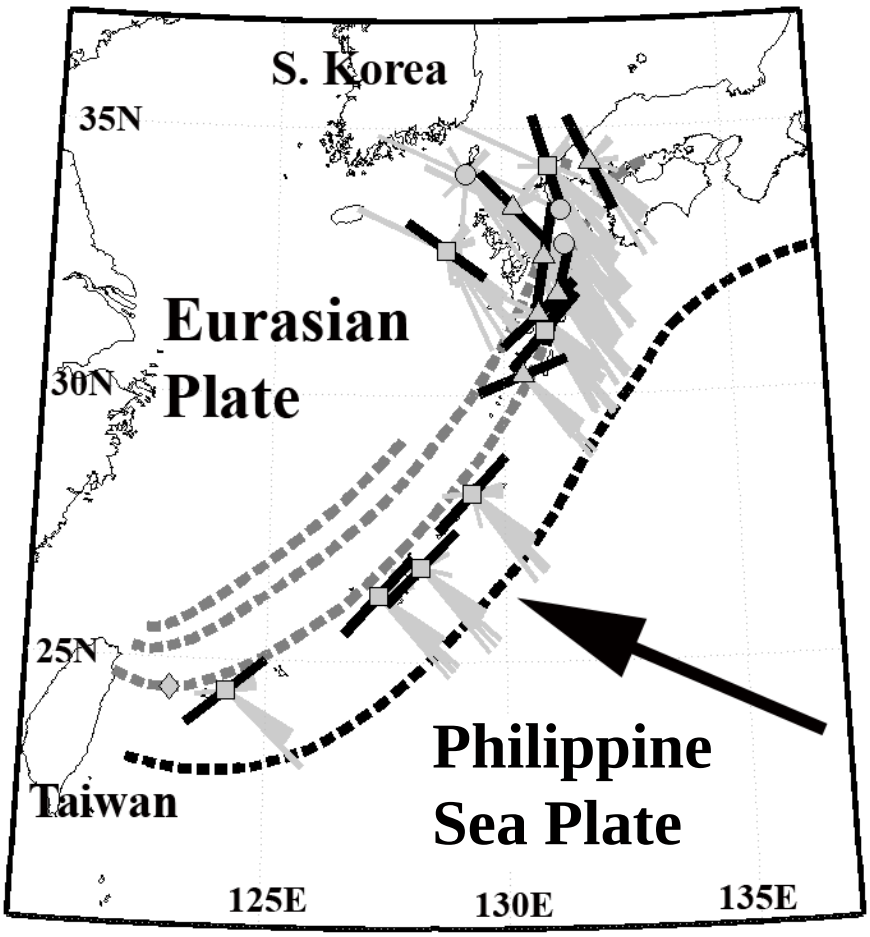
S. Korea
35N
Eurasian
Plate
30N
25N
Philippine
Sea Plate
Taiwan
125E
130E
135E

Figure 2

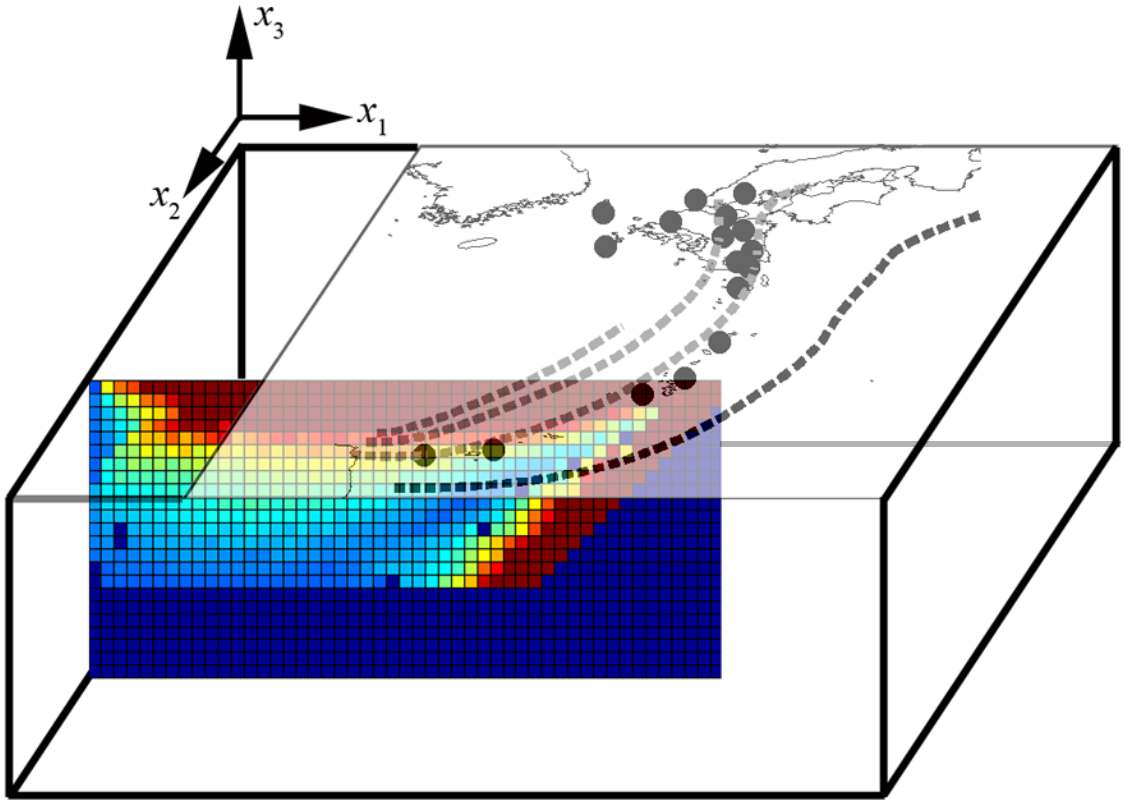

Figure 3

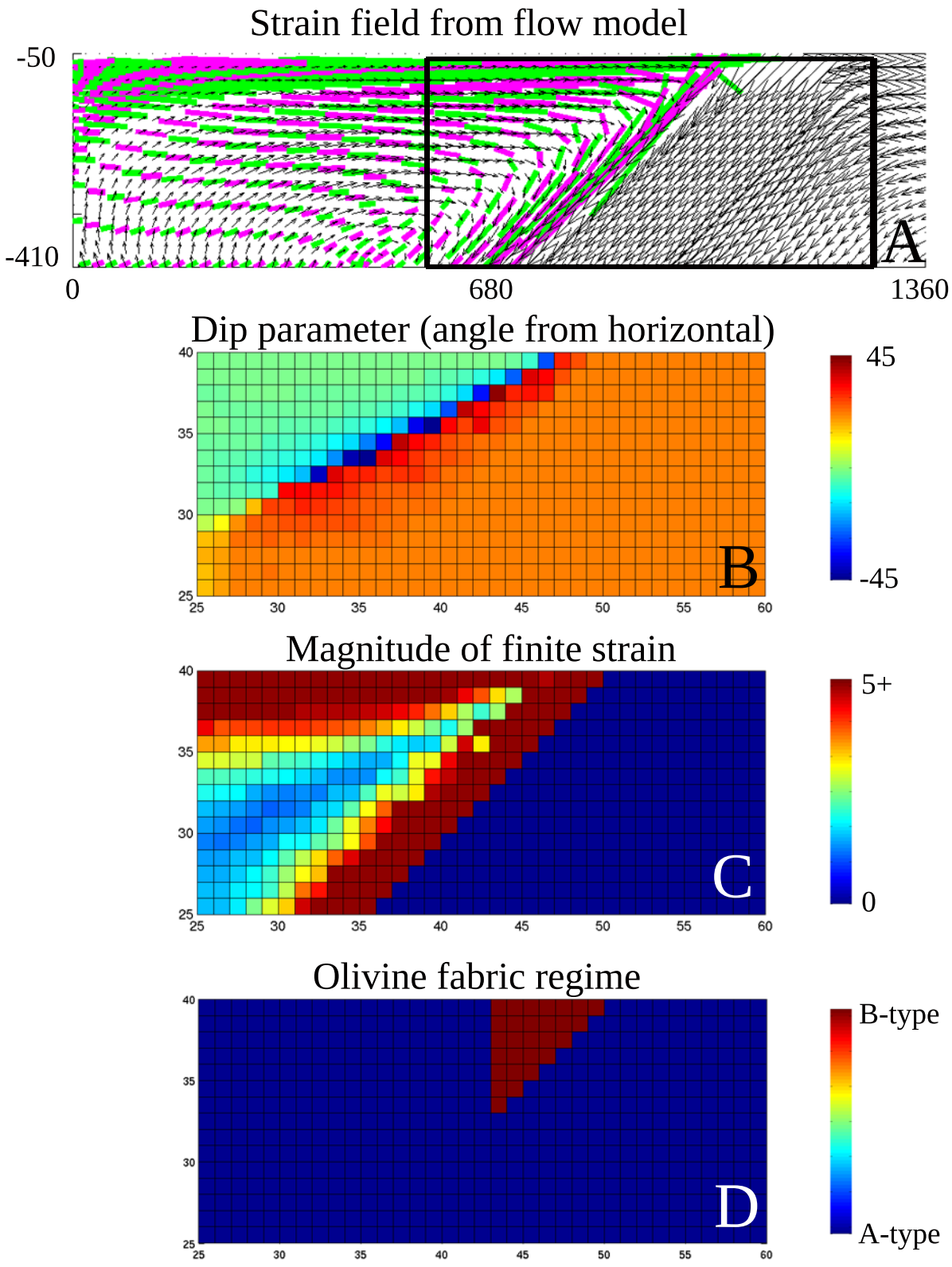
Strain field from flow model
-50
-410
0
680
1360
A
Dip parameter (angle from horizontal)
45
-45
B
Magnitude of finite strain
5+
0
C
Olivine fabric regime
B-type
A-type
D

Figure 4

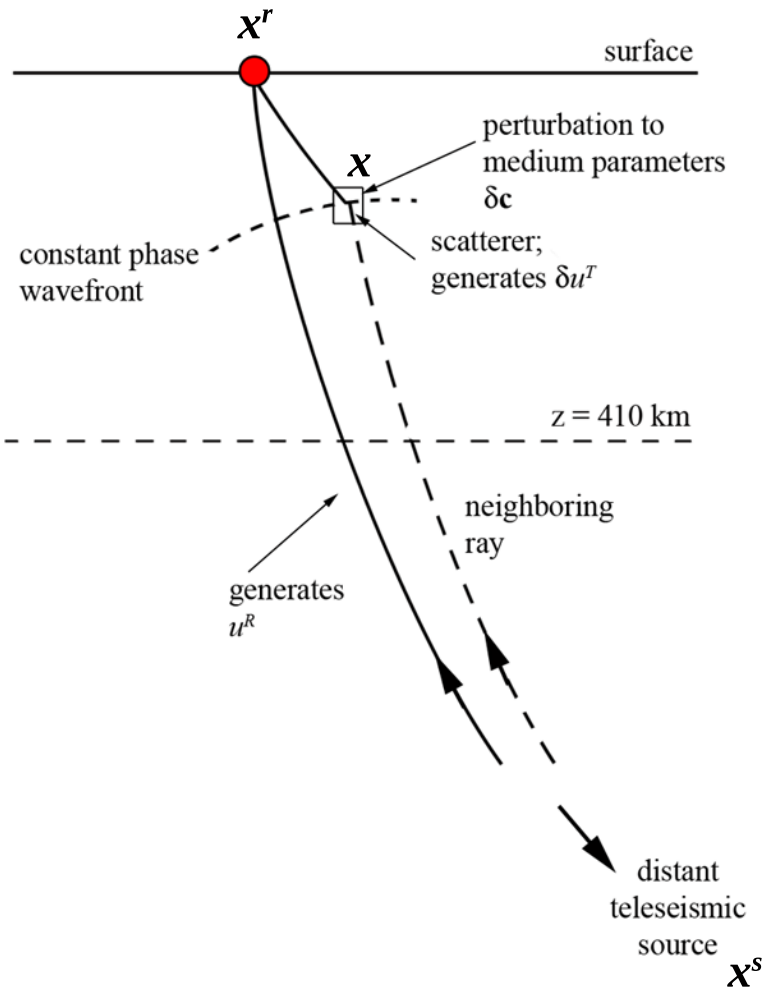
x^r
surface
perturbation to
medium parameters
δc
x
constant phase
wavefront
scatterer;
generates δu^T
z = 410 km
neighboring
ray
generates
u^R
distant
teleseismic
source
x^s

Figure 5

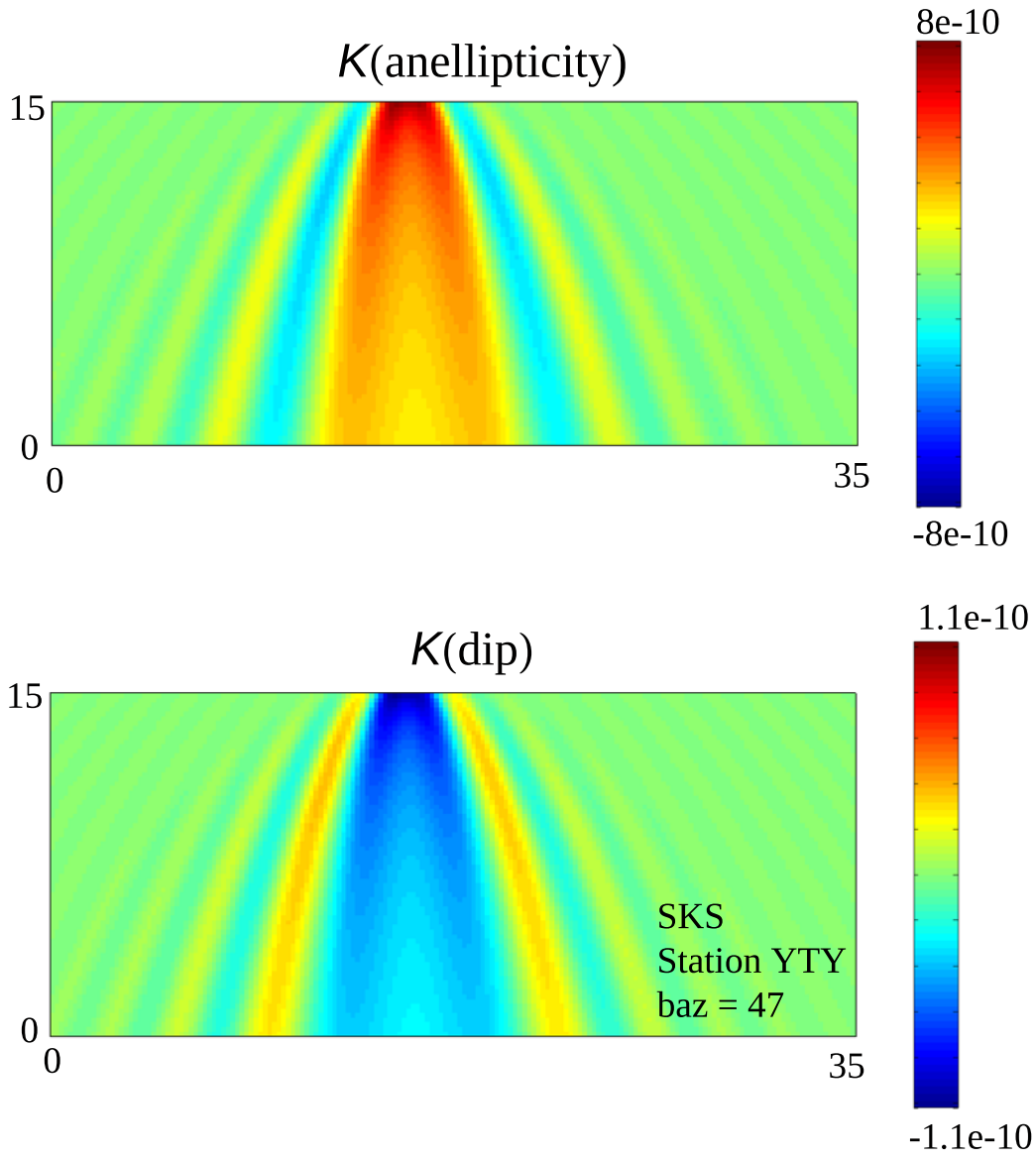
K(anellipticity)
15
0
0
35
8e-10
-8e-10
K(dip)
15
0
0
35
SKS
Station YTY
baz = 47
1.1e-10
-1.1e-10

Figure 6a

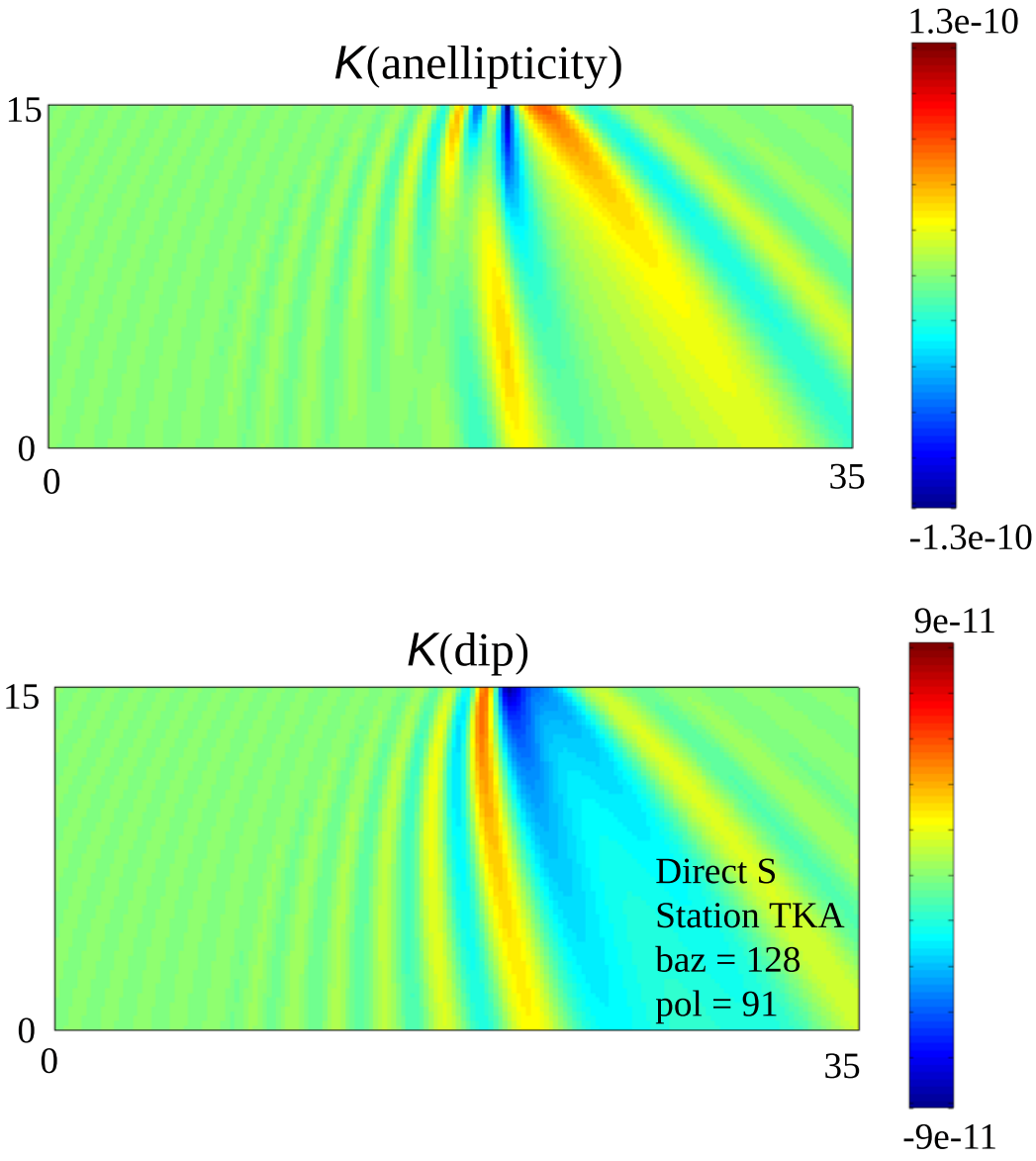
K(anellipticity)
15
0
0
35
1.3e-10
-1.3e-10
K(dip)
15
0
0
35
Direct S
Station TKA
baz = 128
pol = 91
9e-11
-9e-11

Figure 6b

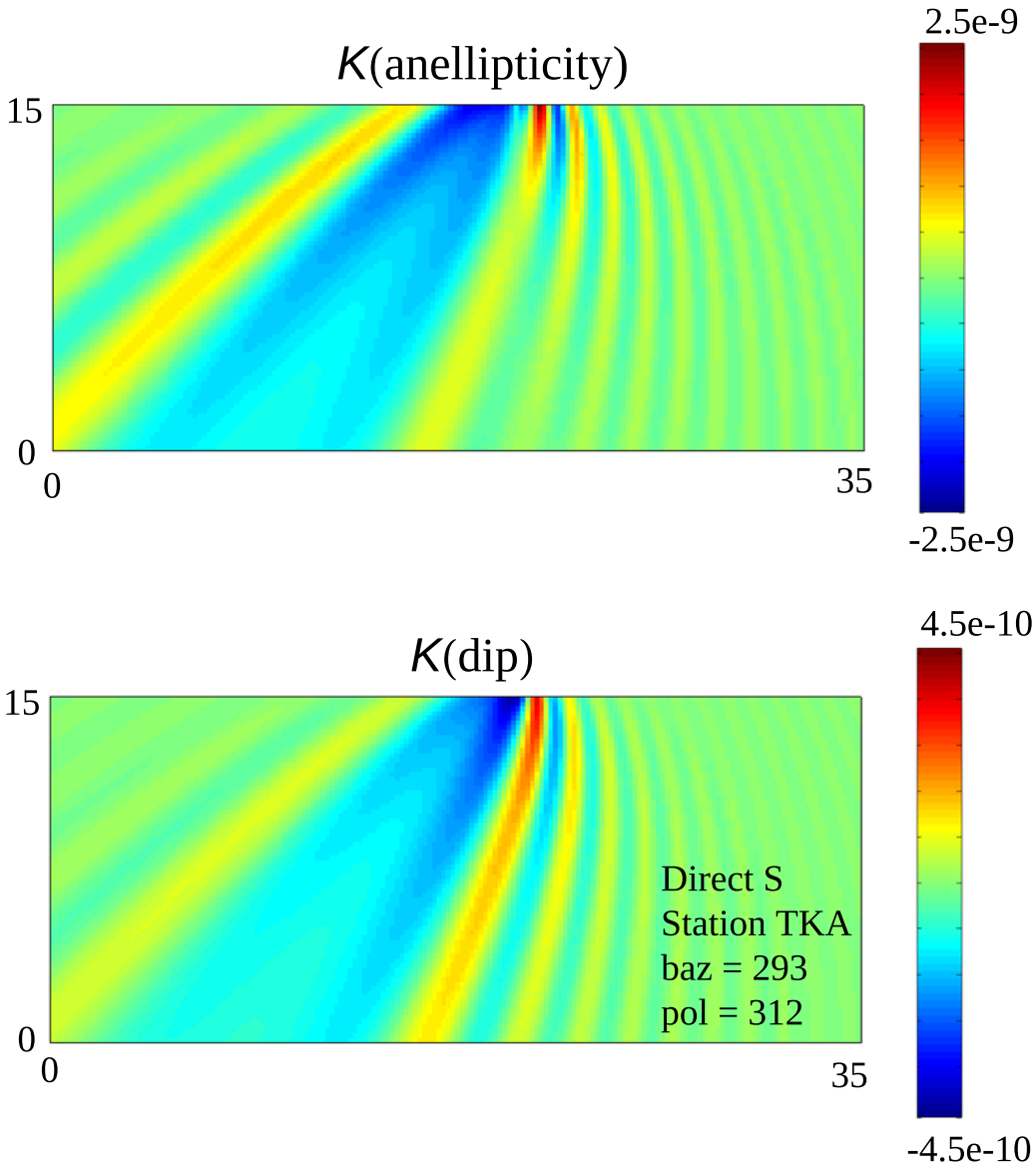
K(anellipticity)
15
0
0
35
2.5e-9
-2.5e-9
K(dip)
15
0
0
35
Direct S
Station TKA
baz = 293
pol = 312
4.5e-10
-4.5e-10

Figure 6c

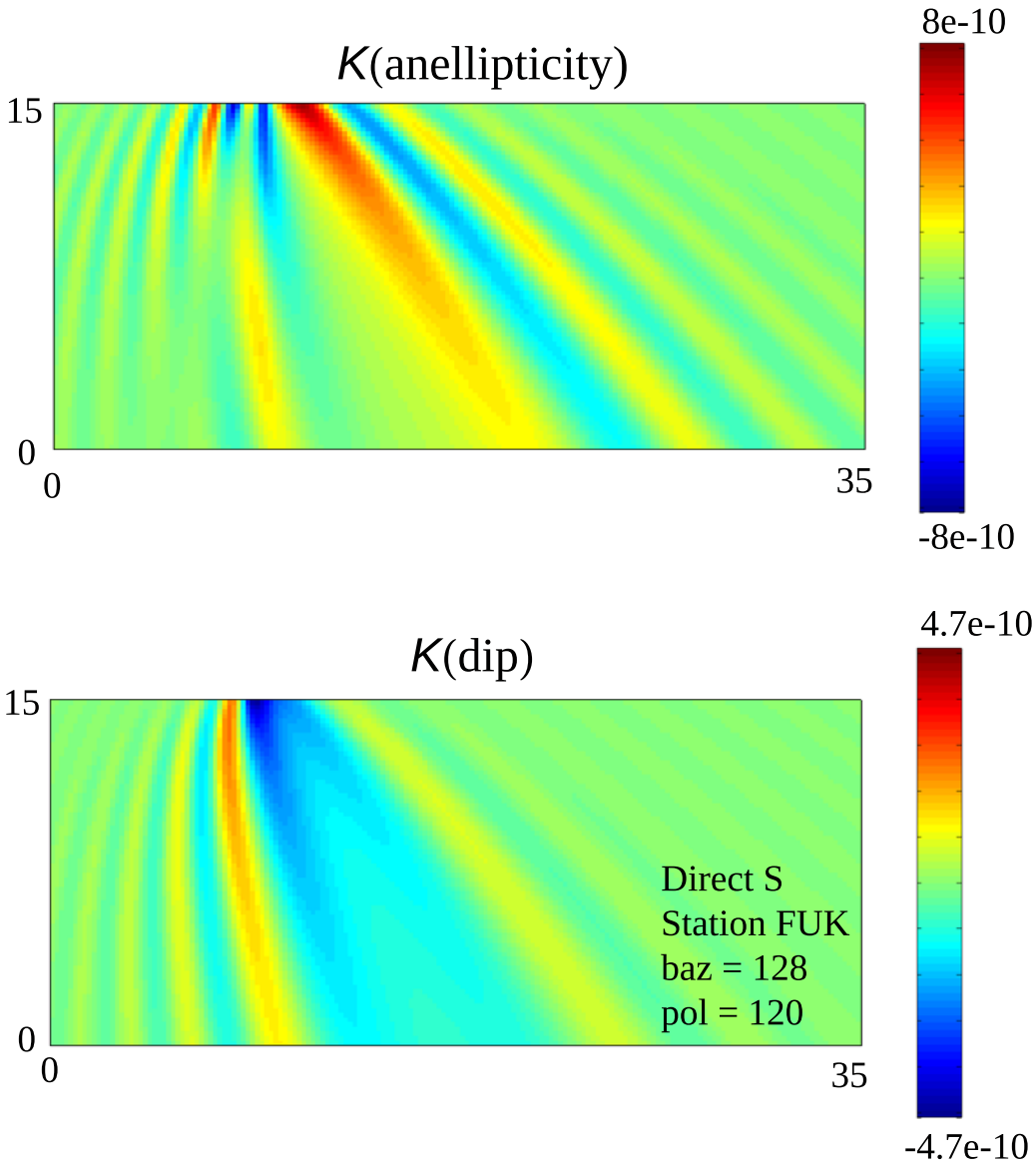
K(anellipticity)
15
0
0
35
8e-10
-8e-10
K(dip)
15
0
0
35
Direct S
Station FUK
baz = 128
pol = 120
4.7e-10
-4.7e-10

Figure 6d

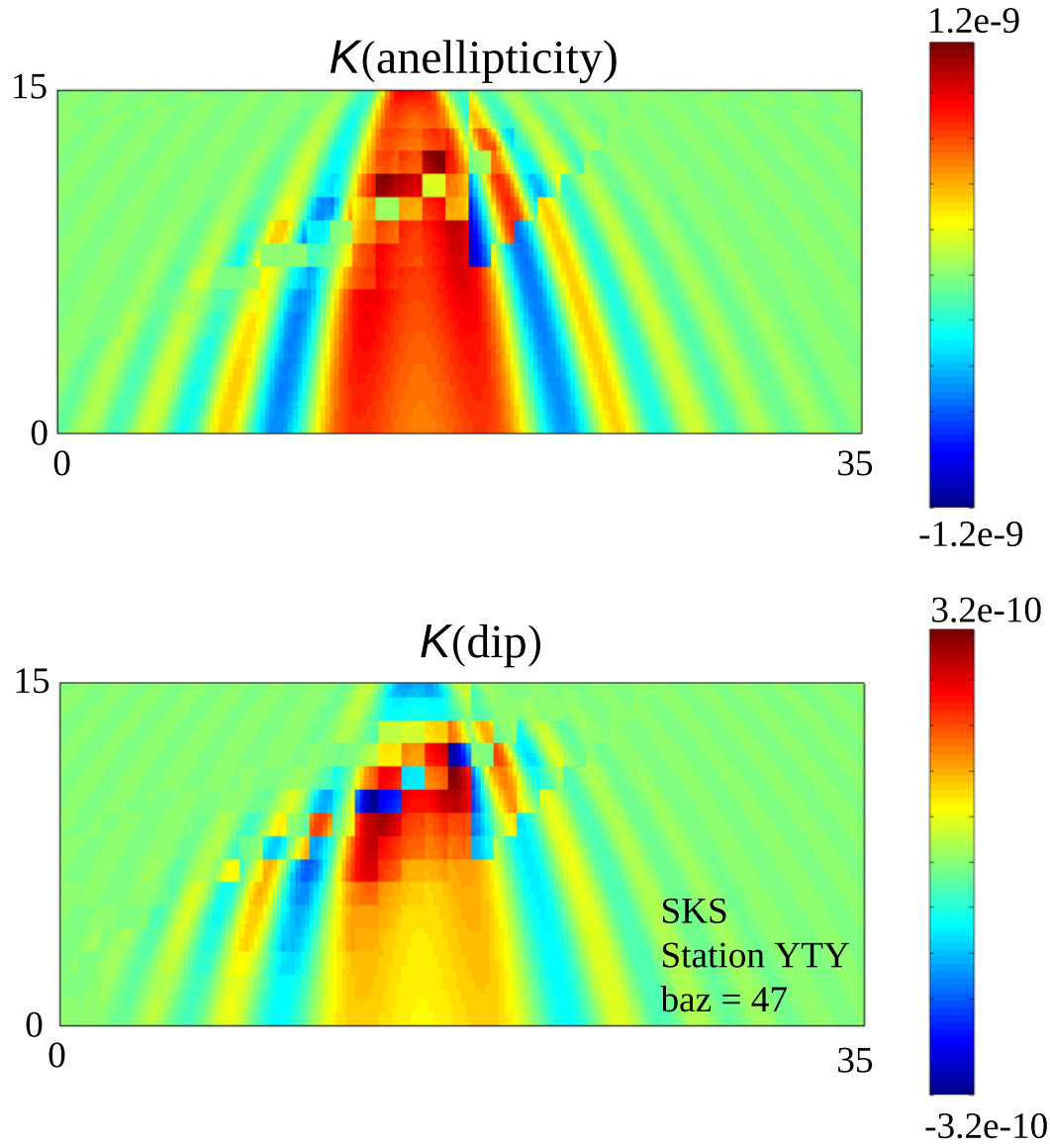
K(anellipticity)
15
0
0
35
1.2e-9
-1.2e-9
K(dip)
15
0
0
35
SKS
Station YTY
baz = 47
3.2e-10
-3.2e-10

Figure 7a

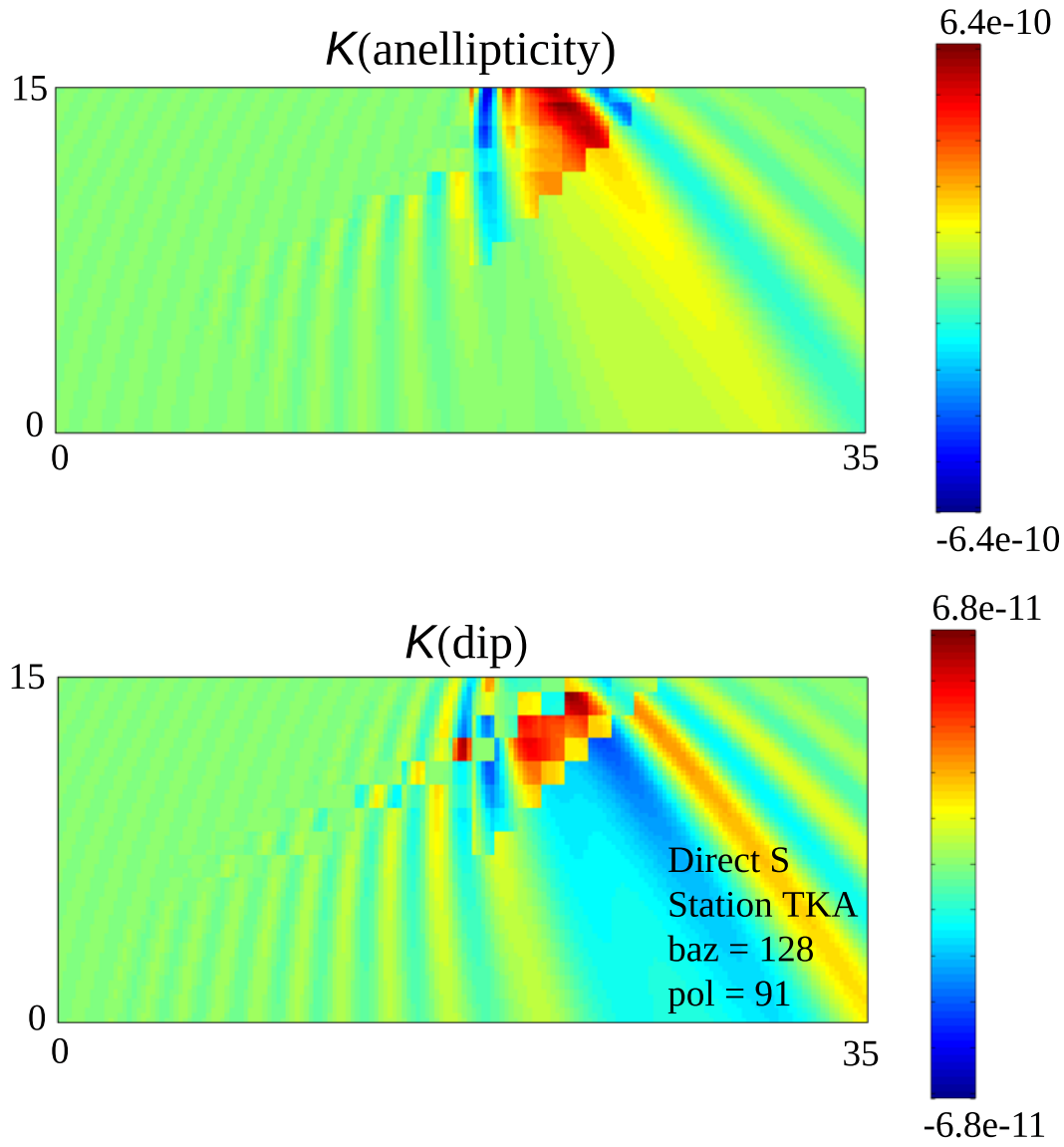
K(anellipticity)
15
0
0
35
6.4e-10
-6.4e-10
K(dip)
15
0
0
35
Direct S
Station TKA
baz = 128
pol = 91
6.8e-11
-6.8e-11

Figure 7b

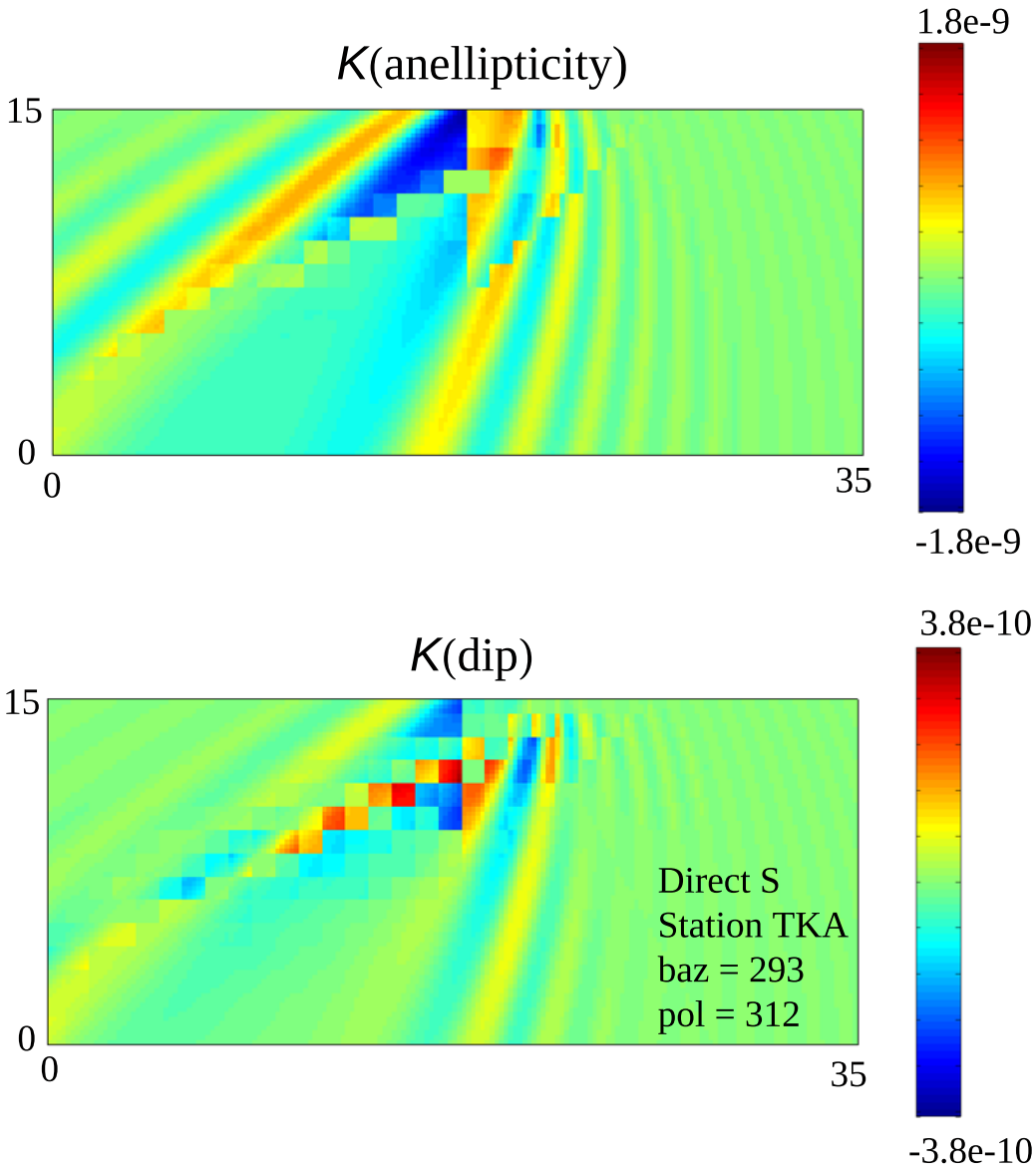
K(anellipticity)
15
0
0
35
1.8e-9
-1.8e-9
K(dip)
15
0
0
35
Direct S
Station TKA
baz = 293
pol = 312
3.8e-10
-3.8e-10

Figure 7c

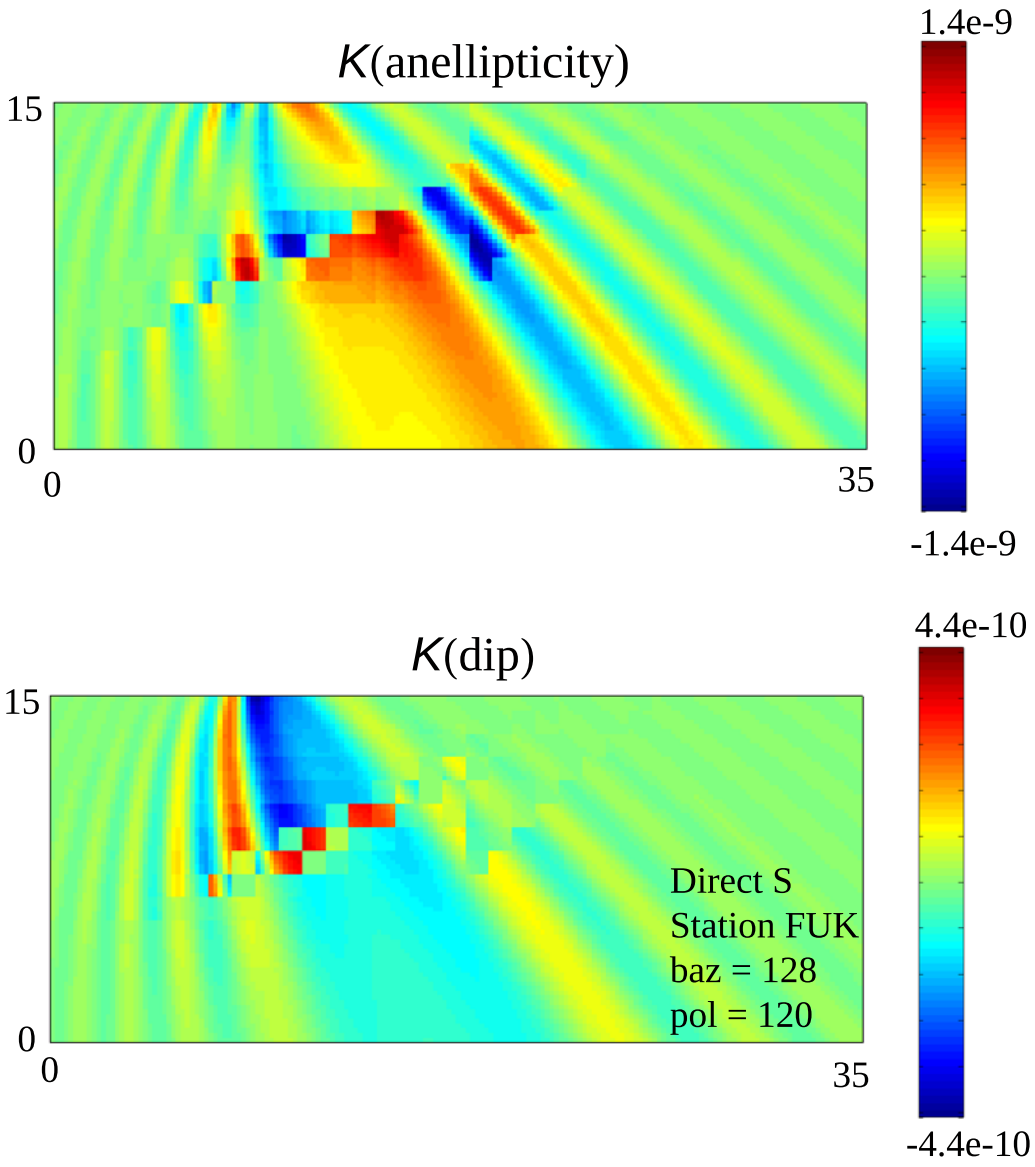
K(anellipticity)
15
0
0
35
1.4e-9
-1.4e-9
K(dip)
15
0
0
35
Direct S
Station FUK
baz = 128
pol = 120
4.4e-10
-4.4e-10

Figure 7d

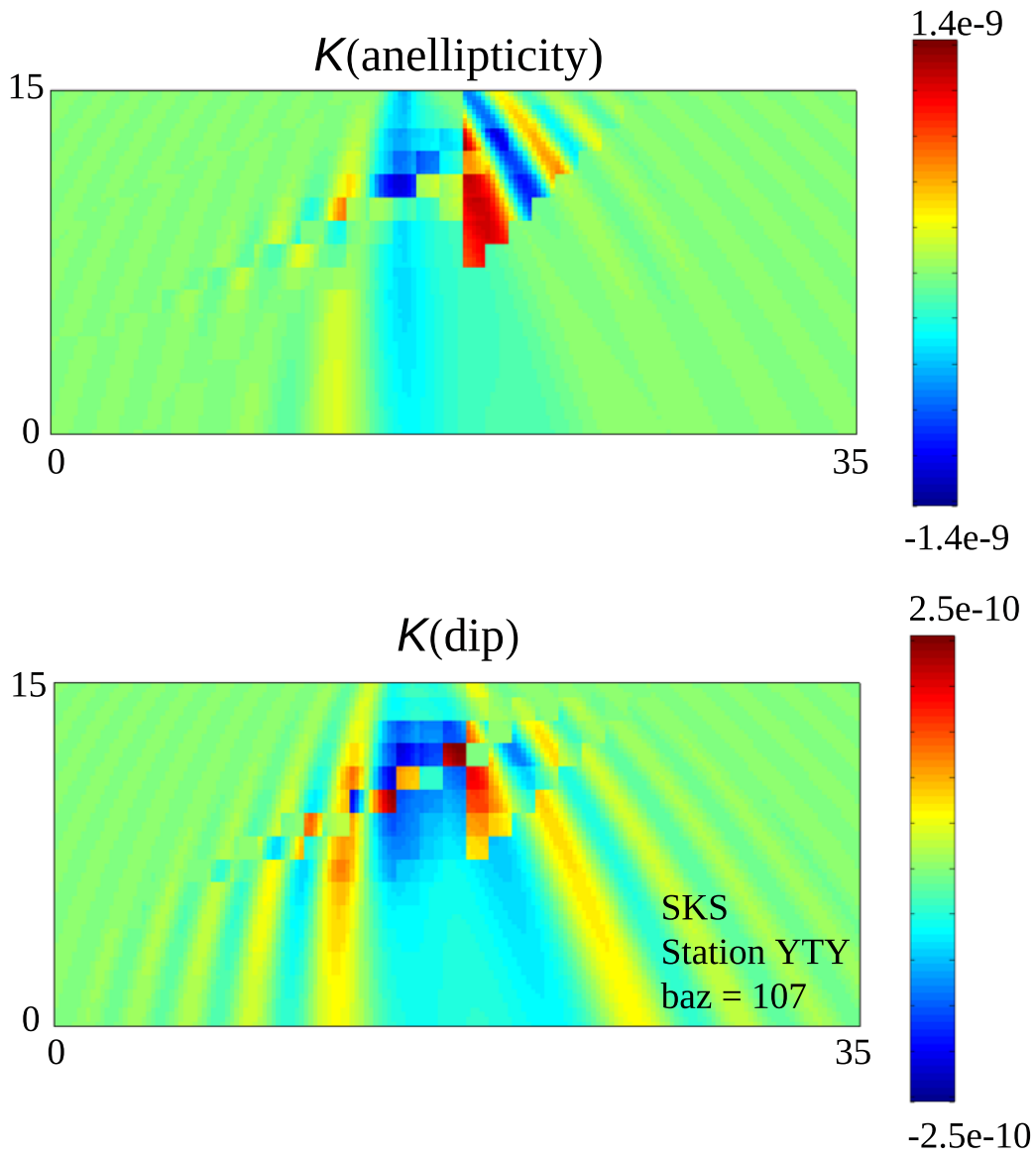
K(anellipticity)
15
0
0
35
1.4e-9
-1.4e-9
K(dip)
15
0
0
35
SKS
Station YTY
baz = 107
2.5e-10
-2.5e-10

Figure 8a

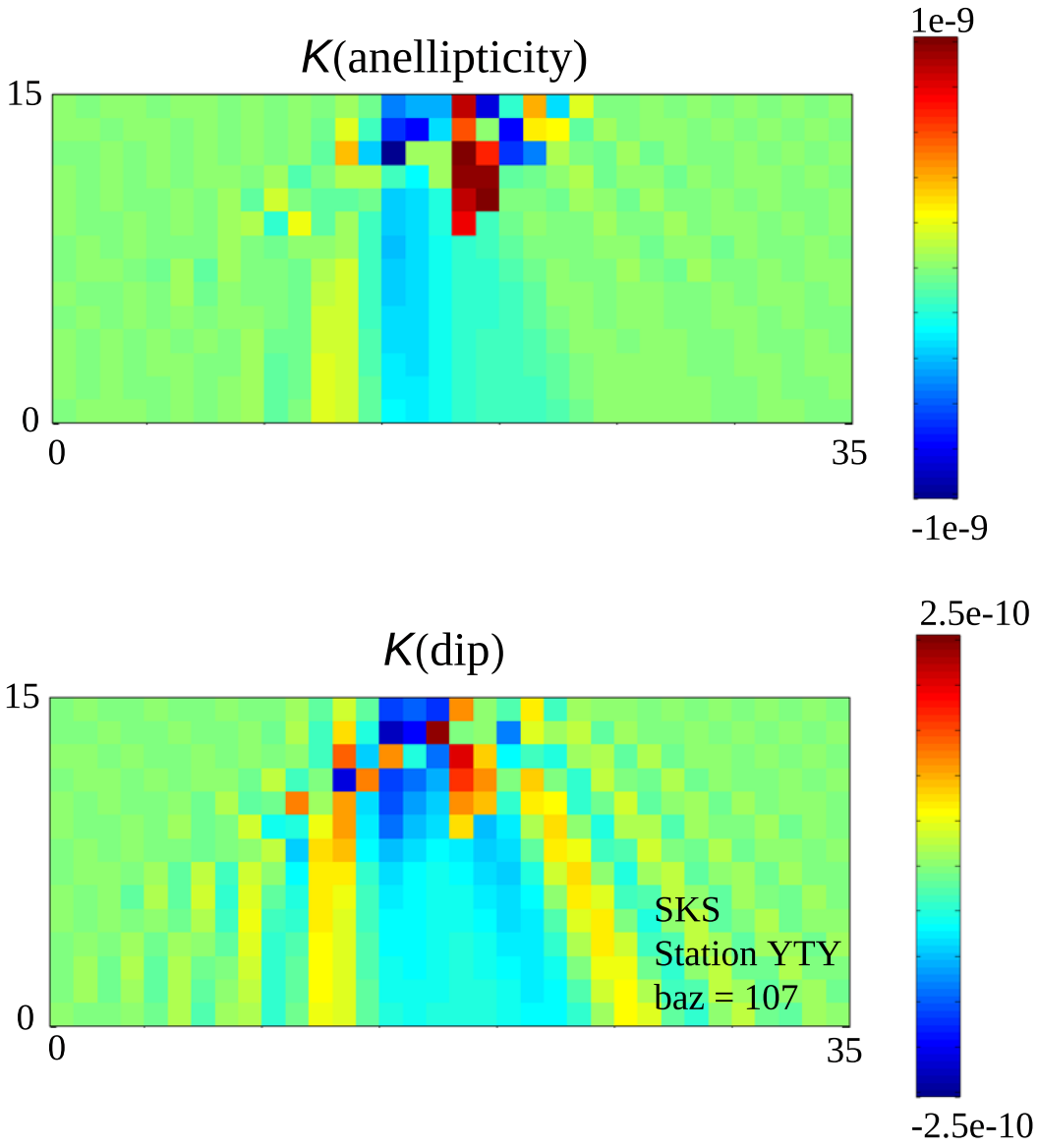
K(anellipticity)
15
0
0
35
1e-9
-1e-9
K(dip)
15
0
0
35
SKS
Station YTY
baz = 107
2.5e-10
-2.5e-10

Figure 8b

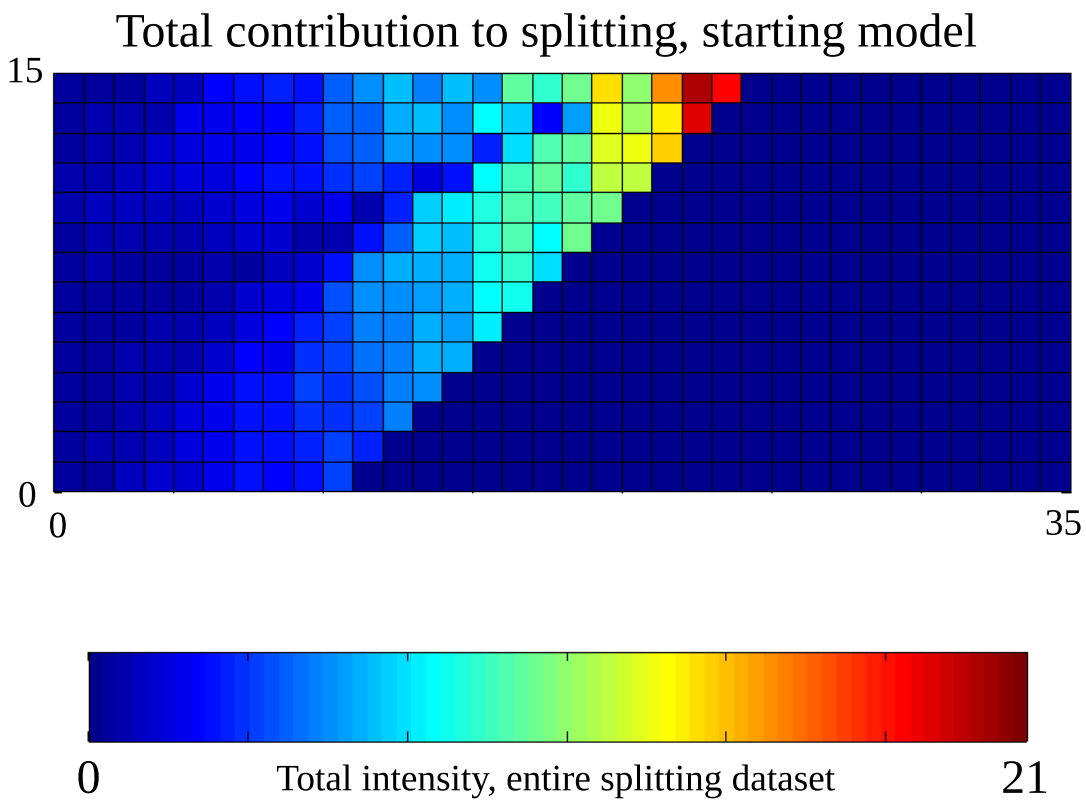
Total contribution to splitting, starting model
15
0
0
35
0
Total intensity, entire splitting dataset
21

Figure 9

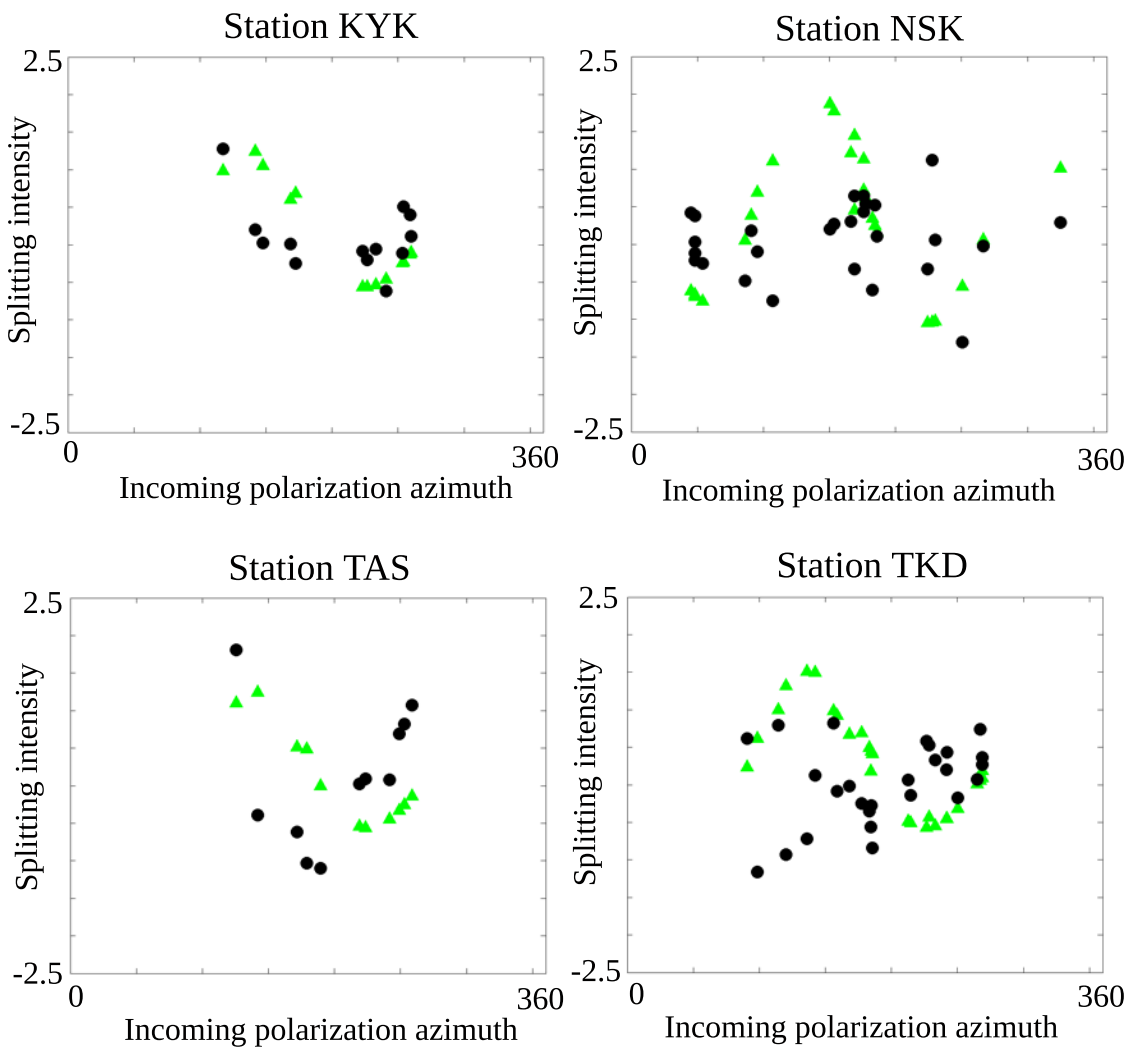
Station KYK
Station NSK
Station TAS
Station TKD
Splitting intensity
Incoming polarization azimuth
2.5
-2.5
0
360

Figure 10

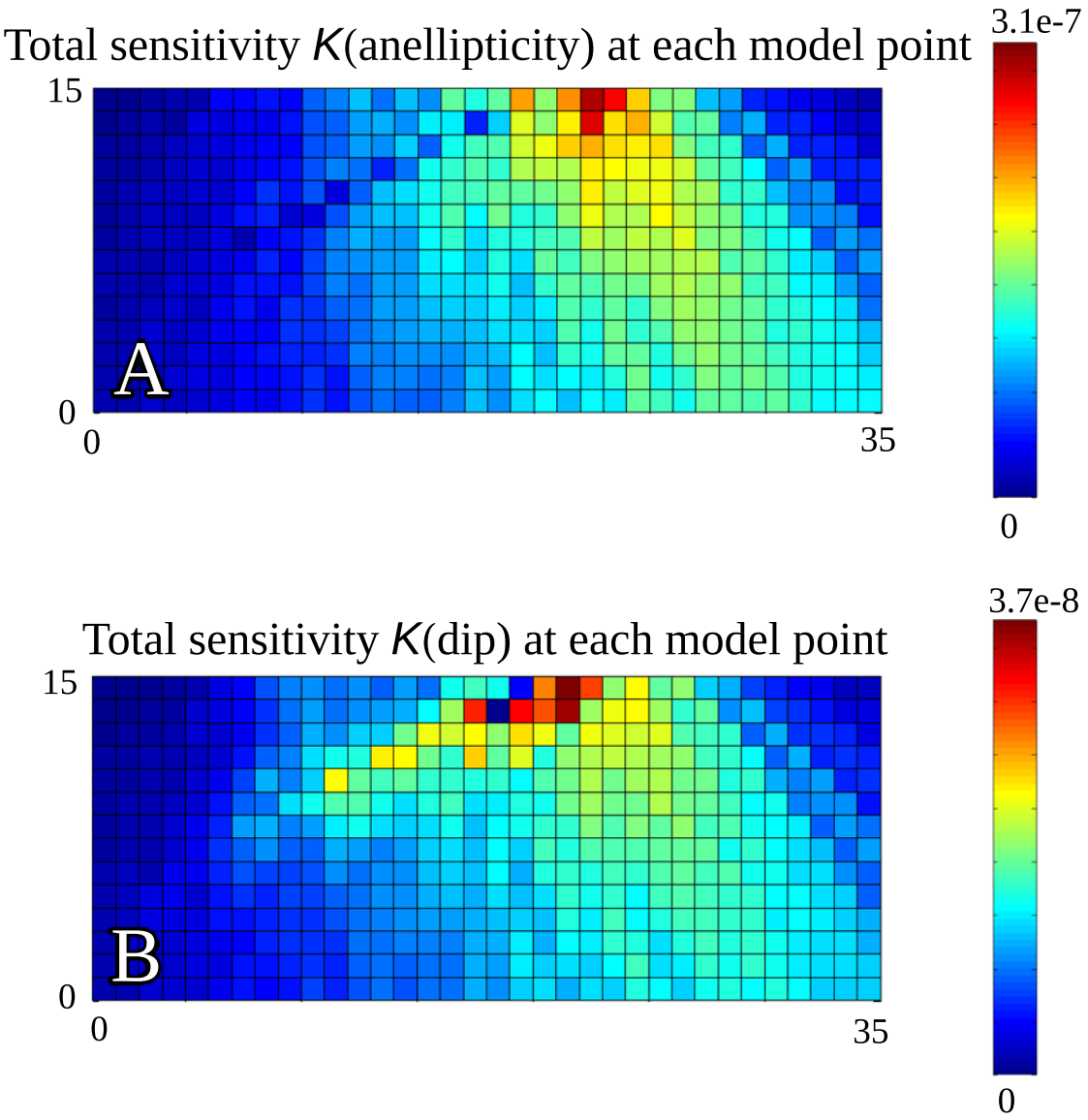
Total sensitivity K(anellipticity) at each model point
15
0
0
35
A
3.1e-7
0
Total sensitivity K(dip) at each model point
15
0
0
35
B
3.7e-8
0

Figure 11

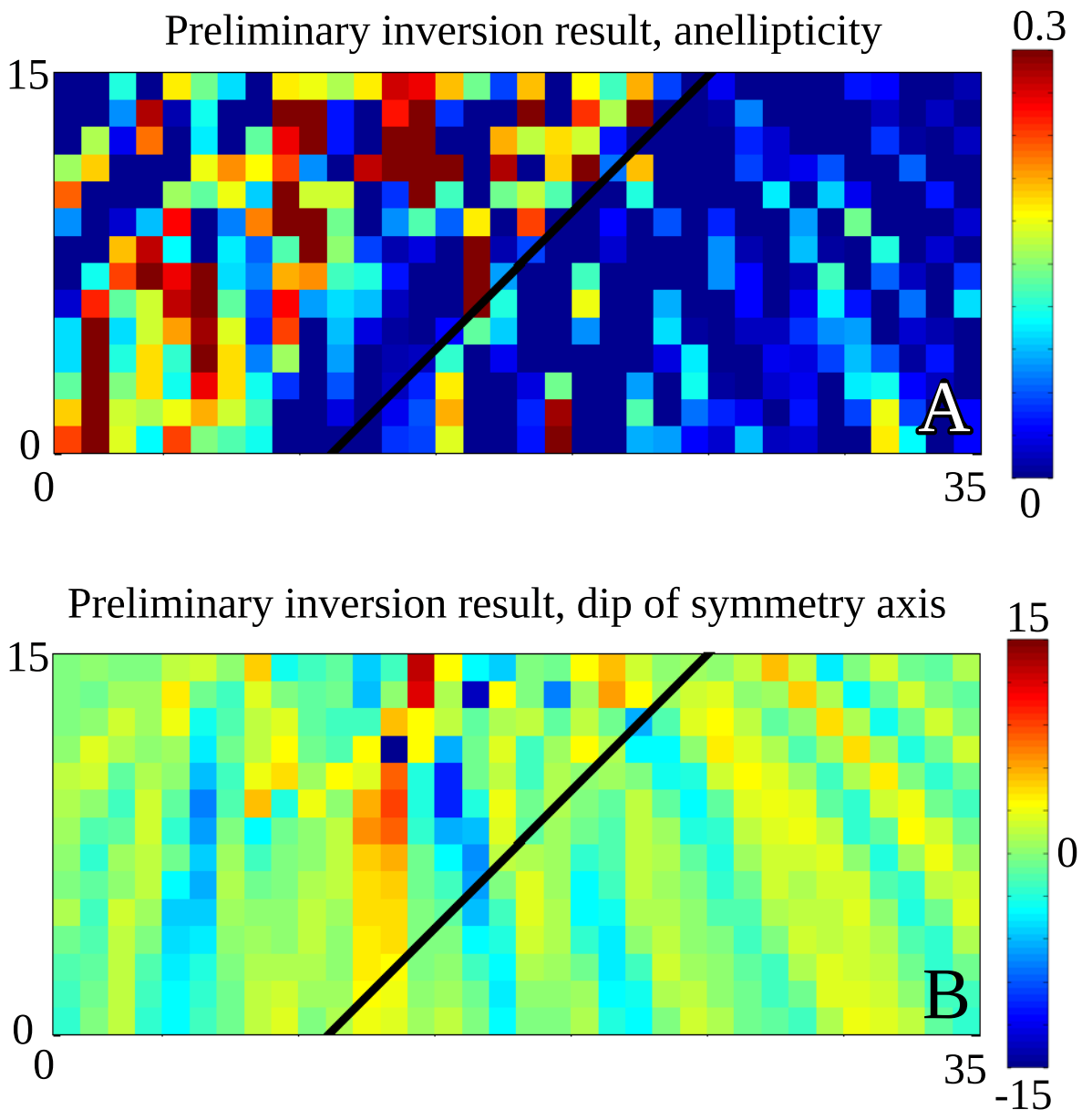
Preliminary inversion result, anellipticity
15
0
0
35
A
0.3
0
Preliminary inversion result, dip of symmetry axis
15
0
0
35
B
15
0
-15

Figure 12

Chapter 6

Deformation and anisotropy in (Mg,Fe)O: Implications for D''[1]

Abstract

Magnesiowüstite [(Mg,Fe)O] is an important constituent of the lower mantle, probably occupying about 20-25% of its volume. Laboratory and theoretical studies have shown this mineral to be highly elastically anisotropic at lower mantle pressures and temperatures. Thus, strain-induced formation of lattice preferred orientation (LPO) in magnesiowüstite is a candidate mechanism for the origin of anisotropic structure in D''. Although observations of seismic anisotropy within D'' are robust, both the occurrence and the style of that anisotropy are spatially variable. Two hypotheses have been offered to explain the observations of D'' anisotropy: LPO of intrinsically anisotropic minerals, or shape preferred orientation (SPO), perhaps in the form of horizontal layering or oriented inclusions. To investigate the first hypothesis, we performed confined simple-shear deformation experiments in the dislocation creep regime using a gas-medium deformation apparatus over a range of compositions: the MgO and FeO endmembers and three intermediate compositions. Samples were deformed at 1273-1473K, at a confining pressure of 300 MPa, to large shear strains (γ = 3.5-4.5) using deformation pistons cut at 45º. After deformation, the LPO was measured by electron backscatter diffraction

[1] In press as: Long, M. D., Xiao, X., Jiang, Z., Evans, B., Karato, S.-i., 2006. Lattice preferred orientation in deformed polycrystalline (Mg,Fe)O and implications for seismic anisotropy in D''. Phys. Earth Planet. Inter., in press.

(EBSD). The LPO produced varied for differing compositions, indicating the activity on individual slip systems and/or the nature of grain boundary migration in (Mg,Fe)O are affected by composition and/or homologous temperature. We predicted seismic anisotropy from the measured LPOs and theoretically determined single-crystal elastic constants. Anisotropic behavior predicted from LPO agrees well with observations of D'' anisotropy, so the LPO hypothesis appears to satisfy the seismological constraints. Our calculated anisotropy patterns suggest that if D'' anisotropy is due to LPO of (Mg,Fe)O, then azimuthal variations in anisotropy in the horizontal plane should be present. Such azimuthal variations are not generally predicted for SPO-type hypotheses, and this may provide a means for distinguishing the cause of D'' anisotropy.

1. Introduction

The D'' layer comprises the bottom 150-300 km of the Earth's mantle and is characterized by unusually small vertical gradients in seismic velocity, laterally heterogeneous velocity structure, and probably by significant thermal and/or chemical heterogeneities (see Wysession et al., 1998, for a review). An understanding of the properties and dynamical processes associated with the core-mantle boundary (CMB) is essential to unravel the nature of mantle convection and coupling between the mantle and the core. To date, seismological observations have provided the strongest constraints on the nature of D'', and among the most important of these have been observations of seismic anisotropy. Although most of the lower mantle appears to be isotropic, at least on the scale of seismic wavelengths (e.g. Meade et al., 1995), several studies have suggested various styles of anisotropy in D'', beginning with Mitchell and Helmberger (1973),

Doornbos et al. (1986), and Cormier (1986). Because anisotropic structures in the Earth's mantle are thought to result from permanent strain, observations of seismic anisotropy in D'' can provide useful insights into deformation geometry.

Although there is ample seismological evidence for anisotropy in D'', it appears that neither the style of anisotropy nor its spatial distribution is uniform. In studies of D'' anisotropy using core-diffracted shear waves (S_{diff}), Vinnik et al. (1989b, 1995, 1998) have noted splitting of S_{diff} and anomalously high SV_{diff} amplitudes and suggested that elastic anisotropy was responsible. Observations of splitting in pre-diffracted *S* phases turning in the lowermost mantle have been interpreted in terms of transverse isotropy (that is, hexagonal symmetry with a vertical symmetry axis). Beneath the northern Pacific and Alaska (Lay and Young, 1991; Matzel et al., 1996; Garnero and Lay, 1997; Fouch et al., 2001), North America and the Caribbean (Kendall and Silver, 1996; Garnero and Lay, 2003), and the Indian Ocean (Ritsema, 2000), there is evidence for anisotropy in D'', apparently with a vertical axis of symmetry. Beneath the southern Pacific, it appears that the lowermost mantle is isotropic, while beneath the central Pacific there is evidence for highly spatially variable anisotropy, possibly with a horizontal axis of symmetry (that is, azimuthal anisotropy) (Lay et al., 1998). These spatial distributions of anisotropy have led to speculation that the mechanisms of anisotropy generation differ in regions associated with mantle upwelling and downwelling (Kendall, 2000).

In the upper mantle, it is generally accepted that seismic anisotropy results from lattice preferred orientation (LPO) produced by dislocation creep of olivine, the major upper mantle constituent (e.g. Zhang and Karato, 1995). Two different mechanisms for generation of anisotropy in D'' have been proposed. First, LPO of anisotropic lower

mantle minerals could result in D'' anisotropy (Karato, 1998a, b), provided that deformation occurs by dislocation creep, rather than diffusion creep (see, for example, Karato, 1989). The observation that the lower mantle is largely isotropic has been interpreted as evidence that the dominant deformation mechanism is diffusion creep or superplasticity (Karato et al., 1995). However, recent geodynamical models (McNamara et al., 2001, 2002) have shown that dislocation creep may occur in the lowermost mantle, due to high stresses associated with the collision of subducted slabs with the CMB.

A second hypothesis suggests that anisotropy in D'' might result from shape preferred orientation (SPO) of inclusions within a matrix of differing elastic properties. For example, Kendall and Silver (1998) considered models consisting of oriented cigar-shaped or disk-shaped inclusions, due to the infiltration of core material or partial melting, and of horizontal layering, due to the presence of a subducted slab "graveyard." These workers concluded that SPO could explain the seismological data well. The SPO mechanism has also been considered by Russell et al. (1998), Garnero and Lay (2003), and Moore et al. (2004). Consensus on which model for anisotropy best explains the seismic data and available dynamical constraints, however, has not been forthcoming, partly because little experimental work has been done to address the formation of LPO in lower mantle materials.

Based on a bulk chemical composition model for the upper mantle (the pyrolite model), the lower mantle should consist of approximately 70% Mg-perovskite, $(Mg,Fe)SiO_3$, approximately 20-25% magnesiowüstite (Mg,Fe)O, and less than 10% Ca-perovskite, $CaSiO_3$ (Ringwood, 1991). New experimental evidence suggests that Mg-perovskite undergoes a phase change to a post-perovskite phase at approximately 115-

125 GPa (Murakami et al., 2004; Oganov and Ono, 2004; Shim et al., 2004). Thus, the dominant phase in the D'' layer may well be post-perovskite instead of perovskite. The question of which phase(s) are most likely to contribute to LPO-induced anisotropy becomes important. Karato (1998a) argued that (Mg,Fe)O is likely to be more elastically anisotropic at D'' conditions than perovskite (see also Wentzcovitch et al., 1998), although both magnesiowüstite and perovskite are probably anisotropic at these conditions (Isaak et al., 1989; Karki et al., 1997a, 1997b). Additionally, the creep strength of magnesiowüstite in the lower mantle is probably much smaller than that of perovskite (Yamazaki and Karato, 2001) and lower mantle deformation may tend to be partitioned into (Mg,Fe)O, the weaker phase. Therefore, the development of LPO in (Mg,Fe)O during simple shear deformation, probably the dominant geometry at the base of the mantle, could be very important for generating seismic anisotropy in D''. However, it is important to keep in mind that LPO in post-perovskite may also play a role in generating D'' anisotropy, and new experimental and theoretical results should shed light on the relative importance of post-perovskite and magnesiowüstite.

The importance of LPO in magnesiowüstite as a possible mechanism for generating seismic anisotropy in the lowermost mantle was first pointed out by Karato (1998a,b), but at this time little experimental work had addressed the development of fabric in (Mg,Fe)O. Stretton et al. (2001) investigated the mechanical behavior and resulting LPO of $(Mg_{0.8},Fe_{0.2})O$ using uniaxial compression tests, and found that significant LPO develops. Simple shear deformation experiments were first performed by Yamazaki and Karato (2002), who carried out a preliminary investigation of LPO development in $(Mg_{0.75},Fe_{0.25})O$ and FeO aggregates deformed in the dislocation creep

regime. The deformation of the MgO endmember was investigated by Merkel et al. (2002) at pressures of the lower mantle, although their experiments were carried out at ambient temperature. Shear deformation experiments on $(Mg_{0.8},Fe_{0.2})O$ using a torsional configuration to very high strains (as large as $\gamma = 15.5$) were carried out by Heidelbach et al. (2003). Although several studies in the past few years have addressed the development of LPO in magnesiowüstite of various compositions, the effect of iron content on LPO has not yet been investigated systematically. In the work reported here, an extension of that of Yamazaki and Karato (2002), we performed simple shear deformation experiments of MgO, FeO, and three intermediate compositions at several homologous temperatures ($T/T_{melting}$). The goal of this study is to investigate the effects of composition and homologous temperature on LPO development and to apply the experimental results to the problem of anisotropic structure in the lowermost mantle.

2. Experimental Procedure

2.1 Sample preparation

Samples were synthesized from powders of oxide reagents. MgO and Fe_2O_3 powders were mechanically mixed and ground in molar ratios yielding the desired compositions (MgO, $(Mg_{0.75},Fe_{0.25})O$, $(Mg_{0.50},Fe_{0.50})O$, $(Mg_{0.25},Fe_{0.75})O$, and FeO). For all compositions except the MgO endmember, powders were then put into a furnace in an alumina crucible at 1273K for ~ 8-12 hours with a CO_2/H_2 gas mixture to buffer oxygen fugacity within the wüstite stability field. After heating, the powders were re-mixed and re-heated at least once to achieve nearly complete reaction. The MgO powder and the conditioned (Mg,Fe)O and FeO powders were then cold-pressed using a split die into an

iron jacket with a uniaxial pressure of ~ 20 MPa. The cold-pressed samples were isostatically hot-pressed in a gas-medium (Paterson) apparatus at 1473K and 300 MPa for 200 minutes. During hot-pressing, the oxygen fugacity was buffered by the iron jacket. An optical micrograph of $(Mg_{0.50},Fe_{0.50})O$ starting material is shown in Figure 1. Because grain growth is slower in MgO than FeO, starting grain sizes for pure MgO (~ 3-5 μm) were much smaller than that for the intermediate compositions (~ 30-70 μm). Although the starting grain size for FeO was not observed due to a pressure vessel leak early in the initial hot-press, we suppose it to be large, as the grain size of FeO deformed at 1473K approached 300-400 μm. Except for FeO, the compositions of all starting materials were analyzed on a microprobe to ensure that an (Mg,Fe)O solid solution had been formed, that the correct molar ratios had been achieved, and that no contamination from the alumina crucibles occurred.

2.2 Deformation experiments

Slices ~ 1 mm thick were cut at an angle of 45° to the long axis from each of the cylindrical hot-pressed mixtures. For two of the experiments, the slices were then cut in half parallel to their thinnest dimension, and a strain marker of 0.1 mm-thick molybdenum foil was inserted. The sample was then sandwiched between two thoriated tungsten deformation pistons, cut at 45º. The surfaces of the deformation pistons had 40 μm deep grooves, spaced ~ 100-200 μm apart, to prevent slip at the sample-piston interface. The pistons and sample were put into an iron jacket and shear deformation was achieved by the uniaxial compression of alumina and zirconia pistons. A summary of the

conditions for each deformation experiment is shown in Table 1, and a schematic diagram of the setup for the deformation experiments is shown in Figure 2.

Deformation experiments were carried out on all compositions in a gas-medium Paterson apparatus at 1473K and confining pressure of 300 MPa. One additional experiment was carried out on a FeO sample at 1273K. For each experiment, the pressure was raised to ~ 220-235 MPa, and then the temperature was raised at a rate of 1.5K per second, resulting in a final pressure of 300 MPa. After the desired pressure and temperature conditions were reached, the sample was annealed for one hour to obtain good contact between the sample and pistons. All experiments were carried out at a constant axial displacement rate of 0.0118 mm per minute, and all experiments achieved a total strain of γ = 3.5-4.5 (corresponding to 3.5-4.5 mm of shear displacement for a 1 mm thick sample). We compared our experimental conditions (starting grain size, temperature, strain rate, and shear stress) with the deformation mechanism maps in Frost and Ashby (1982) and Karato (1998b), and all experimental conditions should fall within the dislocation creep regime. The large amount of total shear strain should ensure that the LPO pattern has reached a nearly steady state; although Heidelbach et al. (2003) showed that larger strains are needed to obtain truly steady-state fabrics in (Mg, Fe)O, Yamazaki and Karato (2002) showed that fabrics and the resulting anisotropy change very little after strains of γ = 4-5.

2.3 Microstructural observations

After deformation, the samples and pistons were cut into two halves parallel to the shear direction and perpendicular to the shear plane. Samples were polished with

progressively smaller grit sizes, ending with 0.1 μm diamond paste and Syton colloidal silica solution. LPO was measured using the electron backscatter diffraction method (EBSD) (Dingley and Randle, 1992) on a scanning electron microscope (SEM). EBSD measurements were made on a Phillips XL30 SEM at Yale University. For five of the six samples, crystal orientations were determined in automatic beam scanning mode (Wright, 2000) with a step size slightly bigger than the average grain size. For the FeO sample deformed at 1473K, the large grain size made automatic scanning impossible, and the orientation of every grain in the sample was measured and indexed manually. The deformed samples were also examined with an optical microscope and rotation and elongation of grains consistent with the sense of shear were observed. An optical micrograph of a deformed FeO sample (deformed at 1273K) is shown in Figure 1.

3. Results

3.1 Mechanical data

We converted the raw force and displacement data into stress-strain curves and measured the steady-state stress as a function of homologous temperature. It is important to note that mechanical data from shear deformation experiments are subject to large uncertainties due to the effects of heterogeneous deformation, change in sample thickness, etc. The measured force was converted into stress by dividing by the sample area and the change in sample area with increasing strain was taken into account in this calculation. The measured displacements were converted into strain using the previously measured stiffness of the Paterson apparatus (61.5 kN/mm in compression). Additionally, we apply a correction for the stiffness of the iron jacket by estimating the cross-sectional

area of the iron jacket for each experiment and using published data for the strength of metallic iron (Frost and Ashby, 1982). A plot of log(σ) vs. homologous temperature T/T_m is shown in Figure 3.

A comparison of the stress/temperature curve in Figure 3 with the deformation mechanism maps for MgO in Frost and Ashby (1982) for various grain sizes (initial grain sizes in our experiments ranged from ~ 5 μm to perhaps 150 μm, see Table 1) confirms that our experimental conditions should lie in the dislocation or power-law creep regime. Deformation in the dislocation creep regime should be governed by the relation

$$d\varepsilon/dt = A\sigma^n \exp(-Q/RT),$$

where ε is strain, σ is stress, n represents the stress exponent, T is the temperature, and A and β are constants (see Evans and Kohlstedt, 1995, for an overview of the dislocation creep constitutive relations). All of our experiments were done at a constant temperature of 1473K (with one exception) and at a constant strain rate. However, because of the dramatically different melting temperatures of the MgO and FeO endmembers, we covered a range of homologous temperatures ($T/T_{melting}$). The above equation predicts a linear relationship between log(stress) and the homologous temperature, which is what we observe in Figure 3. Because the curve in Figure 3 does not flatten, there is no indication that there is a change in deformation mechanism at different homologous temperatures. Dislocation creep is, of course, also indicated by our observations of strong lattice preferred orientation during our experiments (see below).

3.2 Microstructural observations

In Figure 4, a dot map showing all measured crystal orientations for the [001], [011], and [111] axes of the MgO sample is shown, along with the corresponding pole figure plot of the calculated texture. The texture is represented by smoothing the individual orientation measurements with a Gaussian function with a 15° half-width. Pole figures for all six samples are shown in Figure 5. For MgO, the observed texture is quite distinctive, with the [001] directions concentrated roughly in the direction of shear, in the shear plane perpendicular to the direction of shear, and orthogonal to the shear plane. However, the areas of [001] concentration parallel to the shear direction and orthogonal to the shear plane are tilted by ~ 15-20º, a feature that had also been observed in other materials such as olivine (e.g. Zhang and Karato, 1995). This tilt can be observed for all samples except FeO. The pole figures for the [011] and [111] crystallographic directions also show distinctive areas of high concentrations. The observed fabric for $(Mg_{0.75},Fe_{0.25})O$ is quite similar to that of MgO, although the alignment of the [011] and [111] directions in $(Mg_{0.75},Fe_{0.25})O$ is less strong than for MgO. However, there is an interesting transition in fabric from $(Mg_{0.75},Fe_{0.25})O$ to $(Mg_{0.50},Fe_{0.50})O$. For the 50% Fe composition, the concentration of the [001] axis appears to be spread over larger areas. Additionally, there is no longer a peak in [001] concentration in the shear direction or contained in the shear plane, but perpendicular to the shear direction. Instead, these two orthogonal directions of [001] axes appear to be shifted in their plane by about 45º. For the $(Mg_{0.25},Fe_{0.75})O$ composition, a peak in the [001] axis concentration can still be seen roughly orthogonal to the shear plane (tilted ~ 15-20º), but the concentrations in the shear plane appear more spread out than for the other compositions. The [001] concentrations

for the FeO endmember samples lack the distinctive 15-20º tilt that was found for the other four compositions; for these samples, [001] concentrations lie either perpendicular to the shear plane, or in the shear plane at two orthogonal directions 45º from the shear direction, as for the $(Mg_{0.50},Fe_{0.50})O$ sample. (We note, however, that the FeO (1473K) sample has only 155 measured grains, far fewer than the other five samples. This may be approaching the lower limit for number of grains needed to assure that the texture has been adequately statistically sampled.)

3.3 Seismic anisotropy

In order to translate the LPOs measured in this study into seismic anisotropy, several simplifying assumptions must be made. In the following calculations, we use the measured LPOs along with the single crystal elastic constants and density for MgO at 125 GPa (a typical pressure for D'') calculated by Karki et al (1997a). This study and similar studies (Karki et al., 1997b, 1999; Karki and Stixrude, 1999, Wentzcovitch et al., 1998) use a first-principles calculation based on density functional theory to obtain the equation of state and elastic constants for MgO at pressures unattainable in the laboratory. The use of MgO elastic constants calculated for a pressure of 125 GPa and ambient temperature (rather than a temperature characteristic of D'') ignores the effects of temperature on elasticity; however, these effects are much smaller than those due to pressure. According to Yamazaki and Karato (2002), the effects of temperature between 0K and 4000K at 140 GPa should modify the anisotropy by less than 10% (see also Stixrude, 2000, and Liebermann and Li, 1998); the effects of temperature are therefore ignored in this calculation.

We also use the MgO elastic constants for all five compositions, as the elastic constants of (Mg,Fe)O and FeO at lower mantle pressures have not been investigated. We note that significant differences in elastic constants with differing compositions have been observed for single crystal (Mg,Fe)O at ambient conditions, especially for Fe-rich compositions (Jacobsen et al., 2002); in fact, pure wüstite is elastically isotropic at ambient pressures. It is quite likely that the elasticity of Fe-rich magnesiowüstite at lower mantle pressures is significantly different than that of the MgO endmember, and we emphasize that our use of elastic constants for MgO is a significant simplification. However, the details of pressure effects on elasticity in magnesiowüstite are not well known. A transition in spin state in (Mg,Fe)O at lower mantle pressures has been proposed (Badro et al., 2003; Sturhahn et al, 2005); this would likely modify the elasticity, but it is not known how. Given the large uncertainty in the effects of Fe at lower mantle conditions, we believe that the best approach is to use the better-known elastic constants for pure MgO at 125 GPa for our calculations. Subsequent work on the effects of Fe on elasticity at high pressures should allow for more accurate calculations in the future.

Bulk elastic constants C_{ij} from the measured LPOs were calculated using an algorithm by Mainprice (1990). (The notation C_{ij} uses the convention of contracting the fourth-rank elastic tensor c_{ijkl} into a 6x6 matrix C_{ij}, taking advantage of the symmetry properties of c_{ijkl}.) The Voigt-Reuss-Hill averaging scheme was used; this approach takes the arithmetic mean of the Voigt (assumes homogenous strain) and Reuss (assumes homogenous stress) averaging schemes. Calculated bulk elastic constants, along with single-crystal MgO constants, are shown in Table 2; all values are given in GPa. From

the calculated elastic constants, (quasi-) *P* and *S* wave velocities may be calculated by solving the Christoffel equation. This equation if given by

$$\det | T_{ik} - \delta_{ik} V^2 | = 0,$$

where δ_{ik} is the Kronecker delta function, V is one of three seismic velocities, and T_{ik} is the Christoffel stiffness matrix, given by

$$T_{ik} = c_{ijkl} X_j X_i,$$

where X_i and X_j are the direction cosines for the direction of interest. This equation is most easily solved by finding the eigenvalues of T_{ik}; this is the approach that the program by Mainprice (1990) takes. We solve for quasi-*P*, quasi-*S1*, and quasi-*S2* velocities over a range of propagation directions. Additionally, the strength of the *S* wave anisotropy A, given by

$$A = \max [|V_{S1} - V_{S2}| / V_{S2}] \times 100,$$

is calculated, along with the direction of the fast shear wave polarization.

The predicted pattern of anisotropy for single-crystal MgO is shown in Figure 6. As Figure 6 demonstrates, MgO is highly anisotropic at lower mantle pressures. Single crystal MgO has a *P* velocity anisotropy of 19.9% and a maximum *S* velocity anisotropy of 48.1%. The characteristics of shear wave anisotropy along with predicted fast shear wave polarization calculated from the measured LPOs for all six samples are shown in Figure 7. The E-W direction for all plots in this figure represents the shear plane; for D'', we assume that the shear plane is horizontal. Figure 7 demonstrates that composition can have a significant effect on the resulting anisotropy pattern, but also demonstrates that regardless of composition, the predicted patterns of anisotropy for (Mg,Fe)O have several features in common (see Discussion, below). The values of maximum calculated *S*

anisotropy range from 5.0% to 11.6%, compared to the single crystal *S* anisotropy value of 48.1%.

4. Discussion

4.1 Observed LPO

In this study, we observed changes in LPO pattern with increasing Fe content for (Mg,Fe)O samples. All experiments achieved a shear strain of $\gamma = 3.5\text{-}4.5$, which should ensure that LPO has reached a nearly steady state. Because variables such as temperature, axial displacement rate, confining pressure, etc. were carefully controlled, we can attribute the difference in observed LPO for different samples to either 1) effects of composition itself, or 2) effects of homologous temperature. All experiments in this study were performed at 1473K (except for one additional FeO experiment at 1273K), but because the melting temperatures of MgO and FeO are different (3099K as opposed to 1650K), this study covered a range of homologous temperatures ($T/T_{melting} = 0.48\text{-}0.89$). Because LPO is generated through dislocation creep, differences in fabric can be attributed to differences in the dominant slip systems for different materials, or to differences in the nature of grain-boundary migration.

As reviewed by Karato (1998a) and discussed by Stretton et al. (2001), Yamazaki and Karato (2002), Merkel et al. (2002), and Heidelbach et al. (2003), the Burgers vector, which represents the dominant slip direction, is always <110> for cubic NaCl-type crystal structures such as MgO. For NaCl, dislocation creep is dominated by glide on the {110} plane. However, the {100} and {111} glide planes could play an important role in deformation for NaCl-type materials, especially those with less ionic bonding than NaCl,

such as MgO (Yamazaki and Karato, 2002). Karato (1998a) noted that temperature also affects the choice of glide planes, with glide on the {100} plane enhanced at higher temperatures because of the higher activation energy for the <110>{001} slip system. Because the relative importance of glide planes is affected both by temperature and by the degree of ionic bonding, further experiments (for example, holding the homologous temperature constant and varying the Fe content) may be needed to constrain the reasons for the differences in LPO observed in this study. However, the two experiments performed on FeO at different homologous temperatures (T = 1473K and T/T_m = 0.89 vs. T = 1273K and T/T_m = 0.77) resulted in nearly identical LPO, which suggests that changes in observed LPO for (Mg,Fe)O may be primarily due to changes in composition. A part of the difference in fabrics among different compositions may be due to the difference in the degree to which the sample fabric has evolved. We note that although the fabric is nearly steady-state and there is little difference in seismic anisotropy beyond the shear strain of ~4 as noted by Yamazaki and Karato (2002), there is some subtle development in fabric up to strain of ~15 or so (Heidelbach et al., 2003). The fabrics of our more iron-rich samples resemble those at higher strains. It is possible that the compositional dependence of fabric partly reflects the different degree of evolution of fabric among samples with different compositions. This is likely due to the fact that all kinetic processes occur faster for iron-rich samples than iron-poor counterparts compared at the same temperature and pressure. Further work is needed to separate the effects of composition and homologous temperature on LPO in magnesiowüstite and to definitively identify the slip systems that are active under different conditions, but we can use the

range of LPOs observed in this study to make some general predictions about the possible style of anisotropy in the D'' layer.

We can compare our observed LPOs with those observed by previous studies. Specifically, the shear deformation experiments of Yamazaki and Karato (2002) and Heidelbach et al. (2003) are the most comparable to the work presented here. Although these studies examined a much narrower range of compositions than this work, we can compare our observed texture for $(Mg_{0.75},Fe_{0.25})O$ with observed LPOs for this composition from Yamazaki and Karato (2002) and with the intermediate-strain experiments on $(Mg_{0.8},Fe_{0.2})O$ from Heidelbach et al. (2003). While our observed textures (Figure 5, second row from top) are not dramatically different from those of Yamazaki and Karato (2002) and Heidelbach et al. (2003), there are some differences in the details. These studies both observed a peak in the [110] crystallographic direction near the direction of shear. In our sample, this peak is much less well defined and it is shifted about 15°-20° away from the shear direction, although we find that it is more prominent in the more Fe-rich samples. We also compare our observed LPOs for FeO (Figure 5, bottom two rows) to the FeO experiment in Yamazaki and Karato (2002), although this earlier experiment was done at a lower temperature than ours (1073K as opposed to 1273K and 1473K). The distribution of orientations of the [110] and [111] crystallographic axes are quite similar to those observed by Yamazaki and Karato (2002), but the distributions of the [001] axes are somewhat different. However, the lack of dramatic differences in LPO between our FeO experiments and that of Yamazaki and Karato (2002) provides additional support for our hypothesis that the changes in LPO we

observe in our different experiments are due to compositional effects rather than temperature effects.

4.2 Applications to anisotropy in D''

Can we apply the results of this laboratory study to the origin of D'' anisotropy? Before doing so, it is important to examine the assumptions that have been made. We must extrapolate the results of a study done in a laboratory to D'' conditions. The confining pressure used in these experiments was 300 MPa compared with ~ 125 GPa at the base of the mantle; the experimental temperature was 1273-1473K compared to temperatures of 2500-4000K (Jeanloz and Williams, 1998); the laboratory strain rate of ~ $3x10^{-4}$ s^{-1} must be compared to mantle strain rates on the order of ~ $10^{-14\text{-}16}$ s^{-1}. As discussed earlier, several assumptions were made regarding the suitability of single crystal MgO elastic constants at 125 GPa for the anisotropy calculations.

However, if we assume that the LPOs due to dislocation creep observed in this study are comparable to the LPOs that would be generated due to dislocation creep at the conditions of the lowermost mantle, then we can compare the anisotropy patterns calculated in this study to seismological observations. These comparisons will allow us to assess the viability of the magnesiowüstite LPO model for anisotropy in D''. For the purpose of this argument, we assume that in at least come parts of D'', a transition from the diffusion creep that dominates the lower mantle to LPO-forming dislocation creep must occur. Karato (1998a) predicted that both the strain rate and the stresses should be higher at the boundary layers of the mantle such as D'', and that this effect should be enhanced for regions such as the circum-Pacific, where cold slab materials are possibly

colliding with the CMB. Higher strain rates and higher stresses tend to favor dislocation creep over diffusion creep. Geodynamical models by McNamara et al. (2001, 2002) have demonstrated that dislocation creep may indeed be concentrated in the lowermost mantle for a downgoing slab model. We also emphasize that the range of compositions considered in this laboratory study may not all be directly applicable to the D'' layer; the range of iron content in the (Mg,Fe)O system at the base of the mantle is not well constrained (e.g. Mao et al., 1997). However, the range of LPOs observed in the (Mg,Fe)O system in this laboratory study is likely to be representative of the range of LPOs potentially formed in the lowermost mantle due to dislocation creep of magnesiowüstite. Finally, we point out that newly discovered stable phase of $MgSiO_3$ near the conditions of the D'' layer (Murakami et al., 2004) is probably also elastically anisotropic (Tsuchiya et al., 2004). Consequently, a combined effect of anisotropic structure of (Mg,Fe)O and post-perovskite may be responsible for seismic anisotropy near the bottom of the lower mantle. However, the nature of LPO in the post-perovskite phase is not well known, which hampers a detailed assessment of the combined effect of both phases. Oganov et al. (2005) presented a theoretical study of possible slip systems, but their results do not agree with the results of an experimental study on analog material, $CaIrO_3$ (Miyajima et al., 2005).

As summarized by Kendall (2000) and Lay et al. (1998), the main features of D'' anisotropy that have been observed are as follows. First, there is a general lack of splitting, or total splitting of less than 0.3 seconds, of near-vertically propagating *SKS*-type phases. Second, in the circum-Pacific region, core-diffracted or pre-diffracted shear phases that traverse roughly horizontal paths through D'' are significantly split (up to ~

10 seconds), with *SH* arriving before *SV*, indicating $V_{SH} > V_{SV}$ anisotropy with a vertical symmetry axis (transverse isotropy). Third, beneath the central Pacific, anisotropy is highly spatially variable, with some evidence for $V_{SV} > V_{SH}$ anisotropy and azimuthal anisotropy. Are the predicted anisotropy patterns found in this study consistent with these observations? We examine the plots in Figure 7 of calculated *S* anisotropy and fast shear wave polarizations. In these figures, the E-W direction represents the shear plane, which is considered to be horizontal for D''. Most of the predicted anisotropy patterns are consistent with a small amount of splitting of vertically propagating *SKS*-type phases. For the two most Mg-rich samples, no *SKS* splitting is predicted; however, the measured LPO for the FeO samples does predict some splitting of vertically propagating phases. For the remaining two compositions, little splitting is predicted for strictly vertical paths but some splitting is predicted for phases that deviate more significantly from the vertical, such as *SKKS*. The predicted anisotropy for horizontally propagating shear waves is also consistent with the observation that shear wave splitting with $V_{SH} > V_{SV}$ occurs in the circum-Pacific. For all anisotropy patterns, *S* phases propagating in the shear plane (that is, horizontally) should be significantly split at certain azimuths. The pattern of azimuthal anisotropy in the shear plane, however, is different for different compositions. While no $V_{SV} > V_{SH}$ anisotropy is predicted from the LPOs observed in this study, it may be that $V_{SV} > V_{SH}$ anisotropy in the central Pacific region of D'' is generated through a mechanism other than the one examined in this study. The central Pacific is presumably a site of mantle upwelling and the arguments for the localization of dislocation creep may not hold in this region.

Because the patterns of anisotropy calculated from the measured LPOs in this study agree well with most seismological observations of D'' anisotropy, LPO of magnesiowüstite seems to be a viable mechanism for generating anisotropic structure in D''. However, the SPO hypothesis that D'' anisotropy is the result of horizontal layering or oriented inclusions also agrees with the seismological observations discussed above (Kendall, 2000; Kendall and Silver, 1998a). Can the observations of LPO in this study be used to distinguish between the LPO and the SPO models of D'' anisotropy? One testable difference between the two models is the prediction from this study that LPO-generated fabric will result in azimuthal anisotropy in the horizontal plane, while most SPO configurations will not. The splitting of horizontally propagating *S* phases traversing D'' should depend on the direction of propagation if the LPO hypothesis is correct. Azimuthal anisotropy has not been well constrained due to the difficulty of finding suitable source/receiver combinations for a variety of backazimuths, but a recent waveform modeling study by Garnero et al. (2004) found evidence for azimuthal anisotropy in the D'' region beneath the Caribbean. Hall et al. (2004) pointed out that differential splitting of *SKS* and *SKKS* phases may be used to constrain D'' anisotropy, and noted that LPO-based mechanisms should generate azimuthal variations in splitting, which is consistent with our results. Further studies on azimuthal anisotropy in D'' using waveform modeling, differential *SKS*/*SKKS* splitting, or innovative source/receiver geometries may help to differentiate between the LPO and SPO models.

5. Conclusions

We have performed shear deformation experiments in the dislocation creep regime on (Mg,Fe)O aggregates over a range of compositions and homologous temperatures. We find that LPO develops at large strains for all samples, but the style of LPO changes with increasing Fe content. Using the measured LPO patterns and single crystal elastic constants for MgO at lowermost mantle pressures, we calculate bulk elastic constants C_{ij} and resulting patterns of anisotropy for all samples. The predicted patterns of anisotropy are generally consistent with the main features of seismological observations of D'' in the circum-Pacific region, including small amounts of splitting of vertical *SKS*-type phases and splitting of horizontally propagating *S* phases due to $V_{SH} > V_{SV}$ anisotropy. Measured LPOs in (Mg,Fe)O would predict azimuthal anisotropy in the horizontal (shear) plane, however, while most SPO-based models do not. The investigation of azimuthal anisotropy in D'', which has not been well constrained, should provide a means to distinguish between LPO- and SPO-generated anisotropy. Additionally, if strain-induced LPO of (Mg,Fe)O is the cause of anisotropy in D'', the characterization of its azimuthal anisotropy may provide constraints on the composition and/or melting temperature of (Mg,Fe)O in the lowermost mantle.

6. Acknowledgements

The authors thank Tim Grove, Steve Singletary, Jessica Warren, and Mark Zimmerman for technical advice and assistance. The paper was greatly improved by the thoughtful and helpful comments of two anonymous reviewers, and we thank them for

their efforts. This research was partially supported by an NSF Graduate Research Fellowship awarded to M. D. L.

Figure Captions

Figure 1. Optical micrographs of undeformed $(Mg_{0.50},Fe_{0.50})O$ starting material (a) and FeO sample after deformation at 1273K (b).

Figure 2. Schematic diagram of sample assembly for deformation experiments.

Figure 3. Mechanical data from deformation experiments. We plot the log of the steady-state stress in MPa vs. the homologous temperature ($T/T_{melting}$). The line represents the best linear fit to this relation. Black triangles represent deformation experiments at 1473K; the white triangle represents the experiment on FeO at 1273K.

Figure 4. Comparison of dot maps (a) and calculated pole figures (b) for the MgO sample. Dot maps show the lower-hemisphere projection of measured Euler angles for each grain (for the [001], [011], and [111] orientations, respectively). The pole figure representation is obtained using a Gaussian smoothing function with a 15° half-width. The shear plane corresponds to the E-W direction and is shown by the thick black lines on (b). The sense of shear is top to right (dextral) and is shown by the arrows at upper right. Pole figure density is represented by the grayscale and the maximum (black) corresponds to 3 multiples of uniform density (see scale bar at lower right). Projections are equal-area.

Figure 5. Pole figures for the [001], [011], and [111] crystallographic orientations for six samples. Fe content increases from top (MgO) to bottom (FeO). As in Figure 5, the E-W direction corresponds to the shear plane and the sense of shear is dextral. The grayscale is the same as in Figure 4; it is uniform for each sample, and the maximum value corresponds to 3 multiples of uniform density.

Figure 6. Calculated anisotropy for single-crystal MgO at 125 GPa. Shown are contour plots of *P* wave velocity (a), *S* wave anisotropy (b), *S1* polarization directions (c), *S1* wave velocities (d), and *S2* wave velocities (e). All plots are equal-area lower hemisphere projections.

Figure 7. Predicted shear wave splitting behavior based on the measured LPOs for six samples: MgO (a), Mg.75O (b), Mg.50O (c), Mg.25O (d), FeO at 1473K (e), and FeO at 1273K (f). The grayscale indicates the strength of *S*-wave anisotropy; the bars indicate the orientation of the fast splitting direction. Each scale bar is marked with the maximum (top) and minimum (bottom) value of S wave anisotropy, expressed as $A = \max [|V_{S1} - V_{S2}| / V_{S2}] \times 100$.

Table 1. Experimental conditions and LPO measurement results for six deformation experiments.

Table 2. Calculated bulk elastic constants in GPa for six samples, based on measured LPOs and single-crystal MgO elastic constants at 125 GPa from Karki et al. (1997a).

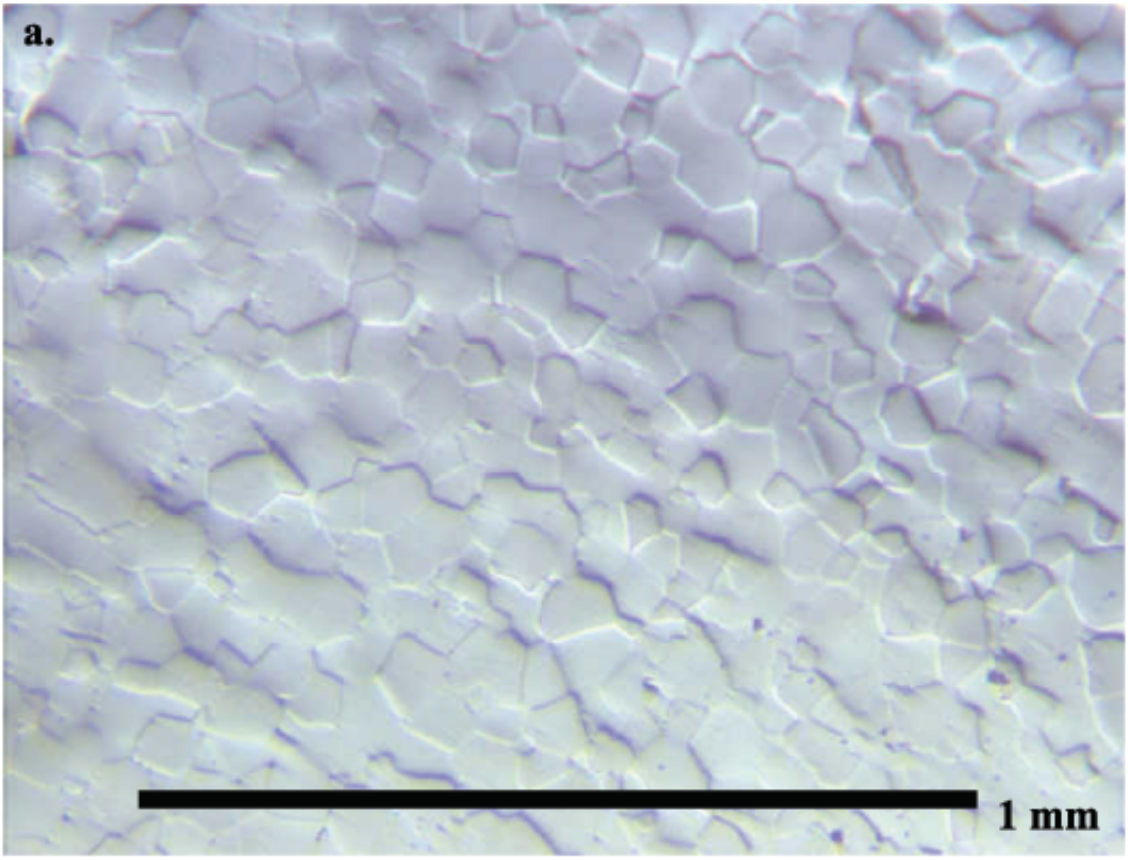

Figure 1a

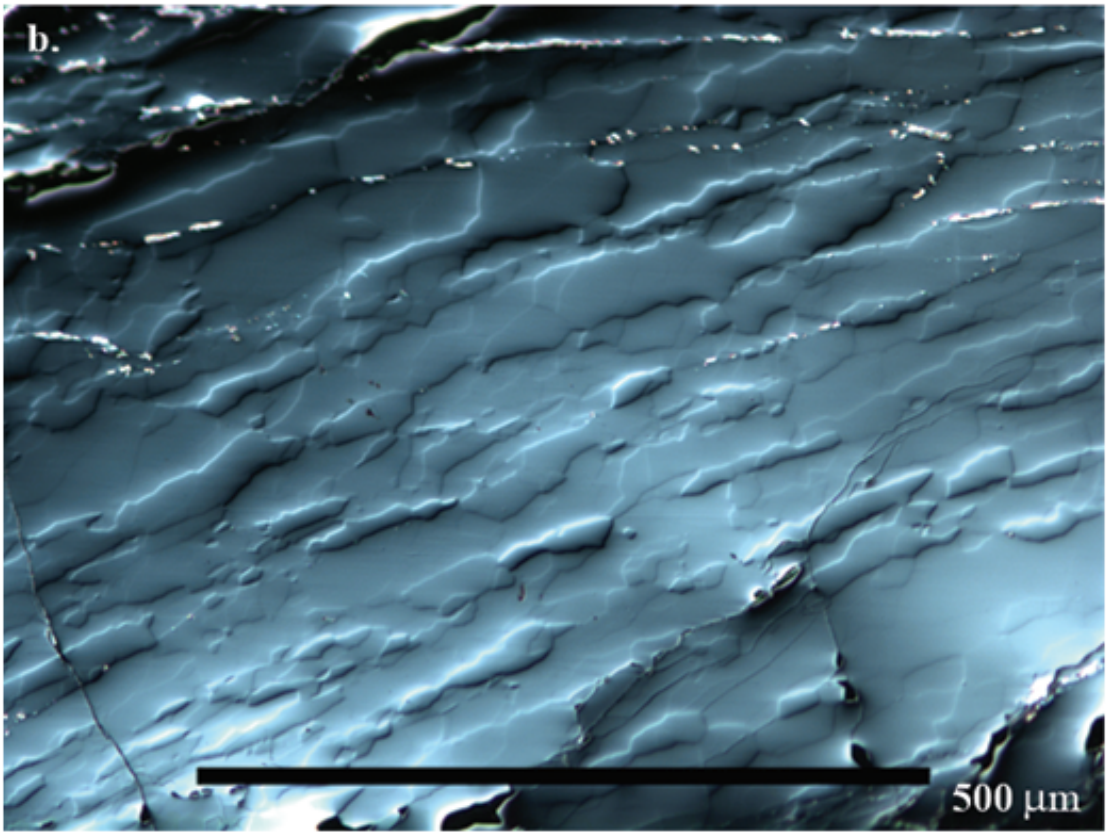

Figure 1b

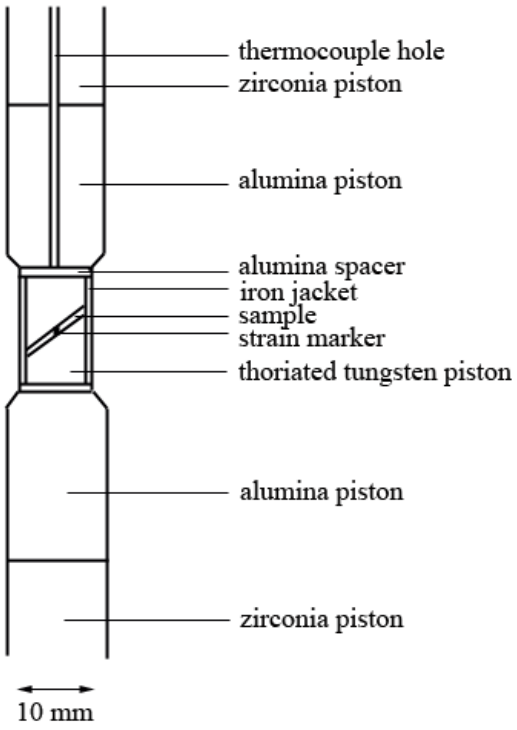
thermocouple hole
zirconia piston
alumina piston
alumina spacer
iron jacket
sample
strain marker
thoriated tungsten piston
alumina piston
zirconia piston
10 mm

Figure 2

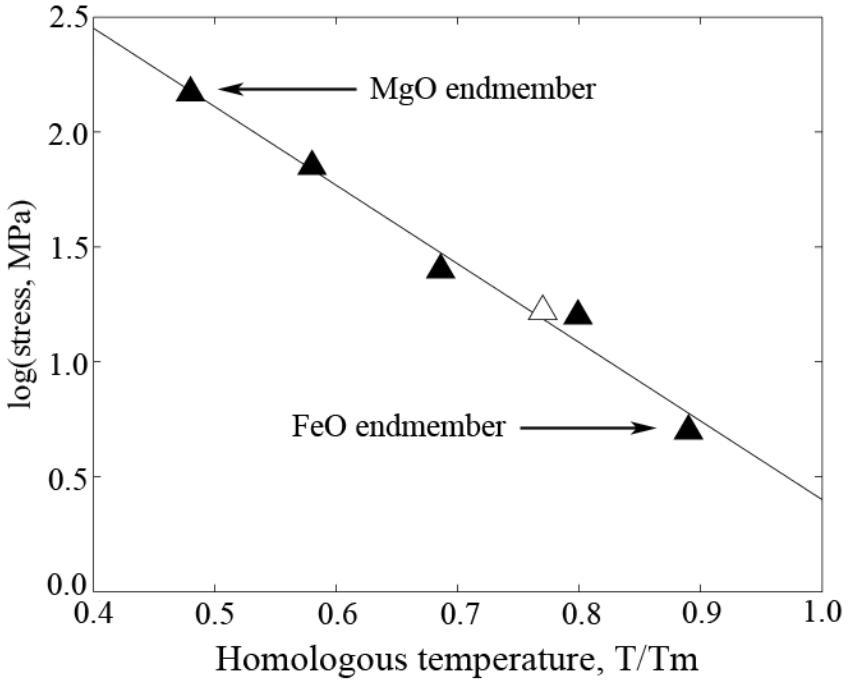
2.5
2.0
1.5
1.0
0.5
0.0
log(stress, MPa)
MgO endmember
FeO endmember
0.4
0.5
0.6
0.7
0.8
0.9
1.0
Homologous temperature, T/Tm

Figure 3

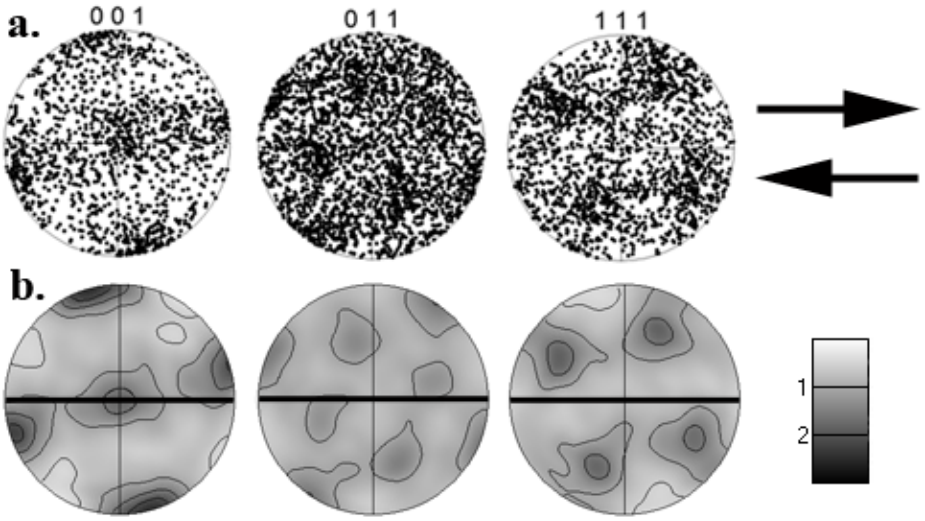

Figure 4

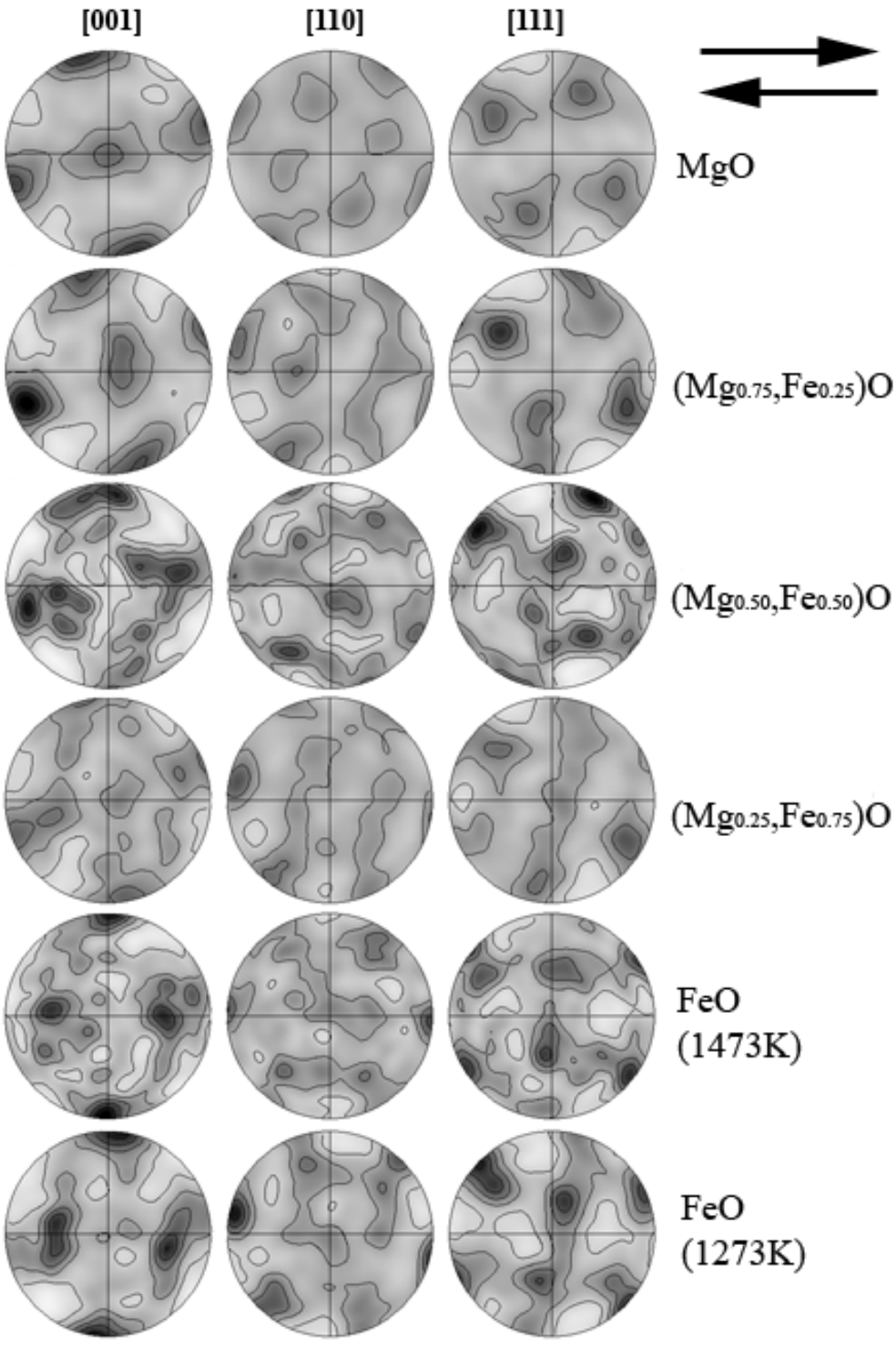
[001]
[110]
[111]
MgO
(Mg0.75,Fe0.25)O
(Mg0.50,Fe0.50)O
(Mg0.25,Fe0.75)O
FeO
(1473K)
FeO
(1273K)

Figure 5

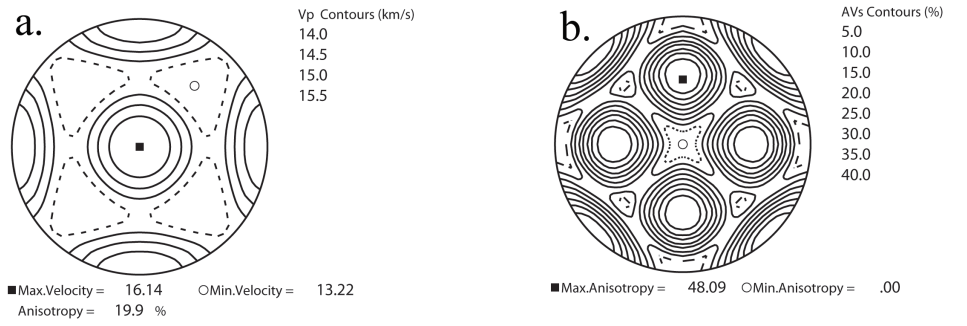
a.
Vp Contours (km/s)
14.0
14.5
15.0
15.5
■Max.Velocity = 16.14 ○Min.Velocity = 13.22
Anisotropy = 19.9 %
b.
AVs Contours (%)
5.0
10.0
15.0
20.0
25.0
30.0
35.0
40.0
■Max.Anisotropy = 48.09 ○Min.Anisotropy = .00
c.
Vs1 Polarisation Planes
d.
Vs1 Contours (km/s)
7.0
7.5
8.0
8.5
9.0
9.5
■Max.Velocity = 10.07 ○Min.Velocity = 6.17
Anisotropy = 48.1 %
e.
Vs2 Contours (km/
6.5
6.8
7.0
7.3
7.5
7.8
8.0
8.3
8.5
■Max.Velocity = 8.83 ○Min.Velocity = 6.17
Anisotropy = 35.6 %

Figure 6

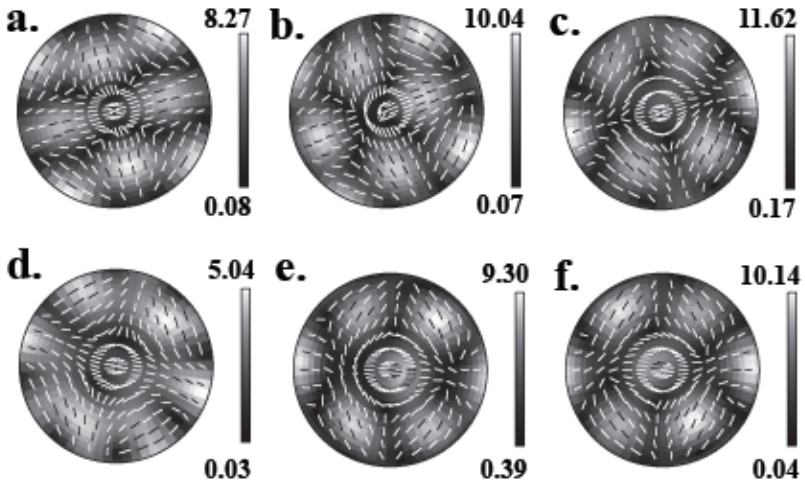

Figure 7

Sample number	Composition	Temp, K	Shear strain, γ	# grains measured	Starting grain size, μm
MDL02	MgO	1473	4.2	1953	5
MDL03	(Mg.50Fe.50)O	1473	4.5	518	30
MDL05	(Mg.75Fe.25)O	1473	3.5	1757	45
MDL07	(Mg.25Fe.75)O	1473	3.7	2055	70
MDL08a	FeO	1473	3.8	155	~ 150
MDL08b	FeO	1273	4.1	827	80

Table 1

	C11	C12	C13	C14	C15	C16	C22	C23	C24	C25
Single	1302	276	276	0	0	0	1302	276	0	0
MgO	1035	411	407	0	1	28	1021	422	0	1
Mg75O	1019	421	415	2	-3	39	1014	419	-17	9
Mg50O	1031	400	422	-3	-11	32	1002	451	-1	7
Mg25O	1014	420	420	4	1	-22	1001	433	-3	0
FeO(high_T)	1039	405	410	6	4	-12	995	454	-14	-2
FeO(low_T)	1005	397	452	5	-9	8	1047	410	-7	-3

		C26	C33	C34	C35	C36	C44	C45	C46	C55	C56	C66
Single		0	1302	0	0	0	190	0	0	190	0	190
MgO		-23	1025	0	-2	-3	286	-3	1	268	0	273
Mg75O		-36	1021	16	-6	-3	279	-3	10	275	1	284
Mg50O		-26	980	5	4	-6	312	-6	7	283	-4	264
Mg25O		21	1000	-5	-1	1	293	0	0	280	3	281
FeO(high_T)		10	990	7	-2	2	315	2	-2	271	5	266
FeO(low_T)		-4	992	2	12	-4	271	-5	-3	313	5	259

Table 2

Bibliography

Alsina, D., Snieder, R., 1995. Small-scale sublithospheric continental mantle deformation: constraints from SKS splitting observations. Geophys. J. Int. 123, 431-448.

Anderson, M. L., Zandt, G., Triep, E., Fouch, M., Beck S., 2004. Anisotropy and mantle flow in the Chile-Argentina subduction zone from shear wave splitting analysis. Geophys. Res. Lett. 31, doi:10.1029/2004GL020906.

Ando, M., Ishikawa Y., Yamazaki, F., 1983. Shear wave polarization anisotropy in the upper mantle beneath Honshu, Japan. J. Geophys. Res. 88, 5850-5864.

Arcay, D., Tric, E., Doin, M. P., 2005. Numerical simulations of subduction zones: Effect of slab dehydration on the mantle wedge dynamics. Phys. Earth Planet. Inter. 149, 133-153.

Babuška, V., Cara, M., 1991. Seismic anisotropy in the Earth. Modern Approaches in Geophysics, vol. 10. Kluwer Academic Publishers, Dordrecht, The Netherlands.

Badro, J., Fiquet, G., Guyot, F., Rueff, J.-P., Struzhkin, V. V., Vankó, G., Monaco, G., 2003. Iron partitioning in Earth's mantle: Toward a deep lower mantle discontinuity. Science 300, 789-791.

Becker, T. W., Kellogg, J. B., Ekstrom, G., O'Connell, R. J., 2003. Comparison of azimuthal seismic anisotropy from surface waves and finite strain from global mantle-circulation models. Geophys. J. Int. 155, 696-714.

Behn, M. D., Conrad, C. P., Silver, P. G., 2004. Detection of upper mantle flow associated with the African Superplume. Earth Planet. Sci. Lett. 224, 259-274.

Ben-Menahem, A., Gibson, R. L., Sena, A. G., 1991. Green's tensor and radiation patterns of point sources in general anisotropic inhomogeneous elastic media. Geophys. J. Int. 197, 297-308.

Billen, M. I., Gurnis, M., 2001. A low viscosity wedge in subduction zones. Earth Planet. Sci. Lett. 193, 227-236.

Billen, M. I., Gurnis, M., Simons, M., Multiscale dynamics of the Tonga-Kermadec subduction zone. Geophys. J. Int. 153, 359-388.

Blackman, D., Kendall, J.-M., 2002. Seismic anisotropy in the upper mantle 2. Predictions for current plate boundary flow models. Geochem. Geophys. Geosyst. 3, 8602, doi:10.1029/2001GC000247.

Bleistein, N., Cohen, J. K., 1979. Velocity inversion for acoustic waves. Geophysics 44, 1077-1087.

Bowman, J. R., Ando, M., 1987. Shear-wave splitting in the upper-mantle wedge above the Tonga subduction zone. Geophys. J. Roy. Astr. Soc. 88, 25-41.

Burridge, R., de Hoop, M. V., Miller, D., Spencer, C., 1998. Multiparameter inversion in anisotropic elastic media. Geophys. J. Int. 134, 757-777.

Buttles, J., Olson, P.,1998. A laboratory model of subduction zone anisotropy. Earth Planet. Sci. Lett. 164, 245-262.

Červený, V., 2001. Seismic Ray Theory. Cambridge University Press, Cambridge.

Chapman, C. H., Pratt, R. G., 1992. Traveltime tomography in anisotropic media – I. Theory. Geophys. J. Int. 109, 1-19.

Chevrot, S., 2000. Multichannel analysis of shear wave splitting. J. Geophys. Res. 105, 21,579-21,590.

Chevrot, S., Favier, N., Komatitsch, D., 2004. Shear wave splitting in three-dimensional anisotropic media. Geophys. J. Int. 159, 711-720.

Chevrot, S., van der Hilst, R. D., 2003. On the effects of a dipping axis of symmetry on shear wave splitting measurements in a transversely isotropic medium. Geophys. J. Int. 152, 497-505.

Christensen, N. I., 1984. The magnitude, symmetry and origin of upper mantle anisotropy based on fabric analyses of ultramafic tectonites. Geophys. J. R. Astron. Soc. 76, 89-111.

Clitheroe, G., van der Hilst, R.D., 1998. Complex anisotropy in the Australian lithosphere from shear-wave splitting in broad-band *SKS* records. In: Braun, J., Dooley, J., Goleby, B., van der Hilst, R., Klootwijk, C., (Eds.), Structure and Evolution of the Australian Continent, Am. Geophys. Union, Geodyn. Ser., vol. 26.

Cohen, J. K., Bleistein, N., 1977. An inverse method for determining small variations in propagation speed. SIAM J. Appl. Math. 32, 784-799.

Conder, J. A., Wiens. D. A., Morris, J., 2002. On the decompression melting structure at volcanic arcs and back-arc spreading centers. Geophys. Res. Lett. 29, (doi:10.1029/2002GL015390).

Conrad, C. P., Hager, B. H., 1999. Effects of plate bending and fault strength at subduction zones on plate dynamics. J. Geophys. Res. 104, 17,551-17,571.

Cormier, V. F., 1986. Synthesis of body waves in transversely isotropic earth models. Bull. Seism. Soc. Am. 76, 231-240.

Crampin, S., 1977. Seismic anisotropy; a summary. J. Geophys. – Z. Geophys. 43, 499-501.

Currie, C. A., Cassidy, J. F., Hyndman, R. D., Bostock, M. G., 2004. Shear wave anisotropy beneath the Cascadia subduction zone and western North American craton. Geophys, J. Int. 157, 341-353.

de Hoop, M. V., Spencer, C., Burridge, R., 1999. The resolving power of seismic amplitude data: An anisotropic inversion/migration approach. Geophysics 64, 852-873.

de Hoop, M. V., van der Hilst, R. D., 2005a. On sensitivity kernels for 'wave-equation' transmission tomography. Geophys. J. Int. 160, 621-633.

de Hoop, M. V., van der Hilst, R. D., 2005b. Reply to comment by F. A. Dahlen and G. Nolet on 'On sensitivity kernels for 'wave-equation' transmission tomography.' Geophys. J. Int. 163, 952-955.

Dingley, D. J., Randle, V., 1992. Microstructural determination by electron backscattered diffraction. J. Mater. Sci. 27, 4545-4566.

Doornbos, D. J., Spilopoulos, S., Stacey, F. D., 1986. Seismological properties of D'' and the structure of the thermal boundary layer. Phys. Earth Planet. Inter. 41, 225-239.

Eberle, M. A., Grasset, O., Sotin, C., 2002. A numerical study of the interaction of the mantle wedge, subducting slab, and overriding plate. Phys. Earth Planet. Inter. 134, 191-202.

Elkins Tanton, L. T., Grove, T. L., Donnelly-Nolan, J., 2001. Hot, shallow melting under the Cascades volcanic arc. Geology 29, 631-634.

Engdahl, E.R., van der Hilst, R.D., Buland, R.P., 1998. Global teleseismic earthquake relocation from improved travel times and procedures for depth determination. Bull. Seism. Soc. Am. 88, 722-743.

Esmersoy, C., 1990. Split-shear wave inversion for fracture evaluation. Soc. Expl. Geophys. Ann. Internat. Mtg. 60, 1400-1403.

Ettrich, N., Sollid, A., Ursin, B., 2002. Out-of-plane geometrical spreading in anisotropic media. Geophys. Prospect. 50, 383-392.

Evans, B., Kohlstedt, D. L., 1995. Rheology of rocks. In: Ahrens, T. J. (Ed.), Rock physics and phase relations. Am. Geophys. Union, AGU Ref. Shelf, vol. 3.

Farra, V., 1989. Ray perturbation theory for heterogeneous hexagonal anisotropic media. Geophys. J. R. Astron. Soc. 99, 723-737.

Farra, V., 2001. High order perturbations of the phase velocity and polarization of *q*P and *q*S waves in anisotropic media. Geophys. J. Int. 147, 93-104.

Favier, N., Chevrot, S., 2003. Sensitivity kernels for shear wave splitting in transverse isotropic media. Geophys. J. Int. 153, 213-228.

Favier, N., Chevrot, S., Komatitsch, D., 2004. Near-field influences on shear wave splitting and traveltime sensitivity kernels. Geophys. J. Int. 156, 467-4482.

Flesch, L. M., Holt. W. E., Silver, P. G., Stephenson, M., Wang, C., Chan, W. W., 2005. Constraining the extent of crust-mantle coupling in central Asia using GPS, geologic, and shear-wave splitting data. Earth Planet. Sci. Lett 238, 248-268..

Fischer, K. M., Fouch, M. J., Wiens, D. A., Boettcher, M. S., 1998. Anisotropy and flow in Pacific subduction zone back-arcs. Pure Appl. Geophys. 151, 463-475.

Fischer, K. M., McCarthy, C. M., Zaranek, S. E., Rychert, C. A., Li, A., 2005. Asthenospheric anisotropy beneath North America. Eos Trans. AGU, 86 (52), Fall Meet. Suppl., Abstract U52A-01.

Fischer, K. M., Parmentier, E. M., Stine, A. R., Wolf, E. R., 2000. Modeling anisotropy and plate-driven flow in the Tonga subduction zone back arc. J. Geophys. Res. 105, 16,181-16,191.

Fischer, K. M., Wiens, D. A., 1996. The depth distribution of mantle anisotropy beneath the Tonga subduction zone. Earth Planet. Sci. Lett. 164, 245-262.

Fischer, K. M., Yang, X., 1994. Anisotropy in Kuril-Kamchatka subduction zone structure. Geophys. Res. Lett. 21, 5-8.

Forsyth, D. W., 1975. The early structural evolution and anisotropy of the oceanic upper mantle. Geophys. J. Roy. Astr. Soc. 43, 103-162.

Foss, S.-K., de Hoop, M. V., Ursin, B., 2005. Linearized 2.5-dimensional parameter imaging inversion in anisotropic elastic media. Geophys. J. Int. 161, 722-738.

Fouch, M. J., Fischer, K. M., 1996. Mantle anisotropy beneath northwest Pacific subduction zones. J. Geophys. Res. 101, 15,987-16,002.

Fouch, M. J., Fischer, K. M., 1998. Shear wave anisotropy in the Mariana subduction zone. Geophys. Res. Lett. 25, 1221-1224.

Fouch, M. J., Fischer, K. M., Wysession, M. E., 2001. Lowermost mantle anisotropy beneath the Pacific; imaging the source of the Hawaiian Plume. Earth Planet. Sci. Lett. 190, 167-180.

Fouch, M. J., Fischer, K. M., Wysession, M. W., Clark, T. J., 2000. Shear wave splitting, continental keels, and patterns of mantle flow, J. Geophys. Res. 105, 6255-6276.

Fouch, M. J., Silver, P. G., Bell, D. R., Lee, J. N., 2004. Small-scale variations in seismic anisotropy near Kimberley, South Africa. Geophys. J. Int. 157, 764-774.

Fournier, M., Fabbri, O., Angelier, J., Cadet, J.-P., 2001. Regional seismicity and on-land deformation in the Ryukyu arc: Implications for the kinematics of opening of the Okinawa Trough. J. Geophys. Res. 106, 13,751-13,768.

Frost, H. J., Ashby, M. F. 1982. Deformation mechanism maps. Pergamon Press, Oxford, U. K.

Fryer, G. J., Frazer, L. N., 1984. Seismic waves in stratified anisotropic media. Geophys. J. Roy. Astron. Soc. 78, 691-710.

Fryer, G. J., Frazer, L. N., 1987. Seismic waves in stratified anisotropic media; II. Elastodynamic eigensolutions for some anisotropic systems, Geophys. J. Roy. Astron. Soc. 91, 73-101.

Fukao, Y., 1984. Evidence from core-reflected shear waves for anisotropy in the Earth's mantle, Nature 309, 695-698.

Fukao, Y., Obayashi, M., Inoue, H., Nenbai, M., 1992. Subducting slabs stagnant in the mantle transition zone. J. Geophys. Res. 97, 4809-4822.

Funiciello, F., Faccenna, C., Giardinni, D., Regenauer-Lieb, K., 2003. Dynamics of retreating slabs: 2. Insights from 3-D laboratory experiments. J. Geophys. Res. 108, 2207, doi:10.1029/2001JB000896.

Funiciello, F., Moroni, M., Piromallo, C., Faccenna, C., Cendese, A., Bui, H. A., 2006. Mapping mantle flow during retreating subduction: Laboratory models analyzed by feature tracking. J. Geophys. Res. 111, doi:10.1029/2005JB003792.

Gaetani, G. A., Grove, T. L., 2003. Experimental constraints on melt generation in the mantle wedge. In: Eiler, J. M. (Ed.), Inside the Subduction Factory. Am. Geophys. Union, Geophys. Monogr. Ser., vol. 138.

Garnero, E. J., Lay, T. 1997. Lateral variations in lowermost mantle shear wave anisotropy beneath the North Pacific and Alaska. J. Geophys. Res. 102, 8121-8135.

Garnero, E. J., Lay, T., 2003. D'' shear velocity heterogeneity, anisotropy, and discontinuity structure beneath the Caribbean and Central America. Phys. Earth Planet. Inter. 140, 219-242.

Garnero, E. J., Maupin, V., Lay, T., Fouch, M. J., 2004. Variable azimuthal anisotropy in Earth's lowermost mantle. Science 306, 259-261.

Gledhill, K., Gubbins, D., 1996. SKS splitting and the seismic anisotropy of the mantle beneath the Hikurangi subduction zone, New Zealand. Phys. Earth Planet. Inter. 95, 227-236.

Gorbatov, A., Kennett, B. L. N., 2003. Joint bulk-sound and shear tomography for Western Pacific subduction zones. Earth Planet. Sci. Lett. 210, 527-543.

Gripp, A. E., Gordon, R. G., 2002. Young tracks of hot spots and current plate velocities. Geophys. J. Int. 150, 321-361.

Gudmundsson, O., Sambridge, M., 1998. A regionalized upper mantle (RUM) seismic model. J. Geophys. Res. 103, 7121-7136.

Hall, C., Fischer, K. M., Parmentier, E. M., Blackman, D. K., 2000. The influence of plate motions on three-dimensional back arc mantle flow and shear wave splitting. J. Geophys. Res. 105, 28,009-28,033.

Hall, S. A., Kendall, J.-M., van der Baan, M. 2004. Some comments on the effects of lower-mantle anisotropy on SKS and SKKS phases. Phys. Earth Planet. Inter. 146, 469-481.

Hartog, R., Schwartz, S., 2000. Subduction-induced strain in the upper mantle east of the Mendocino triple junction, California. J. Geophys. Res. 105, 7909-7930.

Heidelbach, F., Stretton, I., Langenhorst, F., Mackwell, S., 2003. Fabric evolution during high shear strain deformation of magnesiowüstite ($Mg_{0.8}$,$Fe_{0.2}$)O. J. Geophys. Res. 108, 2154, doi:10.1029/2001JB001632.

Helffrich, G., Wiens, D. A., Vera, E., Barrientos, S., Shore, P., Robertson, S., Adaros, R., 2002. A teleseismic shear-wave splitting study to investigate mantle flow around South America and implications for plate-driving forces. Geophys. J. Int. 149, F1-F7.

Hess, H. H., 1964. Seismic anisotropy of the uppermost mantle under oceans. Nature 203, 629-630.

Heuret, A., Lallemand, S., 2005. Plate motions, slab dynamics and back-arc deformation. Phys. Earth Planet. Inter. 149, 31-51.

Hiramatsu, Y., Ando, M., 1996. Seismic anisotropy near source region in subduction zones around Japan. Phys. Earth Planet. Inter. 95, 237-250.

Holtzman, B. K., Kohlstedt, D. L., Zimmerman, M. E., Heidelbach, F., Hiraga, T., Hustoft, J., 2003. Melt segregation and strain partitioning: implications for seismic anisotropy and mantle flow. Science 301, 1227-1230.

Hung, S.-H., Dahlen, F. A., Nolet, G., 2000. Fréchet kernels for finite-frequency traveltimes – II. Examples. Geophys. J. Int. 141, 175-203.

Iidaka, T., Obara, K., 1997. Seismological evidence for the existence of anisotropic zone in the metastable wedge inside the subducting Izu-Bonin slab. Geophys. Res. Lett. 24, 3305-3308.

Isaak, D. G., Anderson, O. L., Goto, T., 1989. Measured elastic moduli of single-crystal MgO up to 1800K. Phys. Chem. Minerals 16, 704-713.

Iwasaki, T., Hirata, N., Kanazawa, T., Melles, J., Suyehiro, K., Urabe, T., Moeller, L., Makris, J., Shimamura, H., 1990. Crustal and upper mantle structure in the Ryukyu Island Arc deduced from deep seismic sounding. Geophys. J. Int. 102, 631-657.

Jacobsen, S. D., Reichmann, H. J., Spetzler, H. A., Mackwell, S. J., Smyth, J. R., Angel, R. J., McCammon, C. A., 2002. Structure and elasticity of single-crystal (Mg,Fe)O and a new method of generating shear waves for gigahertz ultrasonic interferometry. J. Geophys. Res. 107, doi:10.1029/2001JB000490.

Jeanloz, R., Williams, Q. 1998. The core-mantle boundary region. Rev. Mineral. 37, 241-259.

Jech, J., Pšenčík, I., 1989. First-order perturbation method for anisotropic media. Geophys. J. Int. 99, 369-376.

Jung, H., Karato, S.-i., 2001. Water-induced fabric transitions in olivine. Science, 293, 1460-1463.

Kaminski, É., 2004. The influence of water on the development of lattice preferred orientation in olivine aggregates. Geophys. Res. Lett. 29, doi:10.1029/2002GL014710.

Kaminski, É, Ribe, N. M., 2002. Timescales for the evolution of seismic anisotropy in mantle flow. Geochem. Geophys. Geosyst. 3, doi:10.1029/2001GC000222.

Kaminski, É, Ribe, N. M., 2001. A kinematic model for recrystallization and texture development in olivine polycrystals. Earth Planet. Sci. Lett. 189, 253-267.

Kaminski, É, Ribe, N. M., Browaeys, J. T., 2004. D-Rex, a program for calculation of seismic anisotropy due to crystal lattice preferred orientation in the convective upper mantle. Geophys. J. Int. 158, 744-752.

Kaneshima, S., 1990. Origin of crustal anisotropy: Shear wave splitting studies in Japan. J. Geophys. Res. 95, 11,121-11,133.

Kao, H., Huang, G.-C., Liu, C.-S., 2000. Transition from oblique subduction to collision in the northern Luzon arc-Taiwan region: Constraints from bathymetry and seismic observations. J. Geophys. Res. 105, 3059-3079.

Karato, S.-i., 1989. Defects and plastic deformation in olivine. In: Karato, S.-i., Toriumi, M., (Ed.), Rheology of Solids and of the Earth, Oxford University Press, Oxford, U.K.

Karato, S.-i., 1998a. Some remarks on the origin of seismic anisotropy in the D'' layer. Earth Planets Space 50, 1019-1028.

Karato, S.-i., 1998b. Seismic anisotropy in the deep mantle, boundary layers and the geometry of mantle convection. Pure Appl. Geophys. 151, 565-587.

Karato, S.-i., 2003. Mapping water content in the upper mantle. In: Eiler, J. M. (Ed.), Inside the Subduction Factory. Am. Geophys. Union, Geophys. Monogr. Ser., vol. 138.

Karato, S.-i., Zhang, S., Wenk, H.-R. 1995. Superplasticity in Earth's lower mantle: Evidence from seismic anisotropy and rock physics. Science 270, 458-461.

Karki, B. B., Stixrude, L., 1999. Seismic velocities of major silicate and oxide phases of the lower mantle. J. Geophys. Res. 104, 13,025-13,033.

Karki, B. B., Stixrude, L., Clark, S. J., Warren, M. C., Ackland, G. J., Crain, J., 1997a. Structure and elasticity of MgO at high pressure. Am. Miner. 82, 51-60.

Karki, B. B., Stixrude, L., Clark, S. J., Warren, M. C., Ackland, G. J., Crain, J. 1997b. Elastic properties of orthorhombic $MgSiO_3$ perovskite at lower mantle pressures. Am. Miner. 82, 635-639.

Karki, B. B., Wentzcovitch, R. M., de Gironcoli, S., Baroni, S. 1999. First-principles determination of elastic anisotropy and wave velocities of MgO at lower mantle conditions. Science 286, 1705-1707.

Katayama, I., Jung, H., Karato, S.-i., 2004. New type of olivine fabric from deformation experiments at modest water content and low stress. Geology 32, 10045-1048.

Katayama, I., Karato, S., 2006 Effects of temperature and stress on the deformation fabrics of olivine under hydrous conditions: An experimental study. Earth Planet. Sci. Lett., submitted for publication.

Keith, C. M., Crampin, S., 1977. Seismic body waves in anisotropic media: synthetic seismograms. Geophys. J. Roy. Astr. Soc. 94, 225-243.

Kelemen, P. B., Rilling, J. L., Parmentier, E. M., Mehl, L., Hacker, B. R., 2003. Thermal structure due to solid-state flow in the mantle wedge beneath arcs. . In: Eiler, J. M. (Ed.), Inside the Subduction Factory. Am. Geophys. Union, Geophys. Monogr. Ser., vol. 138.

Kendall, J.-M., 1994. Teleseismic arrivals at a mid-ocean ridge: Effects of mantle melt and anisotropy. Geophys. Res. Lett. 21, 301-304.

Kendall, J.-M., 2000. Seismic anisotropy in the boundary layers of the mantle. In: Karato, S.-i. et al. (Ed.), Earth's Deep Interior: Mineral Physics and Tomography from the Atomic to the Global Scale, Am. Geophys. Union, Geophys. Monogr. Ser., vol. 117.

Kendall, J.-M., Silver, P. G. 1996. Constraints from seismic anisotropy on the nature of the lowermost mantle. Nature 381, 409-412.

Kendall, J.-M., Silver, P. G. 1998. Investigating causes of D'' anisotropy. In: Gurnis, M., et al. (Ed.), The Core-Mantle Boundary Region. Am. Geophys. Union, Geodyn. Ser., vol. 28.

Kendall, J.-M., Stuart, G. W., Ebinger, C. J., Bastow, I. D., Keir, D., 2005. Magma-assisted rifting in Ethiopia. Nature 433, 146-148.

Kennett, B. L. N., Engdahl., E. R., 1991. Traveltimes for global earthquake location and phase identification. Geophys. J. Int. 105, 429-465.

Kincaid, C., Griffiths, R. W., 2004. Variability in flow and temperatures within mantle subduction zones. Geochem. Geophys. Geosyst. 5, Q06002, doi:10.1029/ 2003GC000666.

Kincaid, C., Sacks, I. S., 1997. Thermal and dynamical evolution of the upper mantle in subduction zones. J. Geophys. Res. 102, 12,295-12,315.

King, S. D., 1991. The interaction of subducting slabs and the 670 kilometer discontinuity. Ph.D. Thesis, California Institute of Technology.

King, S. D., Raefsky, A., Hager, B. H., 1990. ConMan: vectorizing a finite element code for incompressible two-dimensional convection in the Earth's mantle. Phys. Earth Planet. Inter. 59, 195-207.

King, S. D., Hager, B. H., 1990. The relationship between plate velocity and trench viscosity in Newtonian and power-law subduction calculations. Geophys. Res. Lett. 17, 2409-2412.

Kneller, E. A., Long, M. D., van Keken, P. E., Karato, S.-i., 2006. Olivine fabric transitions and shear-wave anisotropy in the Ryukyu subduction system. In preparation for submission to Nature.

Kneller, E. A., van Keken, P. E., Karato, S.-i., Park, J., 2005. B-type olivine fabric in the mantle wedge: Insights from high-resolution non-Newtonian subduction zone models. Earth Planet. Sci. Lett. 237, 781-797.

Kohlstedt, D. L., Evans, B., Mackwell, S. J., 1995. Strength of the lithosphere: Constraints imposed by laboratory experiments. J. Geophys. Res. 100, 17,587-17,602.

Kosarev, G. L., Makeyeva, L. I., Savarensky, Ye. F., Chesnokov, Ye. M., 1979. Influence of anisotropy under a seismograph station on the records of body waves. Izvestiya, Phys. Solid Earth 15, 102-110.

Kubo, A., Fukuyama, E., 2003. Stress field along the Ryukyu Arc and the Okinawa Trough inferred from moment tensors of shallow earthquakes. Earth Planet. Sci. Lett. 210, 305-316.

Kumazawa, M., Anderson, O. L., 1968. Elastic moduli, pressure derivatives, and temperature derivatives of single-crystal olivine and single-crystal forsterite. J. Geophys. Res. 74, 5961-5972.

Lallemand, S., Liu, C.-S., Dominguez, S., Schnuerle, P., Malavielle, J., 1999. Trench-parallel stretching and folding of forearc basins and lateral migration of the

accretionary wedge in the southern Ryukyus: a case of strain partition caused by oblique convergence. Tectonics 18, 231-247.

Lassak, T. M., Fouch, M. J., Hall, C. E., Kaminski, É., 2006. Seismic characterization of mantle flow in subduction systems: Can we resolve a hydrated mantle wedge? Earth Planet. Sci. Lett., in press.

Lay, T., Williams, Q., Garnero, E., Kellogg, L., Wysession, M. E., 1998. Seismic wave anisotropy in the D'' region and its implications. In: Gurnis, M., et al. (Ed.), The Core-Mantle Boundary Region. Am. Geophys. Union, Geodyn. Ser., vol. 28.

Lay, T., Young, C. J., 1991. Analysis of seismic SV-waves in the core's penumbra. Geophys. Res. Lett. 18, 1373-1376.

Lebedev, S., Nolet, G., 2003. Upper mantle beneath Southeast Asia from S velocity tomography. J. Geophys. Res. 108, 2048, doi:10.1029/2000JB000073.

Lev., E., Long, M. D., van der Hilst, R. D., 2006. Seismic anisotropy in eastern Tibet from shear-wave splitting reveals changes in lithospheric deformation. Earth Planet. Sci. Lett, submitted for publication.

Levin, V., Droznin, D., Park, J., Gordeev, E., 2004. Detailed mapping of seismic anisotropy with local shear waves in southeastern Kamchatka. Geophys. J. Int. 158, 1009-1023.

Levin, V., Menke, W., Park, J., 1999. Shear wave splitting in the Appalachians and the Urals: A case for multilayered anisotropy. J. Geophys. Res. 104, 17,975-17,993.

Levin. V., Menke, W., Park, J., 2000. No regional anisotropic domains in the northeastern U.S. Appalachians. J. Geophys. Res. 105, 19,029-19,042.

Letouzey, J., Kimura, M., 1985. Okinawa Trough genesis: structure and evolution of a backarc basin developed in a continent. Marine Petrol. Geol. 2, 111-130.

Li, C., van der Hilst, R. D., Toksöz, M. N., 2006. Constraining P-wave velocity variations in the upper mantle beneath Southeast Asia. Phys. Earth Planet. Inter. 154, 180-195.

Liebermann, R. C., Li, B., 1998. Elasticity at high pressures and temperatures. Rev. Mineral. 37, 459-492.

Long, M. D., de Hoop, M. V., Hager, B. H., van der Hilst, R. D., 2006a. Two-dimensional modeling of subduction zone anisotropy with applications to southwestern Japan. In preparation for submission to Geophys. J. Int.

Long, M. D., de Hoop, M. V., van der Hilst, R. D., Hager, B. H., 2006b. Inversion of shear wave splitting intensities for anisotropic structure and coupling with numerical flow models. In preparation for submission to J. Geophys. Res.

Long, M. D., van der Hilst, R. D. 2005a. Upper mantle anisotropy beneath Japan from shear wave splitting. Phys. Earth Planet. Inter. 151, 206-222.

Long, M. D., van der Hilst, R. D., 2005b. Estimating shear-wave splitting parameters from broadband recordings in Japan: A comparison of three methods. Bull. Seism. Soc. Am. 95, 1346-1358.

Long, M. D., van der Hilst, R. D., 2006. Shear wave splitting from local events beneath the Ryukyu Arc: Trench-parallel anisotropy in the mantle wedge. Phys. Earth Planet. Inter., in press.

Long, M. D., Xiao, X., Jiang, Z., Evans, B., Karato, S-i., 2006. Lattice preferred orientation in deformed polycrystalline (Mg,Fe)O and implications for anisotropy in D''. Phys Earth Planet. Inter., in press.

MacBeth, C., 1991. Inversion for subsurface anisotropy using estimates of shear-wave splitting. Geophys. J. Int. 107, 585-595.

Mainprice, D., 1990. An efficient Fortran program to calculate seismic anisotropy from the lattice preferred orientation of minerals. Computers & Geosciences 16, 385-393.

Malvern, L. E., 1969. Introduction to the mechanics of a continuous media. Prentice-Hall, Englewood Cliffs, NJ.

Mao, H., Shen, G., Hemley, R. J., 1997. Multivariable dependence of Fe-Mg partitioning in the lower mantle. Science 278, 2098-2100.

Margheriti, L., Nostro, C., Cocco, M., Amato, A., 1996. Seismic anisotropy beneath the Northern Apennines (Italy) and its tectonic implications. Geophys. Res. Lett. 23, 2721-2724.

Marson-Pidgeon, K., Savage, M.K., 1997. Frequency-dependent anisotropy in Wellington, New Zealand. Geophys. Res. Lett., 24, 3297-3300.

Marson-Pidgeon, K., Savage, M. K., Gledhill, K., Stuart, G., 1999. Seismic anisotropy beneath the lower half of the North Island, New Zealand. J. Geophys. Res. 104, 20,277-20,286.

Matcham, I., Savage, M. K., Gledhill, K. R., 2000. Distribution of seismic anisotropy in the subduction zone beneath the Wellington region, New Zealand. Geophys. J. Int. 140, 1-10.

Matzel, E., Sen, M. K., Grand, S. P., 1996. Evidence for anisotropy in the deep mantle beneath Alaska. Geophys. Res. Lett. 23, 2417-2420.

Mazzotti, S., 1999. L'arc insulaire japonais: déformation transitoire et permanente liée à la subduction et à la collision. Ph.D. Thesis, Université Paris-Sud, Orsay-Paris XI.

McCaffrey, R., 1996. Estimates of modern arc-parallel strain rates in forearcs. Geology 24, 27-30.

McKenzie, D., 1979. Finite deformation during fluid flow. Geophys. J. R. Astr. Soc. 58, 689-715.

McNamara, A. K., Karato, S.-i., van Keken, P. E., 2001. Localization of dislocation creep in the lower mantle: implications for the origin of seismic anisotropy. Earth Planet. Sci. Lett. 191, 85-99.

McNamara, A. K., van Keken, P. E., Karato, S.-i., 2002. Development of anisotropic structure in the Earth's lower mantle by solid-state convection. Nature 416, 310-314.

Meade, C., Silver, P. G., Kaneshima, S., 1995. Laboratory and seismological observations of lower mantle isotropy. Geophys. Res. Lett. 22, 1293-1296.

Mehl, L., Hacker, B. R., Hirth, G., Kelemen, P. G., 2003. Arc-parallel flow within the mantle wedge: Evidence from the accreted Talkeetna arc, south central Alaska, J. Geophys. Res., 108, 2375, doi:10.1029/2002JB002233.

Menke, W., Levin, V., 2003. The cross-convolution method for interpreting SKS splitting observations, with application to one and two-layer anisotropic earth models. Geophys. J. Int. 154, 379-392.

Mensch, T., Rasolofosaon, P., 1997. Elastic-wave velocities in anisotropic media of arbitrary symmetry – generalization of Thomsen's parameters ε, δ, and γ. Geophys. J. Int. 128, 43064.

Merkel, S., Wenk, H.-R., Shu, J., Shen, G., Gillet, P., Mao, H.-k., Helmley, R. J., 2002. Deformation of polycrystalline MgO at pressures of the lower mantle. J. Geophys. Res. 107, 2271, doi:10.1029/2001JB000920.

Mitchell, B. J., Helmberger, D. V., 1973. Shear velocities at the base of the mantle from observations of S and ScS. J. Geophys. Res. 78, 6009-6020.

Miyajima, N., Ohgushi, K., Ichihara, M., Yagi, T., Frost, D., Rubie, D. C., 2005. Crystal morphology and dislocation textures of the $CaIrO_3$ phase - TEM study of an analogue of the post-perovskite phase. Eos Trans. AGU, 86 (52), Fall Meet. Suppl., Abstract MR23B-0069.

Mizukami, T., Wallis, S. R., Yamamoto, J., 2004. Natural examples of olivine lattice preferred orientation patterns with a flow-normal a-axis maximum. Nature 427, 432-436.

Montagner, J.-P., Kennett, B. L. N., 1995. How to reconcile body-wave and normal-mode reference Earth models? Geophys. J. Int. 125, 229-248.

Moore, M. M., Garnero, E. J., Lay, T., Williams, Q., 2004. Shear wave splitting and waveform complexity for lowermost mantle structures with low-velocity lamellae and transverse isotropy. J. Geophys. Res. 109 (doi:10.1029/2003JB002546).

Murakami, M., Hirose, K., Kawamura, K., Sata, N., Ohishi, Y., 2004. Post-perovskite phase transition in $MgSiO_3$. Science 304, 855-858.

Nakajima, J., Hasegawa A., 2004. Shear-wave polarization anisotropy and subduction-induced flow in the mantle wedge of northern Japan. Earth Planet. Sci. Lett. 225, 365-377.

Nakajima, J., Shimizu, J., Hori, S., Hasegawa, A., 2006. Shear-wave splitting beneath the southwestern Kurile arc and northeastern Japan arc: A new insight into mantle return flow. Geophys. Res. Lett. 33, doi:10.1029/2005GL025053.

Nakamura, M., Yoshida, Y., Zhao, D., Katao, H., Nishimura, S., 2003. Three-dimensional P- and S-wave velocity structures beneath the Ryukyu arc. Tectonophysics 369, 121-143.

Nicolas, A., Christensen, N. I., 1987. Formation of anisotropy in upper mantle peridotites: a review. In: Fuchs, K, Froidevaux, C., (Ed.), Composition, structure and dynamics of the lithosphere-asthenosphere system, Am. Geophys. Union, Geodyn. Ser., vol. 16.

Niu, F., Perez, A. M., 2004. Seismic anisotropy in the lower mantle: A comparison of waveform splitting of SKS and SKKS. Geophys. Res. Lett. 31, doi:10.1029/2004GL021196.

Oganov, A. R., Martonak, R., Laio, A., Raiteri, P., Parrinello, M., 2005. Anisotropy of Earth's D" layer and stacking faults in the MgSiO3 post-perovskite phase. Nature 438, 1142-1144.

Oganov, A. R., Ono, S., 2004. Theoretical and experimental evidence for a post-perovskite phase of $MgSiO_3$ in Earth's D" layer. Nature 430, 445-448.

Okaya, D. A., McEvilly, T. V., 2003. Elastic wave propagation in anisotropic crustal material possessing arbitrary internal tilt. Geophys. J. Int. 153, 344-358.

Özalaybey, S., Chen, W.-P., 1999. Frequency-dependent analysis of SKS/SKKS waveforms observed in Australia: evidence for null birefringence. Phys. Earth Planet. Inter. 114, 197-210.

Özalaybey, S. and M. K. Savage, 1994. Double-layer anisotropy resolved from S phases, Geophys. J. Int., 117: 653-664.

Özalaybey, S., Savage, M. K., 1995. Shear-wave splitting beneath western United States in relation to plate tectonics. J. Geophys. Res. 100, 18,135-18,149.

Paige, C. C., Saunders, M. A., 1982. LSQR: an algorithm for sparse linear equations and sparse least squares. ACM Trans. Math. Soft. 8, 43-71.

Park, J., Levin, V., 2002. Seismic anisotropy: Tracing plate dynamics in the mantle, Science, 296, 485-489.

Park, J., Levin, V., Brandon, M. T., Lees, J. M., Peyton, V., Gordeev, E., Ozerov, A., 2002. A dangling slab, amplified arc volcanism, mantle flow and seismic anisotropy near the Kamchatka plate corner. In: Stein, S., Freymeuller, J., (Ed), Plate Boundary Zones, Am. Geophys. Union, Geodyn. Ser., vol. 30.

Peyton, V., Levin, V., Park, J., Brandon, M., Lees, J., Gordeev, E., Ozerov, A., 2001. Mantle flow at a slab edge; seismic anisotropy in the Kamchatka region. Geophys. Res. Lett. 28, 379-382.

Pozgay, S. H., Wiens, D. A., Conder, J. A., Shiobara, H., Sugioka, H., 2006. Mantle flow throughout the Mariana subduction system from shear wave splitting. To be submitted to Geophys. J. Int.

Restivo, A., Helffrich, G., 1999. Teleseismic shear wave splitting measurements in noisy environments. Geophys. J. Int. 137, 821-830.

Ringwood, A. E., 1991. Phase transitions and their bearing on the constitution and dynamics of the mantle. Geochim. Cosmochim. Acta 55, 2083-2110.

Ritsema, J., 2000. Evidence for shear velocity anisotropy in the lowermost mantle beneath the Indian Ocean. Geophys. Res. Lett. 27, 1041-1044.

Rümpker, G., Silver, P. G., 1998. Apparent shear-wave splitting parameters in the presence of vertically varying anisotropy. Geophys. J. Int. 135, 790-800.

Rupke, L. H., Phipps Morgan, J., Hort, M., Connolly, J. A. D., 2004. Serpentine and the subduction zone water cycle. Earth Planet. Sci. Lett. 223, 17-34.

Russell, S. A., Lay, T., Garnero, E., 1998. Seismic evidence for small-scale dynamics in the lowermost mantle at the root of the Hawaiian hotspot. Nature 396, 255-258.

Russo, R. M., Silver, P. G., 1994. Trench-parallel flow beneath the Nazca Plate from seismic anisotropy. Science 263: 1105-1111.

Ryberg, T., Rümpker, G., Haberland, C., Stromeyer, D., Weber, M., 2005. Simultaneous inversion of shear wave splitting observations from seismic arrays. J. Geophys. Res. 110 (doi:10.1029/2004JB003303).

Saltzer, R. L., Gaherty, J., Jordan, T. H., 2000. How are vertical shear wave splitting measurements affected by variations in the orientation of azimuthal anisotropy with depth?. Geophys. J. Int. 141, 374-390.

Sandvol, E., Ni, J., 1997. Deep azimuthal seismic anisotropy in the southern Kurile and Japan subduction zones. J. Geophys. Res. 102, 9911-9922.

Savage, M. K., 1999. Seismic anisotropy and mantle deformation: What have we learned from shear wave splitting? Rev. Geophys. 37, 65-106.

Savage, M. K., Silver, P. G., 1993. Mantle deformation and tectonics: constraints from seismic anisotropy in the western United States. Phys. Earth Planet. Inter. 78, 207-227.

Schellart, W. P., Lister, G. S., Jessell, M. W., 2002. Analogue modelling of asymmetrical back-arc extension. J. Virtual Explorer 7, 25-42.

Schoenberg, M. A., de Hoop, M. V., 2000. Approximate dispersion relations for qP-qSV-waves in transversely isotropic media. Geophysics 65, 919-933.

Schulte-Pelkum, V., Blackman, D. K., 2003. A synthesis of seismic P and S anisotropy. Geophys. J. Int. 154, 166-178.

Shim, S.-H., Duffy, T. S., Jeanloz, R., Shen, G., 2004. Stability and crystal structure of $MgSiO_3$ perovskite to the core-mantle boundary. Geophys. Res. Lett 31, doi:10.1029/2004GL019639.

Šílený, J., Plomerová, J., 1996. Inversion of shear-wave splitting parameters to retrieve three-dimensional orientation of anisotropy in continental lithosphere. Phys. Earth Planet. Inter. 95, 277-292.

Silver, P. G., 1996. Seismic anisotropy beneath the continents: probing the depths of geology. Annu. Rev. Earth Planet. Sci. 24, 385-432.

Silver, P. G., Chan, W. W., 1988. Implications for continental structure and evolution from seismic anisotropy, *Nature, 335,* 34-39.

Silver, P. G., Chan, W. W., 1991. Shear wave splitting and subcontinental mantle deformation, *J. Geophys. Res., 96,* 16,429-16,454.

Silver, P. G., Savage, M. K., 1994. The interpretation of shear-wave splitting parameters in the presence of two anisotropic layers. Geophys. J. Int. 119, 949-963.

Simons, F.J., van der Hilst, R.D., Montagner, J.-P., Zielhuis, A., 2002. Multimode Rayleigh wave inversion for heterogeneity and azimuthal anisotropy of the Australian upper mantle. Geophys. J. Int. 151, 738-755.

Simons, F.J., van der Hilst, R.D., 2003. Anisotropic structure and deformation of the Australian lithosphere. Earth Planet. Sci. Let. 211, 271-286.

Skemer, P., Katayama, I., Karato, S.-i., 2006. Peridotite deformation fabrics from Cima di Gagnone, Central Alps, Switzerland: evidence of deformation under water-rich conditions at low temperatures. Contrib. Mineral. Petr., submitted for publication.

Smith, C. M. B., Fouch, M. J., 2005. Shear wave splitting and mantle flow beneath Japan. Earth Planet. Sci. Lett, submitted for publication.

Smith, W. H. F., Sandwell, D. T., 1997. Global seafloor topography from satellite altimetry and ship depth soundings, Science 277, 1957-1962.

Smith, G. P., Wiens, D. A., Fischer, K. M., Dorman, L. M., Webb, S. C., Hildebrand, J. A., 2001. A complex pattern of mantle flow in the Lau Backarc. Science 292, 713-716.

Stacey, F. D., 1992. Physics of the Earth. Brookfield Press, Brisbane, Australia.

Stern, R. J., 2002. Subduction zones. Rev. Geophys 40, 1012, doi:10.1029/ 2001RG000108.

Stixrude, L., 2000. Elasticity of mantle phases at high pressure and temperature. In: Karato, S.-i. et al. (Ed.), Earth's Deep Interior: Mineral Physics and Tomography from the Atomic to the Global Scale. Am. Geophys. Union, Geophys. Monograph Ser., vol. 117.

Stork, C., Clayton, R. W., 1991. Linear aspects of tomographic velocity analysis. Geophysics 56, 483-495.

Stretton, I., Heidelbach, F., Mackwell, S., Langenhorst, F., 2001. Dislocation creep of magnesiowüstite ($Mg_{0.8}Fe_{0.2}O$). Earth Planet. Sci. Lett. 194, 229-240.

Sturhahn, W., Jackson, J. M., Lin, J.-F., 2005. The spin state of iron in minerals of Earth's lower mantle. Geophys. Res. Lett. 32, doi:10.1029/2005GL022802.

Taira, A., Tectonic evolution of the Japanese Island arc system. 2001. Annu. Rev. Earth Planet. Sci. 29, 109-134.

Thomsen, L., 1986. Weak elastic anisotropy. Geophysics 51, 1954-1966.

Tommasi, A., Mainprice, D., Canova, G., Chastel, Y., 2000. Viscoplastic self-consistent and equilibrium-based modeling of olivine lattice preferred orientations: Implications for the upper mantle seismic anisotropy. J. Geophys. Res. 105, 7893-7908.

Turcotte, D. L., Schubert, G., 1982. Geodynamics: Applications of Continuum Physics to Geological Problems. John Wiley & Sons, New York.

Tsuchiya, T., Tsuchiya, J., Umemoto, K., Wentzcovitch, R. M., 2004. Elasticity of post-perovskite $MgSiO_3$. Geophys. Res. Lett. 31, doi:10.1029/2004GL020278.

van der Hilst, R., Engdahl, R., Spakman, W., Nolet, G., 1991. Tomographic imaging of subducted lithosphere below northwest Pacific island arcs. Nature 353, 37-43.

van Keken, P. E., 2003. The structure and dynamics of the mantle wedge. Earth Planet. Sci. Lett. 215, 323-338.

van Keken, P. E., Kiefer, B., Peacock, S., 2000. High resolution models of subduction zones: implications for mantle dehydration reactions and the transport of water into the deep mantle. Geochem. Geophys. Geosyst. 3, doi:10.1029/2002GL015390.

Vidale, J. E., 1986. Complex polarization analysis of particle motion. Bull. Seism. Soc. Am. 71, 1511-1530.

Vinnik, L. P., Farra, V., Romanowicz, B., 1989a. Azimuthal anisotropy in the Earth from observations of SKS at GEOSCOPE and NARS broadband stations, Bull. Seism. Soc. Am., *79,* 1542-1558.

Vinnik, L., Farra, V., Romanowicz, B., 1989b. Observational evidence for diffracted S_V in the shadow of the Earth's core, Geophys. Res. Lett., 16:519-522.

Vinnik, L., L. Bréger, Romanowicz, B., 1998. On the inversion of Sd particle motion for seismic anisotropy in D''. Geophys. Res. Lett. 25, 679-682.

Vinnik, L., Romanowicz, B., Le Stunff, Y., Makeyeva, L., 1995. Seismic anisotropy in the D'' layer. Geophys. Res. Lett. 22, 1657-1660.

Walker, K. T., Bokelmann, G. H. R., Klemperer, S. L., 2001. Shear-wave splitting to test mantle deformation models around Hawaii. Geophys. Res. Lett. 28, 4319-4322.

Waite, G. P., Schutt, D. L., Smith, R. B., 2005. Models of lithosphere and asthenosphere anisotropic structure of the Yellowstone hot spot from shear wave splitting, J. Geophys. Res. 110, B11304, doi:10.1029/2004JB003501.

Wang, T. K., Lin, S.-F., Liu, C.-S., Wang, C.-S., 2004. Crustal structure of the southernmost Ryukyu subduction zone: OBS, MCS and gravity modelling. Geophys. J. Int. 157, 147-163.

Wentzcovitch, R. M., Karki, B. B., Karato, S., Da Silva, C. R. S., 1998. High pressure elastic anisotropy of $MgSiO_3$ perovskite and geophysical implications. Earth Planet. Sci. Lett. 164, 371-378.

Widiyantoro, S., Kennett, B. L. N., van der Hilst, R. D., 1999. Seismic tomography with P and S data reveals lateral variations in the rigidity of deep slabs. Earth Planet. Sci. Lett. 173, 91-100.

Wiens, D. A., Smith, G. P., 2003. Seismological constraints on structure and flow patterns within the mantle wedge. In: Eiler, J. M. (Ed.), Inside the Subduction Factory. Am. Geophys. Union, Geophys. Monogr. Ser., vol. 138.

Wolfe, C. J., Silver, P. G., 1998. Seismic anisotropy of oceanic upper mantle: shear wave splitting methodologies and observations. J. Geophys. Res. 103, 749-771.

Wolfe, C. J., Solomon, S. C., 1998. Shear-wave splitting and implications for mantle flow beneath the MELT region of the East Pacific Rise. Science 280, 1230-1232.

Wright, S. I., 2000. Fundamentals of automated EBSD. In: Schwartz, A. J. (Ed.), Electron Backscatter Diffraction in Materials Science, Kluwer Academic / Plenum Publishers, New York, USA.

Wysession, M. E., Lay, T., Revenaugh, J., Williams, Q., Garnero, E. J., Jeanloz, R., Kellogg, L. H., 1998. The D'' discontinuity and its implications. In: Gurnis, M., et al. (Ed.), The Core-Mantle Boundary Region. Am. Geophys. Union, Geodyn. Ser., vol. 28.

Xue., M., Allen, R. M., 2005. Asthenospheric channeling of the Icelandic upwelling: Evidence from seismic anisotropy. Earth Planet. Sci. Lett. 235, 167-182.

Yamazaki, D., Karato, S.-i., 2001. Some mineral physics constraints on the rheology and geothermal structure of Earth's lower mantle. Am. Miner. 86, 385-391.

Yamazaki, D., Karato, S.-i., 2002. Fabric development in (Mg,Fe)O during large strain, shear deformation: implications for seismic anisotropy in Earth's lower mantle. Phys. Earth Planet. Inter. 131, 251-267.

Yang, M., Elkibbi, M., Rial, J. A., 2005. An inversion scheme to model subsurface fracture systems using shear wave splitting polarization and delay time observations simultaneously. Geophys. J. Int. 160, 939-947.

Yang, X., Fischer, K. M., Abers, G., 1995. Seismic anisotropy beneath the Shumagin Islands segment of the Aleutian-Alaska subduction zone. J. Geophys. Res. 100, 18,165-18,177.

Yu, S. B., Kuo, L. C., 1996. GPS observations of crustal deformation in the Taiwan-Luzon region. Geophys. Res. Lett. 26, 923-926.

Zhang, S., Karato, S.-i., 1995. Lattice preferred orientation of olivine aggregates deformed in simple shear. Nature 375, 774-777.

Zheng, X., 2004. Inversion for elastic parameters in weakly anisotropic media. Geophys. J. Int. 159, 1077-1089.

Zhu, J., Dorman, J., 2000. Two-dimensional, three-component wave propagation in a transversely isotropic medium with arbitrary orientation – finite-element modeling. Geophysics 65, 934-942.

Zimmerman, M. E., Zhang, S., Kohlstedt, D. L., Karato, S.-i. 1999. Melt distribution in mantle rocks deformed in shear. Geophys. Res. Lett. 26, 1505-1508.